# Metabolic nanosensors for the identification of tumoral metabo-phenotypes

**Consuelo Ripoll Lorente**

Directores de la tesis:

Ángel Orte Gutierrez

Mª José Ruedas Rama

Miguel Martín Hernández

Granada, 2019

# TABLE OF CONTENTS

# *Introduction*

# 1. INTRODUCTION

## 1.1. CANCER STATISTICS

Cancer is used to commonly name a set of related diseases, in which there is a process of uncontrolled division of cells of the body. Currently, cancer is the second cause of death in the world. According World Health Organization (WHO), during 2018 there have been 18.1 million new cases of cancer and 9.6 million people have died of cancer (Figure 1.1). Cancer deaths increase every year. It is estimated that throughout the XXIst century will be the main cause of death in developed countries.
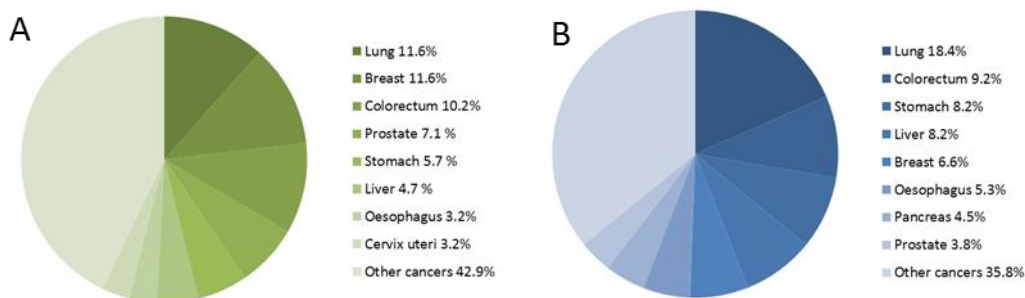


Figure 1.1. A) The graph shows the incidence of cancers diagnosed in both sexes worldwide in 2018. B) The graph shows the mortality due to different types of cancer worldwide in 2018.

In Spain there are 46.4 million inhabitants, of whom 276,363 have been diagnosed with cancer during 2018. 113,584 are the deaths that have been reported during this year due to cancer in Spain. According to the National Institute of Statistics (INE), in 2017 there were 423,643 deaths in Spain, of which 109,425 were due to cancer. Therefore, 25.8% of deaths occurred in Spain in 2017 are due to cancer.

There are more than 100 types of cancer than affect humans. Both worldwide and in Spain, only 5 types of cancers represent approximately 50% of cancer cases, as shown in Figure 1.2.

Worldwide, the most common cancer is lung cancer, followed by breast cancer. However in Spain, the most common cancer is the colorectal cancer and the second most common cancer is the same as breast cancer worldwide. The most notable difference between the data from Spain and worldwide is that bladder cancer appears as the 5th most common type of cancer, in contrast to stomach cancer worldwide.
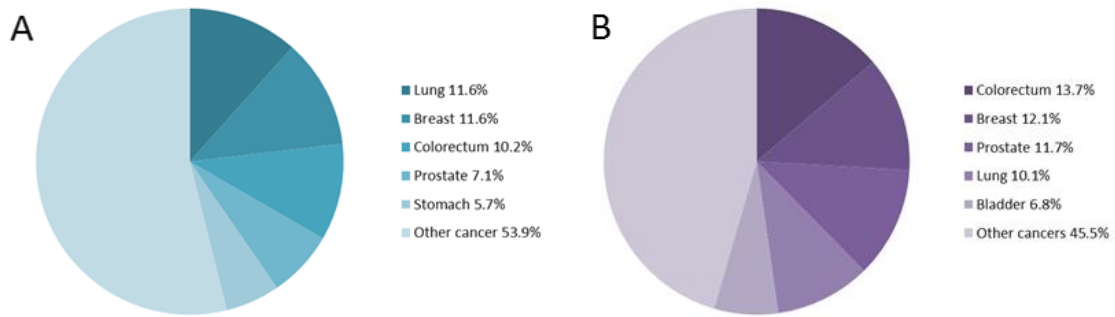
Figure 1.2. A) The graph shows the percentage of the most common types of cancer diagnosed during 2018 in the world. B) The graph shows the percentage of the most common types of cancer diagnosed during 2018 in Spain.

The relative frequency of each type of cancer varies according to age and sex (Figure 1.3). According to data obtained from Asociación española contra el cancer (AECC), the most common cancer in children is leukaemia, follow by cancers in the central system. However, in adolescence the most common cancers are Hodgkin lymphomas, bone tumors and central nervous system. In the case of adult cancer patients, the most common cancers in Spain are colorectal, prostate, lung and breast cancer. Lung cancer is the one that causes more deaths a year in men, however it is breast cancer, which produces the highest mortality in women.
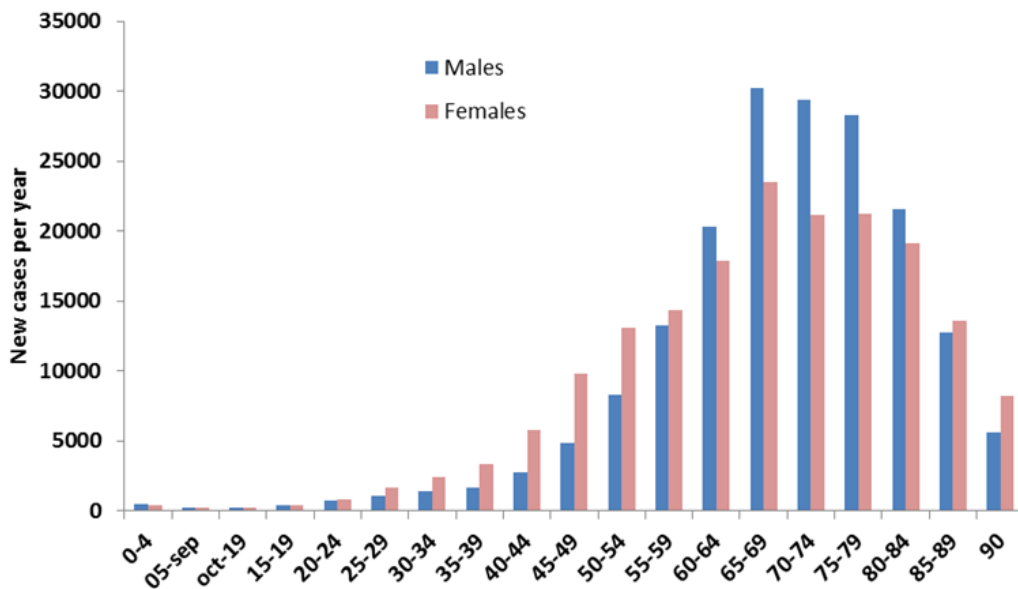


Figure 1.3. The graph shows the distribution of the new cases of cancer by ages and by sexes.

Most new cases of cancer appear between 60-80 years old, both in women and men. Until the age of 40, the cases of cancer diagnosed are below 5,000 cases, well below the 30,000 cases diagnosed around the age of 60.

As mentioned earlier, there are differences between the types of cancer that affect women and men (Figure 1.4).
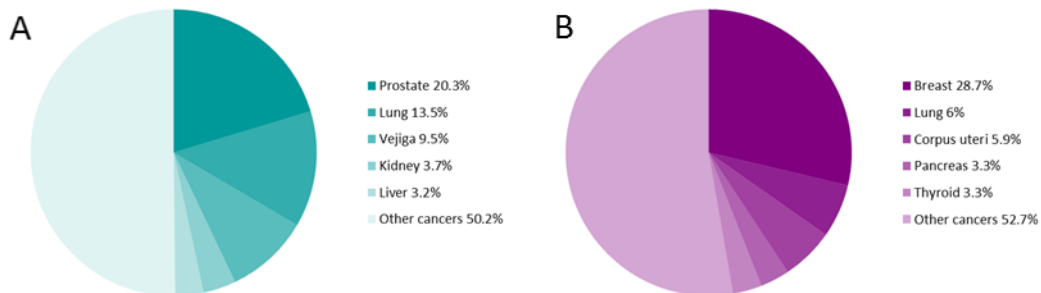


Figure 1.4. A) The graph shows the five main types of cancer in men. B) The graph shows the five main types of cancer in women. This data are in Spain in 2018.

As can be seen in Figure 1.4, the most frequent types of cancer in men and women vary considerably, only coinciding with lung cancer. In men, the most common cancer is prostate cancer and in women the most common type of cancer is breast cancer.

As we see in the data collected above, the numbers that currently exist on cancer are chilling, more than 18 million new diagnoses every year and almost 10 million deaths. Even so the worst thing is that the tendency is to continue increasing. That is why it is so important to strive to achieve early diagnosis that favours survival and new less aggressive and more effective treatments.

Table 1.1. Classification of the most common types of cancers in different age ranges. The table also includes the number of cases of each type of cancer that have been diagnosed during 2018 in the world.

| Age range | Incidence of type of cancer and number of the cases in both sex | | | | | |
|---|---|---|---|---|---|---|
| 0-4 | All cancers 81117 | Leukaemia 27750 | Brain, nervous system 9205 | Kidney 7902 | Non-Hodgkin lymphoma 5332 | Liver 2850 |
| 5-9 | All cancers 61423 | Leukaemia 21047 | Brain, nervous system 8127 | Non-Hodgkin lymphoma 6265 | Kidney 3084 | Hodgkin lymphoma 2807 |
| 10-14 | All cancers 57626 | Leukaemia 16314 | Brain, nervous system 6650 | Non-Hodgkin lymphoma 5615 | Hodgkin lymphoma 4344 | Thyroid 1848 |
| 15-19 | All cancers 72437 | Leukaemia 12958 | Thyroid 7650 | Brain, nervous system 6124 | Non-Hodgkin lymphoma 5752 | Hodgkin lymphoma 5720 |
| 20-24 | All cancers 114390 | Thyroid 17332 | Leukaemia 11603 | Testis 7403 | Non-Hodgkin lymphoma 7050 | Brain, nervous system 6605 |
| 25-29 | All cancers 210924 | Breast 36010 | Thyroid 30382 | Cervix uteri 17874 | Leukaemia 12246 | Testis 9851 |
| 30-34 | All cancers 345803 | Breast 78342 | Thyroid 42922 | Cervix uteri 36730 | Leukaemia 13708 | Non-Hodgkin lymphoma 13233 |
| 35-39 | All cancers 487453 | Breast 122609 | Cervix uteri 50895 | Thyroid 48779 | Colorectum 24139 | Liver 17455 |
| 40-44 | All cancers 721454 | Breast 173181 | Cervix uteri 65456 | Thyroid 58425 | Colorectum 46216 | Liver 33811 |
| 45-49 | All cancers 1095280 | Breast 227662 | Colorectum 85852 | Lung 79306 | Cervix uteri 76909 | Thyroid 70141 |
| 50-54 | All cancers 1514074 | Breast 261645 | Lung 148423 | Colorectum 135697 | Liver 89260 | Stomach 81550 |
| 55-59 | All cancers 1917807 | Breast 264747 | Lung 226402 | Colorectum 188120 | Prostate 118088 | Stomach 111100 |
| 60-64 | All cancers 2285471 | Lung 305860 | Breast 251439 | Colorectum 239554 | Prostate 202127 | Stomach 141301 |
| 65-69 | All cancers 2496078 | Lung 366670 | Colorectum 279842 | Prostate 265334 | Breast 221184 | Stomach 163706 |
| 70-74 | All cancers 2182802 | Lung 323139 | Colorectum 256560 | Prostate 247039 | Breast 166463 | Stomach 141467 |

Table 1.2. Number of worldwide deaths produced in 2018 due to cancer, classified in different age ranges.

| Age range | Mortality of type of cancer and number of the cases in both sex | | | | | |
|---|---|---|---|---|---|---|
| 0-4 | All cancers 28838 | Leukaemia 11223 | Brain, nervous system 5101 | Liver 1804 | Kidney 1476 | Non-Hodgkin lymphoma 1178 |
| 5-9 | All cancers 23691 | Leukaemia 9489 | Brain, nervous system 4854 | Non-Hodgkin lymphoma 1458 | Kidney 730 | Liver 502 |
| 10-14 | All cancers 22427 | Leukaemia 8529 | Brain, nervous system 3687 | Non-Hodgkin lymphoma 3687 | Kaposi sarcoma 587 | Hodgkin lymphoma 479 |
| 15-19 | All cancers 26768 | Leukaemia 8166 | Brain, nervous system 3188 | Non-Hodgkin lymphoma 2184 | Kaposi sarcoma 990 | Liver 885 |
| 20-24 | All cancers 37581 | Leukaemia 8409 | Brain, nervous system 3588 | Non-Hodgkin lymphoma 3334 | Kaposi sarcoma 1729 | Colorectum 1619 |
| 25-29 | All cancers 63237 | Leukaemia 9247 | Breast 5135 | Brain, nervous system 4813 | Non-Hodgkin lymphoma 4737 | Cervix uteri 4008 |
| 30-34 | All cancers 106794 | Breast 14203 | Leukaemia 10130 | Cervix uteri 9859 | Liver 8537 | Brain, nervous system 6630 |
| 35-39 | All cancers 164949 | Breast 24759 | Cervix uteri 16844 | Liver 16004 | Leukaemia 10188 | Colorectum 9214 |
| 40-44 | All cancers 264170 | Breast 36702 | Liver 30337 | Cervix uteri 24798 | Lung 20657 | Stomach 15775 |
| 45-49 | All cancers 449059 | Lung 56180 | Liver 54887 | Breast 51082 | Cervix uteri 33033 | Stomach 31933 |
| 50-54 | All cancers 685678 | Lung 110248 | Liver 77982 | Breast 65377 | Stomach 53631 | Colorectum 47884 |
| 55-59 | All cancers 913039 | Lung 171101 | Liver 91298 | Stomach 74794 | Breast 72495 | Colorectum 67473 |
| 60-64 | All cancers 1138886 | Lung 238821 | Liver 103838 | Stomach 98635 | Colorectum 89483 | Oesophagus 73897 |
| 65-69 | All cancers 1317307 | Lung 297389 | Stomach 121893 | Colorectum 112543 | Liver 109876 | Oesophagus 86974 |
| 70-74 | All cancers 1221873 | Lung 277513 | Colorectum 116659 | Stomach 109786 | Liver 91033 | Oesophagus 72846 |

As we see in the data collected above, the numbers that currently exist on cancer are chilling, more than 18 million new diagnoses every year and almost 10 million deaths. Even so the worst thing is that the tendency is to continue increasing. That is why it is so important to strive to achieve early diagnosis that favours survival and new less aggressive and more effective treatments.

## 1.2 NANOTECHNOLOGY

The approach in this Thesis is the development of new diagnosis strategies, by using novel nanotechnological tools. Hence, it is interesting to introduce the general concepts of nanotechnology.

### 1.2.1 NANOTECHNOLOGY DEFINITIONS

Due to the fact that nanotechnology is still under ongoing development, many different definitions can be found in the literature, some of them contradicting each other. The definitions[1] of nanotechnology have different approaches depending on the aspect in which they are focused. Some of the most known definitions are:

"Structures, devices and systems with novel properties and functions due to the arrangement of their atoms in the scale from 1 to 100 nanometers. Many fields of work contribute to nanotechnology, including molecular physics, materials science, chemistry, biology, computer science, electrical engineering and mechanical engineering" from The Foresight Institute.

"Nanotechnology is the study of phenomena and the development of materials at the atomic, molecular and macromolecular scales, in which the properties differ significantly from those of a larger scale. Products based on nanotechnology are already in use and analysts expect markets to grow by hundreds of billions of euros during this decade" from The European Commission.

"Nanotechnology is the understanding and control of matter in dimensions between approximately 1 and 100 nanometers, where unique phenomena allow novel applications. Nanotechnology, which encompasses nanoscale science, engineering and technology, includes images creation, measurement, modelling and manipulation of matter at this scale of length" from National Nanotechnology Initiative.

In general, we refer to nanotechnology as the wide range of research and applications whose common feature is nanometric size.

### 1.2.2 HISTORY OF NANOTECHNOLOGY

The idea or concept of nanotechnology first emerged on September 29, 1959 in a talk entitled "There is Plenty of Room at the Bottom" by physicist Richard Feynman at a meeting of the Physics Society at the California Institute of Technology (CalTech). In his talk, Feynman described a process in which scientists could manipulate and control individual atoms and molecules. Feynman evokes a possible field of research that was then unexplored: the extremely small, the world of the nanoscale. More than a decade

later in 1974, in his explorations of machining ultraprecision, Professor Norio Taniguchi of the University of Tokyo coined the term nanotechnology.

The development of nanosciences and nanotechnologies is based on the invention of the instruments that allow observing and interacting with matter on an atomic or sub-atomic scale. The first of these devices is the tunnelling microscope that was invented in 1981 by Gerd Binnig and Heinrich Rohrer, and that allows to cover conductive or semiconducting surfaces using a quantum phenomenon called "the tunnel effect", to determine the morphology and density of electronic states of the surfaces that it explores. The second is the atomic force microscope, which is a derivate of the tunnelling microscope, and which measures the interaction forces between the tip of a nanometric, metallic cantilever and the explored surface. Unlike the tunnel microscope, this tool allows the visualization of non-conductive materials. These instruments combined with photolithography allow us to observe, manipulate and create nanostructures.

In 1985, three researchers, Richard Smalley, Robert F. Curl (University of Rice in Houston) and Harold W. Kroto (University of Sussex) discovered a new allotropic form of carbon, the C60 molecule consisting of 60 carbon atoms divided over the vertices of a regular polyhedron formed of hexagonal and pentagonal facets. Each carbon atom has a bond with three others. This form is known as the Buckminsterfullerene, due to the architect Richard Buckminster Fuller who created several geodesic domes whose shape is similar to the C6014.

However it was Eric Drexler who in 1986, made the term "nanotechnology" widely known. With his book "Engines of Creation", he inspired many doctors and scientists to start studying the diverse applications of this new science. In 1986, Drexler co-founded the Institute of Prospective Studies, to promote the study and application of nanotechnology.

In the next table, it is possible see the main discoveries of a resume way, from 1959 to 2011. From 2011, there are so many discoveries and advances in nanotechnology that it would be impossible to mention them all. However, it is important to highlight the Nobel Prize in Chemistry awarded in 2016 to researchers Jean-Pierre Sauvage, Sir J. Fraser Stoddart and Bernard L. Feriga "for the development and synthesis of molecular machines" and the Nobel Prize in Physics in 2018 awarded "for the groundbreaking inventions in the field of laser physics" to Arthur Ashkin, "for the optical tweezers and their application to biological systems" to Gérard Mourou and to Donna Strickland "for their method of generating high-intensity, ultra-short optical pulses".

Table 1.3. Major development in the field of nanotechnology from 1959 to 2011[2].

| Year | Development |
|------|-------------|
| 1959 | Feynman gives after-dinner talk describing molecular machines built with atomic precision |
| 1974 | Taniguchi uses term "nanotechnology" in paper on ion-sputter machining |
| 1977 | Drexler originates molecular nanotechnology concepts at MIT |
| 1981 | First technical paper on molecular engineering for building with atomic precision STM invented |
| 1985 | Buckyball discovered |
| 1986 | First book published, AFM invented, first organization formed |
| 1989 | IBM logo spelled in individual atoms |
| 1991 | Carbon nanotube discovered |
| 1997 | First company founded: Zyvez<br>First design of nanorobotic system |
| 1998 | First DNA-based nanomechanical device |
| 1999 | First nanomedice book published |
| 2000 | President Clinton announces US National Nanotechnology Initiative |
| 2001 | First report on nanotech industry<br>US announces first center for military applications |
| 2002 | First nanotech industry conference, regional efforts multiply |
| 2003 | Congressional hearings in societal implications<br>Call for balancing NNI research portfolio<br>Drexler/Smalley debate is published in *Chemical & Engineering News* |
| 2004 | First policy conference on advanced nanotech<br>First center for nanomechanical system |
| 2010 | DNA-based "robotic" assembly begins |
| 2011 | First programmable nanowire circuits for nanoprocessors<br>DNA molecular robots learn to walk in any direction along a branched track<br>Mechanical manipulation if silicon dimers on a silicon surface |

**1.2.2.1** Physic of nanoscience

At the nanoscale level, materials have particular properties that can justify a specific approach. Of course, they are properties related to quantum mechanics, but also surface effects, and volume or edge effects. Therefore, according to the laws of quantum mechanics, a particle can adopt an undulatory behaviour at the nanoscale at the expense of the normal behaviour we know of particles at the macroscopic level. The wave-particle duality is particularly evident in Young's double-slits experiment. A beam of particles (light, electrons, etc.) interferes with a series of closely spaced slits and creates an interference pattern, characteristic of a wave phenomenon. This particular wave-particle duality of matter remains to this day one of the great questions of physics that will cause various phenomena at the nanometer level, for example:

- Quantization of electricity: in nanowires it was observed that the electric current is no longer constituted by a continuous flow of electrons but is quantized, that is to say that the electrons circulate through "packages" in the circuit.
- Quantization of heat: similarly in a nano-sized circuit, it has been observed that heat propagates in a quantized manner.

These phenomena were observed for the first time in 2001, with the "electrically conductive chain" by its inventor Hurbert Juillet, which allowed confirming the theories of quantum mechanics in this field. This quantum behaviour forces us to revise our thinking: when we want to describe a particle, we no longer speak in terms of position at a given moment, but rather in terms of the probability that the particle is detected in one place instead of another.

The main challenge of the nanosciences is, therefore, to understand these phenomena, but also and above all to benefit from them when designing nanoscale system. Many laboratories around the world are working on this topic.

Nanotechnology is considered one of the fastest growing sciences in this decade. The enormous potential of this new technology has been recognized immediately by both the academic world and the industry. Nanotechnology affects many areas of modern life, which gives it the power to revolutionize our way of doing things, therefore, can present many risks and danger for the future. Human beings have always misused technology to develop destructive things like weapons, detection systems that threaten all levels of privacy, etc. This is a serious concern for human security and generates social, ethical and security concerns. Nanotechnology is very promising, but it would be unwise to ignore its negative aspect and not treat them. Due to it has already entered our lives, it is safe to say that nanotechnology is definitely changing the way we live.

# Aims

# 2. AIMS

This PhD Thesis is a multidisciplinary research, which combines objectives related to the optimization and usage of nanotechnology for the development of new tools for a better understanding of the physiology of cancer. In particular, several nanosensors will be developed and applied in advanced imaging techniques, such as FLIM microscopy. Likewise, it is also an objective of this Thesis to establish a new methodology of classifying tumoral phenotypes based on metabolism. With all these goals in mind, the specific objectives that can be proposed are the following:

1. Development of a series of QD-based nanosensors to be used intracellularly, and specifically for advanced fluorescence lifetime imaging microscopy (FLIM). These nanosensors will report on different physiologically relevant processes. In particular, in this Thesis we will tackle the following aspects:

1.1. Development of a family of intracellular $Zn^{2+}$ nanosensors.

1.2. Development of a set of QD-based pH nanosensors, adequately modified to achieve response to changes in pH levels, and to direct them specifically to the mitochondria.

1.3. Studies of cell permeability, toxicity/viability and location of the nanosensors.

1.4. QDs/mitochondria colocalization studies and measurements of the response of the nanosensors to induced pH changes in cell mitochondria using FLIM microscopy.

2. Study of the metabolic profile of breast cancer cell lines and review of their classification with respect to the current clinical classification.

3. Analysis of pH changes and their relationship with changes in tumour metabolism.

4. Study of metabolic pro-drugs, using dichloroacetate derivatives.

# *Nanosensors*

# 3. NANOSENSORS

## 3.1. INTRODUCTION

### 3.1.1 NANOTECHNOLOGY

Nanotechnology is defined as "the design, characterization, production, and application of materials, devices, and systems by controlling shape and size at the nanoscale"[3]. The nanoscale is in the 1-100 nm range; therefore, nanomaterials have a size in this range. When matter is manipulated on this scale, unexpected properties are obtained. Therefore, nanotechnology is used to create innovative materials, devices and systems with unique properties. More than this concept, what is really interesting is what potentially represents for research and applications, whose purpose is to create new structures and products with a great impact in different sectors, such as industry, medicine, etc.

One of the advantages of certain nanomaterials is that they possess luminescent properties, surpassing conventional fluorescent chemicals and biological probes. For example, nanoparticle-based detection platforms may offer advantages over traditional approaches in terms of sensitivity, stability and multiplexing capacity[4]. Thanks to these advances, organic fluorophores have been encapsulated into a matrix of particles that are much brighter than the individual dyes, since each particle contains several molecules of dye. In addition, they are more photostable because the formation of the capsules increases stability and biocompatibility of the fluorophores. The small size of the nanoparticles provides an opportunity for high signal to noise ratio response and signal amplification, therefore improving the analytical sensitivity and the response time[5].

Nanobiotechnology refers to the use of nanotechnology in biological systems. Nanotechnology is having an impact on bioanalysis, where particles are changing the landscape of bioanalytical measurement, in fact nanoparticles have overcome many of the significant chemical and spectral limitations of molecular fluorophores. Nanoparticles can be used in a great variety of bioanalytical formats such as quantitation tags, substrates, to take advantage of signal transduction[6], drug delivery[7-9], etc.

Nanoparticles can be made of different shapes and materials. Organic matrices, like polymers, such as polystyrene[10, 11] or acrylate derivates[12-14], and dendrimers[15] were reported, even though the majority of the nanoparticles were synthesized with inorganic materials. A family of inorganic nanoparticles that has been widely used is

that made of semiconducting materials. This type of nanoparticles is known as Quantum Dots, and they are one of the main tools of this chapter.

## 3.1.2 QUANTUM DOTS

Quantum Dots (QDs) are nanoparticles made of inorganic semiconductors, which exhibit a series of unique properties, especially those related with luminescence emission. QDs were discovered in a glass matrix in colloidal solutions from 1981 by the Russians Aleksey Ekimov and Alexander Efros[16] and then supplemented by Louis E. Brus[17]. The term Quantum Dot was coined in 1986[18]. In Europe, it was Arnim Henglein, a chemist, who opened the way to QDs in Berlin from 1982[19]. In Asia, Tadashi Itoh in Senday in Japan started working with CuCl QDs in solid matrices in 1984[20].

At Bell Labs, Louis Brus had two promising postdoctoral researchers, Moungi Bawendi and Paul Alivisatos, who become important figures in the field of QDs. Moungi Bawendi would later be in charge of a team at MIT (Massachusetts). Paul Alivisatos would lead a team at UC Berkeley. In 1993, Moungi Bawendi produced the first "high quality" QDs that have a size variation of less than 5% in colloidal suspension[21]. This allowed the researchers to control size of the QDs and adjust the colour of their luminescence. Meanwhile, Philippe Guyot-Sionnest, a young professor at the University of Chicago, was interested in the multi-photon properties of these materials and, in 1996, his team synthesized the first QDs with the core surrounded by a shell[22]. This made it possible to stabilize the properties of the synthesized particles and provide an easier interaction with their surface chemistry.

At the end of the 2000s, teams from MIT, the University of Berkeley, the University of Chicago and Hamburg were particularly active in researching the properties and applications of QDs. In 2014, a conference to celebrate the 30th anniversary of the discovery of QDS was held at The City of Paris Industrial Physics and Chemistry Higher Educational Institution (ESPCI).

Chemically, QD nanoparticles are semiconductor crystal composed of atoms from groups II-VI, III-V, or IV-VI of the periodic table, only several nanometers in size. They have been widely explored in nanotechnological applications. Many types of QDs will emit light of specific frequencies if they are applied electricity or light, and these frequencies can be tuned with precision changing the size, shape, or material of the particles[23], giving rise to many different applications.

Like other nanomaterials, most of their atoms are on their surface, so the surface-volume ratio of QDs is very high, which, along with the effect of quantum confinement, influences the fact that their properties are very different from those of macroscopic

materials. Quantum confinement occurs when electrons are restricted to moving in a very small region, as is the case of QDs less than 10 nm in size. This effect causes the electronic and optical properties of QDs to be determined by their size. A semiconductor has an energy band full of electrons (valence band) and an empty energy band (conduction band) separated by an energy difference (bandgap). This energy difference is greater than that found in an insulating material. A luminescence process basically consists in the excitation of an electron from the valence band to the conduction band and the return of that electron to the valence band with the subsequent emission of a photon with energy equal to that bandgap. As in QDs the bandgap is variable with the size of the QD, the color of the emitted photon will be a function of its size. The excitation of an electron in QDs can be produced by light absorption of various energies (wide absorption spectrum)[24].
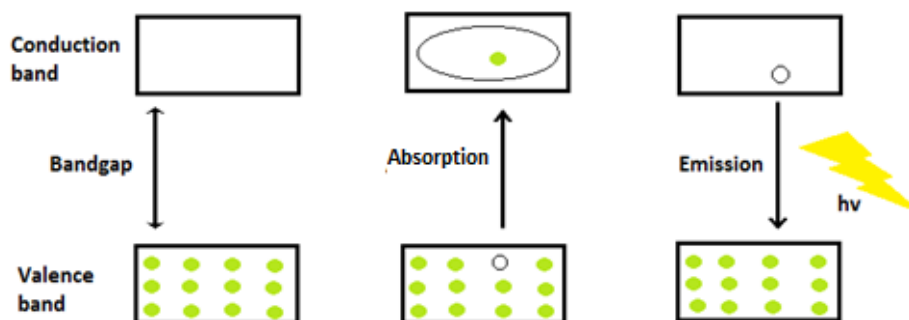


Figure 3.1. Scheme of emission of light after electronic excitation in QDs.

QDs have been proposed recently as an alternative to conventional organic fluorophores because of the unique advantages offered by them. These properties of interest include a high quantum yield, a high molar extinction coefficient, broad absorption bands (Figure 3.2A) with narrow and symmetric photoluminescence spectra (Figure 3.2B) spanning the UV to near-infrared (NIR), large Stokes shifts, and high resistance to photobleaching. Furthermore, compared with molecular dyes, QDs show other particular properties: the control over the size of the photoluminescence (PL) emission and the wide excitation spectrum, which allow the excitation of populations of different QDs mixed with a single wavelength, besides, very far from their respective emissions, which makes them useful for multiplexing applications.
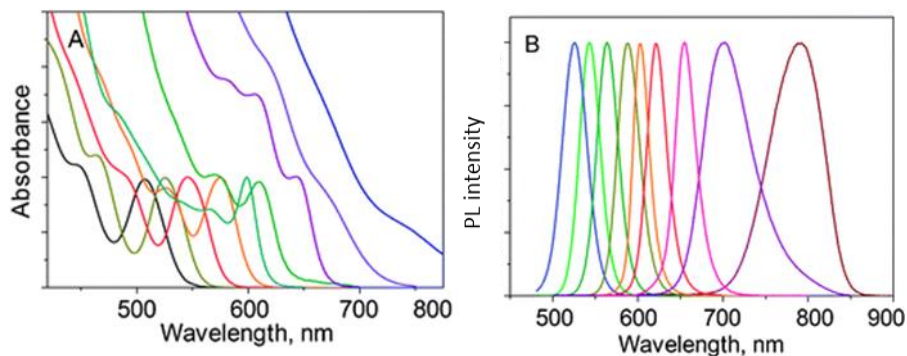
Figure 3.2. Spectral characteristics of QD nanoparticles of different sizes: A) Absorption spectra. B) Photoluminescence emission spectra.

Some of the early and most successful uses of QDs have been in immunofluorescence labeling of fixed cell and tissues[25, 26], cell tracking[27, 28], fluorescence *in situ* hybridazation on chromosomes[29, 30], etc. Many of these reports show that QD labeling permitted extended visualization of cells under continuous illumination as well as multicolor imaging, highlighting the advantages offered by these nanoparticles[25,26, 31, 32].

The QDs are prepared from organometallic precursors at high temperatures, and then they are surrounded by a layer of hydrophobic organic ligands, which makes them incompatible with aqueous solutions. The first methods of synThesis of CdSe/ZnS nanoparticles (core/shell) of various sizes used trioctyl phosphine/trioctyl phosphine oxide (TOP/TOPO) as ligand layer, so that resulting particles were not soluble in aqueous medium and, therefore, they could not have an immediate application in bioanalytical systems[33]. The advance to the stability of the QDs in aqueous solutions, which led to their modification and the use of these in analysis, came in 1998[34,] where the groups of Nie and Alivisatos were pioneers in the development of the modification of the surface of the QDs so that they were soluble in water and therefore biocompatible. The great potential for the application of QDs as fluorescent biomarkers was also raised in these early works[34, 35]. In the following years, the unique properties of the QDs were extensively explored for applications in diagnosis, imaging, optical tracking and detection[36-41].

For the design of different sensor systems, the subsequent modification of the surface is especially important. The surface is usually modified with specific recognition groups that target specific analytes, thus creating a hybrid detection system QD-receptor. The goal to be fulfilled in the design of a proper nanosensor is that some of the properties of the QD-conjugate vary after this modification due to different photophysical mechanisms, and later when the receptor binds with the analyte, a change in the photoluminescence of the QD is created directly or indirectly.

In any case, as an initial step in the preparation of nansensors, one needs to obtain water-soluble QDs. For this, it is first necessary to modify the non-polar ligand layer or change them for polar ligands. The thiol group has been widely used to react directly on the surface (-S) of the QD (Figure 3.3), such as mercaptoacetic acid, mercaptoethane sulfonate and thioglycerol[42-46]. Alternatively, based on the same coupling principle, peptides containing cysteine as a terminal have also been used to replace the organic surfactant on the surface of QDs, and thus make them soluble in aqueous medium[42,44, 47-50].

Although more steps are required in the chemistry, a greater number of ligands can also be coupled to the QDs using a classical covalent bond, by the use of NHS (N-Hydroxysuccinimide) and EDC (N-(3-dimethylaminopropyl)-N'-Ethylcarbodiimide hydrochloride) to activate the amine-carboxyl coupling and give rise to covalently bound ligand receptors (Figure 3.3). In principle, the conjugate molecule can extend from the QD to the outside (equivalent to the synThesis of a divergent dendrimer), starting with any of the exchange ligands discussed above, but if there is no 100% yield at each step it can be problematic, since there would be a heterogeneous population of QDs modified differently. Alternatively, the conjugate can be synthesized with a thiol group in the final zone, so that once it is located on the QD binding with the ligand occurs, as described above.

In a classic approach, very popular and widely used, the streptavidin protein has been used as a bridge, linking QDs with biotinylated biomolecules (Figure 3.3). QDs can be conjugated directly with streptavidin through the coupling reaction mediated by the carbodiimide, so that the biorecognition ligands, such as biotinylated antibodies or DNA strands, are capable of binding through the avidin-biotin interaction. Nowadays, QD-streptavidin conjugates are commercially available, being used to fix the additional biomolecules on the surface of the QDs.

QDs can also be surrounded by an electrically charged ligand layer, so that a negative or positive surface is formed, providing a method that allows electrostatic modification and derivatization for biorecognition systems (Figure 3.3). For example, the widely used dihydrolipoic acid layer provides a negative surface that can be coated with positively charged proteins. These conjugates obtained by electrostatic interactions have successfully created protein surfaces in the QDs with specific functionalities[39, 51-54].

In general, the direct binding of biomolecules such as DNA[29, 55, 56], peptides, proteins and antibodies[57] on the surface of the QD nanoparticles has also been performed through:

- Covalent bonding of the groups carboxy, hydoxyl or amine to the surfaces of the QDs,

- Bonding between QDs surface sulfur atoms and thiol groups on oligonucleotides and antibodies, or cysteine residues in peptides,
- Metal-affinity coordination of polyhistidine residues to the Zn atoms on QDs surfaces,
- Electrostatic interactions between QD surfaces and oppositely charged molecules.
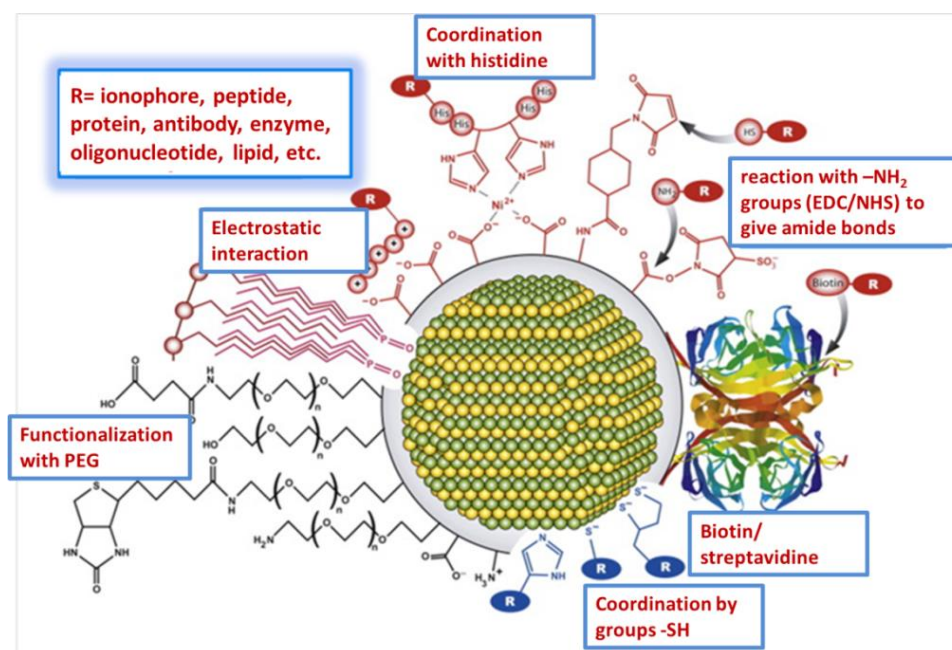


Figure 3.3. Different methods of modification of the QDs surface for the development of nanosensors.

Once the surface of the QDs has been modified to incorporate the receptor or reactive molecule, these can be used as nanosensors. The first system developed with nanoparticles of QDs was directed almost exclusively to the determination of ions. Several sensors based on an increase in the photoluminescence of nanoparticles after reaction or adsorption on the surface of specific analyte ions have been described[42,58, 59]. Similar to this principle, several optical sensors of QDs have also been developed whose response mechanism was based on a quenching of photoluminescence. These mechanisms of quenching include internal filter effects, non-radiative recombination and electron transfer processes[42, 43]. By measuring the increase in fluorescence or quenching of the QDs in aqueous solution, it have been determined the concentration of a multitude of metal cations such as Ag(I)[43, 44, 47, 60], Zn2+[42, 61], Cu (II)[62, 63,42, 47, 64, 65] Hg (II)[50, 66], Cr (iV)[67, 68], Ar(III)[69] and some toxic anions such as cyanide iones[45, 70].

Finally, the recognition of the analyte can also be achieved without the use of QD coating or ligand exchange. It is known that many organic molecules can act as molecular containers, the majority being cyclic macromolecules. These groups can be

designed to selectively encapsulate smaller molecules or ions in their cavities. This type of molecular and ion recognition can also be combined with the optical properties of QDs to build a new generation of QD sensors. Receptor molecules such as cyclodextrins[71-73], calixarenes[74-76], crown ethers[59] and curcubitulirs[71] can be bound to the surface of the QD or can be mixed with the aqueous solution of QD after adding the host molecules. The selective binding of small guest molecules or ions by the host molecules leads to changes in the fluorescence of the QDs, due to the interactions induced with the surface of the QD that vary the recombination of the hollow-electron[77], energy transfer[59, 78, 79], or the electronic transfer[71] that was given with the QDs.

### 3.1.3 PHOTOLUMINESCENCE LIFETIME OF QDs

When QD nanoparticles are used as sensors, the measurement of the PL intensity has been the most popular option, mainly due to that relatively cheap instruments are required. Most of the nanoparticle sensors made so far was based on changes in the emission intensity after the reaction or interaction with the target molecule. However, measurements based on the emission intensity suffer from certain uncertainties in the calibration responses. The PL intensity can, for example, be altered by fluctuations in the fluorophore concentration and heterogeneities in the optical properties of the medium. In addition, more limitations are found when the systems are applied as intracellular nanosensors. Although the distribution of the nanosensor can be optimized, the location of the nanoparticle sensor in certain compartments of the cell can produce erroneous readings. In addition, when the luminescence intensity is very low problems for detection arise and spatial and temporal resolution is limited.

One way to overcome many of these limitations can be by using time-resolved fluorescence spectroscopy to investigate these systems. This family of luminescence techniques report on the value of the PL lifetime, $\tau$, an average measure of the time that a system remains in the electronic excited state, after excitation. $\tau$ is defined as the inverse of the sum of all the rate constants for all depopulation processes occurring in the excited state:

$$\tau = \frac{1}{k_r + k_{nr}}$$
(3.1)

Where $k_r$ is the radiative rate constant, and the non-radiative rate constant $k_{nr}$ is the sum of the rate constant for internal conversion, $k_{ic}$, and the rate constant for intersystem crossing to the triplet state, $k_{isc}$, so that $k_{nr} = k_{ic} + k_{isc}$. In organic fluorophores, the fluorescence emission occurs from the lowest vibrational level $S_1$, a

rule known as Kasha's rule[80], indicating that the fluorophore has no memory of its excitation pathway[81].

In general, the fluorescence lifetimes of organic fluorophores are approximately 1-5 ns in the visible range, and usually show monoexponential decays. This makes these organic dyes suitable for applications based on lifetime, since it is quite simple to identify them by measuring fluorescence lifetimes. However, these fluorescence lifetimes are too short for efficient temporal discrimination of interferences produced by short-lived fluorescence or by excitation of scattered light.

Unlike organic fluorophores, QD nanoparticles show unique properties with respect to their photoluminescence lifetime. The lifetime in the excited state of the colloidal QDs is one of the optical properties that is yet not well understood. Normally, QDs have long lifetime (between five and hundreds of nanoseconds) and mutiexponential fluorescence decays. In addition, the lifetimes of the QDs are significantly longer than the autofluorescence decays of the cells (2-3 ns) and the fluorescence lifetimes of the conventional dyes (1-5 ns), but efficient enough to maintain a high flow of photons[82]. For all this, the use of time-resolved fluorescence techniques has a great potential for the development of QD-based nanosensors, especially in intracellular determinations, being able to obtain a cellular detection with a greater selectivity and sensitivity. Therefore, these are the characteristics that make QD nanosensors ideal as intracellular sensors in combination with the use of fluorescence lifetime techniques.

Recent works have shown that time-resolved fluorescence spectroscopy is a very sensitive technique that can be successfully applied for the detection and quantification of several interactions between QDs and other molecules[25]. Moreover, time-resolved luminescence techniques can also be used for the detection of sensors based on different response mechanisms, such as fluorescence resonance energy transfer (FRET) or electron transfer[34]. For example, our research group has developed a pH sensor by measuring the variation in the average lifetimes of QD nanoparticles coated with a layer of mercaptopropionic acid (MPA). The mean lifetime of the QD-MPA decreased from 16.4 ns in alkaline medium to 8.2 ns when the pH of the medium was less than 4.5, showing a linear response in a pH range of 5.2-6.9[83]. This is a large change in the average lifetime compared to the small changes in the fluorescence lifetime of organic fluorophores[84], which indicates the high sensitivity of these sensors. This QD-MPA nanosensor has been successfully applied for the estimation of pH in simulated intracellular media, obtaining a high sensitivity and a high selectivity towards most of the intracellular components, which demonstrates its high potential as an intracellular sensor.

Our research group also proposed a QD nanosensor for the determination of chloride ions using the PL lifetime as the analytical signal, with similar sensitivity[85]. In this case, an organic molecule, lucigenin, was incorporated onto the surface of the QD-MPA nanoparticles by means of electrostatic interactions, to give rise to QD-lucigenin conjugates. After the union, a drastic decrease in the PL lifetime of the QDs was observed due to a charge transfer mechanism. However, the average lifetime of the QD-lucigenin complex increased when reacted with Cl⁻, with a linear response in the range of 0.5 to 50 mM.

However, these are almost exclusively the works found in bibliography in which the technology of the QDs to the development of nanosensor is combined with the detection of time-resolved fluorescence, which is indicative that it is a new area to be exploited. The works cited above show the results obtained by combining the QDs and time-resolved fluorescence techniques, but making only in vitro applications. However, the greatest potential of this combination is found when nanosensors are used in intracellular applications with imaging techniques, as described below.

## 3.1.4 FLUORESCENCE LIFETIME IMAGING MICROSCOPY (FLIM)

The understanding of fluorescence-related phenomena and the creation of an appropriate theoretical framework to quantitatively interpret and predict fluorescence and to design a fluorescence microscope only occurred 100-150 ago. Over the last 10-20 years the field has advanced rapidly and enormously, mainly due to combination of lasers and beam scanning[86], powerful computers and data analysis software, sensitive detectors and cameras[87] and genetic engineering- the latter effort being recognized by the award of the Nobel Prize in Chemistry in 2008 to Osamu Shimomura, Martin Chalfie and Roger Tsien "for the discovery and development of the green fluorescent protein, GFP". A year later, in 2009, half of the Novel Prize in Physics was given to Willard Boyle and George Smith "for the invention of an imaging semiconductor circuit- the CCD sensor" in 1969[88]- a device which has also played a significant role in advancing fluorescence microscopy. Years later the super-resolution technique was developed that allowed to obtain images far below the spatial resolution[89]. This field has rapidly expanded over the last decade or so, and its importance was recognized by the award of the 2014 Nobel Prize in Chemistry to Eric Betzig, W.E. Moerner and Stefan Hell for the "for the development of super-resolved fluorescence microscopy".

Among the various methods of fluorescence microscopy, the fluorescence lifetime image (FLIM) has emerged as a key technique to image the environment and interaction of specific probes on living cells[90-92]. FLIM microscopy provides not only information about the intensity emitted but also reports on the luminescence lifetime,

τ. The idea of fluorescence measurements resolved over time in the nanosecond timescale of samples under microscope dates back to the 1950s[93], the emergence of FLIM as a technique for mapping fluorescence lifetime began in 1989. In this year, the first reports were published describing a fluorescence imaging technique where the contrast in the image provided by the fluorescence lifetime[94]. There are several technological implementations of FLIM, but they all can report on photophysical events that are difficult or impossible to observe by fluorescence intensity imaging, because FLIM is independent of fluorescence concentration. The fluorescence lifetime provides an absolute measurement which, compared to fluorescence intensity, is less susceptible to artefacts arising from scattered light, photobleaching, non-uniform illumination of the sample, light pathlength, or excitation intensity variations[81]. FLIM has long been used to detect Förster resonance energy transfer (FRET) to identify proteins interactions or conformational changes of proteins in the life and biomedical sciences[95]. However, applications in diverse areas such forensic science[96], microfluidic systems[97, 98], remote sensing[99] and other field have also been reported.

The increasing popularity of FLIM has been facilitated by the commercial availability of FLIM add-on units for conventional microscopes, for wide-field, confocal and multi-photon excitation microscopy, including data analysis software. Since then, the power of FLIM has increased dramatically with the extension to spectrally resolved FLIM, polarization-resolved FLIM and rapid acquisition with single photon sensitivity. FLIM has also been combined with other techniques such as fluorescence correlation spectroscopy (FCS)[100], scanning near-field optical microscopy (SNOM)[101], atomic force microscopy (AFM)[102], fluorescence recovery after photobleaching (FRAP)[103] among others.

### 3.1.4.1 APPLICATIONS OF FLIM MICROSCOPY IN LIFE SCIENCES

It has been previously commented that the fluorescence lifetime is influenced by changes in the physical properties of the medium or by the presence of certain substances. This characteristic is the basic for a wide range of applications of FLIM microscopy in the field of Life Sciences. Some of them are described below:

- **FRET**. One of the most common applications of the FLIM technique in Life Sciences is the detection of interactions between molecules by means of FRET. FRET is an energy transfer process, in which an excited electronic excitation in a second fluorophore (acceptor) with which it interacts at a short distance (the efficiency of the FRET process is very sensitive to the distance between the two fluorophores). For practical purposes, it consists of detecting the emission of the accepting fluorophore, having exclusively excited the donor fluorophore[104]. If the detection of this fluorescent emission occurs, the interaction of both molecules at short distance (<10 nm) is confirmed. In the FLIM-FRET variant, what is recorded are variations in the

fluorescence lifetimes of the acceptor and donor molecules involved[81]. Using this FLIM-FRET technique, the interaction of proteins found in different organelles, such as nucleus, cytoplasm or plasma membrane, has been studied.

- **Physical properties of the medium**. The FLIM technique has been used to measure viscosity using fluorophores whose fluorescence lifetime is affected by the viscosity of the medium. For example, the microviscosity of blood plasma[105], liposomes[106], bacterial membranes[107], living cells[108] and biological structures such as tubulin[109] has been investigated. Another physical parameter that can be measured with FLIM is temperature. For this, small organic molecules have been used, such as derivatives of rhodamine B, whose fluorescence lifetime varies according to the temperature of the surrounding medium. Also, by using a fluorescent polymer sensitive to thermal change, it has been possible to measure the temperature in living cells, and even record differences in it in different areas of the cell. For example, the temperature of the cytoplasm is one degree lower than that of the nucleus, depending on the state of the cell cycle. In addition, it was observed that heat was produced in the mitochondria due to cellular respiration[110]. It is also possible to determine the refractive index using FLIM, since the kinetic cost of radiative decay, and hence the lifetime, is influenced by the refractive index of the medium[111]. In this way, the decay of fluorescence has been analyzed as a function refractive index in GFP. Proteins labeled with GFP have been studied and decay has been shown to be much faster when these proteins are found in the cell membrane than when they are found in the cytoplasm, because the membrane has a higher refractive index.

- **Glucose concentration**. FLIM microscopy has been used to determine the concentration of certain analytes such as glucose, using fluorophores sensitive to glucose. These sensors, generally based on fluorescent proteins, increase their quantum yield and fluorescence lifetime in contact with the glucose molecule. This methodology is a good alternative to electrochemical or glucose oxidase methods, since they have certain limitations when used *in vivo* due to interferences with tissues, proteins, etc[112].

- **Concentration of ions.** Another of the cellular physiological parameters that may be interesting to analyse using this technique is the concentration of certain ions, as this varies depending on the type of cell and the physiological state of the cell[113].

- **Oxygen concentration**. Another interesting application of the FLIM microscopy is the determination of oxygen concentration in different types of cells, such as chondrocytes seeded in agarose gels, in which a decreasing gradient of oxygen available from the outside to the inside of the gel is established. Using an oxygen-sensitive fluorescent ruthenium derivative, a decrease in lifetime was observed as the concentration of this gas increased[113]. Using a similar methodology, the oxygen

gradient has also been studied in three-dimensional tissue models, such as multicellular spheres, using cancer cells or neuronal cells (neurospheres)[114, 115]

- **Cellular autofluorescence**. Through lifetime measurement of endogenous fluorophores, such as NADH or FADH, it has been possible to analyze the cellular metabolic state, the mitochondrial redox state or to distinguish between apoptosis and necrosis[116]. It has also been used in biopsies to distinguish between basal carcinoma cells and the normal cells of around[117].

- **pH**. Finally, and related to the subject of this research work, the FLIM technique has also been used to measure pH in cells and tissue, using different types of compounds such as fluorescence pH probes. The pH will be treated in more depth in this Thesis.

### 3.1.4.2 APPLICATIONS OF FLIM MICROSCOPY WITH QDs

As mentioned earlier, FLIM microscopy can be effective for the quantitative real-time detection of biologically important molecules or ions within living cells. The fluorescence lifetime is a parameter that has numerous advantages, especially when it is intended to make applications inside the cell. For example, the lifetime is independent of the concentration of fluorophore and the excitation power, in addition to possible heterogeneities in the optical properties of the medium in which it is located, which is of special importance in measurements in such complex media as the cellular cytoplasmic medium. However, only a few works use FLIM as a detection technique for intracellular sensors, mainly dealing with the use of organic molecules or fluorescent proteins as fluorophores[36, 118-121], which always show quite low sensitivities. In addition, the use of FLIM with fluorescent nanoparticles has not been exploited yet, and there are only a few examples of applications based on resonance energy transfer (FRET) for FLIM detection[122-125].

But perhaps it is in the combination of QDs with FLIM that the main advantages of this technique are found. The long PL lifetime of the QDs allows for a much more sensitive intracellular determination, in addition to facilitating the discrimination between the autofluorescence signal of the cell and the signal coming from the QD nanoparticles[82, 126]. In Figure 3.4 it is seen that the lifetime of cellular autofluorescence is much shorter than that of the QD nanoparticles, allowing the direct elimination of this important interference found in many other imaging techniques.
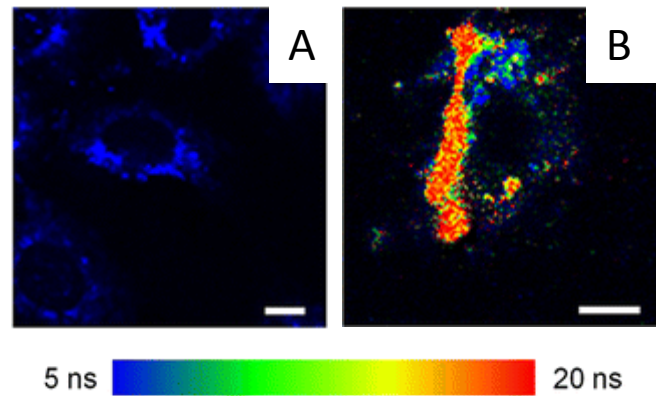
Figure 3.4. FLIM images showing: A) cell autofluorescence, B) QD-MPA in the cellular cytoplasm.

One of the first works in which the potential of the QDs was demonstrated as nanosensor with the FLIM fluorescence imaging technique was the QD-lucigenin sensor[85]. However, all these advantages were amply demonstrated in another work in which pH nanosensors based on QD-MPA were used to determine intracellular pH inside several cell types[126]. In this work, FLIM images were initially collected from nanosensors suspended in synthetic media whose composition mimicked that of the cellular cytoplasm, but adjusted to different pH values (Figure 3.5). After analyzing these images, the lifetime distributions were obtained, and from here the calibration could be obtained that later would allow the determination of the pH in the cytoplasm of living cells (Figure 3.5).
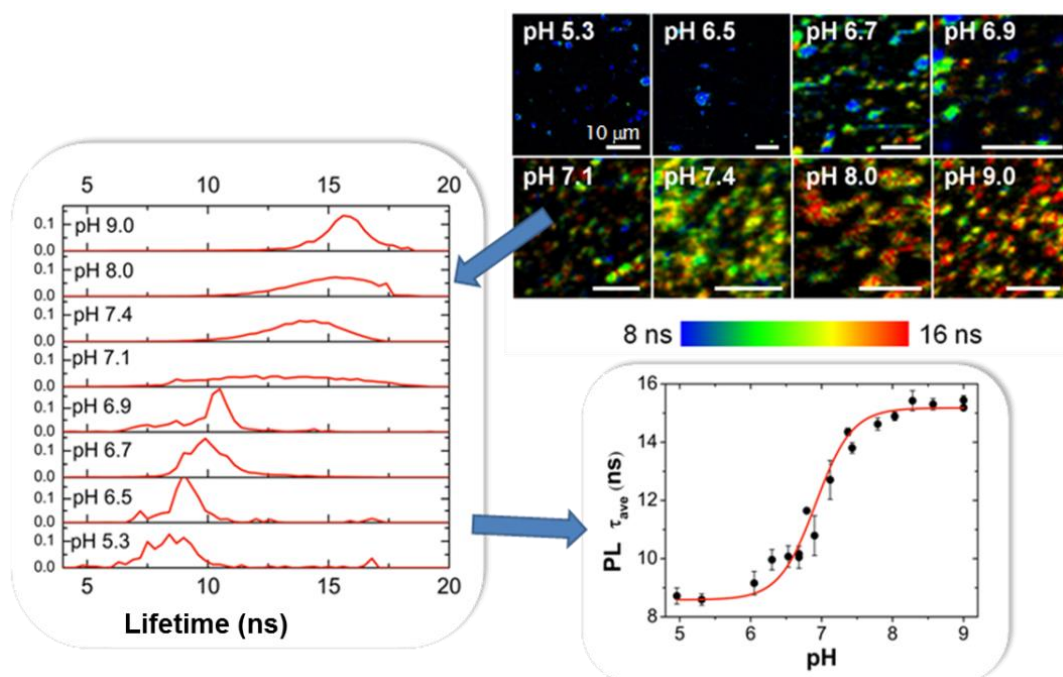


Figure 3.5. FLIM images, lifetime distributions, and lifetime average values of QD-MPA nanosensors in synthetic media[126].

Subsequently, these nanosensors were incorporated into several types of cells, and the intracellular pH value was modified using a molecule, nigericin, which equaled intracellular to extracellular pH[126]. The analysis of the FLIM images collected inside the cells clearly showed that the QD-MPA nanosensors allowed the detection and quantification of the cytoplasmic pH (Figure 3.6).

These results showed that the combination of the FLIM technique with QDs allows the determination and monitoring concentration changes of molecules and ions of biological interest in the cell interior, which would allow the monitoring of such molecules during important cellular processes.
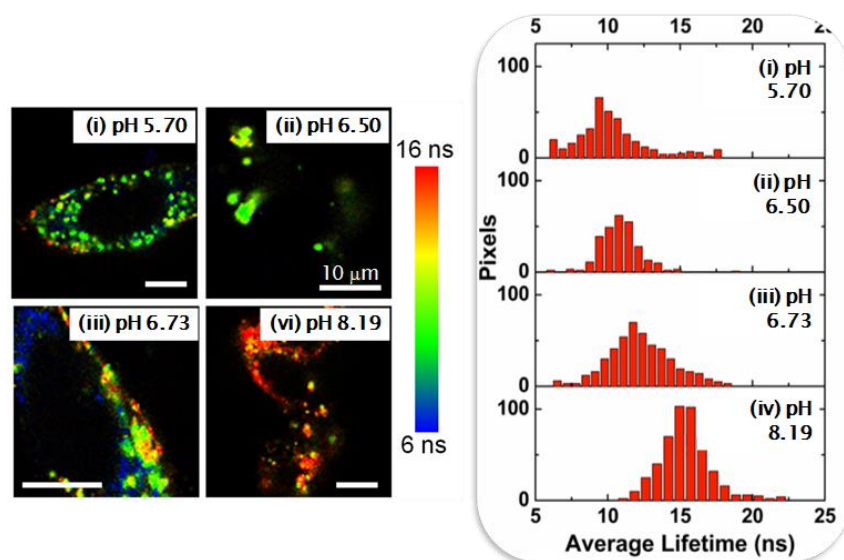


Figure 3.6. FLIM images and lifetime distribution of QD-MPA nanosensors inside CHO cells treated with nigericin at different pH values[126]

## 3.1.5 ZINC IONS NANOSENSOR AND INTRAMITOCHONDRIAL pH NANOSENSOR BASED ON QUANTUM DOTS

To carry out this Thesis, two nanosensors based on QDs have been developed. The first nanosensor was aimed at the detection of intracellular zinc. The second nanosensor had a double functionality, the first being capable of specifically targeting the cellular mitochondria and the second, measuring the pH in that area.

### 3.1.5.1 ZINC$^{2+}$ NANOSENSOR

Zinc is one of the most important transition metals, with great physiological importance due to its intra- and extracellular functions. Zinc intervenes in very important diseases and processes, such as insulin synThesis and in the state of diabetes pathology[127], it also serves as a mediator of cell-cell signals in the central

system, where brain tissue contains a high concentration of zinc[128]. It is also involved in the aggregation of the Amiloyd-β peptides, responsible for the development of Alzheimer's disease[129]. These functions and the participation of zinc in other physiological processes make it interesting to detect the concentrations of zinc in the presence of other cations with physiological relevance. This would allow a greater understanding of its physiological role in nature and in diseases. With this aim, in this Thesis we synthesized and optimized a family of QD-based $Zn^{2+}$ nanosensors.

### 3.1.5.2 INTRAMITOCHONDRIAL pH NANOSENSOR

The pH is a measure that determines the acidity or alkalinity of a solution, indicating the concentration of hydrogen ions present in solution. Although the pH of the cell is regulated, some factors or processes can lead to an alteration in the pH (Warburg effect). A cause-effect relationship of the pH can be observed with different diseases or natural processes, in which the pH can be the cause or effect of these. In addition, the presence of exogenous substances in the cell, such as drugs, can modify the chemical composition of the medium, causing a variation in the cellular pH. Cell pH can also be affected by cellular processes such as senescence or programmed cell death, known as apoptosis. When the cell undergoes a disturbance that it is unable to correct and is damaged, in order to maintain homeostasis, it enters a process of programmed cell death. For example, acidification of the intracellular environment triggers the expression of certain genes that induce apoptosis[130]. If this process, natural and vital to the proper functioning of the body, fails, some diseases occur.

Mitochondria are cellular organelles, which carry out different functions, the most remarkable is the production of cellular energy (ATP), through an oxidative phosphorylation system (OXPHOS). OXPHOS involves the coupling of redox and phosphorylation reactions in the inner membrane of mitochondria. During this process, the electrons of NADH or FADH are transported through the electron transport chain, creating a proton gradient. The movement of the protons from the mitochondrial matrix to the intermembrane space create a pH gradient and an electrical gradient that drives the synThesis of ATP[131]. There are a lot of diseases due to the incorrect functioning of mitochondria such as Leigh Syndrome[132], encephalomyopathy mitochondrial[133], lactic acidosis, strolikes episodes, hepatopathy, tubulopathy[134-136] and cancer[137, 138]. For the development of this Thesis, it was important to understand the relationship between mitochondrial pH and cancer. This relationship is widely described in chapter 4.1, where the Warburg effect[139] is explained. For this purpose, in this Thesis we synthesized and optimized two QD-based nanosensors to measure intra-mitochondrial pH.

## **3.2** Materials AND METHODS

### 3.2.1 STEADY STATE SPECTROFLUOROMETER

Steady state fluorescence spectra were recordered using a Jasco FP-6500. It is a fourth generation instrument, with external control from a computer with the Spectra Manager software. The instrument performs fluorescence, phosphorescence, chemiluminescence and bioluminescence measurements. The light source is a Xenon lamp equivalent to 50 W. The detector is a photomultiplier R3788-01. Monochormators are holographic grids with 1800 slots/nm and cover the intervals between 220 and 750 nm. The sensitivity of the measurements is ± 0.1 nm and the reproducibility of ± 0.3nm. The bandpass of the slits can be selected between 1, 3, 5, 10 and 20 nm fot both excitation and emission. The scanning speed can vary between 20 and 5000 nm/min, depending on the response and sensitivity used. Also, it is possible to select filters for different wavelengths or transmittance attenuator. The sensitivity has a signal-to-noise ratio >200:1 r.m.s., using the Raman spectral band of ultrapure water with excitation at 350 nm. The instrument has a standard cell holder, thermostated by means of a Peltier, with a water ciculation system, and a conventional cuvette cell holder. For correction of the excitation spectra, a beam splitter passes a part of the incident current through a reference photodiode, while the emission spectra can be corrected by computer program.



Figure 3.2.1 Steady state spectrofluorometer Jasco FP-6500.

### 3.2.2. TIME-RESOLVED FLUOROMETER

Time-resolved fluorescence measurements were carried out in a *FluoTime 200* instrument (PicoQuant GmbH) based on the time-correlated single photon counting

(TCSPC) methodology, and equipped with several excitation laser sources, which are described below.
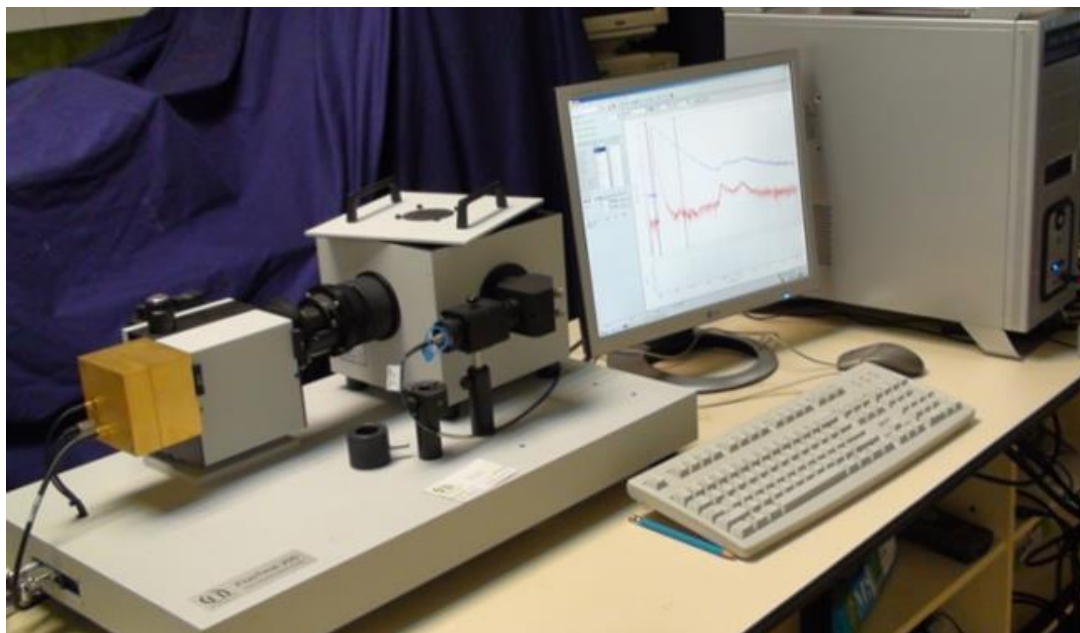


Figure 3.2.2 Time-resolved spectrofluorometer *Fluotime 200.*

### 3.2.2.1 LASER EXCITATION SOURCES

The excitation source employed in the collection of luminescence decay traces consisted on a high-power, pulsed picosecond diode laser, either of 440 nm (LDH-440), 470 nm (LDH-P-470), 485 nm (LDH-P-C-485), or 635 nm (LDH-P-635, all of them from PicoQuant GmbH). The train of pulses of the excitation source was controlled by a PDL 800 D driver system (PicoQuant GmbH), which has a crystal oscillator that generates fluctuations lower than the mother frequency, allowing the pulse frequency to be divided between binary factors (1, 2, 4, 8, or 16) to generate a range of pulse frequencies of 40, 20, 10, 5 and 2.5 MHz. In this Thesis, we used a repetition rate for the train of pulses of 10 MHz and a pulse-width with a minimum amplitude of 40 ps.

In order to have stability on the measurements, the room temperature is controlled by a thermostat that keeps the temperature in the laser source stable.

### 3.2.2.2 TCSPC SYSTEM

Through the TCSPC technique, PL decay traces are acquired, by building up a histogram of the arrival time of individual photons at the detector over many excitation/emission cycles. In the histogram, the time between the generation of the excitation laser pulse and the arrival at the detector of the emission photons corresponding to that excitation is recorded. This technique has been carried out on the aforementioned time-resolved fluorescence spectrophotometer *Fluotime 200*,

based on an L-geometry, and controlled by a computer equipped with the TCSPC *TimeHarp 200* data acquisition card (PicoQuant GmbH).
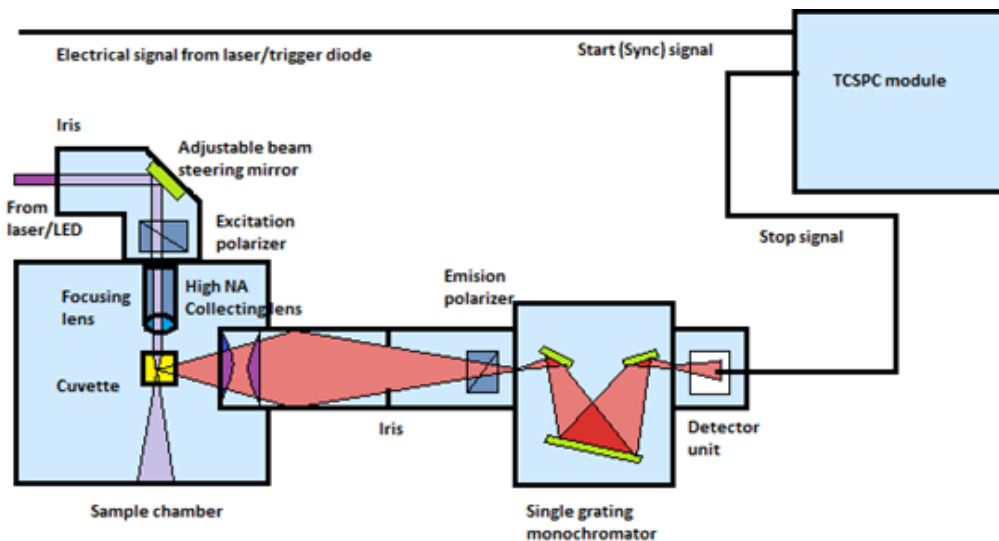


Figure 3.2.3: Scheme of the time-resolved fluorometer Fluotime 200.

As shown in Figure 3.2.3, the pulsed excitation radiation from the laser is directed to the simple chamber through an optical fiber. There, by means of a lens, the beam is focused towards the sample. The emission of the excited sample is collected and collimated through lenses at right angle with respect to the excitation pathway. The emitted light passes through a laminar polarizer set at an angle of 54.7° respect to the direction of polarization of the excitatory light, in order to eliminate the effects of the rotational diffusion of the fluorophores in the fluorescence decays. Subsequently, the emitted light is focused on a Sciencie Tech 9030 monochromator, whose technical specifications are: f/3.5, concave holographic diffraction grating of 1200 lines/mm, 8 nm of angular dispersion and spectral range 350 to 800 nm. After passing through two slits of controlable width, the detection of the emitted photons is carried out in a microchannel plate photomultiplier, whose signal serves as a START pulse. The STOP pulse comes from the oscillator PDL 800 B. Both pulses are connected to a computer equipped with the TimeHarp 200 card and to the control computer program that has the two constant fraction discrimination modules (CDF): the time-amplitud converter (TAC) and the analog-digital converter (ADC). Histograms of fluorescence decays are collected along 1036 channels.

### 3.2.3 FLUORESCENCE LIFETIME IMAGING MICROSCOPY (FLIM)

The system used to perform FLIM measurements is based on an inverted confocal microscope with pulsed laser excitation (*MicroTime 200*, PicoQuant GmbH). The

instrument is not only capable of performing FLIM imaging, but also single molecule fluorescence spectroscopy, and related techniques, such as fluorescence correlation spectroscopy (FCS).

The *MicroTime 200* consists on four main parts:

- Olympus IX71 Microscope: it is an inverted microscope that includes the infinity-corrected optical system (UIS), which allows not to reduce the field of view when intermediate accessories are added. It is equipped with WHN10x optical lenses and the following objectives: Plan-N-x40, Plan-N-x60, and immersion U-Plan-S-Apo-x100 (1.4 NA), being the last one used with immersion oil type DF that has a refraction index of 1.515. The general characteristics of the microscope can be observed in figure 3.2.4. To image a region, the sample are raster-scanned with an x-y piezo-driven device (Physik Instrumente).
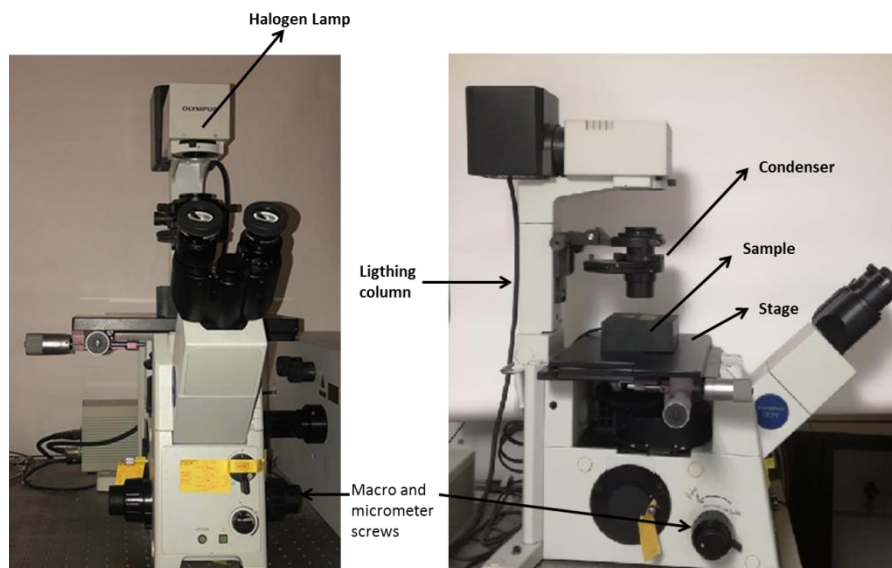


Figure 3.2.4. Olympus IX71 inverted microscope structure.

- Excitation system: The excitation diode lasers were those previously described for the *Fluotime200* instrumentation. However, the lasers were operated with a 'Sepia II' driver (PicoQuant GmbH), which allows the simultaneous use of two different laser heads. The 'Sepia II' driver also allows to generate trains of pulses with the frequencies of 40, 20, 10, 5 and 2.5 MHz. The laser placed on the second channel of the 'Sepia II' driver was delayed with respect to the first laser, using an ORTEC DB463 delay box (AMETEK GmbH), to achieve pulsed interleaved excitation (PIE)[140]. In this Thesis, we used either 440-nm and 485-nm single laser excitation, or 470-nm and 632-nm dual-color excitation under PIE regime. In both cases, the repetition rate for the train of pulses was 10

MHz. For PIE excitation, the 635-nm laser was delayed 56 ns with respect to the 470-nm laser.

Main Optical Unit (MOU): it comprises the following subunits:

- The excitation segment: It is the part where the laser light beam that comes from the excitation system enters into the MOU. It is incorporated by an optical fiber by means of an FC/APC connector and after reflection in a mirror it passes through the excitation shutter (which can be controlled either by softwate or manually). Once the beam passes through the shutter, 10-20% of the intensity is directed to a photodiode that measures the excitation power.

- The basic confocal unit: after passing through the excitation segment the light beam is reflected onto the main dichroic mirror in a 45° geometry that redirects the light to the Olypus IX71 microscope objective that focuses the light into the target specimen.

- The fluorescence emission as well as the reflected excitation light is collected back again by the microscope objective and redirected back to the dichroic mirror, which is optimized to let mainly pass the fluorescence emission radiation. The light transmitted in the dichroic passes a wheel of filters, in which a specific cut-off filter can be used to remove remainings of the excitation light coming to the detection pathway. Then, the light is directed towards an achromatic lens that focuses it onto an aperture pinhole of 75 μm diameter. The distance between the lens and the pinhole is easily controlable to optimize the confocal plane. After the aperture, the beam is recollimated by a second lens and guided to the photon detectors, which will be described below.
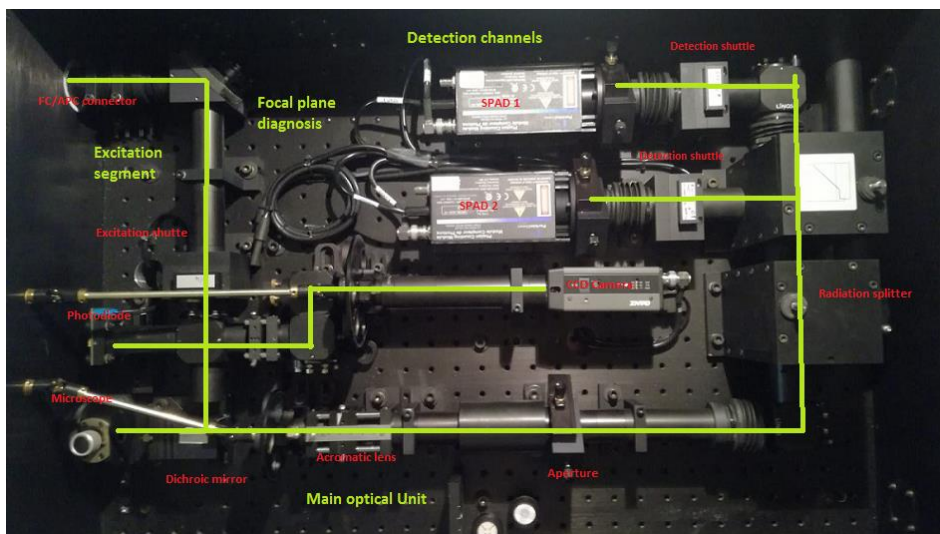


Figure 3.2.5. Main Optical Unit Scheme.

- Focal plane diagnosis: Part of the excitation light reflected and redirected to the dichroic is, in turn, reflected back towards the diagnostic segment of the focal plane. The optical design of the *MicroTime 200* allows a continuous analysis of the excitation light, which makes it possible to control the position and quality of the focal plane and the excitation volumen in the sample. There is a CCD camera (GANZ ZC-F10C2, with 500x 582 pixels (1/3")) that allows the diagnosis and it permanently monitors the image seen by the lens. The obtained images are displayed on the computer. The light arriving at the camera can be regulated by filters of different optical density.

- Detection channels: The collimated beam of the fluorescent emission reaches the detectors through the basic confocal unit. Up to two different detection channels are available, and the emitted light can be directed to just one of the detectors, or to both of them using a 50/50 beam splitter or specific 45° geometry dichroic mirrors. Each detection channel has a mechanical shutter and a lens to focus the incident radiation on the sensitive section of the detectors. The detectors used are single photon avalanche diodes (SPAD), SPCM-AQR-14 (PerkinElmer), with a detection wavelength range from 400 to 1100 nm, and high detection efficiency (more than 70%) at 630 nm. It is possible to use a bandpass filter in front of the detectors to select the broadcast bands in each channel.

- Data acquisition and electronic photon tagging: time-resolved photon arrival time information is collected using two *TimeHarp 200* data collection cards (one for each detection channel). It is a TCSPC system that can operate in several ways, the most relevant for our applications is the Time-Tagged-Time-Resolved (TTTR) methodology. The TTTR method allows the recording of the arrival time of each individual photon to the detectors. On the one hand, the START-STOP time of each photon with picosecond resolution are determined, more specifically it is the time elapsed between the excitation pulse (START) and the arrival of the photon (STOP signal), as the fluorescence time resolved by TCSPC mode is done. On the other hand, the arrival of each photon is recorded by an independent clock that measures the total time of each experiment and it labels each photon to its global time of the arrival to the detector, respect to the overall measurement time. This allows identifying photons that come from the same molecule and also discriminating fluorescence blinkings that are a feature of single molecule fluorescence experiments. Therefore, the most outstanding

applications are: the detection of single molecule diffusion, FCS and single molecule blinking that is obtained by integrating fluorescence lifetimes.

Histograms are not performed in TTTR mode. Instead the START-STOP time of each event is always recorded with a time tag of a separate clock, assigned at the time of arrival of the STOP photon. As a result, recordings made by TTTR mode occupy 12 bits for the START-STOP time and 16 bits for time tag. These 16 bits with the clock at 100 ns cover maximum range of 6.5536ms. It should be noted that it is not possible to combine the START-STOP time of picoseconds and the time tag in the same figure, since the two times are not synchronized. The aim of these two times is, rather, to examine physical processes with two very different time scales and time references. However, sophisticated analysis methods use both times to extract as much information as possible from such physical processes, for example, the diffusion of individual molecules.

It is often desirable to synchronize TCSPC measurements with other information or with other records. In order to perform, for example, images of fluorescence lifetimes, it is also necessary to record the spatial location of the photons. To achieve this, a mechanism is needed that assigns the external synchronization information to the TCSPC data collected independently. To solve this problem, the data set generated by the TimeHarp 200 may contain markers fot the synchronization information derived from the captured images. Figure 3.2.6 shows how the signal of the external marker signal is recorded in the data sequence.
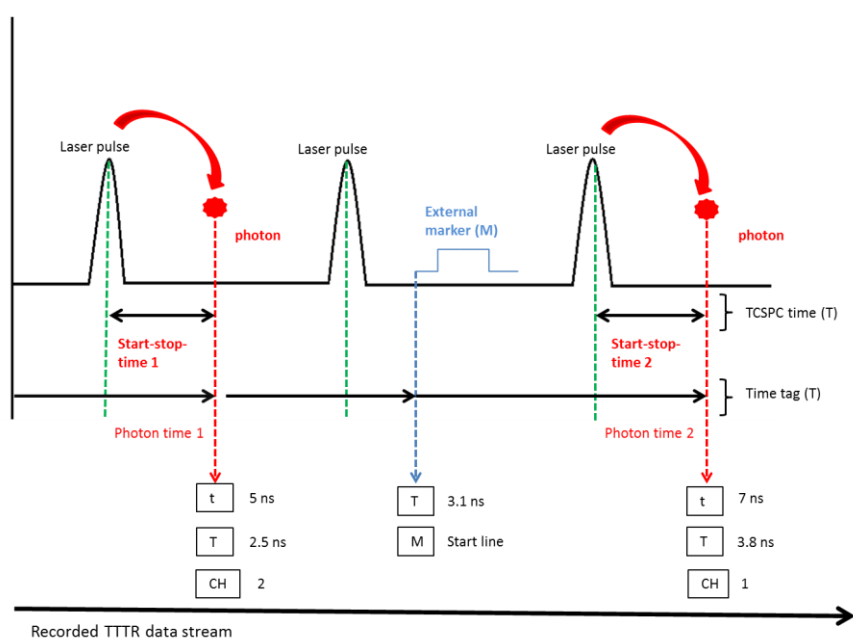


Figure 3.2.6. Measurement scheme of the TTTR methodology.

Like in classical TCSPC the time difference between the moment of excitation and the arrival of the first fluorescence photon at the detector is measured. This TCSPC time (t) is stored into the TTTR data stream along with a global tag (T) and the information about the detection channel (CH). Additional external synchronization signals (markers, M) can be included in the data stream for imaging, for instance recording the XY coordinates of each pixel.

### 3.2.4 OTHER GENERAL LABORATORY EQUIPMENT

#### 3.2.4.1 BALANCE

An electronic analytical Sartorious Balance A-120 S model, provided with an internal and external calibration system, has been used. It has a standard deviation of ± 0.1 mg and 3 s time-response.

#### 3.2.4.2 SONICATOR

An ultrasonic bath Ultrasons Selecta P model 513 with a 150W generator that produces 40 kHz sound waves has been employed. It has a synchronized timer with signaling lamp.

#### 3.2.4.3 PH-METER

pH measurements have been performed with a pH-meter Crison pH-Meter BASIC 20+ that permits measurements from -2 to 16 (mV: ±2000), with a working temperature range between –20 and 150 °C. For its calibration, we have used Crison standard buffer solutions of pH values 4.01, 7.00 and 9.21. Measure error (±1 digit): ≥0.01 pH, ≥ 1mV,≥ 0.2 °C.

#### 3.2.4.4 MAGNETIC STIRRER

A magnetic stirrer Bungen model MC8 has been used to perform several experiments.

#### 3.2.4.5 SHAKER

An Elmi Skyline model DTS-2 shaker has been used in this Thesis. The shaker features are a rotational speed range between 100-1300 rpm, a rotation amplitude of 1.5 mm and a temperature control range between ambient +3 up to 60 °C.

### 3.2.5 REAGENTS

The chemical reagents used in the development of the experimental part of this Thesis have been the following.

- 3-mercaptopropanoic acid. Fluka.
- Acetone. Sigma-Aldrich.
- Calcium chloride. Merck
- Cobalt fluoride. Aldrich.
- Copper II chloride. Merck
- Cyclam (1,4,8,11-Tetrazacyclotetradecane). Aldrich.
- Cyclen (1,4,7,10-Tetraazacyclododecane). Aldrich.
- Double-distilled and de-ionized water in a Milli-Q system, of MilliPore (resistivity: 18 MΩ•cm)
- Ficoll. Sigma.
- Hydrochloric acid. Sigma-Aldrich.
- Iron III chloride.  Fluka.
- Magnesium Chloride. Sigma-Aldrich.
- Manganese II Chloride. Merck.
- MitoTracker Deep Red, Thermo Fisher.
- N-Hydroxysuccinimide (NHS). Aldrich.
- N-(dimethylaminopropyl)-N'-Ethylcabodiimide hydrochloride (EDC). Fluka.
- Nickel II chloride. Merck.
- Phosphate buffer saline. Sigma-Aldrich
- Potassium chloride. Merck.
- CdSe/ZnS (core/Shell) QDs of different sizes, providing luminescence emission at the wavelengths of 520 and 600 nm ($QD_{520}$ and $QD_{600}$). The QDs are supplied with a coating of the lipophilic ligand hexadecylamine. Mesolight.
- Serum Bovine albumin (BSA). Sigma-Aldrich
- Sodium chloride. Sigma.
- Sodium hydroxide. Panreac.
- Tris (hydroxymethyl-aminomethane). Sigma
- Zinc Chloride. Sigma-Aldrich.

In general, the reagents were used without futher purification, after checking the absence of fluorescent emission due to impurities. The chemicals were analytical or biochemical grade purity.

### 3.2.5.1 BUFFERS PREPARATION

- Tris Buffer: For the preparation of 10 mM Tris buffer solutions at pH 7.2, the Tris reagent was used, dissolving the required mass in bidistilled water. To adjust the pH value, solutions of 0.1 M NaOH and HCl were used.

- Phosphate buffered saline solution (PBS): a commercial PBS 10X stock solution (Sigma) was used. The stock PBS buffer was diluted down to 1X in Milli-Q water at 7.5-

8 pH at room temperature. The PBS buffer was filtered using Whatman Anotop TM 0.2 µm filters prior to use.

### 3.2.6. NANOSENSORS PREPARATION

#### 3.2.6.1 SOLUBILIZATION OF QDs IN AQUEOUS MEDIUM AND PREPARATION OF THE pH NANOSENSOR

To be able to work with QDs in aqueous media, it is necessary to solubilize them in water, because commercial QDs are surrounded by a layer of hexadecylamine (HDA), which stabilizes the nanoparticle in a lipophilic medium, in this case toluene. For this purpose, a ligand exchange reaction is carried out in which water-soluble functional groups will be incorporated and will allow the subsequent modification of the sensor. In particular, 3-mercaptopropionic acid (MPA) has been used, which will act by binding to the surface of the CdSe / ZnS QDs through the thiol group due to its high affinity, and leaving the free carboxyl group in contact with the aqueous solution. To do this, the QDs are left to react for 24 h at room temperature and in the dark with an excess of MPA in a 1:2 ratio (QDs:MPA, v:v). To make each batch, 200 µL of QDs and 400 µL of MPA were used. The thiol group of the MPA has a high affinity for binding on the surface of the CdSe/ZnS QDs, so that a ligand exchange is fulfilled, and the initial HDA ligands are substituted by the MPA, making the QDs soluble in aqueous medium.
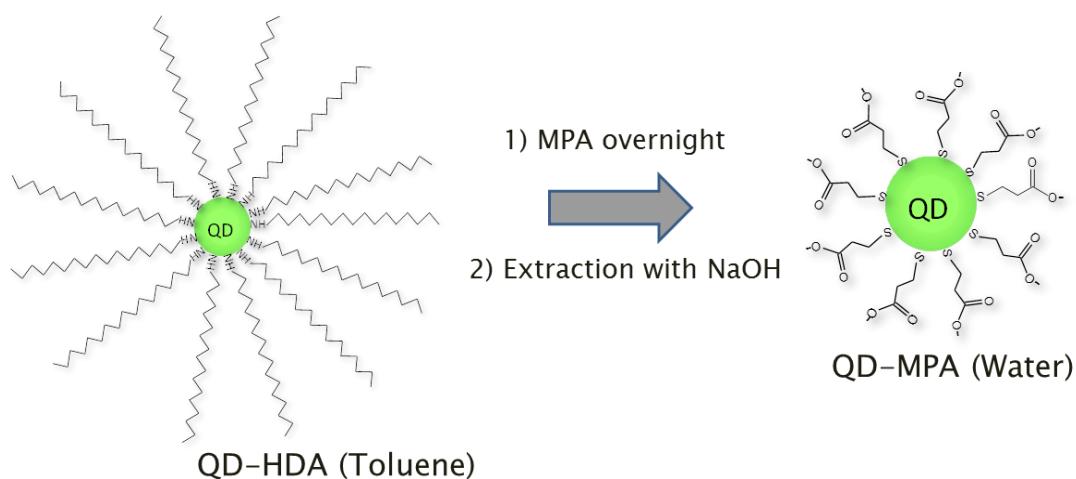


Figure 3.2.7. Scheme of the reaction of modification of the QDs surface to make them soluble in water.

After 24 h of reaction, the QDs are purified by changing the continuous phase of the dispersion. For this, 2 mL of 1 M sodium hydroxide solution are added, to favor the deprotonation of the carboxylic acid groups on the surface of the QDs, hence favouring the dispersion into the aqueous phase. The different phases are then separated with a

separatory funnel (Figure 3.2.8), discarding the organic phase (toluene), which remains in the upper part of the funnel, and collecting the aqueous phase where the nanoparticles are now located.



Figure 3.2.8. Decantation of the QDs after ligand exchange. Upper organic phase (toluene) and lower aqueous phase.

Then, acetone is added to this aqueous phase, which causes the QDs to precipitate, and the mixture is centrifuged at 13400 rpm for 10 min. The next step is to remove the supernatant, and the residue is resuspended using 500 µL of distilled water. Subsequently, more acetone is added and the purification step is repeated by centrifugation to eliminate the MPA groups that have not been immobilized on the surface of the QDs. Finally, the last step is to remove the supernatant and resuspend the residue (QD-MPA) in the same volumen of Tris buffer as initially taken.

Those experiments were carried out with nanoparticles of QDs with a maximum emission of 520 nm (green, $QD_{520}$) and 600 nm (red, $QD_{600}$), obtaining similar efficiency in the preparation of the water-soluble nanoparticles. The emission maxima of the QDs did not show notable differences after the incorporation of the MPA group when compared with the initial values of the maxima of the QD-HDA in toluene (Figure 3.2.9). The $QD_{520}$ nanoparticles did not show changes in the emission maximum, whereas in the $QD_{600}$ a 2.8 nm red-shift was observed after the modification, from 602.8 to 605.6 nm.
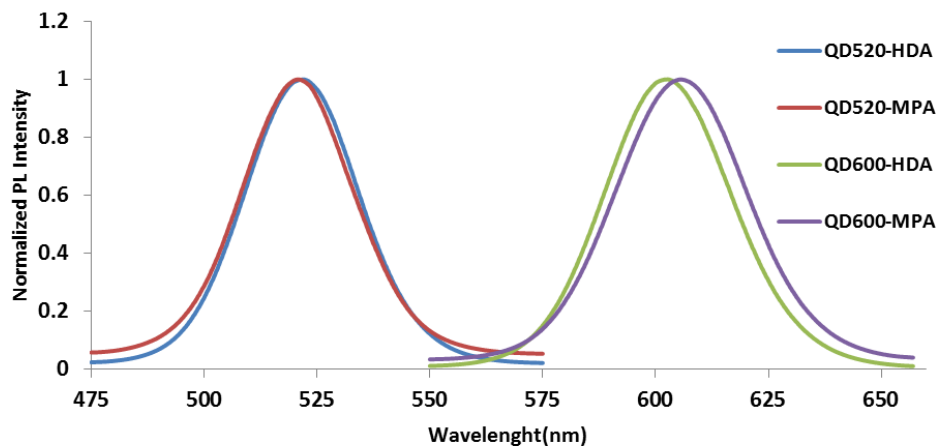
Figure 3.2.9. Emission spectra of the QD-HDA (in toluene) and the QD-MPA (in Tris Buffer 10 mM, pH 7.2) obtained after modification.

Importantly, the final QD-MPA product obtained exhibits a pH-dependency of its luminescence emission properties, as previously described in the literature[83, 126]. These QD-MPA conjugates can be used as pH nanosensors. Moreover, the QD-MPA constructs also represent the initial step to achive further modifications in the design of other nanosensors developed in this Thesis.

In this Thesis, two different types of pH nanosensors were developed. The first type was designed to report on the pH value in liquid biopsies, whereas the second type was developed to measure the pH inside living cells, specifically in the mitochondrial area. Specifically, the first type of pH nanosensor is indeed the QD-MPA construct described herein. For measurements of PL decay traces of the QD-MPA nanosensor in extracellular media, a new batch of the nanosensor was prepared for each series of measurements. First, a calibration was carried out and then the samples were measured. The preparation of the samples in which the QD-MPA nanosensors were employed is detailed in the corresponding chapter 3.3.

### 3.2.6.2 Zn$^{2+}$ IONS NANOSENSOR

The incorporation of the groups that will selectively react with Zn$^{2+}$ ions on the surface of the QDs is carried out by a covalent coupling reaction between the carboxylic acid of MPA, in the QD-MPA described above, and an amine group of an azacycle to form an amide bond. The azacycle group will be used to coordinate Zn$^{2+}$ ions, altering the luminescence emission properties of the nanosensors[141]. The coupling reaction was done by adding N-(3-dimethylaminepropyl)-N'-Ethylcarbodiimide hydrochloride (EDC), N-Hydroxysuccinimide (NHS) and the azacycle receptor to the QD-MPA.

Since the reagents are easily hydrolyzed, they must be freshly prepared just before they are needed. To carry out the reaction, 200 μL of QD-MPA are mixed with EDC. The EDC is added up to a final concentration of 100 mM, and the mixture is left in a magnetic stirrer for 10 min. The next step is the addition of NHS up to a final concentration of 50 mM. Finally, the azacycle is added up to a final concentration of 10 mM. The reacting mixture is completed with the necessary volumen of 10 mM Tris buffer at pH 7.2 to reach the concentrations previously detailed. This reaction mixture is left under magnetic stirring for 3-4 h at room temperature, protected from light by covering with aluminum foil.

For the purification of the reaction product and the separation of excess reactants that have not reacted, the mixture is centrifuged for 10 min at 13400 rpm. After centrifugation, the supernatant is removed and the residue containing the QDs with the azacycle on the surface (QD-azacycle) is resuspended in 200 μL of Tris buffer.

The working solutions of the QD-azacycle nanosensors, prepared to collect absorption and emission spectra and PL decay traces, had a final volume of 1 mL in 10 mM Tris buffer at pH 7.2, and contained 10 μL of the corresponding solution of QDs and varying concentrarions of $Zn^{2+}$.

In order to study the interferences caused by other ions and the competition between $Zn^{2+}$ and these interferents, a series of solutions of different ions and other possible substances that can be found in the cellular cytoplasm or biological samples were prepared. Different concentrations of the interfering species were added to the working solutions until the difference of the analytical signal obtained was greater than 5%.

### 3.2.6.3. INTRAMITOCHONDRIAL pH NANOSENSOR

The objective of this nanosensor is to report on the pH valueinside a particular organelle, in this case the mitochondria. Due to this difference, it was necessary to design another nanosensor. Although MPA was also the molecule on the QD surface providing the pH-dependency of the photophysical properties, the synthesis of nanosensor was completely diferent, since it required the addition of chemical groups that achieve mitochondrial delivery of the nanocomposites. We focused our attention on the Szeto-Schiller(SS) peptides as efficient mitochondrial targeting molecules[142]. Hence, for the preparation of the mitochondrial pH nanosensors, it was necessary to include the SS peptides and the MPA groups onto the surface of the QDs.

### SYNTHESIS OF SZETO-SCHILLER PEPTIDES

The synthesis of the Szeto-Schiller peptides was performed by Rafael Contreras-Montoya, from the company Nanogetic S.L. (Granada, Spain) within the context of the collaboration between this company and our research group. The company provided

the final materials, after the synthesis reactions were optimized. Since this optimization is part of the research project, it is described in this Thesis.

Coupling reactions were carried out in solid phase, using 10 mL of solvent per gram of resin. To test each coupling reaction, a qualitative Ninhydrin Test was carried-out after each coupling reaction as described in literature[143].

The solid phase synthesis of the peptides was carried out using the reagents depicted in Table 3.2.1 and a series of common protocols described below. The first step was the obtention of the modified Rink polystyrene resin (Scheme 3.2.1). Then, the serial addition of the corresponding reagents resulted in the final synthesis of the SS peptides. Three different SS peptides were prepared, including a final modification with a thiol-undecyl chain for the interaction with the QDs via the sulfur, as it is described in the next section.

The common methods in each step of the syntheses were:
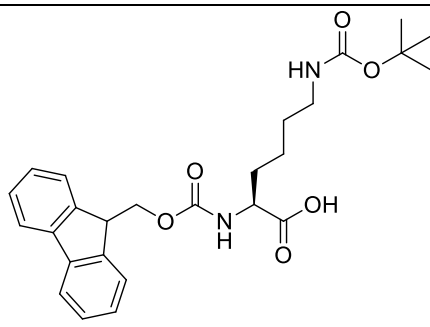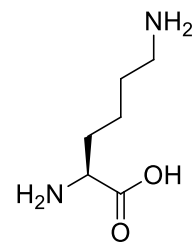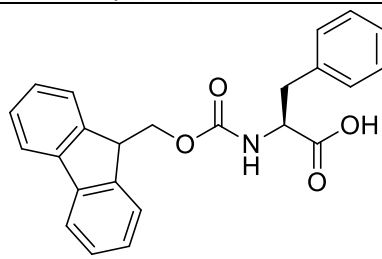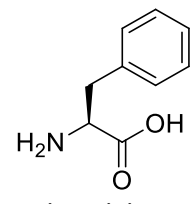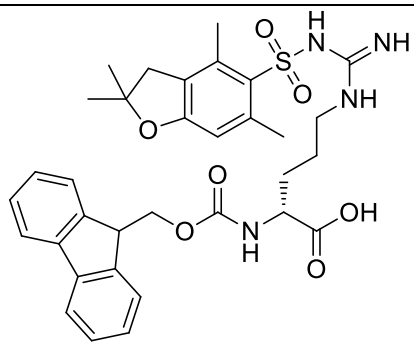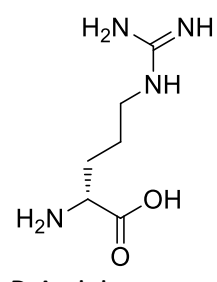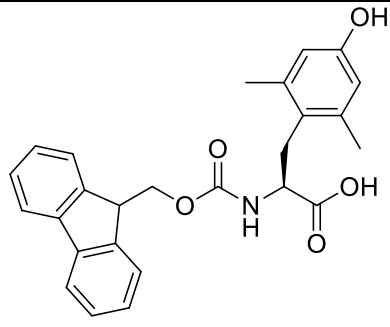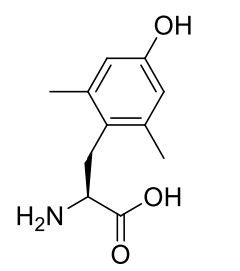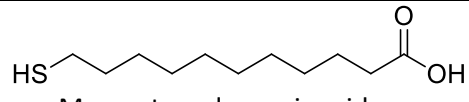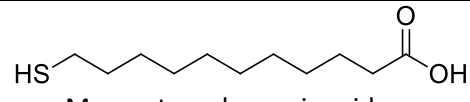
*Method A* – solid phase peptide coupling conditions using carboxylic acids and free primary amines: Resin was previously swollen in dimethylformamide (DMF). Then, carboxylic acid (3.5 equiv) and hydroxybenzotriazole (HOBt) (5 equiv) were dissolved in DMF. Diisopropylcarbodiimide DIC (5 equiv) was added and the mixture was stirred for 15 min before addition to the resin. The mixture was agitated for 2 h at 60 °C to favour coupling. The resin was washed with DMF (x5), dichloromethane DCM (x5) and diethyl ether (x2).

*Method B* – free amine acetylation: Resin was suspended in DMF. Then pyridine (2 equiv) and anhydride acetic (2 equiv) were added to the suspension. The mixture was agitated for 15 min. The resin was washed as in Method A.

*Method C* – N-terminal Fmoc removal: Fmoc removal was performed using 20% piperidine in DMF with two sequential treatments of 45 min. The resin was then filtered and washed with DMF (x5), DCM (x5) and diethyl ether (x2).

*Method D* – cleavage of peptides from resin and acid labile protecting groups removal: Dry Resin was suspended in 20 mL per gram of resin of TFA/$H_2O$/EDT/TIS (93.5/2.5/2.5/1.5) and agitated for 2 h. The TFA solution was filtered, vacuum concentrated and added to cold (4 °C) diethyl ether in a centrifuge tube. The resulting precipitate was collected by centrifugation and washed with diethyl ether (x3).

Table 3.2.1. Reagents used in each stage of the solid-phase synthesis of the SS peptides.

| Reagent code | Carboxylic acid as reagent | Amino acid coupled |
|---|---|---|
| I | <br>Fmoc-L-Lys(Boc)-OH | <br>L-Lysine |
| II | <br>Fmoc-L-Phe-OH | <br>L-Phenylalanine |
| III | <br>Fmoc-D-Arg(Pbf)-OH | <br>D-Arginine |
| IV | <br>Fmoc-L-Dmt-OH | <br>L-Dimethyltyrosine |
| V | <br>Mercaptoundecanoic acid | <br>Mercaptoundecanoic acid |

Once these common procedures were established, the synthesis reactions for the Rink polystyrene resin, and the mercapto-modified SS20, SS02 and SS31 are depicted in Schemes 3.2.1, 3.2.2, 3.2.3, and 3.2.4, respectively.
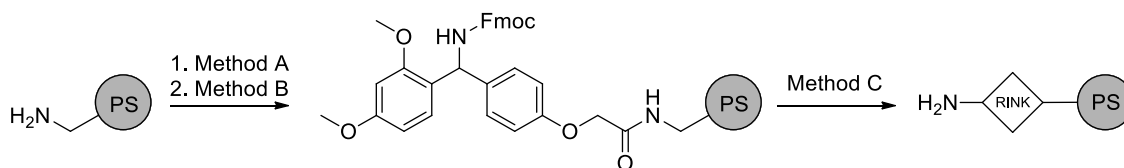


Scheme 3.2.1. Synthesis of Rink polystyrene resin.
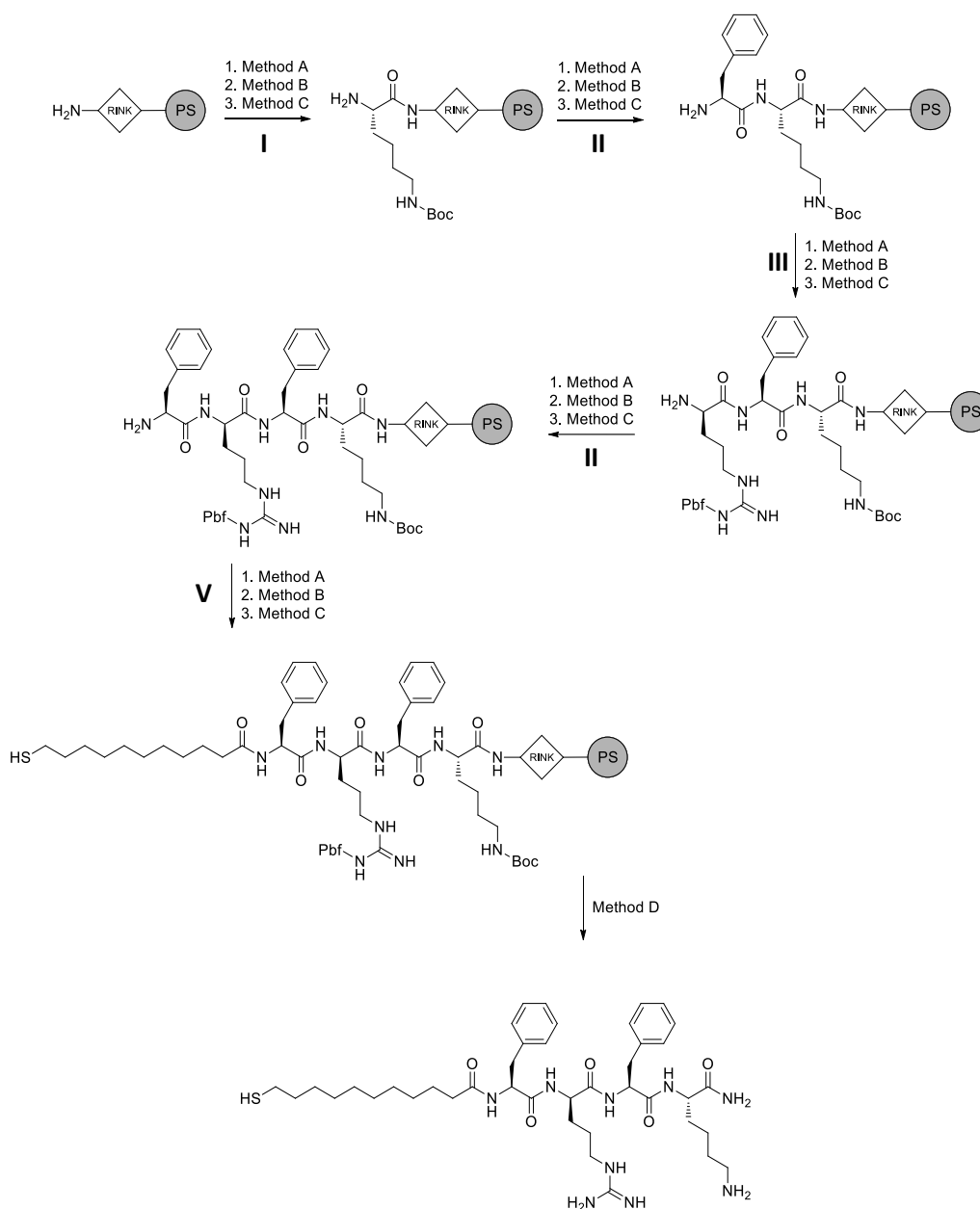


Scheme 3.2.2. Synthesis of the SS20-MERCAPTO peptide.
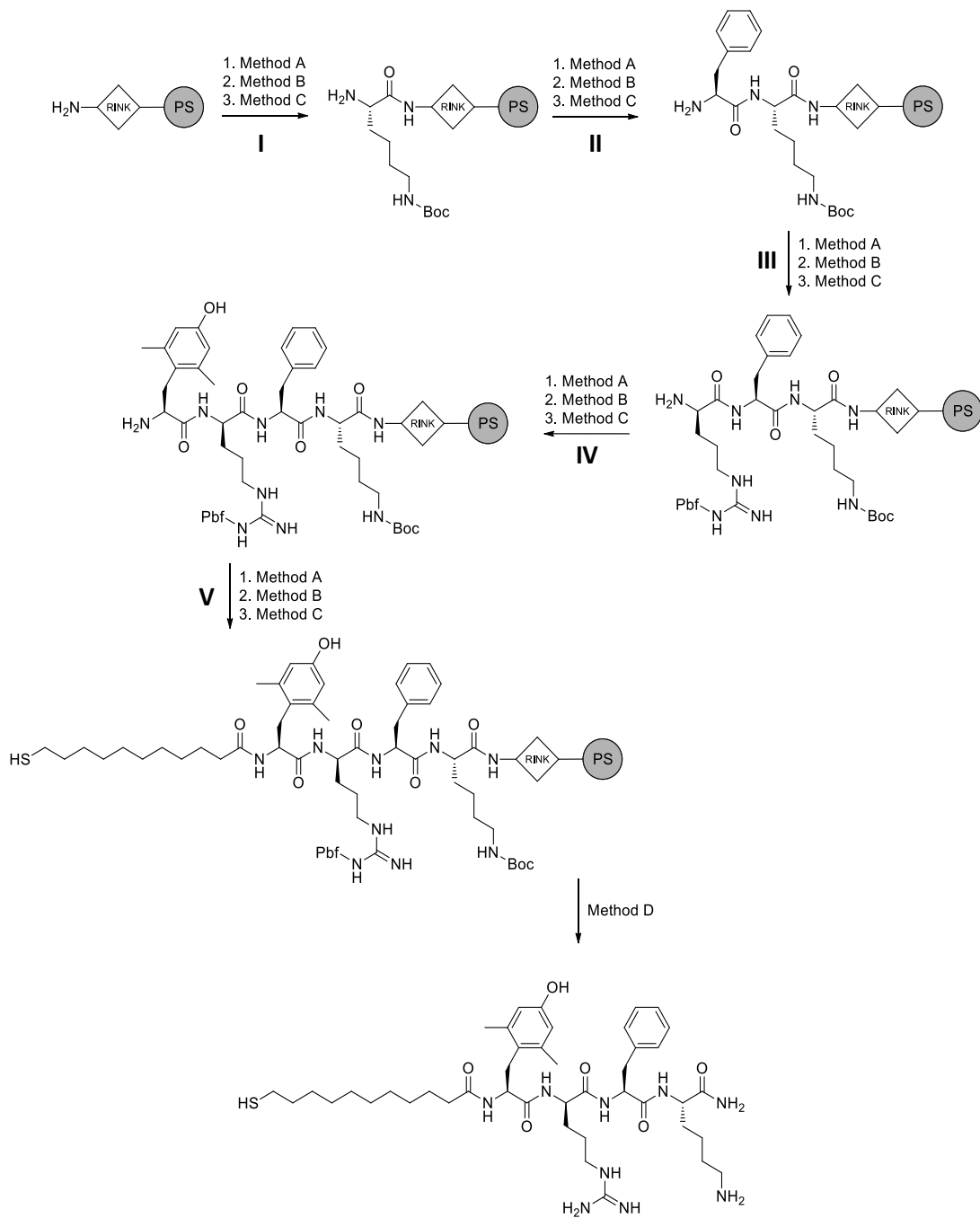
Scheme 3.2.3. Synthesis of the SS02-MERCAPTO peptide.
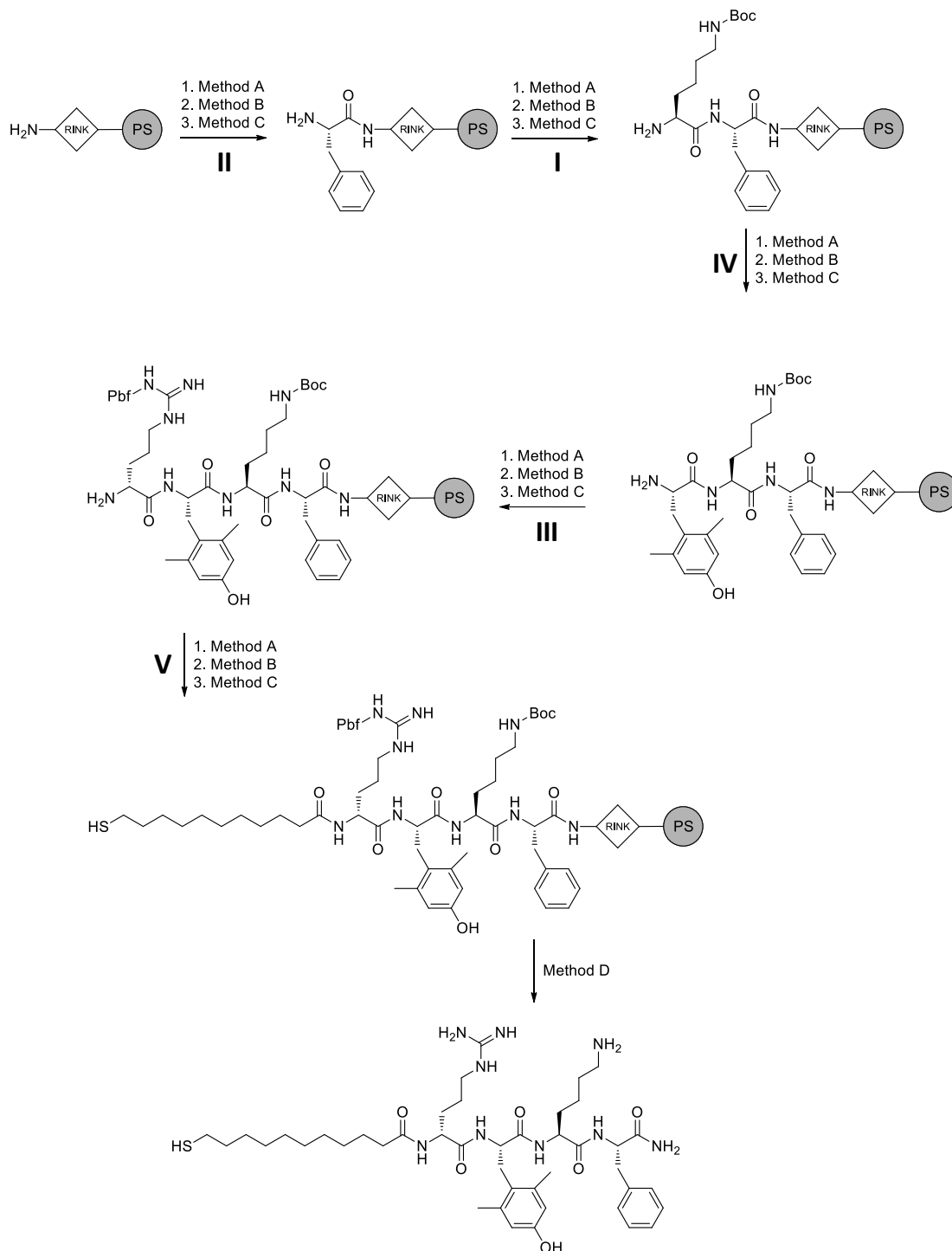
Scheme 3.2.4. Synthesis of the SS31-MERCAPTO peptide.

## SYNTHESIS OF SSPEPTIDE-MPA-CAPPED CDSE/ZNS NANOPARTICLES

The synthesis of the conjugates designed as intramitochondrial pH nanosensors started from the commercial QDs, covered with a layer of HAD ligand on the surface, and dissolved in toluene. The first step consisted on evaporating the toluene by

heating up to 85 °C 200 μL of the QD suspension during 5 min. Meanwhile, a quantity of the corresponding SS peptide was weighted to reach the amount of $1.65 \times 10^{-3}$ moles and dissolved them in 10 mL of MiliQ water. This peptide solution was added to the QDs and stirred vigorously. The mixture was sonicated for 2 h, under continuous manual agitation. Then, 400 μL of MPA were added to the mixture and sonicated for 60 min. The mixture was left to react overnight. The solution was divided into twelve eppendorf tubes and centrifuged at 13000 rpm for 10 min. After the centrifugation step, the supernatant was removed and the pellet was resuspended in PBS buffer pH 8. Then, 100 μL of MPA were added on each eppendorf and sonicated for 30 min. Finaly, QD-SSpeptide-MPA nanoparticles were separated from the aqueous solution by precipitation using acetone and centrifugation, followed by the resuspension of the nanosensors in PBS buffer pH 8.

## 3.2.7 BIOLOGICAL SAMPLES PREPARATION

To carry out this thesis, five breast cancer cell lines have been used to provide a representative subtype according to the current clinical classification, each cell line is classified within a different clinical subtype, which is discribed more extensively in Chapter 4. The selected cell lines were: MCF7, ZR751, SKBR3, MDA-MB-231 and MDA-MB-468.

### 3.2.7.1 MEASUREMENTS OF EXTRACELLULAR pH VALUES BY QD-BASED pH NANOSENSOR

The extracellular pH values were determined for each breast cancer cell line by using the QD-based pH nanosensor designed and optimized in this work (section 3.2.6.2).

The cell lines were subcultured in 6 well plates at a density for SKBR3, MDA-MB-231 and MCF7 of $1.6 \times 10^4$ cells/cm$^2$, for MDA-MB-468 of $1.3 \times 10^4$ cells/cm$^2$ and for ZR751 $2.1 \times 10^4$ cells/cm$^2$ for 24h. After 24h, the medium was exchanged for the same medium corresponding to each cell line, but without sodium pyruvate. Next, four different experimental conditions were performed to analyse possible pH differences between the different cell lines, and between different experimental conditions. The experimental conditions were:

a) Complete medium

b) Medium without sodium pyruvate

c) Complete medium with aminooxiacetate

d) Medium without sodium pyruvate and with aminooxiacetate.

The plates were incubated overnight at 37 °C. Next day, 1.2 mL of media from each well were aliquoted in Eppendorf and stored at -20 °C until all the experimental replicates were obtained to be analysed simultaneously by fluorescence. 4 replicas of each treatment were collected for each cell line.

The pH values were measured using the QD-based pH nanosensors (section 3.2.6.2) and the time resolved spectrofluorometer (Chapter 3.2.2). First, a pH calibration was performed using the culture medium of each cell line. To modify the pH of the culture medium, hydrochloric acid and sodium hydroxide were used and the pH was measured with a pH-meter. For the measurement, 2 µL of the pH nanosensors were added to 1 mL of culture medium in a spectrofluorometer cuvette. Three decays were collected for each sample and the fitting of the decay traces was made as detailed in chapter 3.2.2.

### 3.2.7.2 Intramitochondrial pH quantification by QD-based pH nanosensor and FLIM

Intamitochondrial pH quantifications were performed taking advantage of our optimized method, combining the use of the QD-based pH nanosensor synthesized with a mitochondrial delivery peptide, and the high resolution FLIM technology (Sections 3.2.6.1 and 3.2.10.2)

For this assay, the cell lines were also subcultured in 6-well plates, at the same densities as indicated in previous section. Particularly in this case, it was necessary to add a 25 mm microscopy sterilized round slide to the wells, suitable to be placed by its dimension on the microscope objective once that the experiments is ended.

Following an optimized routine protocol, the cells were subcultured on Monday with their regular culture conditions, and incubated at 37 °C and 5% $CO_2$ until Wednesday. On Wednesday morning, before to work with the cells, it was necessary to sonicate the solution of QDs-MPA-ppetideSS (pH nanosensor) for 30 min in cold water. After sonication of the nanoparticle solution, 3 µL of the solution were added in 3 mL of culture medium per well. Next, the cell plates were incubated at 37 °C for 2h to allow entering the nanosensors into the cells and mitochondria by diffusion. After the delivery incubation, the culture medium was removed, and the wells were washed twice with PBS at pH 8, taking special care to avoid cell detachments from the microscopy slides. Then, 2 mL of fresh culture medium was added per cell wells, with 16 µL of a solution of Mitrotracker Deep Red dye of 0.5 mM for the mitochondrial colocalization analysis by FLIM, and the plates were incubated at 37 °C for 20 min. The commercial Mitotracker has a very high concentration, so it was necessary to prepare a working solution. To this, 10 µL of MT was diluted in 990 µL of MiliQ water. Finally, the culture medium was again removed, the wells were washed twice, and fresh culture medium was placed to adequately maintain the cells at 37 °C, until the

moment to start the FLIM measurements. For FLIM analysis and pH quantifications, the slides were placed in the microscope objective with 1 mL of PBS at pH 8. The microscopy methodology used is detailed in chapter 3.2.3.

### 3.2.7.3 CITOTOXICITY EXPERIMENTS

Citotoxicity assays were performed using Celltiter Blue viability assay. Celltiter Blue is an assay based on the ability of living cells to convert resazurin (a redox dye) into resorufin (a fluorescent product).

To carry out these experiments, the cell lines were seeded in 96-well plates and the QDs nanosensor were added. Then, the plates were incubated for 2h, 6h and 24h in the incubator at 37 °C. After the incubation, 20 µL of Celltiter Blue reageant were added per 100 µL of culture medium to each well, then the cell were incubated for 20 min at 37 °C. Finally, the fluorescence was measured in a GloMax®-Multi+ Detection System (Promega)(Chapter 4.2.1.6).

## 3.2.8. STEADY STATE FLUORESCENCE MEASUREMENTS

The steady state PL measurements were recorded in the Jasco FP-6500 spectrofluorometer described above, using quartz cuvettes of internal dimensions 5x10 mm. The scan speed and integration time were selected in such a way that a good signal-to-noise ratio was achieved, and that a subsequent smoothing of the spectra was not necessary. The excitation wavelength was always 440 nm, the width of the excitation and emission slits were set at 3 nm and 5 nm respectively, and the detector sensitivity was kept at "medium".

## 3.2.9 TIME-RESOLVED FLUORESCENCE MEASUREMENTS

The measurements of time-resolved PL decay traces were carried out with the instrumentation described above, using 5x10 mm quartz cuvettes. The PL decay traces were collected in histograms of 1036 channels. The time value per channel used was 36.7 ps/channel, covering a time window of 100 ns, corresponding to the repetition frequency of 10 MHz. Using this time window ensured that the whole decay trace was collected (the number of counts at the end of the decay was less than 0.5% of the counts at the maximum). The histograms were collected until the maximum peak channel reached 20000 counts. The excitation wavelength used was 440 nm. Three PL decay traces were collected at the emission wavelengths of 520, 522 and 524 nm for the $QD_{520}$ sensors, and 598, 600 and 602 nm for the $QD_{600}$ sensors. To obtain the instrument response function (IRF), the histogram was obtained by placing a colloidal

silica dispersion (LUDOX) in the sample compartment, collecting the scattered light with the monochromator set at the excitation wavelength. During the realization of the measurements several instrumental profiles were collected, thus verifying the high stability of the laser with time.

## 3.2.10 CONFOCAL FLUORESCENCE AND FLIM MICROSCOPY MEASUREMENTS

### 3.2.10.1 FLIM IMAGING OF THE QD-BASED $Zn^{2+}$ NANOSENSOR

PL lifetime images were recorded with a *MicroTime 200* fluorescence lifetime microscope system described earlier. The excitation source was the 485-nm pulsed laser operated with the 'Sepia II' driver set at a repetition rate of 10 MHz. The laser power at the microscope entrance was between 0.2 and 4.4 μW. The specific optical settings for the microscope were as follows. The excitation beam passed through an achromatic quarter-wave plate (AQWP05M-600, Thorlabs), set at 45° from the polarization plane of the laser, and was directed by a dichroic mirror (510DCXR, AHF/Chroma) to the oil immersion objective (1.4 NA, 100×) of the inverted confocal microscope. The PL emission was collected through the same objective and directed into a 75-μm pinhole after passing through a 500LP (AHF/Chroma) cutoff filter. The PL emitted photons were detected in a single SPAD channel after crossing a 600/40 bandpass filter (AHF/Semrock). Individual photons time tagging was performed within the *TimeHarp 200* module, with a time resolution of 29 ps per channel. The imaging data were normally acquired with a 512 × 512 pixel resolution and a collection time of 0.60 ms per pixel.

### 3.2.10.2 MITOCHONDRIAL LOCALIZATION AND FLIM IMAGING OF THE QD-BASED pH NANOSENSOR

Colocalisation of the designed QD nanosensor and mitochondria organelles, and the correspondng pH studies using dual-colour FLIM were performed on the *MicroTime 200* fluorescence lifetime microscope system. The excitation sources were the 470 nm and 635 nm pulsed diode lasers, operated with the "Sepia II" driver set at a repetition rate of 10 MHz, and working under the PIE excitation regime. The laser power at the microscope entrance was between 0.2 and 4.4 μW. The 635 nm laser was delayed 56 ns to the middle of the detection window using a delay box. In this configuration, the 470-nm laser was used to directly excite the QD nanosensors, whereas the 635-nm laser caused the direct excitation of the mitochondrial staining fluorophore, Mitotracker Deep Red (MT). The PIE excitation scheme reduces artifacts due to cross-talk between channels. The excitation laser beams passed through an acromatic quarter-wave plate (AQWP05M-600, Thorlabs), set at 45º from the

polarization plane of the laser, and were directed by a specific dual-band dichroic mirror (AHF/Chroma), prepared for the 470/635 dual excitation, into the specimen through the apochromatic oil immersion objetive (100x, 1.4NA). The collected PL emission was focused into a 75-μm pinhole after passing through a LP500 long pass filter (AHF/Chroma). Finally the emitted light was separated into two SPAD detection channels, using a 600DCXR (AHF/Chroma) dichroic mirror. The first channel was dedicated to the tested QD nanosensor, using a 520/35 bandpass filter (AHF/Chroma), whereas the second channel was solely dedicated to the red fluorescence from the MT, using a 685/70 bandpass filter (AHF/Chroma). Time tagging of the detected photons was performed in the *TimeHarp 200* modules, with a time resolution of 29 ps per channel. Images were collected with a 512 × 512 pixel resolution and a collection time of 0.60 ms per pixel.

## 3.2.11. ANALYSIS METHODS

### 3.2.11.1 ANALYSIS OF PL DECAYS IN BULK SOLUTION

The PL lifetimes of QD nanosensors in bulk solution were obtained by fitting the PL decay traces to multi-exponential decay functions, using the iterative deconvolution analysis in the FluoFit 4.4 package software (PicoQuant), via a least squares minimization deconvolution method based on the Levenberg-Marquard nonlinear algorithm.

For the experiments with QD-based nanosensors, up to four exponential components were used to fit the experimental PL decay traces of the QD nanoparticles. The quality of the fitting was judged by the reduced chi-square method, $\chi^2$, and the visual inspection of random distributions of the weighted residuals and the autocorrelation functions. To determine the average lifetimes of the QD emission, $\tau_{ave}$, equation (1) was used, in which $a_i$ represents the preexponential factors and $\tau_i$ represents the individual decay times[111].

$$\tau_{ave} = \sum a_i \tau_i^2 / \sum a_i \tau_i \qquad (3.2)$$

### 3.2.11.2 ANALYSIS FLIM IMAGES

The images obtained by FLIM were analyzed using the software SyphoTime 32 (PicoQuant). The FLIM images were reconstructed by classifying all the photons corresponding to a single pixel in a temporal histogram by the Time Tagged Time Ressolved (TTTR) methodology. The regions of interest were selected (the pixels that

contained the QDs emissions and that had at least 200 photons per pixel), in this way the global PL decay of these regions was obtained. The decay was adjusted with a biexponential decay function, and was subjected to the iterative reconvolution method based on the maximum likelihood estimator (MLE), which is a more reliable method for decays with low counting rates. The IRF for the iterative reconvolution analysis was obtained by reconstruction and deconvolution of an experimental PL decay from an image with a lare number of counts, by means of an algorithm implemented in the SimphoTime software. To obtain the FLIM image, a spatial binning of 5x5 pixels and a temporal binning of 4 time channels (for a final temporal resolution of 464 ps/channel) were applied to obtain higher counts in each pixel. The individual decays of each pixel were fitted to the same multiexponential function, leaving the first decay time ($\tau_1$) as a fixed parameter with a value of 1.5 ns, which accounts for the autofluorescence contribution of the cell, and the second decay time ($\tau_2$) and the pre-exponential factors as adjustable parameters. Finally, the FLIM image is obtained using an arbitrary color scale that shows the values of the adjustable lifetime ($\tau_2$) in each pixel. After the analysis, the distribution of the lifetime $\tau_2$ in the pixels of interest is obtained. These distributions give an idea of the average value of the lifetime, as well as the precision of the measurements (width of the distributions). The selection of pixels of interest and the reconstruction of $\tau_2$ distributions have been implemented in home-coded scripts in MathCad 15.0 (PMC). In the case of colocalization studes with the MT deep red dye, the pixels of interest were those in which the intensity in both the QD and the MT channels were larger than a specific threshold, as depicted in Figure 3.2.10.
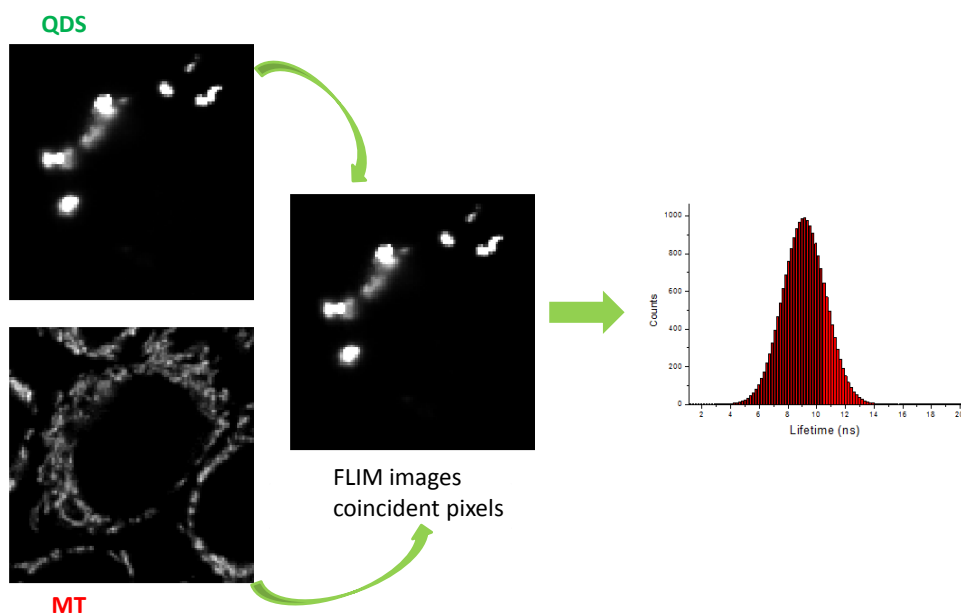


Figure 3.2.10. Method of analysis of the FLIM imaging of the QD nanosensors, selecting only those pixels that are colocalized in the QD and MT images. Average PL lifetime distributions are obtained from the FLIM image of those pixels.

# 3.3. Zn$^{2+}$ NANOSENSORS

### 3.3.1 OPTIMIZATION OF THE COUPLING REACTION OF THE QD-MPA WITH THE AZACYCLE

In this section of the Thesis, it was proposed to develop a Zn$^{2+}$ nanosensor. For this, we proposed the conjugation of the QD nanoparticles with azacycles[141]. It is known that azacycles have the ability to chelate several metal ions, including Zn$^{2+}$. It is also known the relevance of these compounds in pharmacological therapy. For instance, some azacycles such as cyclam and derivatives (Xylil-bicyclam) have anti-HIV activity, as they inhibit the entry of the virus to white blood cells[144]. To incorporate the azacyle that will act as the analyte receptor group in the sensor, a covalent coupling reaction was carried out between the carboxylic acid of the MPA on the surface of the QDs and an amine group of the azacycle, for the formation of an amide group. For this purpose, we used a reaction between a carbodiimide, N-(3-dimethylaminepropol)-N'-ethylcarbodimide hydrochloride (EDC) and a succinimide ester, N-hydroxysuccinamide (NHS)[35, 56, 145, 146]. The function of the EDC is to activate the –OH of the carboxyl of the MPA chain, while the NHS will favor the union of the –OH of the MPA and the –NH of the azacycle, thus obtaining the covalent binding between the QDs and the molecule of azacycle.

In this Thesis two azacycles of the same family had been used, the 1,4,8,11-Tetraazacycletetradecane (cyclam) and the 1,4,7,10-Tetraazacycedodecane (cyclen), whose structures are shown in Figure 3.3.1.
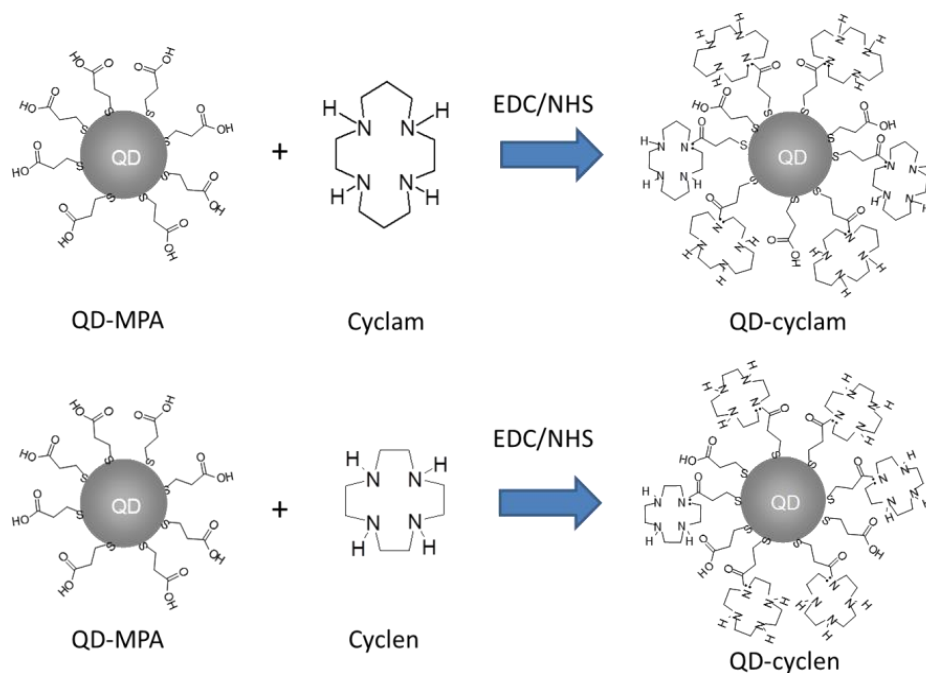


Figure 3.3.1. Scheme of the coupling reaction of QD-MPA with the azacycles.

As the first step, the concentration of EDC and NHS was optimized. For this, the amount of QD-MPA was set at 120 µL and the concentration of the azacycle at 10 mM, while for the EDC and NHS, four different concentrations were chosen, in which the EDC was always twice as concentrated as the NHS. The concentrations were: EDC 200 mM and NHS 100 mM, EDC 100 mM and NHS 50 mM, EDC 50 mM and NHS 25 mM and finally EDC 20 mM and NHS 10 mM. All solutions were prepared in a 10 mM Tris Buffer at pH 7.2.
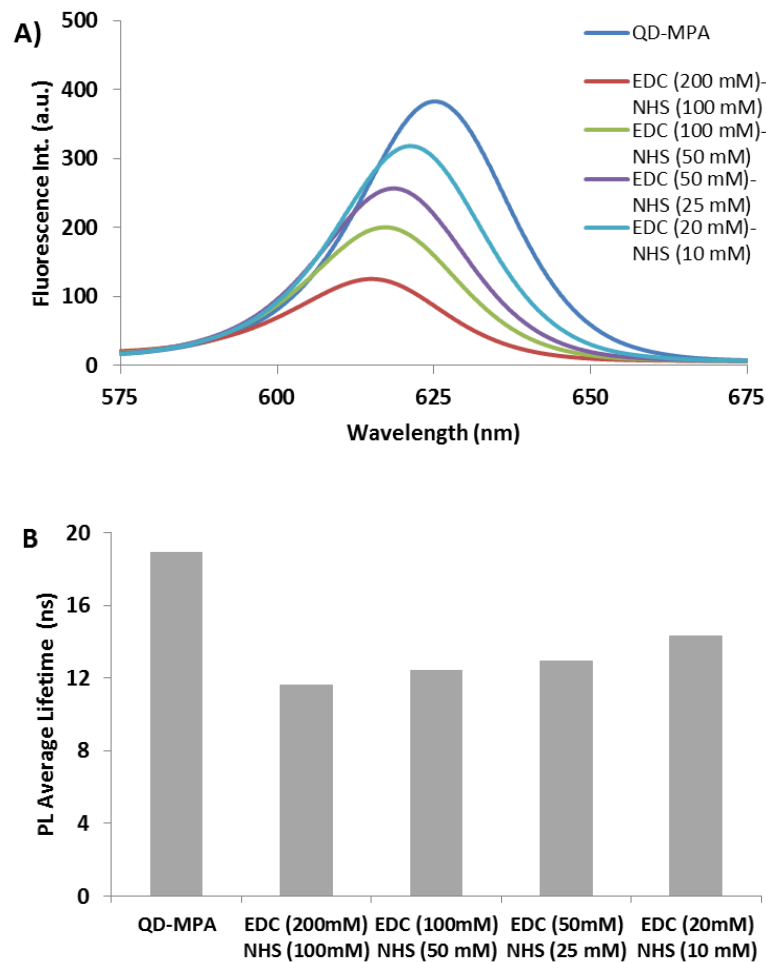


Figure 3.3.2. Emission spectra (A) and PL average lifetime (B) of the $QD_{600}$-MPA and the QDs after the reaction with a fixed amount of the azacycle cyclam ($QD_{600}$-cyclam) and different concentrations of EDC/NHS.

After each reaction, the emission spectra of the obtained QD-azacycle conjugate were collected and, as can be seen in Figure 3.3.2A, the coupling reaction causes a decrease in the PL intensity of the QDs. Similarly, the PL decays of the QD-MPA were collected before and after the corresponding reaction to incorporate the azacycle. In all cases, the PL average lifetime of the QDs decreased after the reaction (Figure 3.3.2B).

In both cases, it was observed that as the concentration of EDC and NHS increases, a decrease in both the PL and the average PL lifetime of the QDs did occur, as a consequence of the coupling reaction. As a trade-off solution between a good reaction and a saving of reagents, concentrations of EDC and NHS of 100 mM and 50 mM, respectively, were chosen to be used in the following experiments.

The next step was to optimize the concentration of the azacycle. For this, three different concentrations of azacycle were tested during the coupling reaction: 50 mM, 20 mM and 10 mM, fixing the previously chosen concentrations of EDC and NHS (100 mM and 50 mM, respectively) and the amount of QD-MPA (120 µL), again in a medium of 10 mM Tris buffer at pH 7.2.

As seen in Figure 3.3.3A, the binding of the azacycle on the surface of the QDs causes a quenching of its PL intensity (Figure 3.3.4). The greater the quantity of azacycle in the surface is, the greater the efficiency of its quenching is, and therefore the lower the QD emission intensity is. Likewise, the average PL lifetime of the QD-azacycle decreased with the azacycle concentration immobilized on the surface. (Figure 3.3.3B).
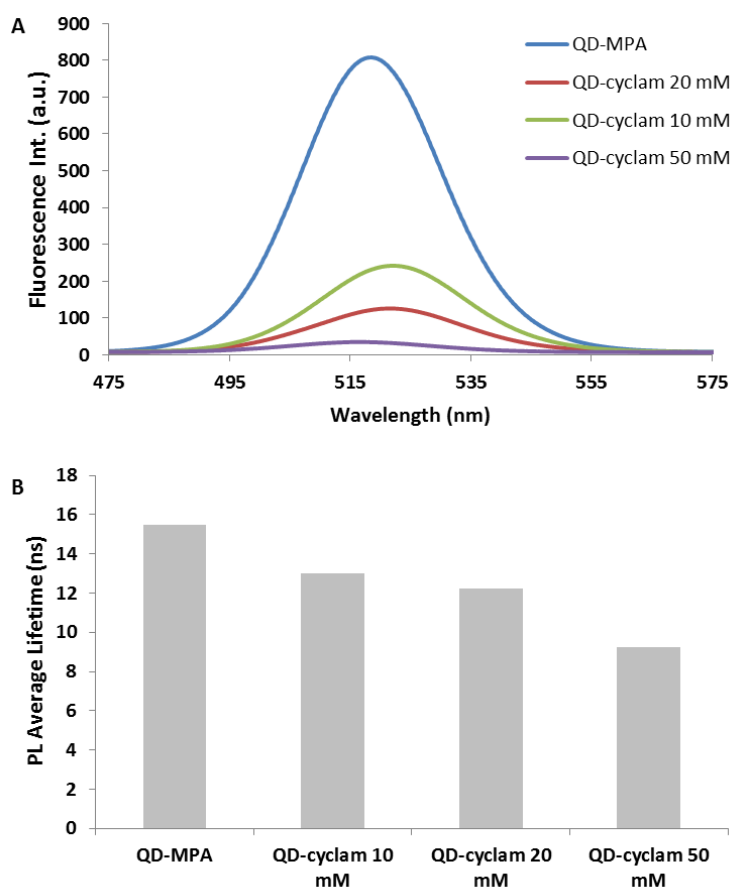


Figure 3.3.3. Emission spectra (A) and PL average lifetime (B) of $QD_{520}$-MPA and $QD_{520}$-cyclam conjugates prepared in reactions with various concentrations of the azacycle cyclam.

In addition, to select the most appropriate conditions for the development of a high sensitivity sensor, the response to changes in $Zn^{2+}$ concentration of the three QD-cyclam conjugates, with different amounts of cyclam in their surface, was tested. For this, the PL intensity and the PL decay of each one were measured after the addition of 1 mM of $Zn^{2+}$ (the response mechanism will be explained in the following section). In these experiments, the QD-cyclam nanosensors that had been synthesized with a concentration of 10 mM azacycle were the ones that showed the greatest response to $Zn^{2+}$ ions. This may be due to the fact that when there is an excessive amount of azacycle during the reaction, and therefore immobilized on the surface of the QDs, it is possible the coupling of one molecule of azacycle with more than one nanoparticle of QD, which causes the aggregation of the sample and a decrease of the response to $Zn^{2+}$. Therefore, in order to achieve maximum sensitivity in the proposed nanosensors, an azacycle concentration of 10 mM was selected during the synthesis process for the successive experiments.

## 3.3.2 NANOSENSOR QD-AZACYCLE RESPONSE TO $Zn^{2+}$ IONS

The binding of azacycle at the surface of the QDs produces a quenching of its PL emission caused by a photo-induced electronic transfer (PET) from the pair of unpaired electrons that remains in the nitrogen of the amide towards the QDs. This translates into a decrease in both the intensity and the PL lifetime of the nanoparticles (Figure 3.3.3). However, when $Zn^{2+}$ is bound inside the azacycle, it requires the pair of unpaired electrons from the nitrogen for coordination, which interrupts the PET and, as a consequence, the PL of the QDs is recovered, observing an increase in both the intensity and the PL lifetime of the nanoparticles (Figure 3.3.4). Therefore, this mechanism allows the use of the QD-azacycle conjugates as nanosensors of $Zn^{2+}$ ions.
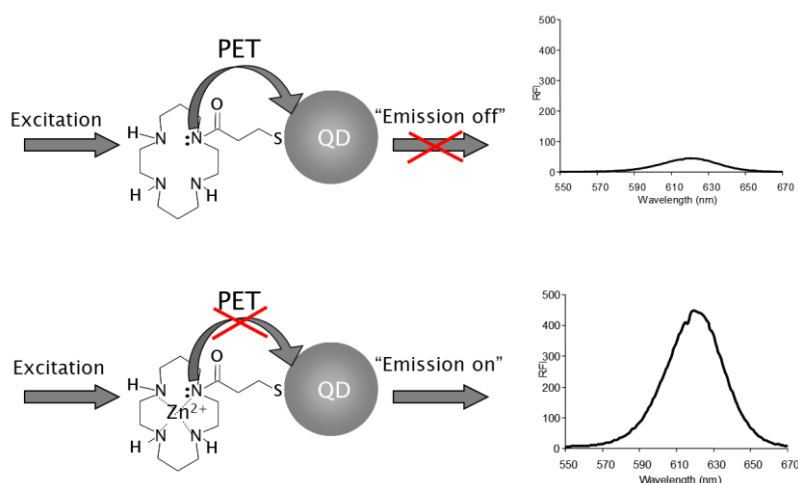


Figure 3.3.4. Mechanism of response of QD-azacycle sensors against $Zn^{2+}$ ions.

Once the QD-azacycle conjugates were optimized, a calibration of the proposed nanosensor was carried out. To do this, the QD-cyclam and QD-cyclem conjugates were prepared according to the conditions described above, and their emission spectra and PL decays were collected in the absence and in the presence of different concentrations of $Zn^{2+}$. All solutions were prepared in 10 mM Tris Buffer at pH 7.2. As an example, Figure 3.3.5 shows the decay curves of the QD-cyclam and the QD-cyclen nanosensor at different concentrations of $Zn^{2+}$.
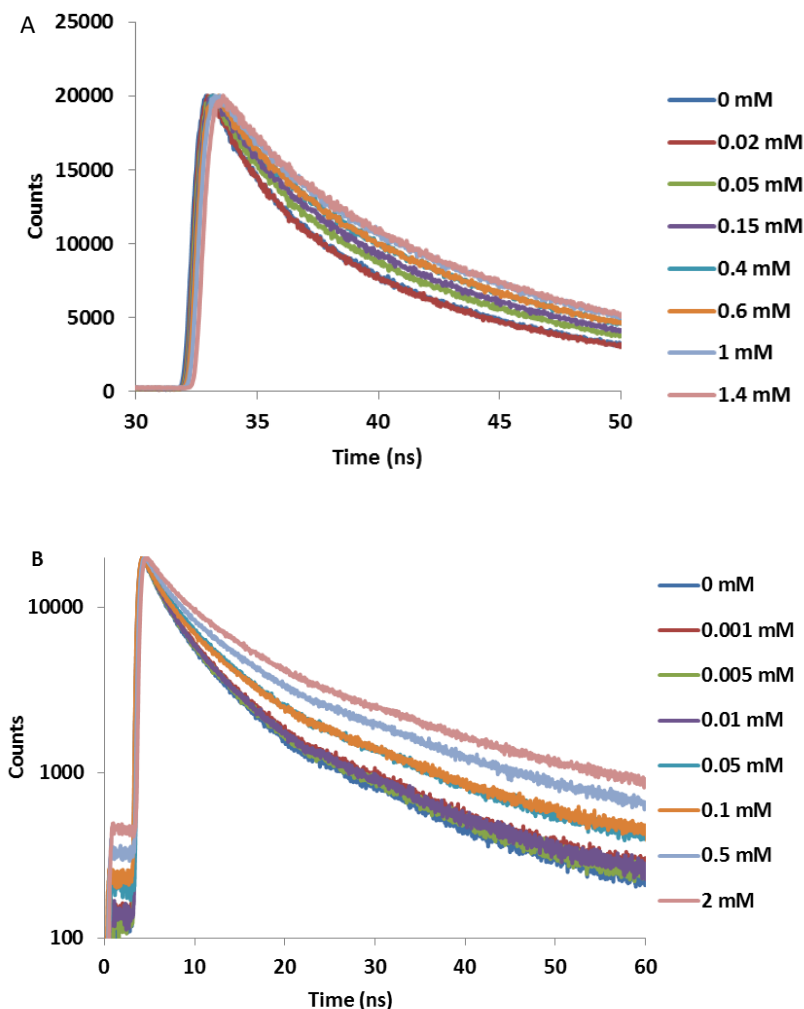


Figure 3.3.5. Decay curves of the $QD_{520}$-cyclam (A) and $QD_{600}$-cyclen (B) in the absence and in the presence of the different concentrations of $Zn^{2+}$.

As seen in Figures 3.3.6A and 3.3.7A, the PL intensity of both nanosensors increase with the amount of $Zn^{2+}$ added. In addition, after analyzing de decay curves to calculate the average lifetime, their PL lifetime also increases gradually as the concentration of $Zn^{2+}$ ion in the medium increases. (Figures 3.3.6B and 3.3.7B). Similar results were obtained with QDs of different size.
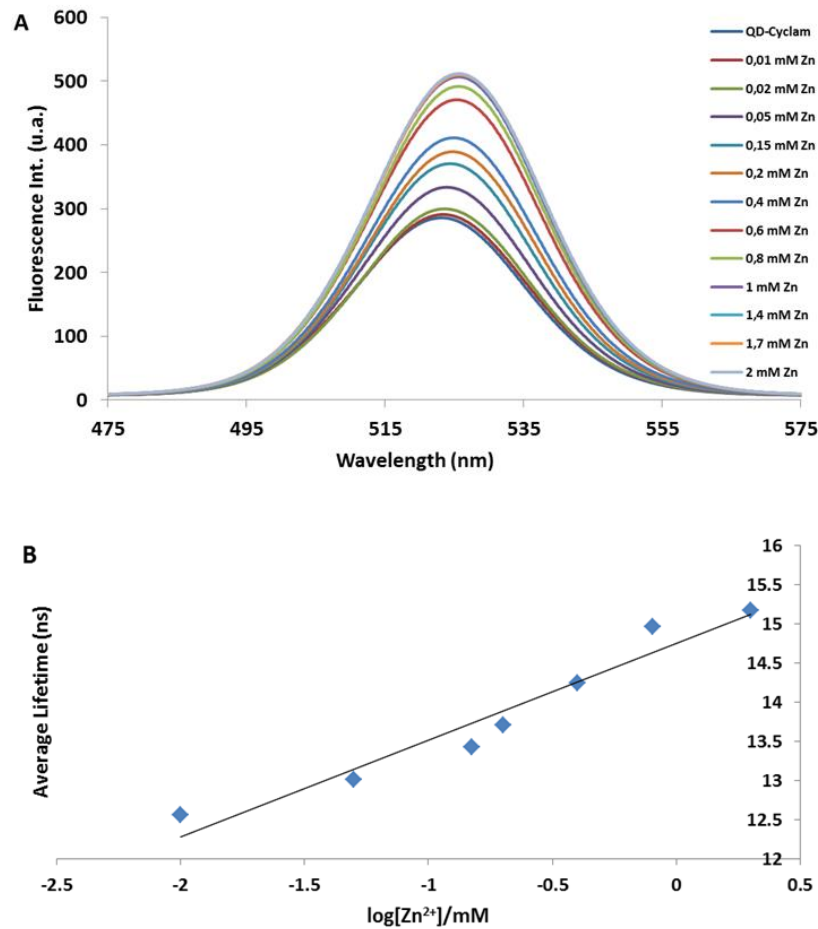
Figure 3.3.6. A) PL emission spectra of $QD_{520}$-cyclam nanosensor at different concentrations of $Zn^{2+}$. B) Calibration of the $QD_{520}$-cyclam nanosensor: PL average lifetime against the logarithm of the $Zn^{2+}$ concentration. (The PL average lifetime was calculated from decays collected at $\lambda_{em}$ = 522 nm).

In the case of QD-cyclam nanosensors, increasing the concentration of $Zn^{2+}$ resulted in an increase in the PL lifetime until reaching the concentration of 1 mM $Zn^{2+}$. From this concentration no further increase in the lifetime is produced, as is the case with PL intensity (Figure 3.3.6A). Figure 3.3.6B shows that there is a linearity between the average lifetime of the QD-cyclam and the logarithm of the concentration of $Zn^{2+}$ in the interval between 0.01 mM and 1 mM of $Zn^{2+}$.
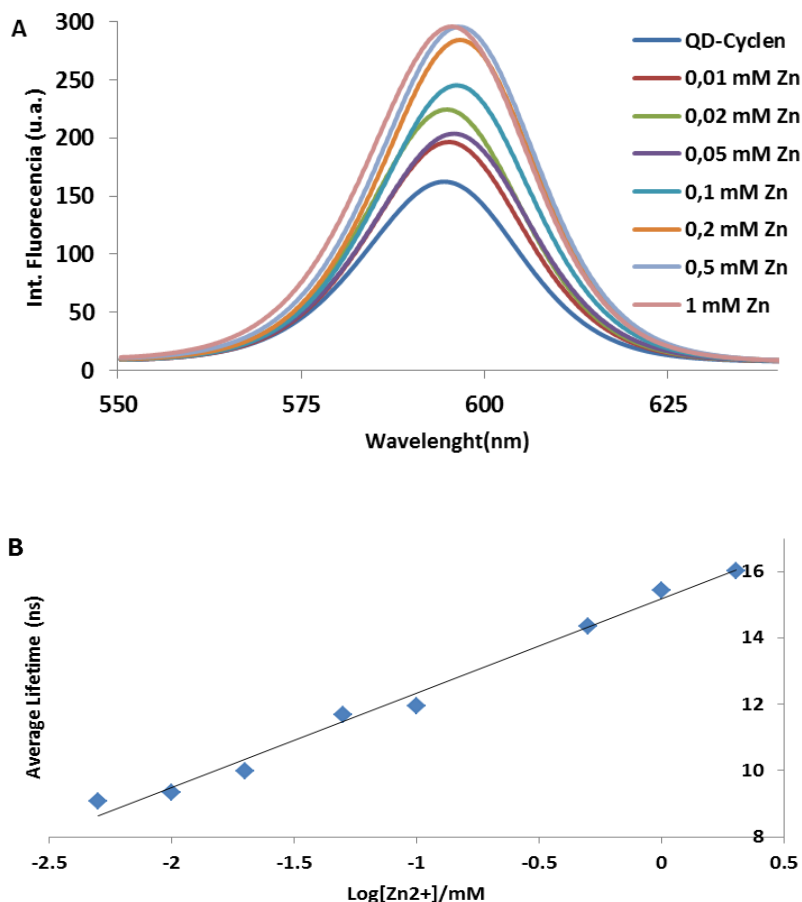
Figure 3.3.7. A) PL emission spectra of $QD_{600}$-cyclen nanosensor at different concentrations of $Zn^{2+}$. B) Calibration of the $QD_{600}$-cyclam nanosensor: PL average lifetime against the logarithm of the $Zn^{2+}$ concentration. (The PL average lifetime was calculated from decays collected at $\lambda_{em}$ = 598 nm).

Something similar can be observed for the QD-cyclen nanosensor (Figure 3.3.7). In this case, an increase in the average lifetime is detected by adding a somewhat lower $Zn^{2+}$ concentration, and no response is observed for concentrations above 1 mM. Specifically, this nanosensor shows a linear response in the range between 1 μM and 1 mM of $Zn^{2+}$, which indicates that it is more sensitive that the QD-cyclam nanosensor, and therefore, would allow its application to real samples with lower $Zn^{2+}$ concentrations.

### 3.3.3 INTERFERENCES STUDY

A study of the selectivity in the response of the nanosensors towards $Zn^{2+}$ ions has been carried out. For this, the effect of the presence of other substances has been explored first, placing special emphasis on other metal ions and molecules that can be

found in the matrix of biological and physiological samples to which the sensor could be applied.

First, the emission spectra and the PL decays of both nanosensors, QD-cyclam and QD-cyclen, were collected with increasing amounts of the interfering species until the analytical signal (PL intensity or average lifetime) would undergo a variation of more than 5% with respect to the signal in the absence of the potential interference. The maximum tolerated concentrations of each one of the tested interferences for each sensor, QD-cyclam and QD-cyclen, are listed in tables 3.3.1 and 3.3.2.

Table 3.3.1. Maximum concentration of potential interfering species tolerated by the $QD_{520}$-cyclam nanosensor.

| Potential interfering Ion/Molecule | Maximum tolerated concentration |
|---|---|
| Sodium (I) | 100 mM |
| Potassium (I) | 100 mM |
| Calcium (II) | 0.5 mM |
| Magnesium (II) | 0.1 mM |
| Manganese (II) | 0.5 mM |
| Nickel (II) | 0.5 mM |
| Cobalt (II) | 0.01 mM |
| Iron (II) | 0.001 mM |
| Iron (III) | 0.0002 mM |
| Copper (II) | 0.0001 mM |
| Ficoll | 0.05 % |
| BSA | 0.05 mg/mL |

Table 3.3.2. Maximum concentration of potential interfering species tolerated by the $QD_{520}$-cyclen nanosensor.

| Potential interfering Ion/Molecule | Maximum tolerated concentration |
|---|---|
| Sodium (I) | 100 mM |
| Potassium (I) | 100 mM |
| Calcium (I) | 5 mM |
| Magnesium (II) | 1 mM |
| Manganese (II) | 0.5 mM |
| Nickel (II) | 0.5 mM |
| Cobalt (II) | 0.01 mM |
| Iron (II) | 0.001 mM |
| Iron (III) | 0.005 mM |
| Copper (II) | 0.0001 mM |
| Ficoll | 0.5 % |
| BSA | 0.5 mg/mL |

In addition, Figures 3.3.8 show the relative variation in the PL lifetime obtained after the addition of these quantities of interfering agents. As seen in these figures, both nanosensors show good selectivity in the presence of most of the ions and molecules commonly found in the cell cytoplasm and other physiological samples. The most abundant ions in living cells, such as $Na^+$, $K^+$, $Ca^{2+}$ and $Mg^{2+}$, do not cause changes in the average lifetime of the nanosensors, even at higher concentrations than they are usually found in the cellular cytoplasm.
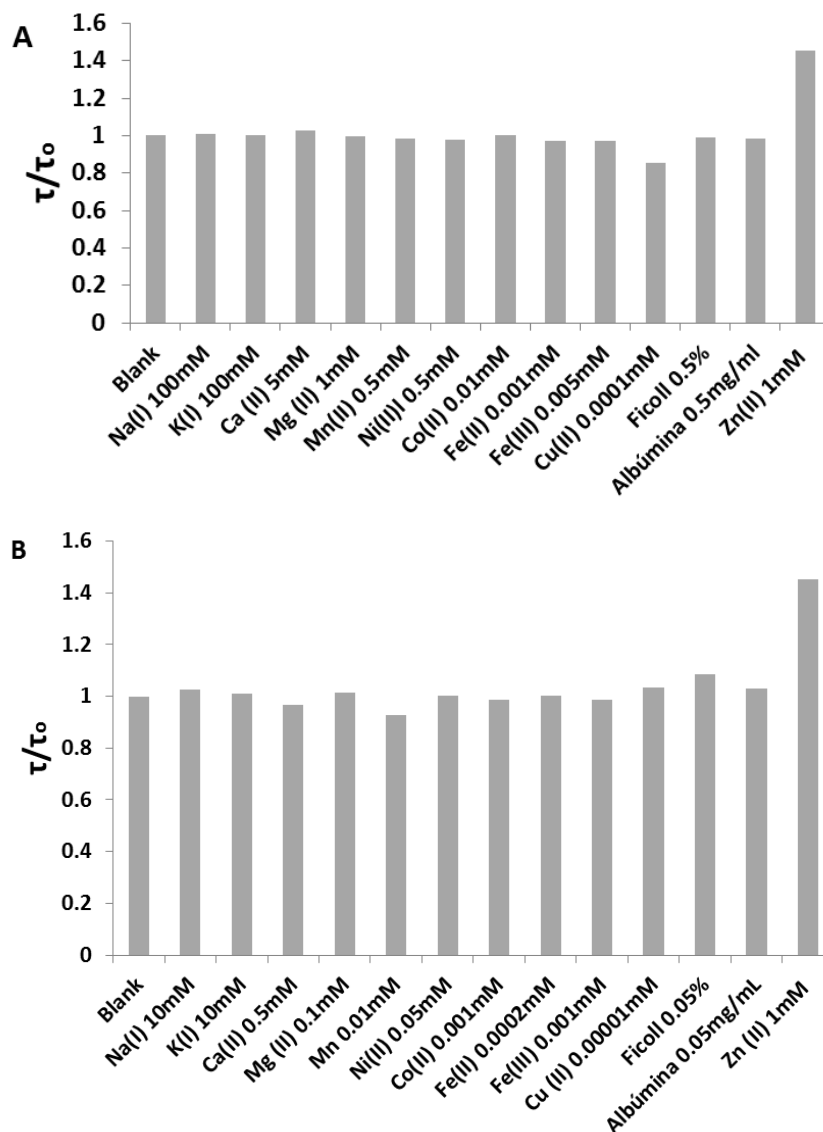


Figure 3.3.8. Relative variations in the average PL lifetime of the $QD_{520}$-cyclam (A) and $QD_{520}$-cyclen (B) in the presence of different interefering species. $\tau_0$ is the PL average lifetime of the QD-azacycle in the absence of $Zn^{2+}$ ions.

As it can be seen in Figure 3.3.8, only metals such as $Fe^{2+}$ and $Fe^{3+}$ produce a remarkable quenching of the fluorescence of the QD sensors due to an internal filter

effect[42]. As it is also known, the adsorption of $Cu^{2+}$ on the surface of the nanoparticles also causes a quenching of its PL[42]. $Ni^{2+}$ and $Mn^{2+}$ could also be coordinated inside the azacycle, which produces a slight modification of the luminescence signal. However, fortunately, the concentration of these ions in cellular media is so low that they would not cause possible interference during the applications.

Next, a competition study between $Zn^{2+}$ ions and any of these interfering species was performed. For this, the previous experiments were repeated with one of the designed sensors, in particular with the $QD_{520}$-cyclam nanosensor, but this time in the presence also of 1 mM of $Zn^{2+}$, and the obtained signal was compared, in both the PL intensity and the average lifetime, with that of a solution containing only the corresponding nanosensor and 1 mM $Zn^{2+}$ in the absence of interference. These results are summarized in Figure 3.3.9.
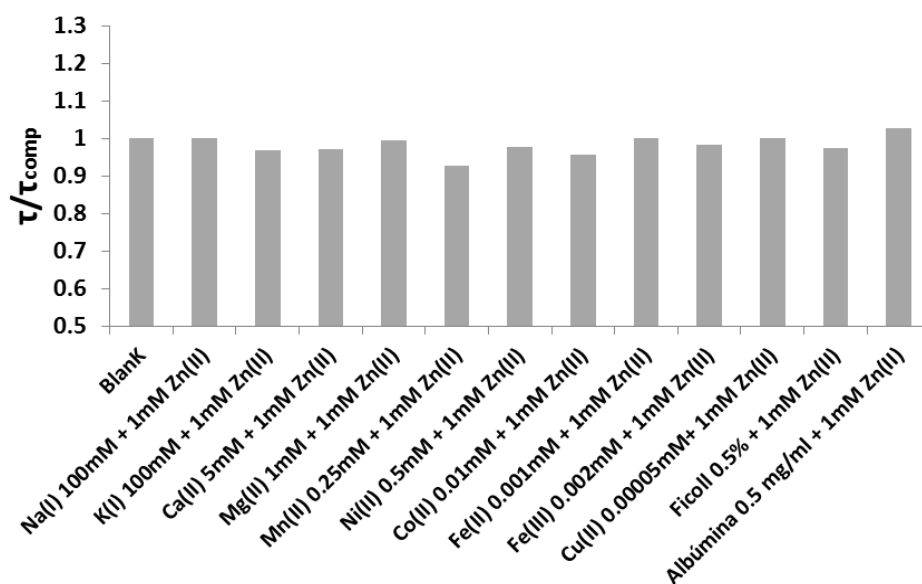


Figure 3.3.9. Relative variation of the average PL lifetime of the $QD_{520}$-cyclam in the presence of the maximum concentration tolerated in the different interfering species and 1 mM of $Zn^{2+}$. $\tau_{comp}$ represents the average PL lifetime of the $QD_{520}$-cyclam nanosensor in the presence of 1 mM of $Zn^{2+}$.

As seen in the previous figure, there is no marked variation between the sensor average lifetime with $Zn^{2+}$ in either the presence or the absence of the interfering ion or molecule. Hence, it can be drawn that the presence of these potential interfering species does not actively compete with $Zn^{2+}$ in terms of their interaction with the sensor. Thus, it can be concluded that the sensor will work selectively for $Zn^{2+}$ in the presence of the ions and molecules studied, which represent the most frequent potential interfering species that could be found in the cytoplasm or in any other physiological sample.

Other factor that was considered in this interferences study was the effect of the pH of the medium on the nanosensor response. For this, several solutions were prepared using 10 mM Tris buffer to adjust the pH to different values: 5.47, 6.49 and 7.2. Then, the PL decays of $QD_{600}$-cyclen were measured in each of these buffer solutions of different pH, in the absence and in the presence of 1 mM $Zn^{2+}$ (Figure 3.3.10)
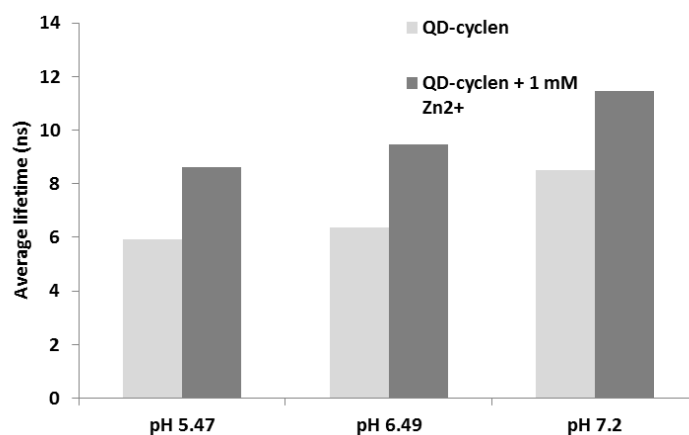


Figure 3.3.10. PL average lifetime of $QD_{600}$-cyclen nanosensor in the absence and in the presence of 1 mM of $Zn^{2+}$ at different pH values.

Figure 3.3.10 shows the variation of the average lifetime of the QD-cyclen sensor at different pH values, which have been chosen to be close to the physiological pH or to be close to the pH of some cellular organelles, such as endosomes or lysosomes. As it can be observed, the average lifetime of the nanosensor depends on the pH of the medium, exhibiting an increase at higher pH values. This is due to the protonation and deprotonation of the remaining carboxylic acid groups from the MPA residues at different pH[147]. However, it is also observed that the increase of the lifetime in the presence of $Zn^{2+}$ does not depend greatly on the pH, since this increase in the PL emission is a consequence of the response of the sensor is similar in all the pH values tested.

These results indicate that the proposed nanosensors could be applied without major drawbacks when the pH of the samples to which they are applied to is known or can be controlled. In the case of cellular interior application, the QD-azacycle nanosensors could be applied satisfactorily to monitor changes in $Zn^{2+}$ concentration if there are no simultaneous variations in pH.

### 3.3.4 APPLICATIONS INSIDE LIVING CELLS

The next step in the study of these sensors was the demonstration of their usefulness as intracellular nanosensor. It is very important to note that these nanosensors respond to $Zn^{2+}$ ions through both PL emission intensity and PL lifetime. The latter is very significant, as it allows that these sensors can be applied inside the cell using FLIM microscopy technique, gaining all the advantages of the long PL lifetimes of the QDs. The FLIM technique has been described earlier, in section 3.1.4.

Initially, to demonstrate that the response of the QDs sensor to changes in the $Zn^{2+}$ concentration could also be observed in FLIM microscopy, FLIM images were collected from the $QD_{600}$-cyclen nanosensors deposited on glass slides and suspended in Tris buffer solutions 10 mM at pH 7.2, in the absence of $Zn^{2+}$ and in the presence of 0.1 mM $Zn^{2+}$ and 1 mM $Zn^{2+}$ (Figure 3.3.11).
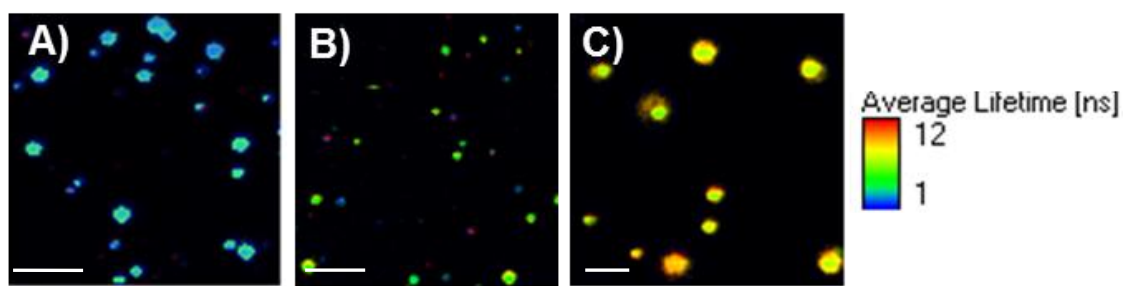


Figure 3.3.11. FLIM images of $QD_{600}$-cyclen conjugates suspended in 10 mM Tris buffer pH 7.2 deposited on glass slides in the presence of different concentration of $Zn^{2+}$: (A) 0 mM $Zn^{2+}$; (B) 0.1 mM $Zn^{2+}$; and (C) 1 mM $Zn^{2+}$. Scale bars represent 5 μm.

As explained in the Material and Methods chapter (chapter 3.2), each pixel of the image also has information about the PL decay time, so after analyzing the images as explained in section 3.1, the PL lifetime distributions that are shown in Figure 3.3.12 were obtained.
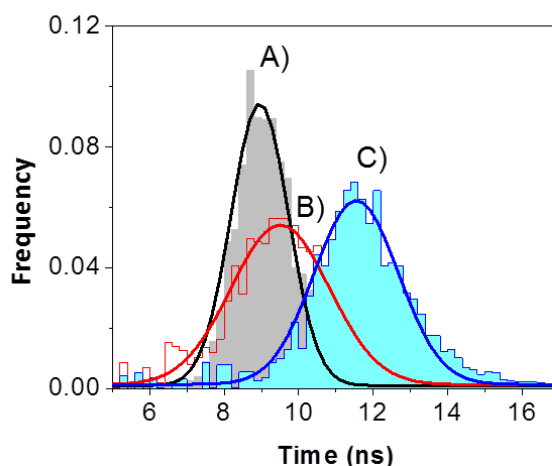
Figure 3.3.12. Distribution of the average PL lifetimes of the $QD_{600}$-cyclen nanosensors suspended in aqueous solutions, obtained from the FLIM images of Figure 3.3.11. A) 0 mM $Zn^{2+}$, B) 0.1 mM $Zn^{2+}$ and C) 1 mM $Zn^{2+}$.

Clear changes in the PL lifetime distributions can be observed in the absence and presence of $Zn^{2+}$ ions. As expected, the lifetime of the QDs increases with the concentration of $Zn^{2+}$ in the medium, as previously observed in the measurements in aqueous solution. In the absence of $Zn^{2+}$ the analysis of the FLIM images provided a distribution of the lifetime centered around 9 ns. However, the distribution that was obtained when analyzing the FLIM images of the sensor in presence of 1 mM $Zn^{2+}$ was centered at approximately 11.7 ns, whereas the distribution obtained in presence of 0.1 mM $Zn^{2+}$ was centered at 9.8 ns (Figure 3.3.12). These results showed that the response of the proposed nanosensor could be satisfactorily observed also by FLIM imaging.

Finally, the QD-cyclen nanosensor was applied to the detection of changes in $Zn^{2+}$ levels inside living cells. For this, HepG2 cells were used, cultured on microscope slides. The cells were subsequently incubated with the $QD_{600}$-cyclen nanosensor. In these experiments FLIM images were first collected from cells without incubating with nanoparticles, to observe cellular autofluorescence, and then cells incubated with the nanosensors in Tris buffer 10 mM at pH 7.2. Finally, to ensure that the concentration of $Zn^{2+}$ inside the cells was greater, a solution of 1 mM $Zn^{2+}$ was added to the cells in the extracellular medium, and a reasonable time was left for the $Zn^{2+}$ to spread to the cellular interior.
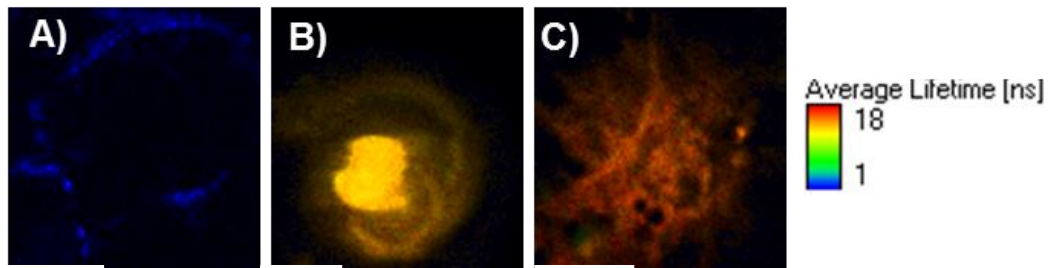
Figure 3.3.13. FLIM images of HepG2 cells: (A) cellular autofluorescence; (B) cells with $QD_{600}$-cyclen conjugates; and (C) cells with $QD_{600}$-cyclen conjugates incubated with 1 mM $Zn^{2+}$. Scale bars represent 5 μm.

Figure 3.3.13 shows an example of the FLIM images collected in these experiments. As observed in the arbitrary color scale, the lifetime of the nanosensor in the cell cytoplasm increases when there is $Zn^{2+}$. In addition, after analyzing the decays collected in these images, as in the previous experiment, the distributions of the average lifetimes obtained were graphically represented (Figure 3.3.14). These results indicate that after the incorporation of $Zn^{2+}$ in the extracellular medium there was diffusion to the interior through the membrane, and therefore there was an increase in the concentration of this ion inside cell, causing a subsequent increase in the PL lifetime of the nanosensor (Figure 3.3.14). Therefore, an excellent response of the proposed nanosensors is observed, which indicates that these sensors are valid for measuring $Zn^{2+}$ ion concentration inside living cells.
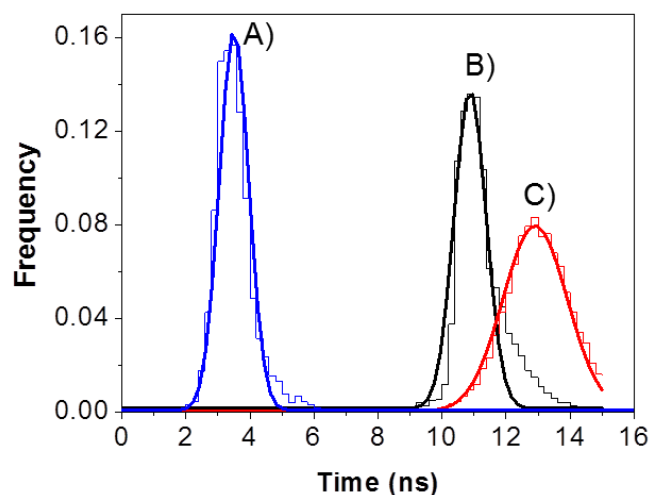


Figure 3.3.14. PL lifetime distributions obtained from the FLIM images in Figure 3.3.13. (A) cellular autofluorescence; (B) cells with $QD_{600}$-cyclen conjugates; and (C) cells with $QD_{600}$-cyclen conjugates incubated with 1 mM $Zn^{2+}$.

Moreover, one of the main advantages of the proposed QD-based nanosensors for their use as intracellular nanosensors is the long PL lifetimes found for the QD nanosensors. As it can be seen in Figure 3.3.14, the QD nanoparticles display PL lifetime extremely higher (B and C) than the lifetime of the cellular autofluorescence (A). The long PL lifetime of the QDs allows a more sensitive intracellular determination, in addition to facilitating the discrimination between the autofluorescence signal of the cell and the signal coming from the QD. Therefore, the use of FLIM technology in combination of the proposed QD based nanosensors achieves the direct elimination of this important interference found in many other imaging techniques.

# 3.4 SENSING OF EXTRA-CELLULAR AND INTRAMITOCHONDRIAL pH OF BREAST CANCER CELLS USING QD-BASED NANOSENSORS

As it was explained in the introduction of this chapter, an important objective of this Thesis is taking benefit from the advantages of QD-based nanosensors for *in vitro* and *in vivo* bioimaging to report on the pH values of the extracellular environment and the intramitochondrial pH, as potential biomarkers of different metabophenotypes in breast cancer cell lines. The main goal behind this study is the correlation of the results obtained herein with the different metabolic profiles of breast cancer cells, which will be discussed in chapter 4.

Cancer cells have an adaptation of their metabolism, known as the Warburg effect, widely described in chapter 4.1. In proliferating or cancerous cells, most of the pyruvate resulting from glycolysis is derived to lactate. This lactate is sent to the cellular exterior by the monocarboxylate transporters, thus altering the pH of the culture medium where the cells grow. Depending on the degree of glycolysis in each cell line, more or less lactate is produced, so it should be possible to differentiate the cell lines according to the amount of lactate excreted and, therefore, the pH value.

With this background, the model of breast cancer was chosen in this Thesis. The breast cancer model presents a series of features that make it ideal to work with in this study. First, this model is very well known and studied. Second, it is clinically classified into five subtypes depending on its location and immunological profile. This feature is the most important, because it permits to search metabolic differences between the breast cancer subtypes using, for instance, our QD-based nanosensors combined with advanced fluorescence instrumentation (more details in chapter 3.2.9 and chapter 3.2.10). Hence, we chose five different breast cancer cell lines, according to the current clinical classification[148]: MCF7, SKBR3, ZR751, MDA-MB-231 and MDA-MB-468 (see chapter 4.2.2 for further details).

## 3.4.1 pH SENSING OF THE EXTRACELLULAR MEDIA OF BREAST CANCER CELL LINES

### 3.4.1.1 RESPONSE OF THE QD-BASED pH NANOSENSOR

As previously mentioned, for the development of QD-based nanosensors, the QD surface is usually modified with different molecules in order to incorporate specific groups which will react selectively with the analyte of interest. In particular, pH nanosensors can be obtained with QDs in which thioalkyls have been immobilized on

their surface. Examples of reactive thioalkyls found in the literature to prepare pH nanosensors are mercaptoacetic acid, mercaptopropionic acid, and mercaptosuccinic acid[149-151]. In these functionalized QDs, the PL intensity was sensitive to the degree of protonation of the carboxylic acid,[152] and thus it was used as analytical signal. However, the use of the PL intensity presents drawbacks when these nanosensors are to be used intracellularly, particularly due to fluctuations in the concentration of the nanosensors in some parts of the cell, and due to the intrinsic background autofluorescence of the cells.

In order to overcome these limitations, a pH nanosensor was proposed for the first time by Drs Ruedas-Rama and Orte[83] based on the use of the PL emission lifetime of QD-MPA nanoparticles. This technique has the advantage that the PL emission lifetime of QD is independent of the excitation power, the total concentration of the QD, and also is notably higher than the lifetime of the cellular autofluorescence.

Based in this work, we have used the previously optimized QD-MPA pH nanosensors for the study of the pH of the extracellular media of breast cancer cells. The pH nanosensor was synthetized as explained in chapter 3.2.6.1, and its pH response was tested by measuring the PL decay traces of the QD-MPA in buffered solutions at different pH values. Figure 3.4.1 shows the effect of the pH in the PL average lifetime of $QD_{520}$-MPA.
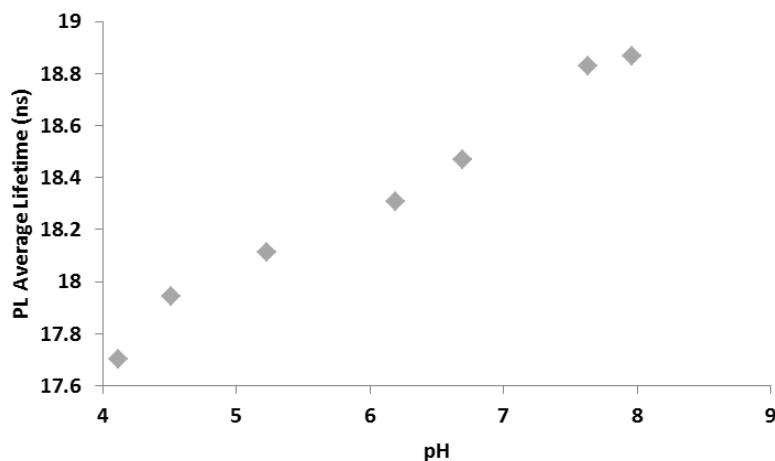


Figure 3.4.1. Response of the $QD_{520}$-MPA nanosensor towards the pH value of buffered solutions.

Once the pH sensitivity of the nanosensors was demonstrated, the next step was the use of these QD-MPA for the determination of the pH in the extracellular media of the different breast cancer cell lines under study in this Thesis.

### 3.4.1.2 CALIBRATION OF THE pH NANOSENSOR USING CELL CULTURE MEDIA

In this chapter, we will apply the $QD_{520}$-MPA pH nanosensor described earlier to extracellular media. However, it is very important to note that cell lines use different culture media for their growth. Due to their different composition, culture media may exhibit an effect on the PL lifetime values of the sensors. Therefore, in order to account for matrix effects, a calibration of the response of the QD nanosensor with each cell media was performed. The culture media employed in each cell line are the following:

- MEM: MCF7
- McCoy: SKBR3
- RPMI: ZR751
- DMEM: MDA-MB-231 and MDA-MB-468

Figure 3.4.2 shows examples of the PL decay traces of the QD nanosensor in the distinct culture media at different pH values. After the analysis and fitting of the PL decays to multi-exponential decay functions, the PL average lifetime was extracted and then the calibration plots were obtained.

As it can be seen in Figure 3.4.2, the PL lifetime of the QD nanosensor increased when the pH value increased. Moreover, there was a good response of the nanosensor to changes in the pH values of the different culture media, presenting in all cases an adequate linearity. The equations obtained after the fitting of the data by linear regression are gathered in table 3.4.1.
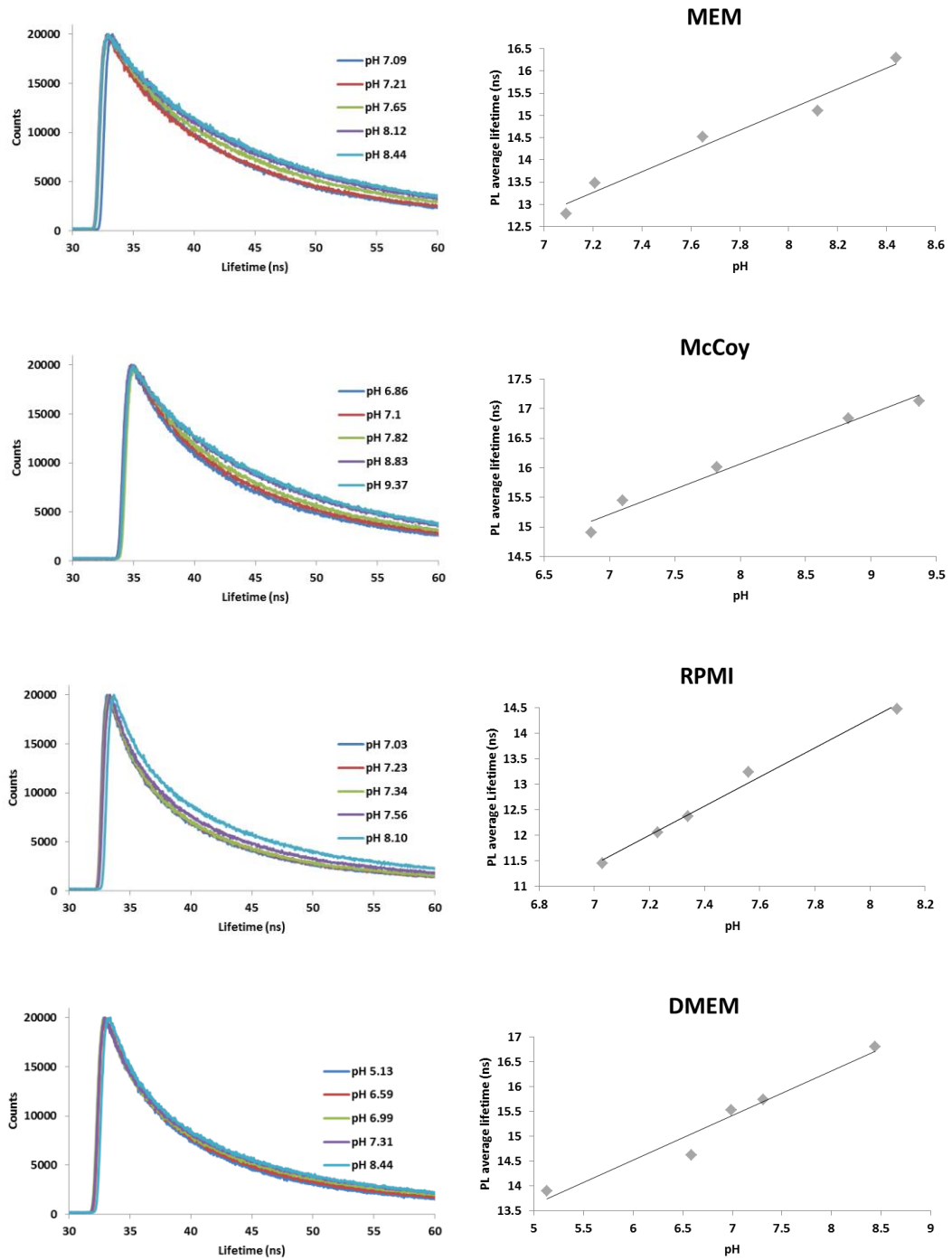
Figure 3.4.2. PL decay traces (left) of the QD$_{520}$-MPA pH-nanosensor and the corresponding response calibration (right) in each cell culture medium.

Table 3.4.1. Fitting equations obtained from linear regression of the pH calibrations of the $QD_{520}$-MPA nanosensor in the different cellular media.

| Cellular medium | Equation |
|---|---|
| MEM | $\tau_{ave}$ /ns = 2.3249 * pH - 3.4703 |
| McCoy | $\tau_{ave}$ /ns = 2.8503 * pH - 8.9580 |
| DMEM | $\tau_{ave}$ /ns = 0.9293 * pH + 8.5257 |
| RPMI | $\tau_{ave}$ /ns = 0.8473 * pH + 9.2903 |

### 3.4.1.3 EXTRACELLULAR pH MEASUREMENTS OF DIFFERENT CELL LINES

To perform the experiments on the extracellular pH of breast cancer cell models, the cell lines were cultivated in the corresponding media, which was collected after 2 days of cell growth (widely explained in chapter 3.2.7). Then, the $QD_{520}$-MPA pH-nanosensor was resuspended in the collected media and PL decay traces were measured as described in chapter 3.2.9. The PL decay traces at three different emission wavelengths were globally fitted to a sum of 3 exponential functions, and the PL average lifetime was calculated as indicated in section 3.2.9. The average values of each PL lifetime component from four different repetitions and the global average PL lifetime are shown in table 3.4.2.

Table 3.4.2. PL lifetime components and average lifetimes obtained in the measurement of the extracellular pH of each cell line. The associated error is the standard deviation of four different replicas.

| | $\tau_1$ (ns) | $\tau_2$ (ns) | $\tau_3$ (ns) | $\tau_{average}$ (ns) |
|---|---|---|---|---|
| MCF7 | 18.13 ± 0.31 | 6.15 ± 0.32 | 0.73 ± 0.48 | **15.53 ± 0.21** |
| ZR751 | 17.85 ± 0.15 | 4.95 ± 0.05 | 0.32 ± 0.03 | **14.21 ± 0.05** |
| MDA-MB-231 | 19.54 ± 0.32 | 5.87 ± 0.30 | 1.98 ± 0.15 | **13.68 ± 0.16** |
| MDA-MB-468 | 17.92 ± 0.16 | 5.18 ± 0.31 | 0.95 ± 0.25 | **13.85 ± 0.13** |
| SKBR3 | 19.36 ± 0.13 | 6.42 ± 0.25 | 1.48 ± 0.12 | **15.39 ± 0.07** |

The obtained average PL lifetimes were interpolated in the corresponding calibration plot, taking into account the different matrix. The estimated pH values of the extracellular medium of each cell line are represented in Figure 3.4.3. This Figure shows that it is possible to classify the five cell lines into two clearly differentiated

groups: a first group that includes the lines MCF7, ZR751 and SKBR3; and a second group containing the lines MDA-MB-231 and MDA-MB-468. The first group presents the most basic pH in the extracellular medium, between 7-8, what suggests less excretion of lactate. The second group has a pH around 5.2, which means higher output of monocarboxylate to the cell exterior.

These promising results, exhibiting differences in the cellular metabolism, support the need to carry out an in-depth study of the metabolism of each cell line using different inhibitors of the tricarboxylic acids (TCA). The experiments carried out in this context are shown in chapter 4, and the joint discussion of the results is gathered in chapter 5.
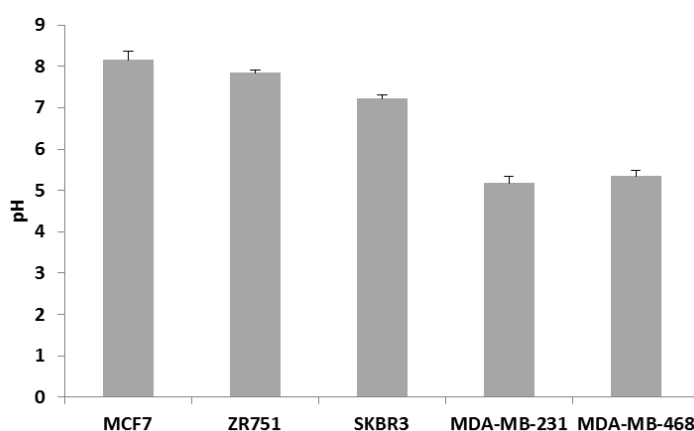


Figure 3.4.3. Extracellular pH of each breast cancer cell line as obtained by PL lifetime measurements of the $QD_{520}$-MPA nanosensor. Error bars represent standard deviation from 4 different samples.

### 3.4.2 INTRAMITOCHONDRIAL pH SENSING IN DIFFERENT BREAST CANCER CELL LINES

Another important factor characterizing the metabolic behaviour of cancer cells lies in the actual metabolic reactions taking place inside mitochondria. Hence, the next step in this Thesis was to develop intramitochondrial pH nanosensors and to test the behaviour of the different breast cancer cell lines studied. This is due to the fact that the different cell lines may show distinct pH values depending on the mitochondrial metabolism they possess, what may lead to differences in the subtypes of breast cancer.

The design of the nanosensor involved a double modification of the QD-surface. On the one hand, the nanoparticle included MPA as pH-sensitive group. On the other hand, an SS peptide was added to the surface for mitochondrial delivery. Further details on the preparation of the QD-SS-MPA nanoparticles are described in chapter 3.2.6.3. Three different conjugates were tested, depending on the SS-peptide employed: QD-SS20-MPA, QD-SS02-MPA, and QD-SS31-MPA. The initial tests with the

conjugated demonstrated that the only useful nanosensor was QD-SS20-MPA. The QD-SS02-MPA nanoparticles did not show an adequate response towards pH, whereas the QD-SS31-MPA had a good response to pH, but did not penetrate in the cells.

### 3.4.2.1 MITOCHONDRIAL DELIVERY AND LOCALIZATION OF THE NANOSENSORS

The first step of the study was to confirm that the nanosensor penetrated into the cell and was then located in the mitochondrial zone. To do this, the breast cancer cell lines were cultured on glass slides for two days and then the intramitochondrial pH nanosensor was added to the culture medium. The cell lines were incubated for 2 hours for the nanosensor to enter the cells. Then, the mitochondria staining dye, Mitotracker Deep Red, was also added to the medium. We used dual-colour FLIM-PIE to follow the location of the QD-SS-MPA nanosensor, and to verify the colocalization with mitochondria organelles.

Figures 3.4.4 – 3.4.7 show some examples of images of the QD-SS20-MPA nanosensor in different breast cancer cell lines stained with Mitotracker Deep Red, and the intensity plots corresponding to the line drawn in yellow in each image. The arrows in the intensity plots show the colocalization that the QDs have with respect to the Mitotracker. These experiments demonstrated that the QD-SS20-MPA nanosensors were successfully delivered to the mitochondria, and very good colocalization was obtained in the cell lines MCF7, MDA-MB-231, MDA-MB-468, and SKBR3. In the case of ZR751, the nanosensors did not enter in the interior of the cell. Hence, our results in the next section are limited to the four cell lines in which the nanoparticles were incorporated.
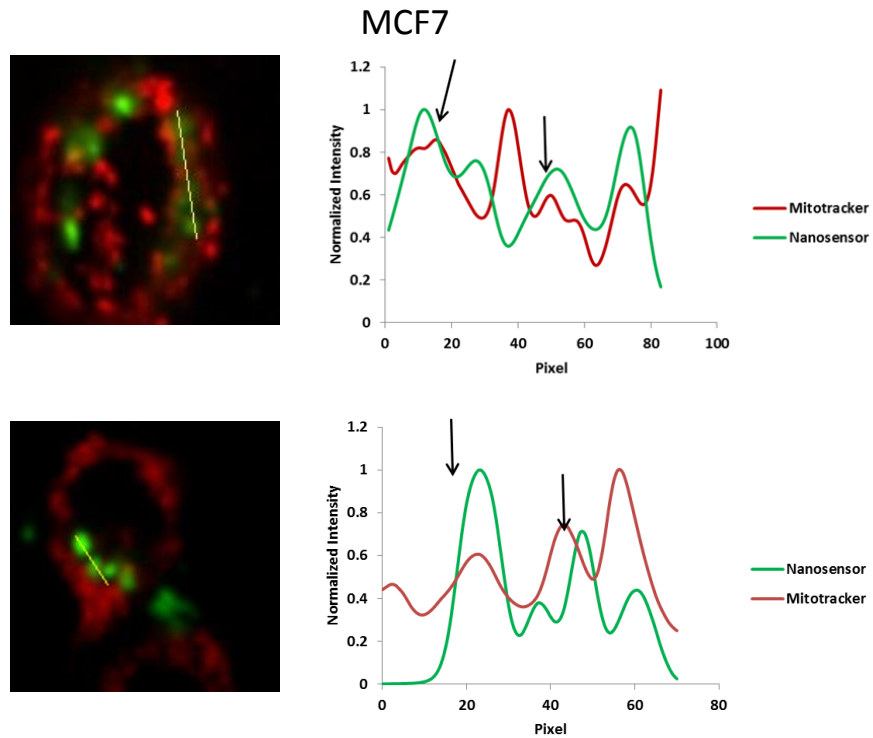
## MCF7

Figure 3.4.4. MCF7 colocalization images. The images show the QD-based nanosensor (in green) and the Mitrotracker (red), and the corresponding intensity plot from the yellow line.
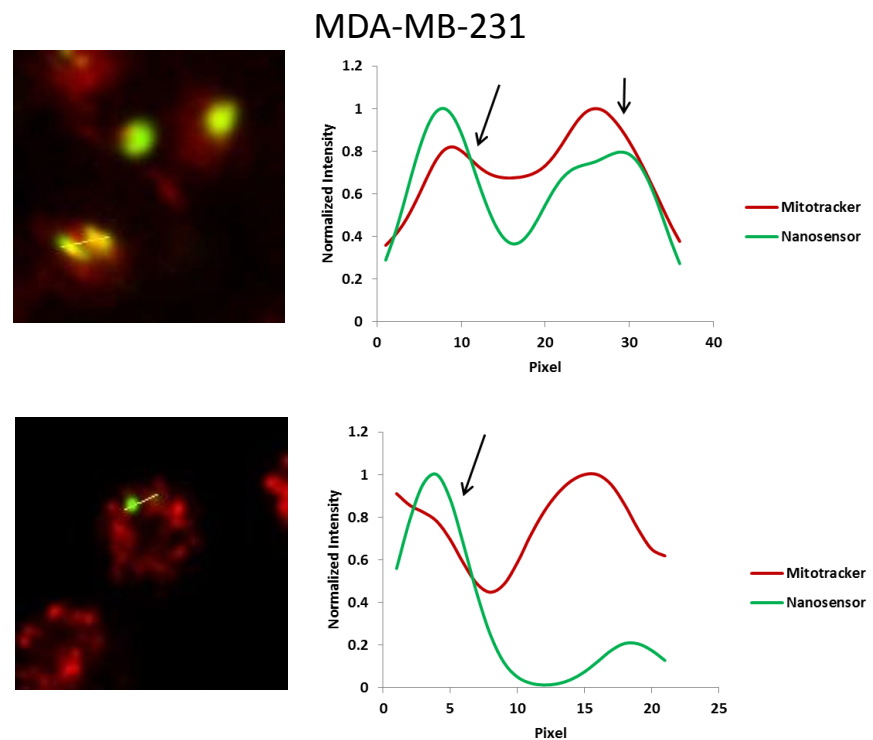


## MDA-MB-231

Figure 3.4.5 MDA-MB-231 colocalization images. The images show the QD-based nanosensor (in green) and the Mitrotracker (red), and the corresponding intensity plot from the yellow line.

84
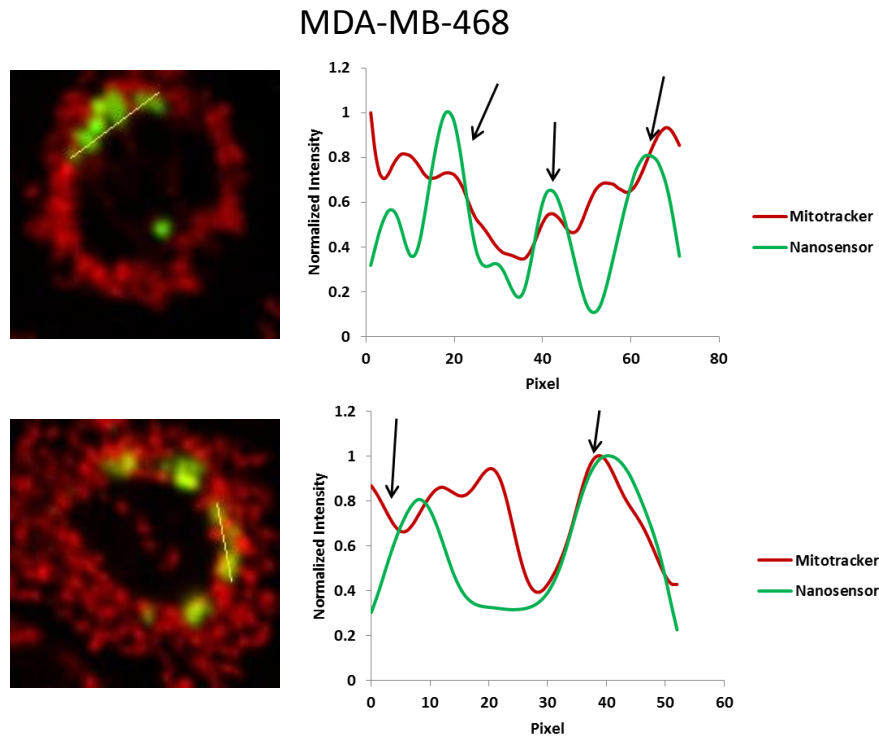
## MDA-MB-468



Figure 3.4.6. MDA-MB-468 colocalization images. The images show the QD-based nanosensor (in green) and the Mitrotracker (red), and the corresponding intensity plot from the yellow line.
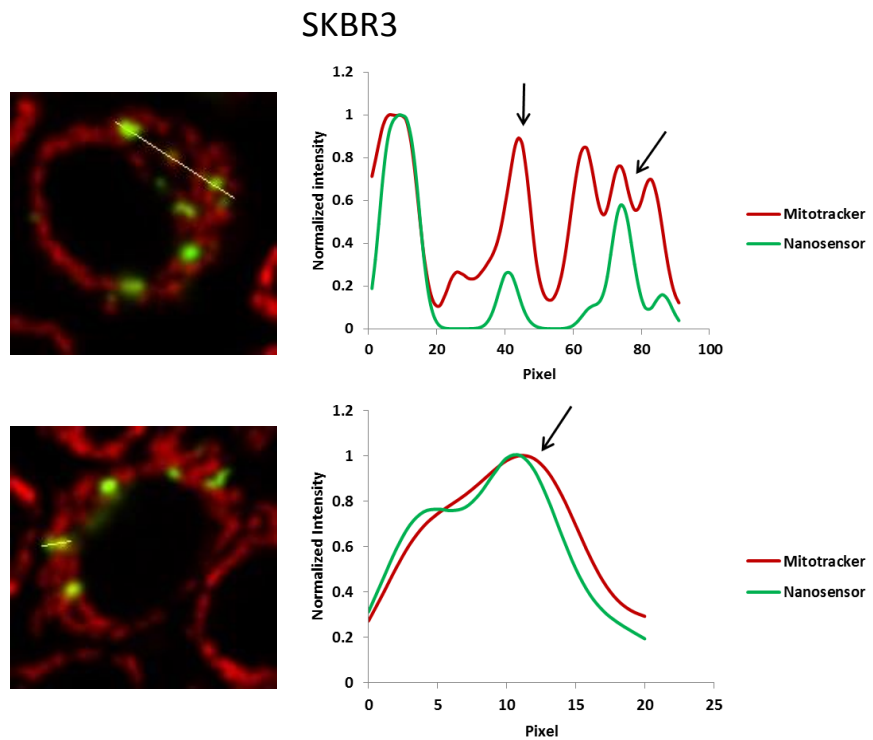
## SKBR3



Figure 3.4.7. SKBR3 colocalization images. The images show the QD-based nanosensor (in green) and the Mitrotracker (red), and the corresponding intensity plot from the yellow line.

### 3.4.2.2 INTRAMITOCHONDRIAL PH ESTIMATION THROUGH FLIM IMAGING

The next step of this chapter consisted in the study of the mitochondrial pH of the MCF7, MDA-MB-231, MDA-MB-468 and SKBR3 cell lines. ZR751 could not be studied because as mentioned in the previous section, since the nanosensors did not penetrate the cells due to its morphological features.

In order to unify the data obtained, it was necessary to calibrate the response of the QD-SS-MPA nanosensor. To do this, 1 mL of each solution with different pH value was placed on a slide and 3 µL of the nanosensor were added. FLIM images of the QD-SS-MPA nanosensors were obtained and the PL lifetime distributions were analysed for each pH value (Figure 3.4.8). With the average PL lifetime from 6 different images, a pH calibration was reconstructed (Figure 3.4.9). The calibration displayed a range of PL lifetimes between 4.6 and 7.8 ns (Figure 3.4.9), with the following calibration equation:

$$\tau \text{ (ns)} = 1.2143 \cdot \text{pH} - 2.9651 \tag{3.3}$$

We employed this equation to interpolate the average lifetime data obtained from the QD-SS-MPA nanosensors incorporated in mitochondria in each cell line, thus obtaining a quantitative estimation of the intra-mitochondrial pH value.
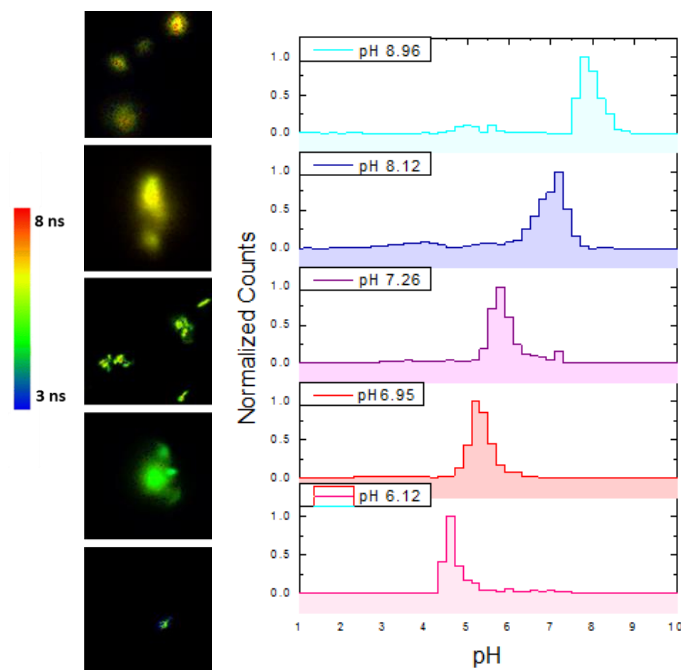


Figure 3.4.8. Representative FLIM images from QD-SS-MPA nanosensors on glass slides, suspended on PBS buffer at different pH values, and their corresponding PL lifetime normalized distributions.
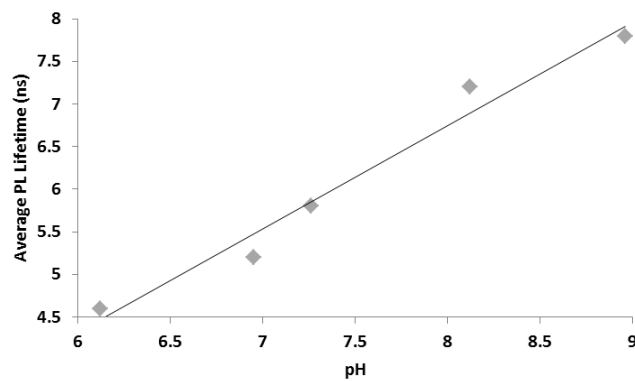
Figure 3.4.9. Calibration of the response of the QD-SS-MPA nanosensor at different pH values.

After performing the calibration, FLIM images from QD-SS-MPA nanosensors incorporated in breast cancer cell lines were collected. To this, the samples were prepared as explained in the previous section (3.4.2.1). At least, 20 different images from different preparations and different cultures were collected per each cell line. The FLIM images were analysed using the software SyphoTime 32 (see section 3.2.11.2 for more details). Importantly, the pixels of interest were selected as those in which colocalization of the QD-SS-MPA luminescence was coincident with Mitotracker fluorescence emission in the red channel (using a home-coded script in MathCad 15.0, as explained in the Methods section). Figures 3.4.10 – 3.4.13 show representative FLIM images of the QD-SS-MPA sensors in the different cell lines, but only showing those pixels selected. The PL lifetime distributions were obtained from these pixels.
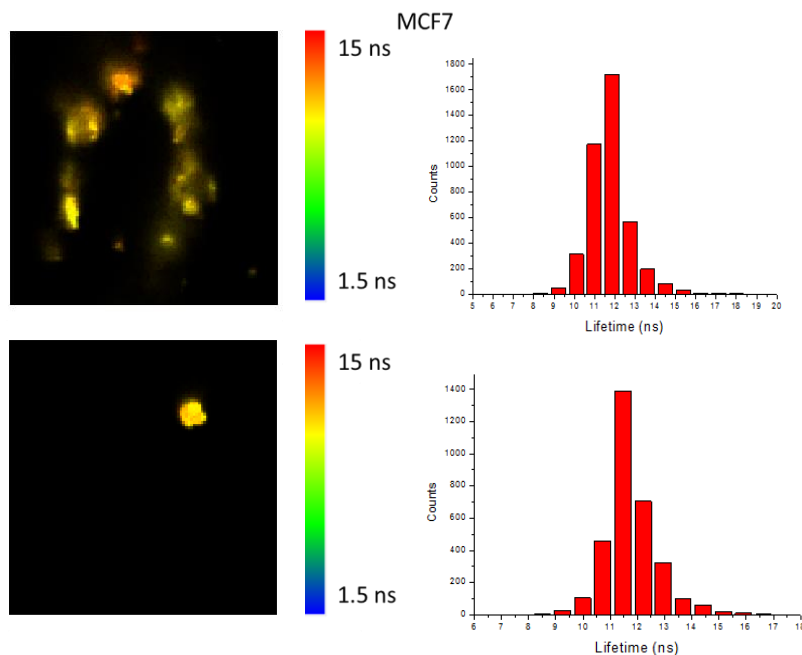


Figure 3.4.10. Representative FLIM images and the corresponding PL lifetime distributions of QD-SS-MPA nanosensors incorporated in mitochondria of MCF7 cells.
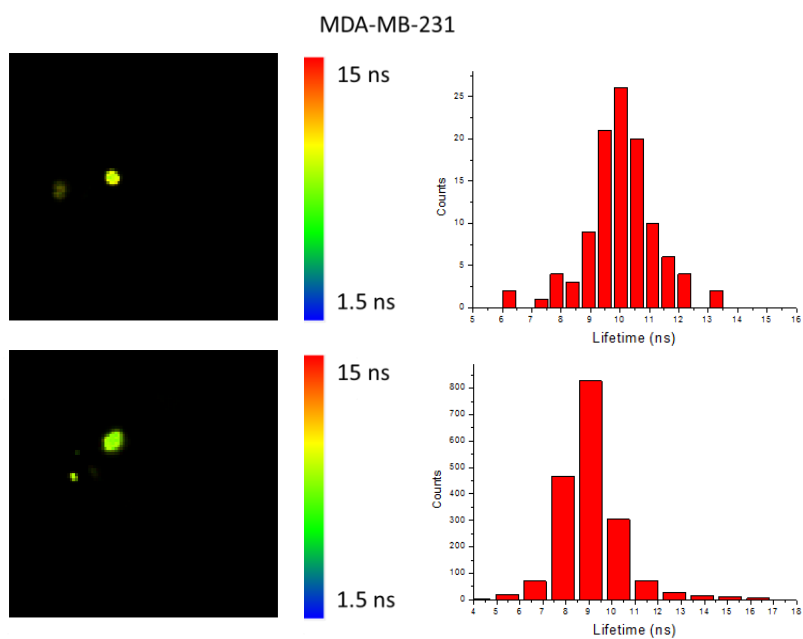
Figure 3.4.11. Representative FLIM images and the corresponding PL lifetime distributions of QD-SS-MPA nanosensors incorporated in mitochondria of MDA-MB-231 cells.
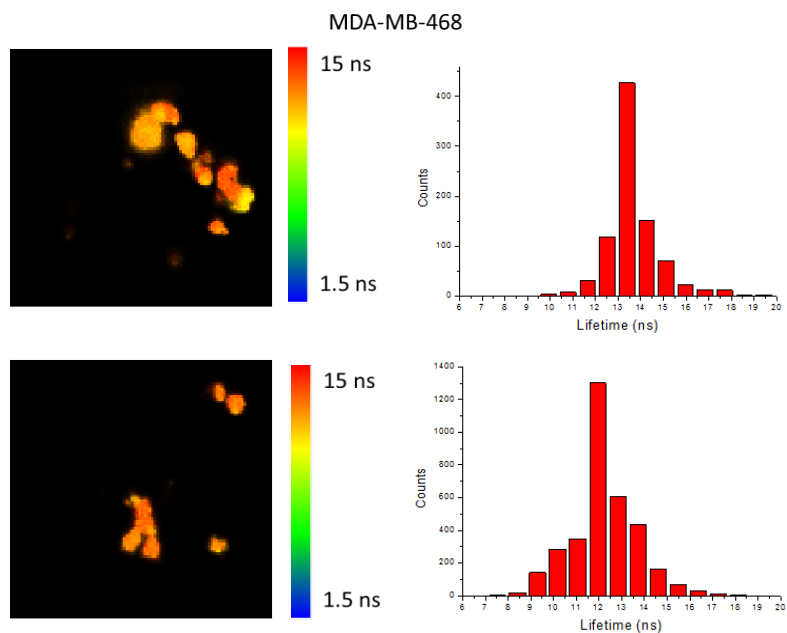


Figure 3.4.12. Representative FLIM images and the corresponding PL lifetime distributions of QD-SS-MPA nanosensors incorporated in mitochondria of MDA-MB-468 cells.
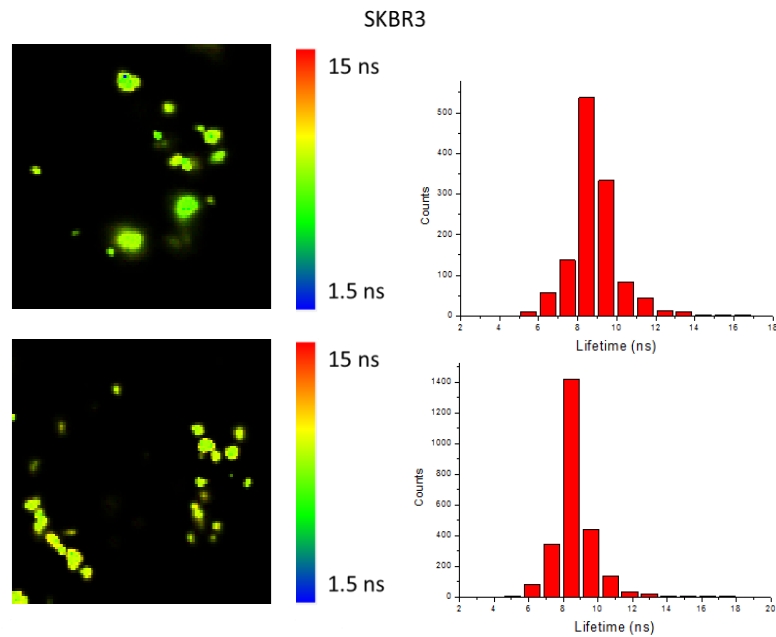
Figure 3.4.13. Representative FLIM images and the corresponding PL lifetime distributions of QD-SS-MPA nanosensors incorporated in mitochondria of SKBR3 cells.

After the analysis of each image, the average of all the lifetime distributions of all the repetitions in each cell line was obtained. These PL lifetime distributions were converted into pH distributions using the calibration equation 3.3 obtaining the estimated pH values in the mitochondrial area (Figure 3.4.14A and B).

We then performed statistical study to compare the pH obtained in cell line, and to check whether the differences between the obtain pH values were significant. To this purpose, the Bonferroni statistical test was performed, with a significance level of 0.01 (Figure 3.4.14C).
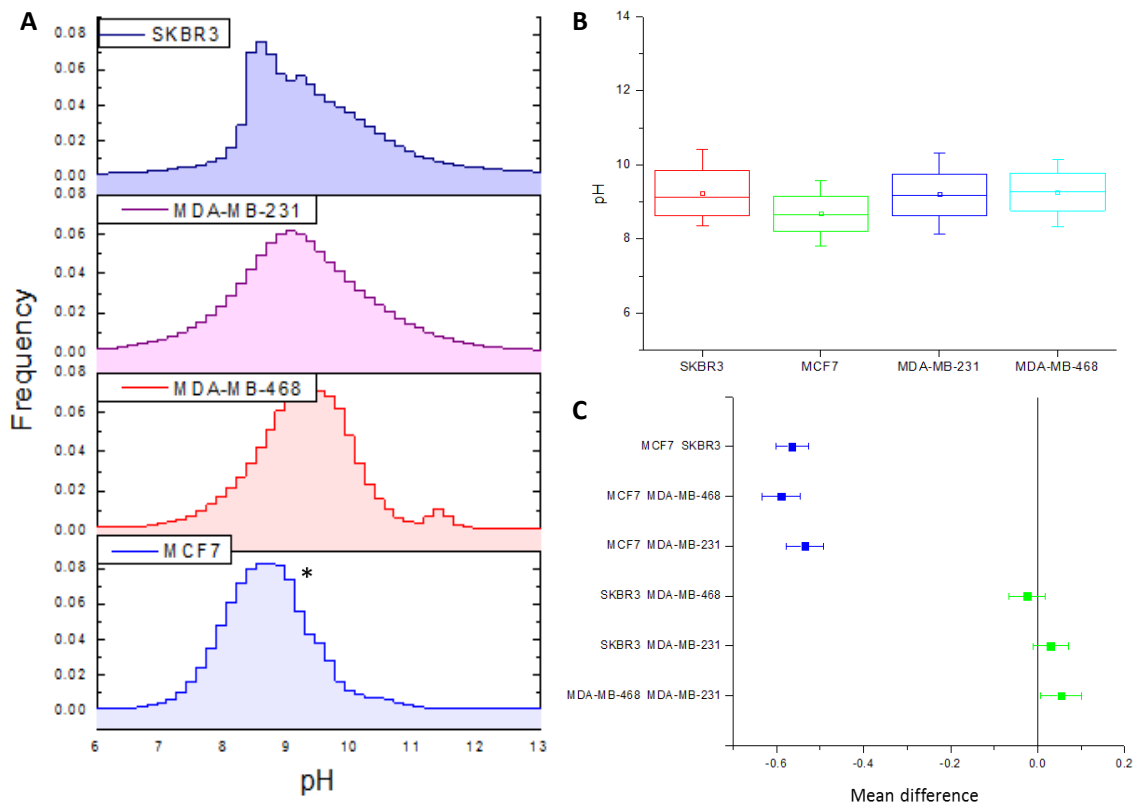
Figure 3.4.14. A) Overall intra-mitochondrial pH distributions for each cell line. The asterisk represents that the distribution is significantly different from the other three, at a significance level of 0.01. B) Box plot of the pH distributions, where the box includes 75% of the pixels, and the whiskers represents 90% of the pixels. C) Difference of the means of the pH distributions compared with the Bonferroni statistical test. Blue squares indicate significant differences whereas green squares represent non-significant differences, at the significance level of 0.01.

As it can be seen in Figure 3.4.14, the MCF7 cell line displayed a significantly lower pH value in the mitochondrial area than that exhibited by triple negative cell lines (MDA-MB-231 and MDA-MB-468). However, the SKBR3 cell line displayed an intermediate profile. Interestingly, SKBR3 cells exhibited a bi-modal distribution, with two differentiated populations. The first population displayed a lower pH value, similar to the MCF7 cell line, while the second population had a higher pH value, similar to the triple negative cell lines. When observing the cell lines compared in pairs, using the Bonferroni statistical test (Figure 3.4.14C), it was found that the pH values measured for the MCF7 cell line was significantly different from the pH values measured for the rest of the cell lines. In contrast, we did not find statistical differences between the pH populations from the cell lines MDA-MB- 231, MDA-MD-468 and SKBR3.

### 3.4.3 QDs CITOTOXICITY

The QDs used in this Thesis are formed by a core of CdS, with an external layer of ZnS. Therefore, as an important control, it was essential to rule out that QDs would affect cell viability. Some studies published several years ago, found that QDs were toxic in biological samples[153-155]. Due to these studies, we tested the citotoxicity of the QDs in two of the breast cancer cell lines used in this Thesis (MCF7 and MDA-MB-468).

The cells were incubated for two hours with three different amounts of QD (1 µL, 2 µL, and 4 µL per mL of culture medium), and cell viability was measured using Celltiter Blue. This test is based on the ability of living cells to convert a non-fluorescent molecule (resazurin) into another fluorescent molecule (resorufin) (more details in chapter 4.2.5.2). Starting from 1 µL/mL, since it is the amounts that has been used for colocalization experiments and intramitochondrial pH measurements, the concentration was doubled and quadrupled to ensure that the QDs did not adversely affect the cells. Although our incubation time of QD in cells for the experiments described in this chapter is 2 h, three additional viability tests were performed, after 2 h of incubation, after 6 h and finally after 24 h. For these tests 1 µL/mL of QDs was used.
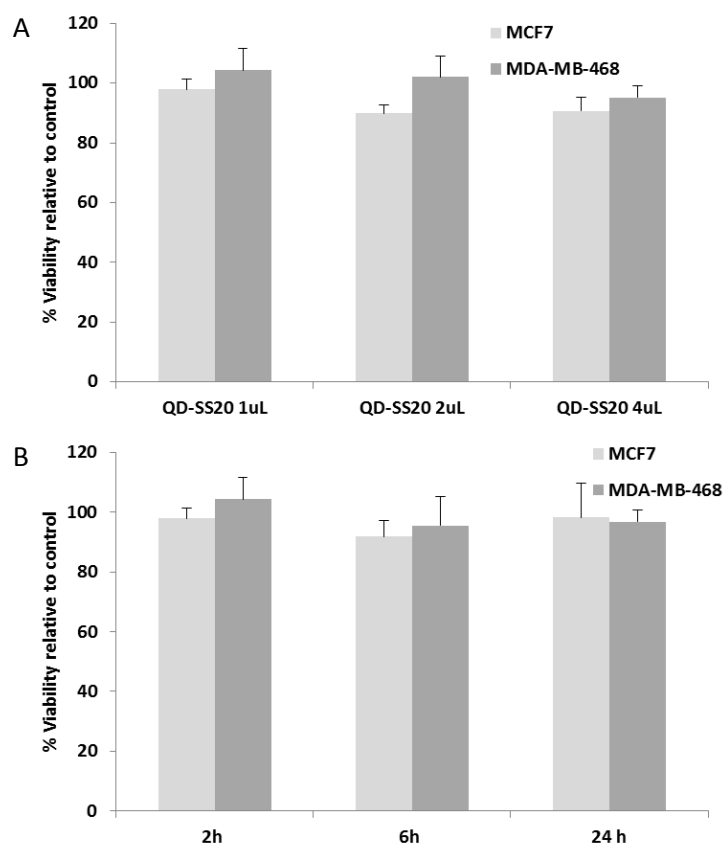


Figure 3.4.15. Viability of MCF7 and MDA-MB-468 cell lines after 2h of incubation with three different amounts of QDs (A) and with 1 µL of QDs after 2h, 6h and 24h of incubation time (B).

As seen in figure 3.4.15, cell viability was not significantly affected in any of the treatments tested; neither with higher concentrations of QDs (panel A) nor with longer incubation times (panel B). Therefore, these QDs can be considered suitable for use with biological samples, at least under the conditions that we have employed in our experiments.

### 3.4.4 DISCUSSION

In this chapter we have used a nanotechnological approach to study two different parameters related with the metabolism of five different breast cancer cell lines: the extracellular pH and the intramitochondrial pH. For this, we have designed and optimized two different nanosensors, including the incorporation of SS-peptides as mitochondria-targeting groups on the surface of the nanosensors.

The extracellular pH results showed that it is possible to clearly differentiate between two types of metabolism in the studied lines (Figure 3.4.3). On the one hand, the cell lines MCF7, ZR751 and SKBR3 exhibited higher pH values, and on the other hand, the cell lines MDA-MB-231 and MDA-MB-468 presented a different metabolism leading to lower extracellular pH values. According to these results, the lower pH of the MDA-MB-231 and MDA-MB-468 cell lines suggests that these lines excrete more lactate into the culture medium, so they should have a metabolism with a high glycolysis activity. The cell lines MCF7, ZR751 and SKBR3 should therefore have a metabolism based on the mitochondrial respiratory chain, since less lactate is present in the culture medium, as indicate the higher pH values calculated for those cell lines.

However, we cannot only rely on these results as a direct expression of the typical metabolism of each cell line, as there is another variable involved in the process: the membrane transporters. Depending on the membrane transporters expressed by each cell line, one can find differences in the excreted metabolites. This is why the direct measurement of the pH in the mitochondrial area is so important, and we studied it using a pH nanosensor, specially designed for the selective delivery to the mitochondria.

Interestingly, as shown in Figure 3.4.14, the results obtained in the determination of the mitochondrial pH indicate an opposite behaviour to that shown in the extracellular media. The cell lines MDA-MB-23 and MDA-MB-468 showed higher intramitochondrial pH values, which correspond to low glycolytic activity and high mitochondrial activity. The cell line MCF7 showed the lowest intramitochondrial pH value, what can be attributed to a higher glycolytic metabolism. The SKBR3 cells displayed two different populations, one population with a similar behaviour to that of the MCF7 cell line, and a second population showing similar pH values to that of the

triple negative cell lines. Therefore, it can be concluded that the MCF7 cell line has a glycolytic metabolism and the MDA-MB-231 and MDA-MB-468 lines have a mitrochondrial oxidative phosphorylation-dependent metabolism. The SKBR3 cell line behaviour does not stick to any particular metabolism, but seems to alternate the two metabolisms according to its needs. In any case, the statistical study drew that the behaviour of the SKBR3 cell line was not significantly different from that of the MDA-MB-231 and MDA-MB-468 cells.

In the next chapter, we have performed a thorough study on the metabolic features of the different cell lines. With this information, we have been able to establish different metabo-phenotypes. In chapter 5, a joint discussion of the results from chapters 3 and 4 does correlate the metabolic features with the results obtained using luminescent nanosensors.

# *Metabolic*

# *Profiling*

# 4. METABOLIC PROFILING

## 4.1 INTRODUCTION

### 4.1.1 FROM WARBURG EFFECT TO CURRENT METABOLIC REPROGRAMMING PARADIGM

Metabolism encompasses all the reactions that occur in a cell or organism. It is divided into two groups of antagonist reactions: catabolism, which refers to the disintegration of molecules into smaller metabolites to release energy; and anabolism, which refers to the energy consumption necessary for cell proliferation carrying out the synthesis of macromolecules[156]. The relationship between these opposing reactions depends on the cellular context and the state of differentiation. Likewise, the metabolic mechanism varies greatly between resting cells and cells that are proliferating. On the one hand, the quiescent cells are metabolically active, adopting a catabolic metabolism focused on maximizing the production efficiency of ATP from limited nutrients. On the contrary, the cells stimulates by the growth factor increase their absorption of nutrients and adopt and anabolic metabolism. These proliferating cells absorb excess nutrients, convert them into biosynthetic building blocks in the form of amino acid, fatty acids and nucleotides, to generate macromolecules for growth and cell division[157, 158]. Cancer cell are proliferating cells that may have the pathway of instructional signalling downstream of growth factor receptors constitutively even in the absence of extracellular growth factors (Figure 4.1.1) That allows them to keep their metabolic needs[158].
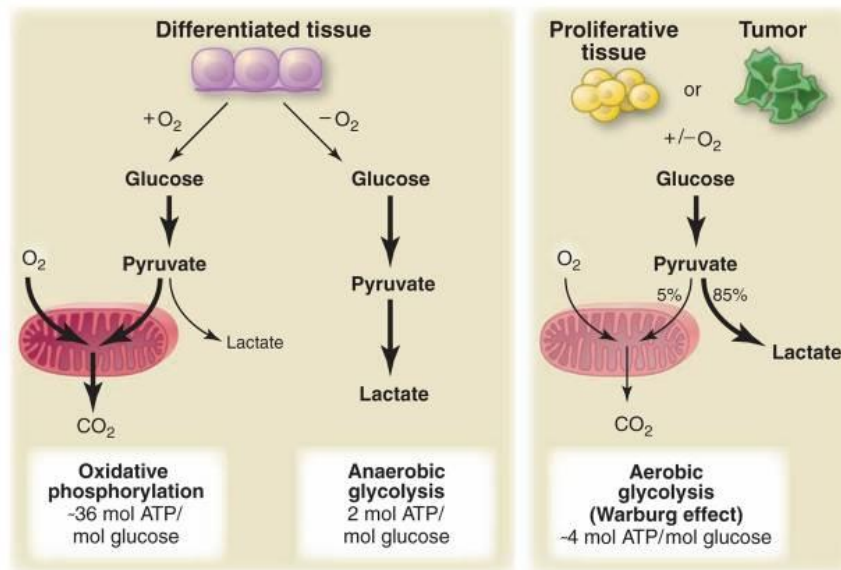
Figure 4.1.1. Schematic representation of the differences between oxidative phosphorylation, anaerobic glycolysis and aerobic glycolysis. In the presence of oxygen, nonproliferative (differentiated) tissues first metabolize glucose into pyruvate through glycolysis and then completely oxidize the majority of that pyruvate in the mitochondria to $CO_2$ during the oxidative phosphorylation process. When oxygen is limiting, cells can redirect the pyruvate generated by glycolysis away from mitochondrial oxidative phosphorylation by generating lactate (anaerobic glycolysis)[159].

### 4.1.1.1 REWIRING OF CELLULAR METABOLISM IN CANCER

In the presence of oxygen, most differentiated cells maximize ATP production by oxidative phosphorylation, with minimal lactate production. For this purpose, they metabolize glucose to carbon dioxide by oxidation of glycolytic pyruvate in the mitochondrial tricarboxylic acid (TCA) cycle. Since the 1920s the field of cancer metabolism has been dominated by the discoveries of the German biochemist Otto Warburg. He observed that cancer cells consume glucose at a very high speed compared to normal cells. In addition, cancer cells metabolize this glucose predominantly through glycolysis, producing high levels of lactate even in oxygen-rich conditions[160, 161]. This increase on glycolytic activity is known as aerobic glycolysis or "Warburg effect"[162, 163]. This glucose fermentation is much less efficient than the TCA cycle and the subsequent oxidative phosphorylation for the generation of ATP[163].

The observation of the predominant aerobic glycolysis in cancer cells led Warburg to suggest that these cells arise due to a defect in mitochondrial respiration. Accordingly, the cancer cells show a permanent deficiency of oxidative metabolism which makes dependent on improved glycolysis[139]. However, it is now known that respiration is not altered in most cancer cells[164-166]. Even then, aerobic glycolysis has been observed in a wide variety of tumors from different cell types. But most normal cells in adult tissues from which cancer cells are derived do not generally use aerobic

glycolysis[157]. Therefore, the fact that cancer cells are converted to a characteristic metabolic phenotype in which they divide rapidly suggests that aerobic glycolysis should provide proliferative advantages[167].

Later, similar patterns of glucose metabolism were observed in studies of primary lymphocyte proliferation[168-170], rejecting the possibility that aerobic glycolysis is exclusive of tumor cells, or that the Warburg effect only develops when oxidative capacity is damaged. These studies suggest that aerobic is a common phenomenon among many proliferating cells[162].

For a time, it was thought that cancer was a disease caused by genetic alterations, and the Warburg effect was considered an indirect secondary phenomenon as a consequence of tumorigenesis[171]. However, the question remained as to why cancer cells do not favour oxidative phosphorylation, which is more efficient that the process of aerobic glycolysis. After long absence of interest, the research carried out over the last fifteen years has begun to answer this question. The key lies in the discovery that oncogenes and tumor suppressors are intricately related to the regulation of cancer metabolism[163, 172]. Both oncogenes and tumor suppressor gene products can influence the shift between aerobic glycolysis and more extensive use of the TCA cycle to generate ATP. In addition, it has been demonstrated that several transcription factors and metabolic enzymes are crucial in mediating the aberrant metabolic behaviour of tumor cells[158, 171, 172]. Therefore, in 2011, the importance of reprograming energy metabolism for tumor progression was signified by its addition as an emerging stamp to the revised list cancer hallmarks[173].

Therefore, in recent years a renewed vision emerged under the concept of "metabolic reprogramming". This term describes conventional metabolic pathway whose activities are enhanced or suppressed in tumor cells in relation to benign tissues as a consequence of tumorigenic mutations and/or another factor[174]. Recent studies have provided a greater understanding of cancer metabolism and the underlying rewiring of the tumor metabolic pathway are being elucidated. Some of the most notable changes in the metabolism of tumor cells are detailed below.

### 4.1.1.2 GLYCOLYSIS

Glycolysis is a series of nine enzymatic reactions, in which glucose is converted into 2 molecules of pyruvate, and as a result there is a net gain of two molecules of ATP and two molecules of NADH. The fate of pyruvate produced in glycolysis depends on the cellular oxygen state. In well-oxygenated differentiated tissue, pyruvate enters the mitochondria and is completely oxidized to $CO_2$, this process generates approximately 36 molecules of ATP per molecule of glucose. Under oxygen deprivation, pyruvate is converted to lactic acid by lactate dehydrogenase (LDH) and facilitates the conversion of NADH to $NAD^+$, which is a necessary cofactor for glycolytic

flow. As mentioned, in the proliferation of tissue and cancer cells, pyruvate is converted to lactate regardless of the concentration of oxygen[157]. This reaction benefits cancer cells, since it allows NAD+ to regenerate to accelerate glycolysis and reduces intracellular oxidative stress, promoting the survival of tumors[162, 163]. Previously, excess production of lactate by tumors was considered simply as a byproduct of the Warburg effect, it is now known that lactate intervenes in a considerable amount of tumor effects, such as growth promotion, invasion and metastasis[175].

To avoid intracellular acidification and death due to the high concentration of intracellular lactate, this metabolite is exported from the cell by a family of passive proton-lactate membrane transporters called monocarboxylate transports (MCT). It has been shown that MCTs, especially the MCT1 and MCT4 isoforms, are over-expressed in most cancers to facilitate the overload of lactate production that occurs with the Warburg effect[176]. In fact, it decreases the proliferation of breast cancer cells in vitro and tumor growth in vivo by inhibitors of MCT as therapeutic agents against cancer[177].

On the other hand, the ATP derived from glycolysis is really important for cellular functions and has an important role in the proliferation of cellular biosynthesis. However, the importance of aerobic glycolysis goes beyond the production of ATP to allow the assimilation of nutrients in biosynthetic precursor[157]. This was reinforced by the discovery of the embryonic M2 isoform of the pyruvate kinase (PK) enzyme which is the isoform that is expressed in both cancer cells and normal proliferating cells. Recently, several papers have reported that PK is crucial in the reprogramming of glycolytic metabolism. Pyruvate kinase is a limiting enzyme that catalyzes the final reaction of glycolysis, converting phosphoenolpyruvate (PEP) into pyruvate and producing ATP[178-181]. It has seen both in vitro and in cells that PKM1 is more active than PKM2[182]. In addition, the effect of PKM2 on glycolysis depends on whether it is found as a highly active tetramer that will favour the formation of pyruvate and ATP, or a less active dimer, which predominates is tumor cells[183, 184]. In fact, cancer cells can revert to the highly regulated M2 isoform because it can switch between active and inactive forms to control the flow of glycolytic carbons leading to biosynthesis of metabolites or to the production of mitochondrial ATP[157].
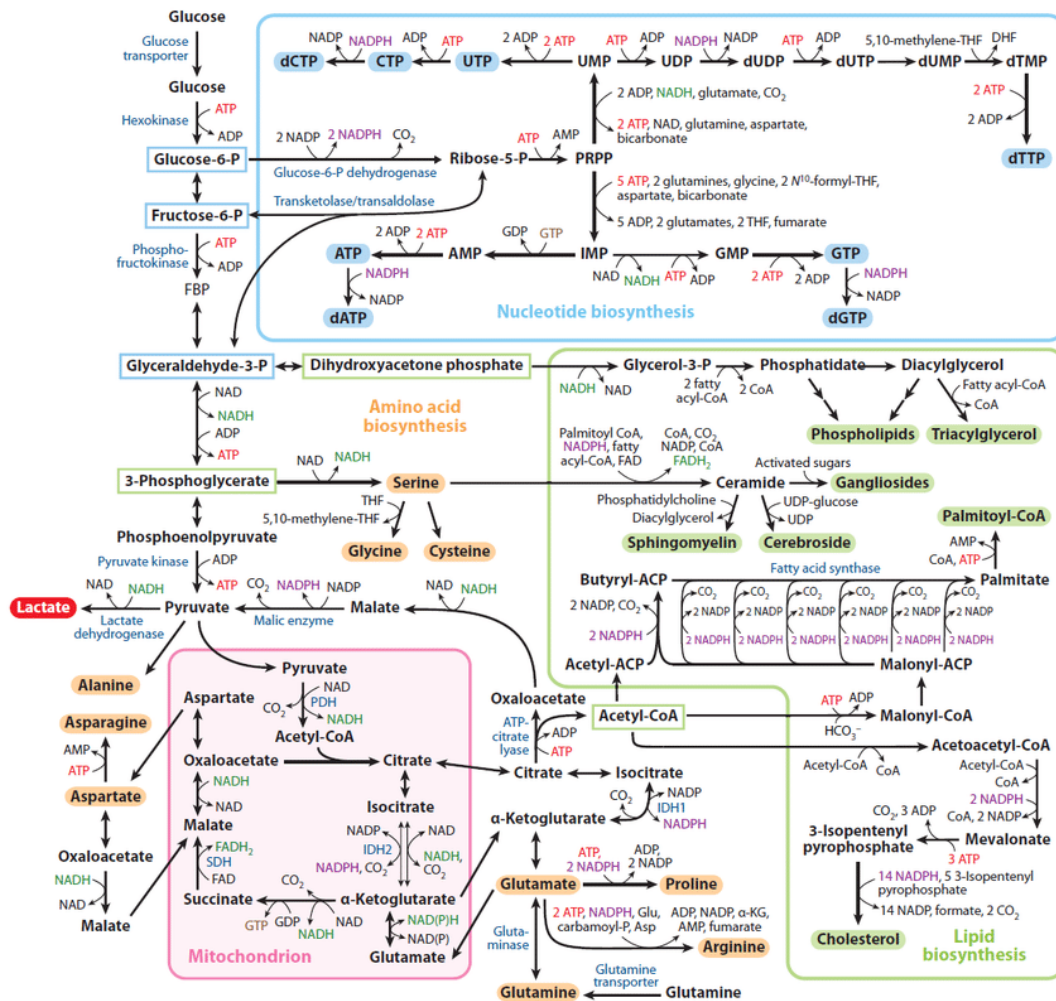
Figure 4.1.2. Metabolic pathway active in proliferating cells. This schematic represents our current understanding of how different pathways in central carbon metabolism contribute to biomass precursors. Enzymes that control critical steps and are often overexpressed or mutated in cancer cells are shown in blue[157].

Replacement of the isoform PKM2 by PKM1 constitutively active tetrameric form in tumor cell lines makes them less active glycolytically and decreases the growth of the tumor xenograft, suggesting that PKM2 promotes both aerobic glycolysis and anabolic metabolism[179]. The suppression of PKM2 by release of FBP catalysed by phosphotyrosine of the enzyme impairs the formation of pyruvate, resulting in accumulation of upstream intermediates. These intermediates of the glycolysis can be directed towards anabolic processes for the synthesis of nucleic acids, phospholipids and amino acids, increasing the availability of metabolites for rapid growth[185]. Until now, it has been described aerobic glycolysis is not selected for increased ATP production, otherwise a major function for proliferating cells likely extends beyond rapid ATP production to support macromolecular synthesis providing biosynthetic precursors.

It has been shown that many glycolytic enzymes are positively regulated during tumorigenesis. The increase in glucose uptake capacity in cancer cells is due to the positive regulation of GLUT1 and GLUT3 glucose transporter[186, 187].

### 4.1.1.3 THE KEY ROLE OF ANAPLEROSIS AND CATAPLEROSIS FOR TCA CYCLE FUNCTION

In quiescent cells, pyruvate derived from glycolysis is converted to acetyl-CoA and oxidized in the TCA cycle generating ATP by oxidative phosphorylation. In cancer cells, acetyl-CoA is introduced into a truncated TCA cycle, where is converted into intermediates that can be used for macromolecular biosynthesis. The truncated TCA cycle appears to be compatible with cell proliferation[188]. This indicates the two activities necessary for cell growth: generate reducing equivalents for oxidative phosphorylation by the electron transport chain and supply carbons for the production of precursors. This is possible both for the oxidative and reductive branches of the TCA cycle.

The carbon entry and exit of the TCA cycle is carried out by reciprocal and correlative reactions called anaplerosis and cataplerosis. Cataplerosis includes reactions involved in the conversion of TCA cycle intermediates to a product that is used in the biosynthetic pathway[189]. In quiescent cells, the main function of the TCA cycle is the production of ATP from oxidizable substrates. However, in proliferating cells, most of the carbon entering the TCA cycle is used as an important source of biosynthetic pathway. This gives a continuous efflux of TCA intermediates[162]. The majority of the TCA derivatives of the cataplectic substrate is citrate, which is transferred to the cytosol to convert it to oxaloacetate. From this oxaloacetate, the lipogenic precursor acetyl-CoA can be synthesized to produce fatty acids, cholesterol and isoprenoids, resulting in truncated TCA cycle[162]. In addition, oxaloacetate and also α-ketoglutarate provide intracellular groups of nonessencial amino acids (aspartate, asparagine, glutamate and proline) to be used in the synthesis of proteins and nucleotides[157].
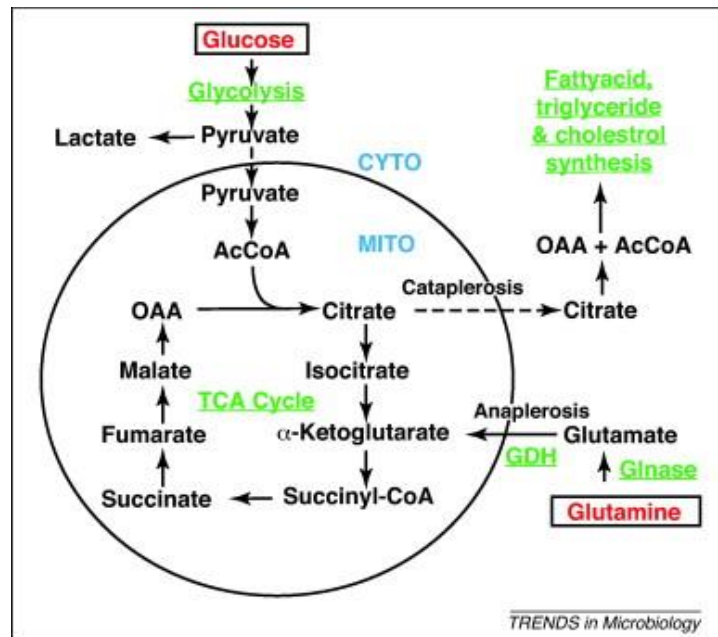
Figure 4.1.3. Schematic representation of pyruvate and glutamine metabolism and fatty acid synthesis[190].

It is necessary to replace the intermediaries of the TCA cycle so that the cataplerosis is sustainable. Intermediates are replaced by a process called anaplerosis[189]. There are several mechanisms that cells can used to produce anaplerotic activity, remain prominent pyruvate and several amino acids in tumor metabolism (Figure 4.1.3). It is known that pyruvate carboxylase, which synthesizes oxaloacetate from pyruvate in the mitochondrial matrix, is an important anaplerotic enzyme[191]. Amino acids can enter the TCA cycle through several compounds such as pyruvate, acetyl-CoA, acetoacetyl-CoA, α-ketoglutarate, succinil-CoA, fumarate and oxaloacetate[189]. The amino acid glutamate is the main contributors to the anaplerotic flow, providing carbons for the TCA cycle that serve as precursors of many macromolecules/nonessencial amino acids[192]. Glutamine is metabolized to glutamate and glutamate is converted to α-ketoglutarate by glutaminalysis or another transamination reaction, thus it can enter the TCA cycle. Furthermore, by reductive carboxylation, α-ketoglutarate derived from glutamine is reduced by consuming NADPH in the non-canonical reverse reaction, to form citrate[193]. Once in the TCA cycle, α-ketoglutarate continues to be metabolized to finally form oxaloacetate, an important anabolic precursor that will condense with acetyl-CoA to produce citrate.

### 4.1.1.4 GLUTAMINE: MAJOR METABOLIC AND BIOSYNTHETIC FATES

In addition to glucose, glutamine is the main source of energy and carbon for cancer cells[162]; it is a key substrate required for several important metabolic roles in the cell. It serves as a carbon source for the production of energy, provides carbon and nitrogen to biosynthetic reactions, regulates redox homeostasis and modulates the activity of the signal transduction pathway[194]. These functions of glutamine

metabolism that help support cell growth and proliferation in cancer cells are detailed below.
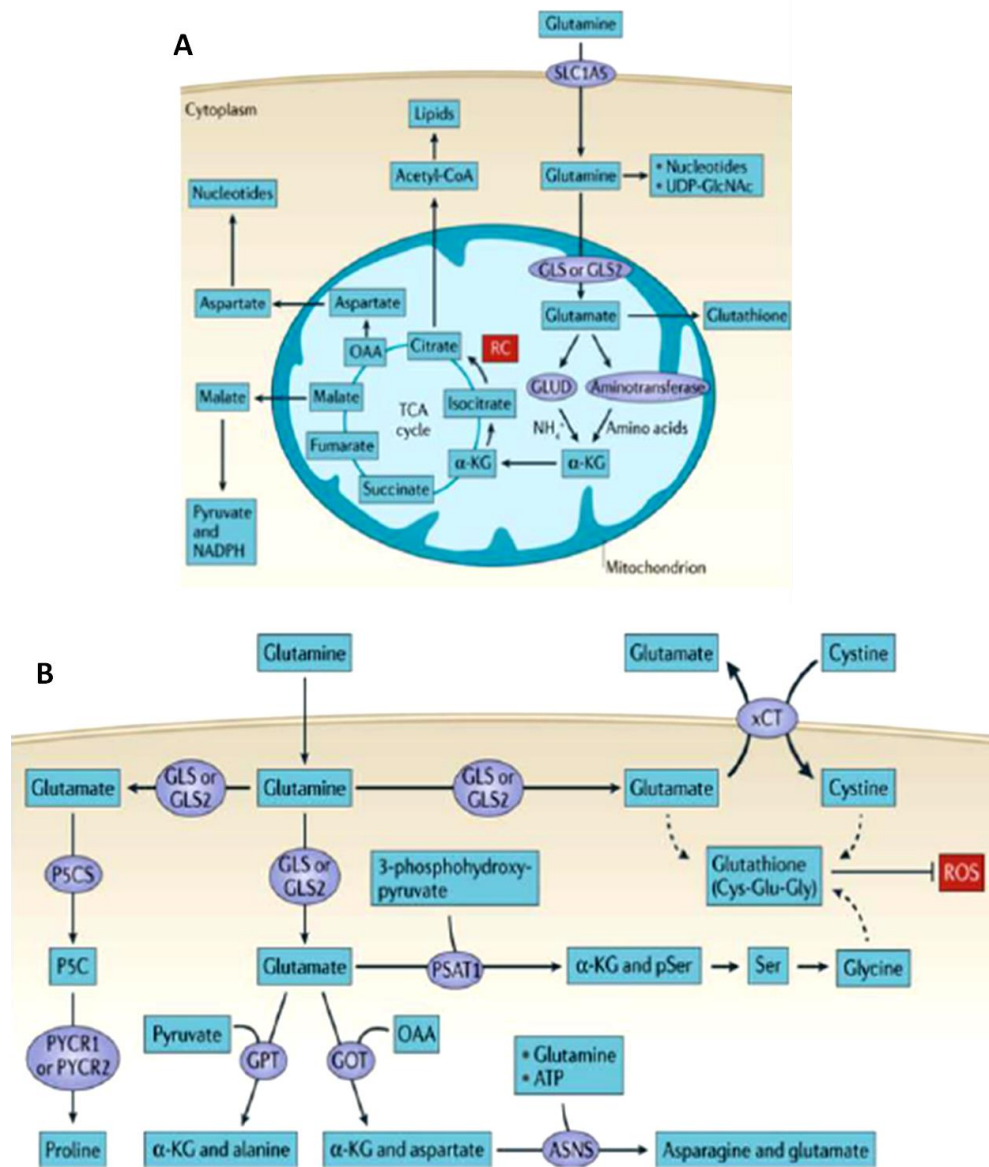


Figure 4.1.4. Glutamine metabolism A) Major metabolic and biosynthetic fates of glutamine. B) Glutamine control of amino acids pools and reactive oxygen species[78].

As primary carbon source for energy production and biosynthesis, glutamine acts as an important anaplerotic substrate in the replacement of intermediaries of the TCA cycle. Based on the analysis of isotopologues $^{13}$C, a cycle of TCA independent of glucose has been discovered, fully supported by glutamine. This efficient route of glutaminolysis, in which glutamine can be used for anabolic purposes or to produce energy, involved the supply of acetyl-CoA and oxaloacetate to the TCA cycle[195, 196]. Glutamine often plays a supporting role in lipogenesis by allowing the transfer of

acetyl-CoA derived from the mitochondria to the cytoplasm through citrate. In addition, the glutamine carbon can also support *de novo* lipogenesis that supplies acetyl-CoA through two mechanisms. First, provide pyruvate from malate that can re-enter the TCA cycle as acetyl-CoA[195]. Second, glutamine, after conversion to α-ketoglutarate, can be subjected to reductive carboxylation to generate isocitrate, which is then converted to citrate[194, 197]. This direct contribution to *de novo* lipogenesis has been observed particularly in conditions of hypoxia or mitochondrial dysfunction, in which it was shown that the cells depend almost exclusively on glutamine-reducing metabolism[188, 196].

- As a nitrogen donor: The amido and amino groups of glutamine contribute to multiple biosynthetic pathways, including synthetic non-essencial amino acids, nucleotides and hexosamines. On the one hand, the nitrogen from glutamine via glutamate supports the levels of many amino acid pools in the cell through the action of aminotransferases[198]. It has been demonstrated that amino acids derived from glutamine, alanine, aspartate and serine, contribute to the survival of cancer cells[199] (FIG4b). On the other hand, the intervention of glutamine in the biosynthesis of purine and pyrimidine nucleotides, as a nitrogen donor, is involved in the continuous support of proliferation[200] (FIG4a). The importance of glutamine as a reservoir of nitrogen was demonstrated by the fact that cancer cells deprived of glutamine undergo an arrest of the cell cycle that cannot be rescued by the intermediates of the TCA cycle, but can be rescued by exogenous nucleotides[201].

- As regulator of redox homeostasis: Several metabolic pathways of glutamine lead to products that directly control ROS levels. In addition to the metabolism of glutamine that contributes to the production of mitochondrial ROS by its oxidation in the TCA cycle, the important glutamine-ROS-control is through synthesis of glutathione. Glutathione is a tripeptide (glutamate-cysteine-glycine) that neutralizes peroxide free radicals (Fig4b). It has long been known that the entry of glutamine is the limiting step of the synthesis of glutathione and is also responsible for the synthesis of two of its components[193]. In its antioxidant function, glutathione cancels the electrons and oxidazes. To restore glutathione to its reduced form, NADPH is required, and the metabolism of glutamine can also lead to increased production of NADPH, through the malic enzyme[194, 199].

- As modulator cell signalling pathway: To control cell survival and growth, cells have developed glutamine-dependent mechanism that includes the modulation of signal transduction pathway. The metabolism of glutamine has been linked to the stress response, folding and protein trafficking and stress of the endoplasmic reticulum[193, 202].

### 4.1.1.5 BRANCHING PATHWAYS FOR MACROMOLECULAR BIOSYNTHESIS

Glucose and glutamine are the main nutrients to fuel the proliferation of cancer cells. Recently, the relationship between the metabolism of these two nutrients and their active coordination in the reprogramming of proliferating cells has been reported[194]. Carbon derived from glucose has diverse destinations. Through glycolytic intermediates, glucose can provide the precursors of the chemical components needed to build macromolecules essential for cell division. In addition to replacing the intermediates of the TCA cycle, glutamine contributes more to protein biosynthesis (Fig2). Changes in branching pathways that lead to higher levels of biosynthetic activities more commonly studied in cancer metabolism are discussed in the next section.

#### NUCLEOTIDES BIOSYNTHESIS

To generate the ribose 5-fosfato needed for nucleotide biosynthesis, the cells divert carbon from glycolysis to the pentose phosphate pathway (PPP)[184]. Both the rescue synthesis route and the *de novo* pathway of purine and pyrimidine biosynthesis lead to the production of nucleoside-5'-phosphates by the use of an activated sugar intermediate (5-phosphoribosyl-1-pyrophosphate, PRPP). PRPP is generated from ribose-5-phosphate deviated from the glycolytic flow to PPP, and requires energy in the form of ATP (Figure 4.1.5).

The purine and pyrimidine bases are constructed from several nonessential amino acids and methyl groups donated from the assembly of a carbon/folate. The TCA cycle contributes with oxaloacetate, which is transaminated in aspartate, the intermediate required to synthesize purine and pyrimidine bases. Aspartate is becoming essential in this route to maintain a high flow a nucleotide biosynthesis[174] (FIG5). In addition, glutamine is the nitrogen donor required in up to three independent enzymatic steps for purine synthesis and in two independent enzymatic steps for the synthesis of pyrimidine[199] (Figure 4.1.5).
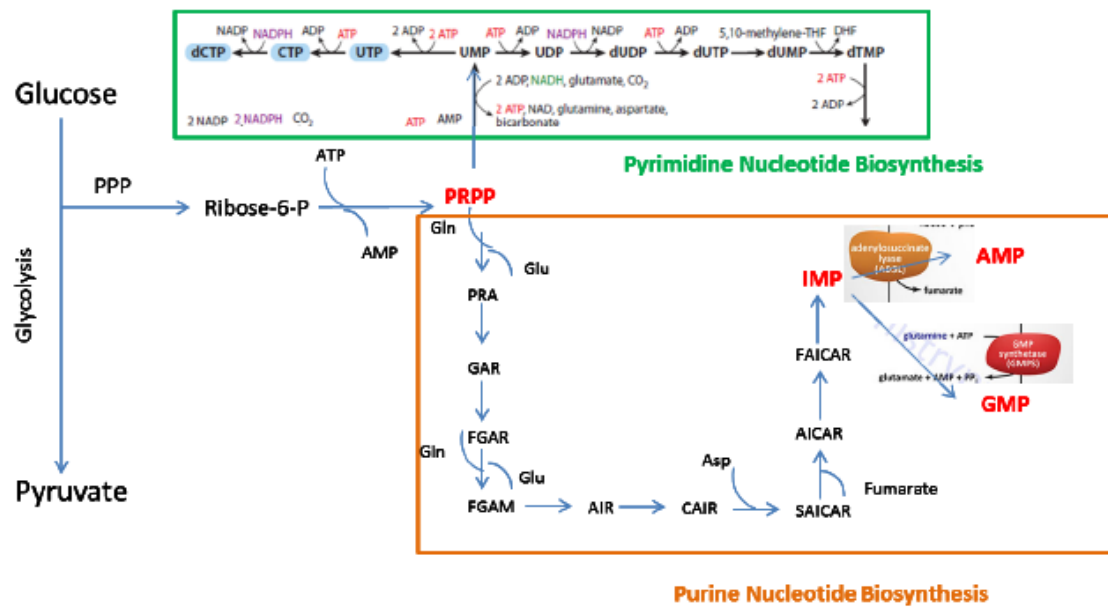
Figure 4.1.5. Nucleotide biosynthesis pathway. The novo pathways for purine and pyrimidine biosynthesis.

It has been known for a long time that tumor cells depend on *de novo* nucleotide synthesis to support increased RNA production and DNA replication. In addition, elevated nucleotide biosynthesis has been observed in many cancers. The metabolism of altered nucleotides in tumor cells has been demonstrated in comparison with normal cells, as manifested by the larger nucleotide group size, higher activity of the anabolic nucleotide pathway as well as the activity of different enzymes involved in the synthesis pathway of nucleotides[203]. That means high adaptation requirements to increase the rate of nucleotide biosynthesis in order to support the proliferation of cancer cells. This adaptation involves the consumption of ATP (Figure 4.1.5), which suggests that the proliferating cells are capable of sacrificing energy for the maintenance of purine and pyrimidine proliferative pulls. In addition, aspartate and glutamine play a key role in these pathways as precursors, therefore, they are more indispensable for proliferating cells[199, 204].

#### LIPID BIOSYNTHESIS

Like proliferating cells, cancer cells depend on the synthesis of *de novo* fatty acids, while they are suppressed in adult cells due to excessive nutritional availability[205]. Although tumor tissue also absorbs lipids from the tissue environment, it has been observed that *de novo* provides most of the lipids necessary for the rapid proliferation of cancer cells[206].

Lipids synthesis describes the processes that convert carbon derived from nutrients into fatty acids. Fatty acids are carboxylic acids that contain a long chain of

hydrocarbon acids and are the precursors of cholesterol esters, phospholipids and triacylglycerides. The synthesis of fatty acids requires integration with other carbon pathway and redox metabolism, in order to obtain sources of acetyl-CoA and reduce potency in the form of cytosolic NADPH (Figure 4.1.2)
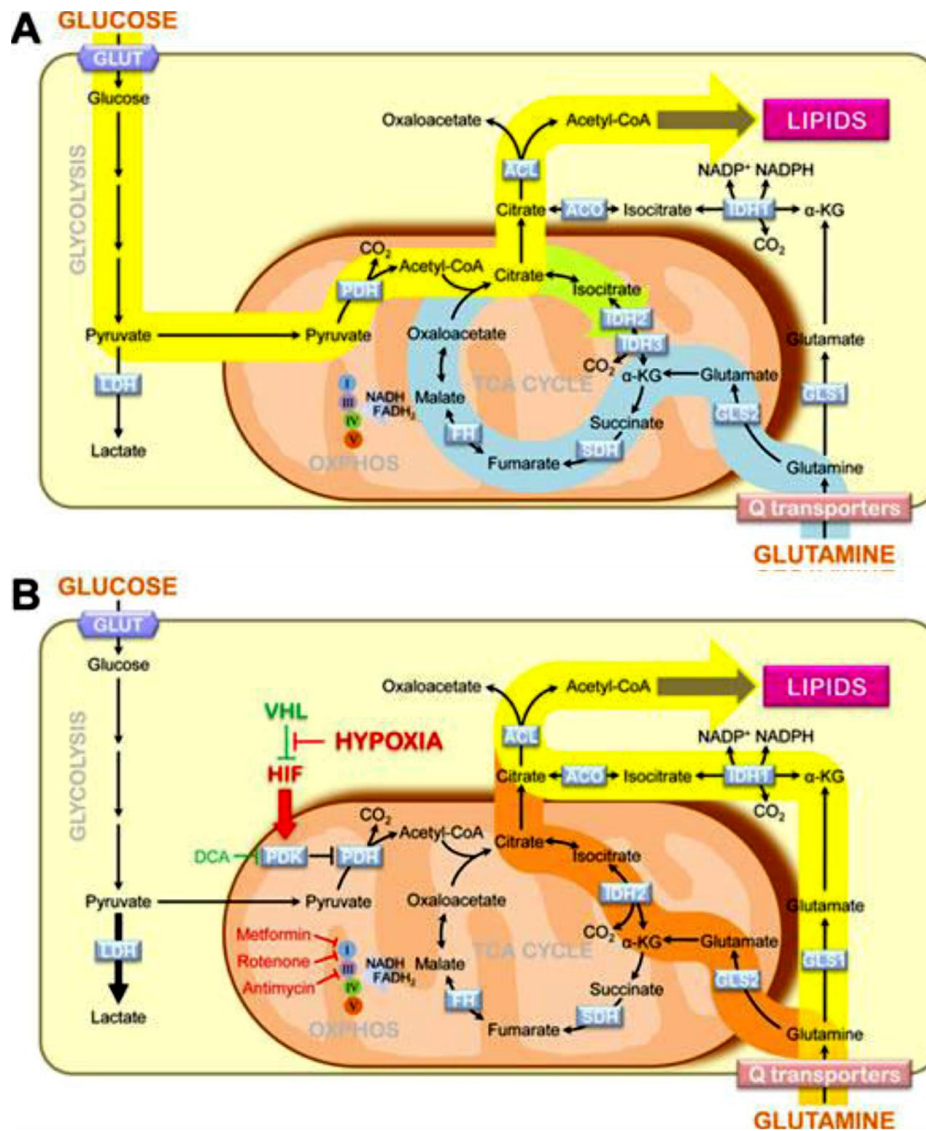


Figure 4.1.6. A metabolic switch in carbon source for lipid synthesis. A) Under conditions when mitochondrial respiration is fully functional, glucose is the major source of carbons for acetyl-CoA synthesizes lipids. The yellow block arrows the route of carbons from glucose to lipids. The blue block arrow indicates oxidative glutamine metabolism (anaplerosis). The green block arrow shows the metabolic pathway of citrate generated from glucose-derived acetyl-CoA and glutamine-derived oxaloacetate. B) Under conditions where hypoxia inducible factor (HIF) is stabilized (such as hypoxia or upon VHL deletion) or when mitochondrial respiration is limited, glutamine predominantly provides carbons for lipogenic acetyl-CoA either via cytoplasmic IDH1 (yellow block arrow) or mitochondrial IDH2 (orange block arrow). This pathway is referred to as reductive glutamine metabolism[183].

Glucose is the largest source of acetyl-CoA for the synthesis of fatty acids[192]. The acetyl-CoA derived from glycolysis obtained in the mitochondrial matrix is used to

synthesize citrate in the TCA cycle. Citrate is transported to the cytosol where acetyl-CoA is recovered from citrate and used as a carbon source for the growing acyl chain (Figure 4.1.6). Acetyl-CoA is carboxylated in the cytosol by acetyl-CoA synthetasa to give manonyl-CoA. Malonyl-CoA is converted to palmitate, a saturated fatty acids that is the precursor of many saturated and unsaturated fatty acids[207]. Another use of acetyl-CoA is to generate cholesterol through the mevalonate pathway, and important component for the synthesis of steroids and membranes[208] (Figure 4.1.2). In cases of hypoxia or mitochondrial dysfunction, access to glucose-derived from acetyl-CoA is altered and an alternative glucose source such as glutamine is used to generate citrate for fatty acid biosynthesis[196, 209] (Figure 4.1.6b).

Another carbon source or the glycolytic pathway required for lipogenesis is dihydroxyacetone phosphate. This glycolytic intermediate is the precursor of glycerol-3-phosphate, which is crucial for the biosynthesis of phospholipids and triacylglycerols that serve as the major structural lipids in cell membranes. Another glycolytic intermediate, 3-phosohiglycerate, is the precursor if sphingolipids, another important class of lipids in cells[157] (Figure 4.1.2).

It should be noted that cell growth is supported by the synthesis of fatty acids in multiple ways. On the one hand, it provides lipids for the biogenesis of the membrane. It also provides cancer cells with fuel can be mobilized in times of nutrient deficiency through the oxidation of fatty acids and precursors of lipid synthesis. On the other hand, these products can also function as second messengers and signalling molecules[208, 210]. Aberrant activation of *de novo* lipogenesis due to increased expression of metabolic enzymes involved in lipogenesis has been reported in numerous studies[208, 211, 212]. In fact, inhibition of different enzymes within the fatty acid biosynthesis pathway can block cancer cell growth[213, 214].

### AMINO ACIDS BIOSYNTHESIS

Amino acids are the building blocks of proteins and can be provided primarily by the cellular environment (essential amino acids). However, some of them are synthesized by intracellular reactions (non-essential amino acids). The main routes involved in the synthesis of amino acids are glycolysis, the TCA cycle and glutaminolysis (Figure 4.1.2).

On the one hand, glycolytic intermediates are direct precursors for the biosynthesis of some amino acids, 3-phosphoglycerate provides the carbons for cysteine, glycine and serine, and pyruvate provides the carbons for alanine[157]. On the other hand, glutamate derived from glutamine is the main nitrogen donor for the synthesis of amino acids non-essential through transamination reactions using the transaminases enzyme. These enzymes transfer amino groups from glutamate to α-ketoacids. These α-ketoacids can come from glucose or glutamine and are used to

synthesize alanine, serine, aspartate and ornithine[199]. Particularly, upregulation of glutamate-dependent transaminases, PSAT1 and GOT in cancer cells has been observed[215].

Alanine is used in protein synthesis, but is also secreted by tumor cells, to remove excess carbon from glycolysis[192]. In contrast, aspartate remains inside the cell. It is a precursor to asparagine biosynthesis and refers to the synthesis of proteins and nucleotides and electron transfer reactions through the malate-aspartate shuttle[202]. Serine, on the other hand, is necessary for biosynthetic and signalling pathways, including the synthesis of amino acids, such as glycine and cysteine, and the production of phospholipids, such as sphingolipids and phosphatidylserine[157].

Serine also participates in the metabolism of folate as a carbon donor. The one-carbon units derived from serine are used for the *de novo* synthesis of adenosine, guanosine and thymidylate, and to support the methionine cycle[216]. In addition, the cofactors NADPH, NADH and ATP can be regenerated from serine or folate pathway[217]. It has been shown in numerous studies that alterations in serine metabolism have profound effects that may contribute to the development of cancer/being crucial in the metabolism of cancer[216].

## 4.1.2 REGULATION OF CANCER CELL METABOLISM BY ONCOGENES AND TUMOR SUPPRESSORS

Initially it was thought that tumor metabolism was an indirect effect of oncogenic mutations, and even evidence suggest that one of the main primary function of activated oncogenes and inactivated tumor suppressors is to reprogram cellular metabolism. It is increasingly evident that many of the main oncogenic signalling pathways converge to adapt the tumor metabolism in order to favour growth and survival in cancer cells[158]. Unlike normal cells, cancer cells accumulate oncogenic alterations that give them independence from external requirements and signalling inputs driven by growth factors[218]. The activation of these oncogenes and tumor suppressors that ensure metabolic robustness and stress resistance are described below.

### 4.1.2.1 ONCOGENIC ALTERATION INVOLVED IN METABOLIC REPROGRAMMING: GLYCOLYTIC PROMOTERS AND MITOCHONDRIAL FUNCTIONAL CAPACITY ASSISTANTS

#### THE PI3K/AKT/MTOR PATHWAY

The master regulator of glucose metabolism is the PI3K/Akt/mTOR pathway. The phosphoinositide-3-kinases (PI3Ks) are a family if lipid kinases that propagate intracellular signalling cascades that regulate a wide range of cellular processes[219]. In

non-transformed cells, the PI3K pathway is activated in response to growth signals. However, it was reported that the PI3K pathway is constitutively activated by several different mechanisms in a number of cancers. These mechanisms include mutations in tumor suppressor genes, such as PTEN, mutations in the components of the PI3K complex itself or aberrant signalling of tyrosine kinase receptors (EFGR, IGF-1, HER2, etc.)[220].

Once activated, the subsequent activation of Akt and mTOR kinases is induced. The PI3K/Akt/mTOR system supports cells biosynthesis through several routes: first, increases expression and translocation of nutrient transporters through the membrane, allowing greater absorption of glucose, amino acids and other nutrients; second, Akt increases glycolysis, by phosphorylating key glycolytic enzymes, and stimulates lactate production, being sufficient to induce a Warburg effect non-transformed cells or cancer cells; third, enhance the biosynthesis of macromolecules. PI3K and Akt stimulate the expression of lipogenic genes and lipid synthesis, while mTOR functions as a key regulator of nutrient availability[162, 221]. Activated mTOR stimulates the biosynthesis of proteins and lipids, activats glycolysis and de novo lipids biosynthesis using transcription factors such as HIF-1 and SREBP[222].

### c-Myc

The highly expressed oncogenic c-Myc transcription factor has been related to the activation of several glucose transporter and glycolytic enzymes, as well as LDHA[223] and PDK1[224]. With respect to proliferation, c-Myc promotes the accumulation of cellular biomass by activating the transcription of targets that increase nucleotide biosynthesis, ribosome and mitochondrial biogenesis. In turn, c-Myc controls many components of mitochondrial intermediate metabolic pathway. The components affected in these pathways include enzymes involved in the synthesis of purine and pyrimidine, in the folate pathways and in the vast majority of the enzymes of the TCA cycle[225].

c-Myc also promotes glutamine metabolism inducing the expression of glutamine transporters and indirectly by positively regulating glutaminase levels through the repression of miRNa miR-23[226, 227]. It has been observed that the overexpression of c-Myc results in the concurrent conversion of glucose mainly to lactate and the oxidation of glutamine through the TCA cycle. As a result, some cells transformed with c-Myc have demonstrated an absolute requirement of glutamine as a bioenergetics substrate to maintain the continuous replenishment of the TCA cycle intermediates and mitochondrial integrity[225, 228].
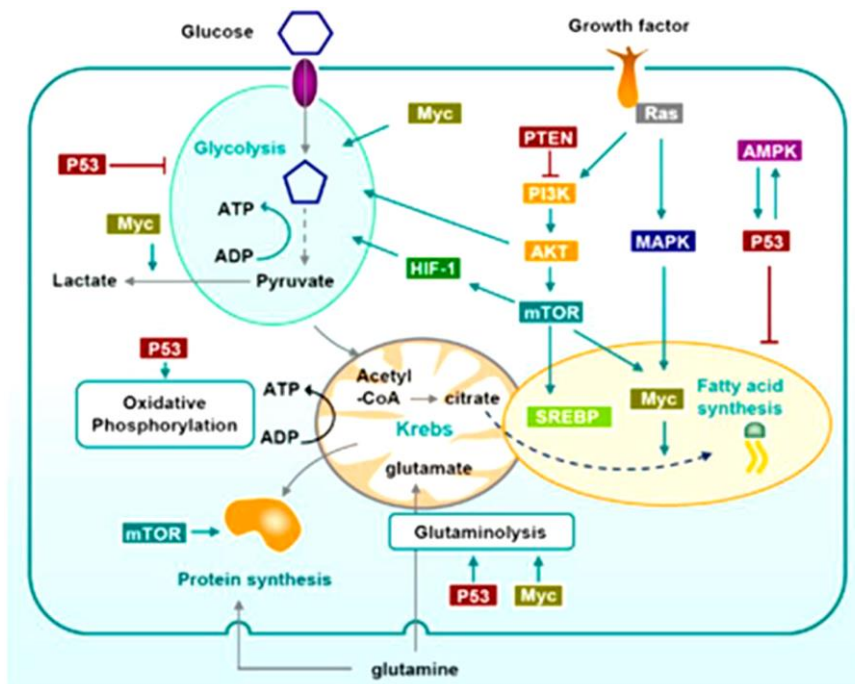
Figure 4.1.7. Signaling pathways that regulate metabolism of proliferating and cancer cells. Growth factors influence metabolism through Ras and PI3K. Both PI3K/Akt and MAPK increase glycolysis. They also induce the upregulation of the transcription factor SREBP which promotes lipogenesis. mTOR, downstream of PI3K7Akt also plays a central role in the metabolic switch observed in highly proliferating cells: it activates protein translation, glycolysis (through HIF-1 dependent and independent pathways) and lipogenesis through the transcription factors SREBP and Myc. Myc is also the main oncogene implicated in glutamine addiction of cancer cells, through the upregulation of glutamate synthesis. It also contributes to the Warburg effect by increasing glycolysis and lactate production. AMPK activation, which is often impaired in tumors, allows the cells to switch their metabolism to catabolism when the nutrients are scarce. p53 regulates metabolism at multiple steps, notably through the upregulation of glutamine synthesis and inhibition of fatty acid synthesis and glycolysis[229].

### Ras

Ras proteins function as molecular switches interacting with signalling molecules that regulate cellular activities such as proliferation, apoptosis and cell migration[230]. Ras is stimulated by growth factors and among the metabolic effects that mediates the activation of several routes, such as the PI3K/Akt/mTOR and MAPK routes, involved in lipid biosynthesis[229]. K-Ras supports the decoupling of glycolysis and the metabolism of TCA with glutamine that supplies carbon to drive the TCA cycle. In cells transformed with K-Ras, the decoupling between glucose metabolism and glutamine leads to efficient utilization of glutamine carbon and nitrogen in building blocks of biomass (amino acids and nucleotides) and glutathione. In addition, K-Ras reprograms the metabolism of glutamine by the negative regulation of GLUD1 and the up-regulation of GOT1 to support the production of NADPH dependent on the malic enzyme for redox balance[231]. K-Ras also increases the uptake of glucose and helps generate nucleotide precursors[232].

### 4.1.2.2 ONCOGENIC STRESS SENSORS AS METABOLIC CHECKPOINTS: PROMOTING TUMOR GROWTH

#### HYPOXIA INDUCIBLE FACTORS (HIFs)

In tumors, it can be observed that the availability of oxygen in variable. Hypoxia arises when there is a rapid proliferation of cancer cells. The inducible hypoxia factor 1 (HIF-1) allows cells to adapt to hypoxia[233]. HIF-1 is a heterodimer (HIF-1α and HIF-1β), these subunits determine its the biological activity. Oxygen levels will regulate the activity of HIF-1α by inactivation a family prolyl hydroxylases (PHD)[157, 234].

In hypoxia, the ability of tumor cells to consume glucose and produce lactate by performing glycolysis increases. HIF-1 induces the expression of increasing proteins: glucose uptake (GLUT1); conversion of glucose to pyruvate[235, 236]; lactate generation (LDHA), and efflux of these molecules outside the cells (MCT4)[172]. In addition, HIF-1 will activate pyruvate dehydrogenase kinase 1 (PDK1), which phosphorylates and inhibits the mitochondrial PDH complex, which limits the entry of glycolytic carbon into the TCA cycle, thus reinforcing the glycolytic phenotype[237, 238].

HIF-1 can be stabilized even under normoxic by oncogenic signalling pathways and by mutations in tumor suppressor proteins[162]. Mutations in SDH and FH stabilize HIF-1α by interfering with the hydroxylation of HIF-1α, which is competitively inhibited by accumulation of TCA cycle metabolites succinate or fumarate[162, 221].

#### p53

The tumor suppressor p53 is best known for its role in apoptosis, DNA damage and cellular stress response. p53 is also being reconsidered from a metabolic perspective as a regulator of glycolysis and oxidative phosphorylation[239]. In its normal function, p53 decreases the glycolytic rate but, in cancer cells, often loss of control of its functions by mutation or suppression, thus promoting glycolysis. Mutant p53 cells have shown higher rates of glycolysis, producing lactate and exhibiting decreased mitochondrial respiration compared to wild-type cells[240]. Therefore, the loss of p53 has been recognized as one the main forces behind the acquisition of the glycolytic phenotype[221].

#### AMPK

The AMPK complex regulates the cellular response to energy availability. AMPK is activated in response to a higher AMP/ATP ratio during periods of energy stress and is responsible for changing the oxidative metabolic phenotype, negatively regulating anabolic pathways and promoting catabolism[221]. In addition, AMPK participates in the inactivation of mTOR by working against the effects of Akt[229]. Several oncogenic mutations and signalling pathways surpass the AMPK checkpoint, which allows tumor cells to proliferate under abnormal nutrient conditions[241]. Consequently, many cancer

exhibit a loss of appropriate AMPK signalling, which contributes to a glycolytic phenotype.

## 4.1.3 BIOENERGETICS AND REDOX-COFACTORS

### 4.1.3.1 ENERGY PRODUCTION IN CANCER CELLS

The tumor cells have an altered energy metabolism compared to their tissue of origin. For years it has been assumed that the conventional view that improved glycolysis is induced by a decrease in oxidative phosphorylation. However, a renewed dynamic vision of tumor bioenergetics has recently been observed. Different types of cancer cells undergo different bioenergetics alterations, from exclusively glycolytic to mainly OXPHOS, depending on the use of the energy substrate according to the tumor stage, the oncogenic activation in series and the fluctuating conditions of the microenvironmental substrate[242]. In addition, contrary to traditional assumption, mitochondrial function is not affected and has a key role for the cancer cell. Although mitochondrial gene mutations have been described in cancer cells, it is now known that they do not inactive mitochondrial energy metabolism but alter the bioenergetics state and mitochondrial biosynthesis[138]. This bioenergetics and energy reduction process necessary to maintain the proliferation of tumor cells is discussed in this section.

#### CONTRIBUTION OF GLYCOLYSIS AND OXPHOS TO ATP SUPPLY

Cellular energetics in primarily supplied by either glycolysis or mitochondrial oxidative phosphorylation (OXPHOS). In terms of terms of ATP production, aerobic glycolysis is less efficient than the complete oxidative metabolism of glucose. The ATP yielded through OXPHOS is 18 times greater than that generated via glycolysis, but the rate of ATP production through glycolysis is 100 times faster than via OXPHOS[157]. Nevertheless, it has been demonstrated that oxidative phosphorylation supplies the majority of ATP for most proliferating cells. That comparison of several cell lines found that glycolysis ATP contributions are entirely dependent on the cell context and have a wide range (0.3%-64%) depending in cell/tissue type, thereby not supporting the hypothesis that cancer cells could exhibit aerobic glycolysis to generate ATP faster[166]. As commented before, it was observed that limiting glycolytic ATP production by inhibiting the activity of pyruvate kinase fails to prevent tumorigenesis, suggesting that the major role of high glycolysis ratio is not to supply ATP[243].

Thus, most cancer cells generate the majority of ATP through mitochondrial function, with the exception of tumors bearing mutations in enzymes involved in mitochondrial respiration. In these cells, nicotinamide adenine $NAD^+$ from NADH is highly required for high glycolytic flux maintenance. This NAD may be efficiently

generated from conversion of pyruvate into lactate by lactate dehydrogenase isoform A (LDHA). This metabolic conversion, maintaining ratio NADH/NAD+, makes glycolysis self-sufficient as long as elevated glucose uptake is possible[244].

### ALTERNATIVE ENERGY SUBSTRATES FOR ATP SYNTHESIS PATHWAYS IN CANCER CELLS

The importance of cancer cells maintaining their ATP/ADP ratio to maintain viability in poor nutrient and oxygen environments has been reported. Consequently, it has been observed that the cancer cells exhibit metabolic flexibility thanks to multiple possible entries in the TCA cycle, which allows an adequate response to the fuels available in the changing microenvironment during the evolution of the tumor. In this way, in addition to pyruvate derived from glycolysis, fatty acids, amino acids and ketone bodies can supply substrates to the TCA cycle to maintain mitochondrial ATP production. On one side, the decomposition of fatty acids in mitochondria generates acetyl-CoA and the reducing equivalents NADH and $FADH_2$, which ETC uses to produces ATP. Glutamine can generate glutamate and, subsequently, α-KG to feed the TCA cycle by glutaminolysis[245]. In addition, branched-chain amino acids isoleucine, valine and leucine can be converted to acetyl-CoA and other organic molecules that also enter the TCA cycle[246]. On the other hand, ketone bodies prevent cytoplasmic glycolysis and enter directly into the mitochondria where they are oxidized to acetyl-CoA, which contributes to the production of ATP[247].

### 4.1.3.2 NAD(H) AND NADP(H): THE UNIVERSAL REDOX-COFACTOR

Energy transduction through catabolic pathways and also biosynthetic processes depend on the ability to carry redox equivalents. The pyridine nucleotides NAD(H) and NADP(H) play fundamental roles in the redox metabolic reactions, not only serve as electron acceptors in the decomposition of catabolic substrates but also provide the cell reducing power necessary in the reactions energy-conserving redox. They can accept electrons when they are present in their oxidized state ($NAD^+$ and $NADP^+$) or donate electrons from their reduced state (NADH and NADPH). The relative abundance of the oxidized and reduced forms of these cofactors is also an important regulator of metabolic activity[244].

Both nicotinamide enzymes act as coenzymes of dehydrogenases. Dehydrogenases linked to NAD are involved in the oxidative pathways of metabolism, such as glycolysis, the TCA cycle and the mitochondrial respiratory chain. On the other hand dehydrogenases linked to NADP are involved in reductive biosynthetic reactions, such as the synthesis of fatty acids and the synthesis of cholesterol. In addition, coenzyme flavin adenine dinucleotide (FAD) also linked to dehydrogenase and β–oxidation of fatty acids by acetyl-CoA dehydrogenase.

## MOVEMENT OF REDUCING EQUIVALENTS: CELLULAR SHUTTLE SYSTEMS

Due to the internal mitochondrial membrane is very impermeable to $NAD^+$ and NADH, the NADH generated by glycolysis depends in the indirect transfer of reducing equivalents to the mitochondria through special shuttle systems. Such shuttles involve the movement of oxidizable material between subcellular compartments made by mechanisms based on antiporters. Two shuttle systems of this type have been described that can lead to the transport of cytoplasmic reduction equivalent to the mitochondria: shuttle of malate/aspartate and shuttle glycerol/phosphate[248].

- **Malate/Aspartate shuttle**

In the shuttle malate/aspartate (Figure 4.1.8A), the reducing equivalents of cytosolic NADH are first transferred to cytosolic oxaloacetate to produce malate by cytosolic malate dehydrogenase, and in the process, $NAD^+$ is generated from NADH, eliminating the cytosolic $NADH/NAD^+$ imbalance that results from glycolysis. Malate transported through the inner membrane by an anti-carrier mechanism coupled to the mitochondrial export of α-KG to cytosol. Upon entering the mitochondria, mitochondrial malate dehydrogenase converts malate into back OAA. In this reaction, the reducing equivalents transported by malate are then transferred to mitochondrial $NAD^+$ generating NADH. Through a transamination reaction, OAA is converted to aspartate with the nitrogen glutamate donor converted back to α-KG, and then transported to cytosolic side in exchange for cytosolic glutamate via an amino acid antiporter. In the cytosol, a reversal of aspartate aminotransferase reaction, results in oxaloacetate from aspartate, and simultaneously converts the cytosolic GLU to α-KG, thus completing the shuttle system. The redox imbalance of glycolysis is satisfied with the conversion of NADH to $NAD^+$ in the cytosol and the NADH generated in the mitochondria enter the electron transport system to generate more ATP[248].

The shuttle malate/aspartate is active in the neoplastic cells of several types of tumors[249, 250]. In fact, it was shown that about one-third of the respiratory ATP to be generated by electron flow originating from cytosolic NADH via the malate-aspartate shuttle[251]. In addition, malate dehydrogenase and aspartate aminotransferase have been highlighted as the key enzymes required for this shuttle system in cancer cells.

On the other hand, malate dehydrogenase (MDH) represents a key binding enzyme between mitochondrial and cytosolic groups of metabolic intermediates. This is the case of the oxidation of glutamine which generates several intermediates of the TCA cycle that can be transferred from the mitochondrial matrix to the cytoplasm that involves the conversion to and from malate[192]. In addition, elevated MDH expression has been observed in prostate cancer cell lines compared to benign prostatic epithelial cells and their metabolic inefficiency induced by inactivation, decreasing cell proliferation and increasing drug sensitivity[252]. In addition, MDH inhibitors that have

shown strong antitumor activity are being tested to mediate drug resistance of cancer cells[253, 254].
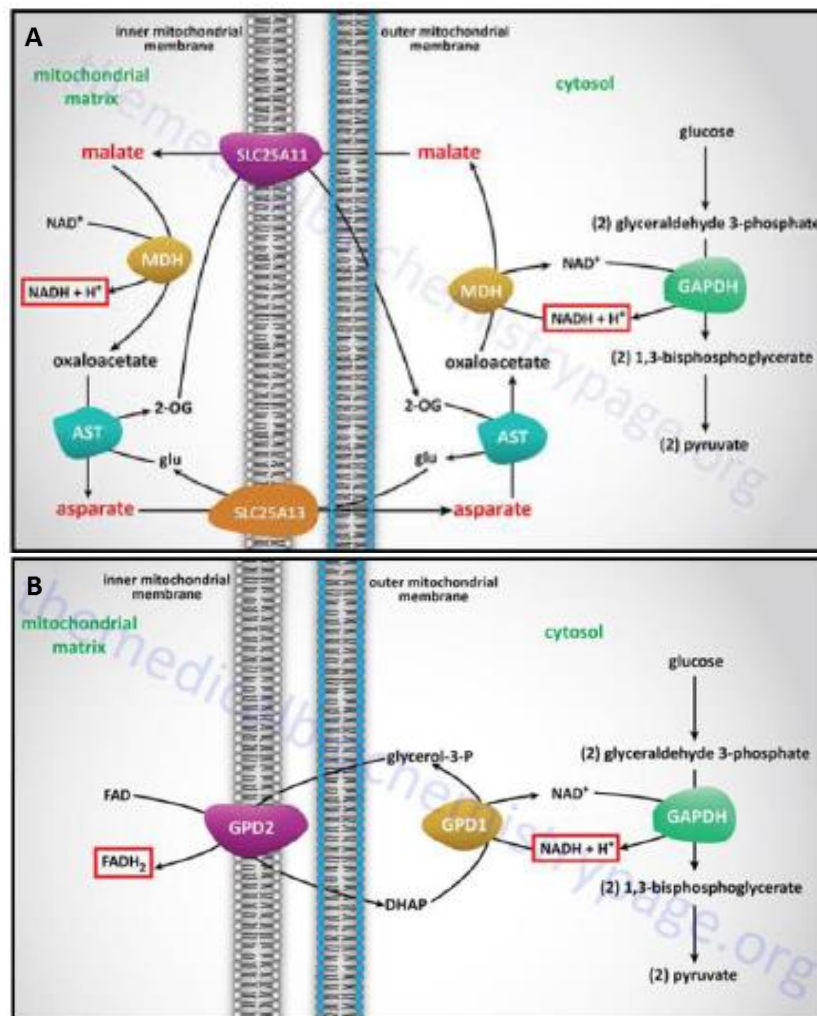


Figure 4.1.8. Shuttle mechanism for cytoplasmic NADH. The malate-aspartate shuttle (A) produces NADH in the matrix for entry into the ETC at NADH-Q reductase. The glycerol phosphate shuttle (B) produces FADH$_2$ in the mitochondrial inner membrane so that it enters the ETC at complex II by reducing coenzyme Q.

On the other hand, transamination reactions are increasingly important in tumor metabolism because studies of transaminases inhibition by gene silencing or use of aminooxyacetate acid (AOA) have shown cytotoxic effect in certain cancer cell lines[228, 255, 256]. In recent years, aspartate aminotransferase has become a critical enzyme for the reprogramming of tumor pathways. A strong dependence of GOT transaminases has been reported for the metabolism of the glutamine carbon skeleton in PDAC[231]. Therefore, glutamine metabolism reprogrammed through GOT1 activation mediated by kras and repression GLUD1, drives the flow of glutamine through the aspartate aminotransferase pathway in pancreatic cancer cells, decoupling canonical

malate/aspartate shuttle from TCA reactions[255]. In addition, a synthetic lethal interaction between the loss of GOT1 and the ETC dysfunction has recently been proposed. This lethality is generated by the deactivated aspartate biosynthesis since after the inhibition of ETC the cells use glutamine reducing carboxylation to feed the synthesis of compensatory aspartate through a route requires GOT1[257]. The activity of the shuttle system malate/aspartate becomes essential in the presence of an excess of cytosolic NADH that is not efficiently eliminated when the respiratory chain is altered. In addition, from these findings, the main role of aspartate biosynthesis in tumor metabolism began to emerge.

- **Glycerol phosphate shuttle**

This shuttle is a secondary mechanism for the electrons transport from cytosolic NADH to mitochondrial carriers of the OXPHOS pathway. A similar concept exists with the glycerol phosphate shuttle in which glycerol-3-phosphate is transported to the mitochondria where it is reoxidized to dihydroxyacetone phosphate, regenerating $NAD^+$ from NADH in the cytosol and producing reducing equivalents for oxidative phosphorylation in form of $FADH_2$ [248] (Figure 4.1.8B).

Two enzymes are involved in this shuttle, cytosolic (GPD1) and mitochondrial glycerol-3-phosphate dehydrogenase (GPD2). It has been shown that GPD2 activity is elevated in several human prostate cancer cell lines compared to normal prostate epithelial cells, leading to ROS levels related to cancer progression[258]. In addition, inhibitors of mitochondrial GPD2 activity have shown antiproliferative effects on cancer cells[259].

## 4.1.4 ASPARTATE AND PYRUVATE AS KEY GROWTH FACTORS IN CELL PROLIFERATION

As noted above, in cancer cells, the importance of the shuttle malate/aspartate has been reported beyond the classical role of reducing the movement of equivalents for energy production. This importance lies in the fact that aspartate and pyruvate play a fundamental role in several metabolic pathways that are positively regulated in the metabolism of cancer. Therefore, both metabolites directly involved in the malate/aspartate transport system have become key metabolites related to tumor reprogramming.

### 4.1.4.1 ASPARTATE

It has been widely recognized that this non-essential amino acids contributes to the production of proteins and is one of the main precursors of the nucleotides that make up DNA. Within its classic role, in the process of cells proliferation the following key destination of aspartate has been remarkable:

The *de novo* purine nucleotide synthesis pathway, through a series of reactions using ATP, this route produces IMP, which represents a branch point for purine biosynthesis. This nucleotide can serve as a precursor for the synthesis of AMP and GMP. Aspartate is involved in the ATP-consuming synthesis of SAICAR from CAIR (Figure 4.1.5).

Purine nucleotide cycle, that amino group of aspartate is transferred to the nucleotide purine IMP to generate adenylosuccinate, which is broken down by the activity of lyase to generate fumarate and AMP. Fumarate performs the anaplerotic function of replenishing the TCA cycle by becoming oxaloacetate (Figure 4.1.5)

Biosynthesis of pyrimidine nucleotides. Carbamoyl phosphate derived from glutamine is condensed with aspartate in the cytosol in one of the steps of the synthesis of UMP by the trifunctional enzyme CAD (carbamoyl-phosphate synthetase 2, aspartate transcarbamoylase and dihydoorotat) (Figure 4.1.6).

Precursor of ornithine for the urea cycle. In the cytosol, aspartate can also serve as a substrate for arginiosuccinate synthase (ASS1) producing argiosuccinate to continue the urea cycle. It has been shown that the deficient of ASS1 in cancer increases the levels of cytosolic aspartate, which increases the activation of CAD and the synthesis of pyrimidines. The negative regulation of ASS1 is presented as a new mechanism that supports cancer proliferation, which shows a metabolic link between enzymes of the urea cycle and pyrimidine synthesis[260].

In recent years, a renewing role of aspartate in the reprogramming of tumor metabolism has emerged, centering it as a key regulator of the malate/aspartate shuttle[204, 257]. Aspartate biosynthesis has assumed a leadership role in tumor metabolism instead of aspartate consumption. These studies have revealed that the main function of respiration in cell proliferation is not the production of energy, but the production of aspartate. In addition, aspartate biosynthesis involves the coordination of compartmentalized mitochondrial and cytoplasmic transamination enzymes and mitochondrial transporters, members of the aforementioned malate/aspartate shuttle (Figure 4.1.9). After the inhibition of ETC, it was shown that the cells use this GOT1-dependent pathway to generate aspartate, which indicates that the loss of GOT1 has a synthetic lethal interaction with the ETC dysfunction. However, no complete compensation was observed for the loss of mitochondrial aspartate synthesis, which allowed other possible key pathways or metabolites involved[257]. This major role for mitochondrial respiration in cell proliferation has focused on providing access to electron receptors in support of aspartate synthesis[204]. Moreover, aspartate transaminases have been suggested as a promising target for cancer[231, 256]. On the other hand, it has been shown that not only is a functional TCA cycle key generate

aspartate, but a differential ability to use aspartate as anaplerotic sources can dictate the ability of cells to survive and grow in TCA cycle conditions interrupted[261].
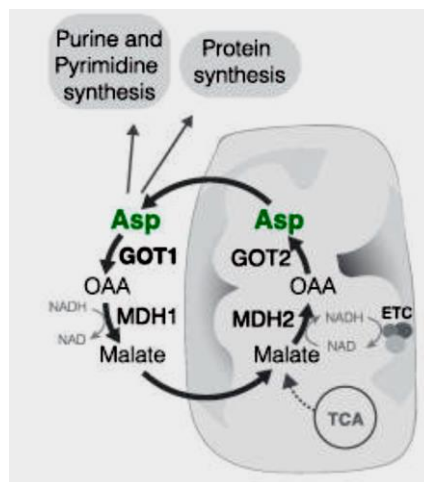


Figure 4.1.9. Schematic depicting the malate-aspartate shuttle. Normally, the malate-aspartate shuttle runs in the forward direction to transfer reducing equivalents across the mitochondrial membrane. GOT1 is part of the malate-aspartate shuttle and consumes aspartate to generate oxaloacetate (OAA). Aspartate produced by mitochondria is a precursor for protein and nucleotide biosynthesis[257].

Additionally, aspartate is becoming a diagnostic view. It has been shown that breast cancer is associated with significantly lower levels of plasma aspartate and, in addition, a higher level of aspartate has been found in breast cancer tissues than in adjacent non-tumor tissues. These findings have suggested that the reduced level of aspartate on blood of breast cancer patients is due to increased use of tumor aspartate and reduced circulating aspartate could be a key metabolic feature of human breast cancer[262].

#### 4.1.4.2 PYRUVATE

Pyruvate, a product oxidized by glucose, is the branch point molecule of glycolysis, being a key intersection in the network of metabolic pathways. In the presence of oxygen, pyruvate can be converted to acetyl coenzyme A and can be transported to the mitochondria to participate in the TCA cycle. Moreover, pyruvate can be converted to oxaoloacetate by an anaplerotic reaction and can be decomposed into carbon dioxide. Pyruvate can also be converted to carbohydrates through gluconeogenesis, fatty acids or energy through acetyl-CoA and the amino acid alanine[263].

If oxygen is not sufficiently available, the pyruvate from glycolysis thus becomes lactate in a reaction that regenerates $NAD^+$ from NADH, which is reduced during glycolysis. In cancer cell, this flow, observed even under aerobic conditions (Warburg effect), increases due to the need to replenish $NAD^+$ to maintain a high flow of glucose metabolism[264]. It is known that alterations of pyruvate metabolism observed in the

tumor (increased glycolysis and glutaminolysis and decreased oxidation of pyruvate) increase lactate and alanine yield[192]. It has been shown that the reduction of the pyruvate entry rate in the TCA cycle and the concurrent increase in lactate production is vital for the growth and survival or tumor[265]. Furthermore, the reduction in tumor growth is xenograft models has been observed when knocking down LDHA or inhibiting PDK1 (using RNAi or dichloroacetate)[164, 266], strongly supporting the fate of the game of pyruvate a determining role in the tumorigenic process.

However, new roles in tumor metabolic reprogramming have been associated with pyruvate. Evidence that pyruvate can regulate gene expression induced by hypoxia independently of hypoxia by stimulating HIF-1α accumulation have been reported[267]. Thus, through its ability to stabilize HIF-1α, pyruvate can inhibit the PDH complex in cancer cells enhancing Warburg metabolism and malignant phenotype, besides promoting resistance to anti-cancer therapies[263]. Moreover, the revolutionary role of pyruvate as an electron acceptor in deficient respiratory cells has recently been discovered[204, 257]. It has been observed that cells with defects in their electron transfer chains become dependent on pyruvate as an alternative electron acceptor for the synthesis of aspartate catalysed by GOT1. In addition, it has been observed the recovery of cellular aspartate levels by the addition of exogenous pyruvate, which increases the cellular $NAD^+$/NADH ratio by normalizing redox levels and restores proliferation in cells with severe ETC defect[268].

### 4.1.5 BREAST CANCER MODEL

Breast cancer remains to be one of most commonly diagnosed and death-related cancer in women in the world, resulting in an estimated 627000 new death in 2018, according world health organization data. The long-term survival of women with breast cancer depends on the stage of disease at the time of diagnosis: the 5-year survival rate is 99% for localized disease, 85% for regional stage and 25% for distant-stage tumor. Therefore, attempts to reduce breast cancer deaths have relied greatly on early cancer detection and treatment. The most widely used screening method for breast cancer mammography, with the sensitivity of the method ranging from 54% to 77%[269]. Despite the fact that image resolution continues to improve through the use of digital technology, tumors less than 5 mm are difficult to detect[270]. Other imaging methods such as thermography and magnetic resonance imaging are frequently used, but equally insensitive[271]. As the need for a screening test that would ideally be noninvasive highly sensitive and specific continues to increase, considerable efforts have been devoted to search for biomarkers for early diagnosis of breast cancer.

Metabolomics has recently become a new driving force in cancer biology research shown some promise in identifying key metabolic path ways in various types of

cancers[272-275]. Recent metabolomics studies of breast cancer have provided important metabolomics signatures in serum, plasma[276-278] and tissue[279] that differentiate breast cancer from healthy controls. However, the significantly differential pathways and metabolites identified are not consistent among these studies[277, 280, 281], primarily due to the inter-individual variability of patients and the different analytical and clinical protocols used in various studies. Moreover, none of the previous studies have evaluated selectivity of panels for breast cancer versus other malignancies[262].

The first human cell was established in a Baltimore laboratory over 50 years ago by George Gey. This cell line was HeLa,named after Henrietta Lacks, the lady from whom the cell line derived, who had cervical carcinoma. The first breast cancer cell line to be established was BT-20 in 1958[282]. It was another 20 years, however, before establishing breast cancer cell lines became more widespread, including the MD Anderson series[283] and what still remains the most commonly used breast cancer cell line in the world, MCF7 established in 1973 at the Michigan Cancer Foundation[284]. The popularity of MCF7 is largely due to its exquisite hormone sensitivity through expression of oestrogen receptor (ER), making it an ideal model to study hormone response[285]. Despite these early accomplishments, relatively few breast cancer cell lines have been established in the more recent past, mainly because of difficulties in culturing homogeneous populations without significant stromal contamination and, partly due to rigorous ethical regulations surrounding obtaining human tissue for research. Successes include the SUM series of 10 cell lines derived from either breast primary tumours, pleural effusions or various metastatic sites in individual patients[286]. These cell lines are now widely available through commercial cell banks.

### 4.1.5.1 BREAST CANCER HETEROGENEITY

Long before the advent of modern molecular profiling techniques, histopathologists recognised the breast cancer was heterogeneous through morphological observations. Classification was based on the following measures: histological type, tumour grade, lymph node status and the presence of predictive markers such as ER and, more recently, human epidermal growth factor receptor 2 (HER2). The development of molecular profiling using DNA microarrays proved this heterogeneity, demonstrating through gene expression profiling and the immune-histochemical expression of ERα, progesterone receptor (PR) and HER2 that breast cancer could be classified into at least five subtypes: luminal A, luminal B, HER2, basal and normal[287, 288]. Molecular characteristics of these subtypes are summarised in Table 4.1.1. Each subtype has different prognosis and treatment response[289]. Because ER is a therapeutic target, the luminal A and luminal B subtypes are amenable to hormone therapy. Similarly the HER2 group are potential candidates for trasuszumab therapy. In the current absence of expression of a recognised therapeutic target, basal tumours are difficult to treat, more biologically aggressive and often have a poor prognosis.

Because the basal phenotype is characterised by the lack of expression of ERα, PR and HER2, it is sometime referred to as triple-negative. Although there are similarities in the basal and triple-negative phenotypes, the terms are no strictly interchangeable; as outlined in a recent review, there is still no unifying definition for basal cancers and while triple-negative enriches for basal breast cancer, the phenotypes are not identical[290]. More recently the claudin-low subtype was described by interrogating established human and murine datasets[291]. Initially clustered with the basal subtype as a result of a lack of ERα, PR and HER2 expression and associated poor prognosis, these tumours were shown to be unique by the additional downregulation of claudin-3 and claudinin-4, low expression of the proliferation marker Ki67, enrichment for markers associated with the epithelial-mesenchymal transition and expression of features associated with mammary cancer stem cells (CSCs)[292].

Table 4.1.1. Molecular classification of breast carcinoma

| Classification | Inmunoprofile | Other characteristics | Example cell lines |
|---|---|---|---|
| Luminal A | $ER^+$, $PR^{+/-}$, $HER2^-$ | Ki67 low, endocrine responsive, often chemotherapy responsive | MCF7, T47D, SUM185 |
| Luminal B | $ER^+$, $PR^{+/-}$, $HER2^+$ | Ki67 high, usually endocrine responsive, variable to chemotherapy. $HER2^+$ are trastusumab responsive | BT474, ZR751 |
| Basal | $ER^-$, $PR^-$, $HER2^-$ | $EGFR^+$ and/or cytokeratin $5/6^+$, Ki67 high, endocrine nonresponsive, often chemotherapy responsive | MDA-MB-468, SUM190 |
| Claudin-low | $ER^-$, $PR^-$, $HER2^-$ | Ki67, E-cadherin, claudin-3, claudin-4 and claudin-7 low. Intermediate response to chemotherapy | BT549, MDA-MB-231, Hs578T |
| HER2 | $ER^-$, $PR^-$, $HER2^+$ | Ki67 high, trastusumab responsive, chemotherapy responsive | SKBR3, MDA-MB-453 |

## 4.2 MATERIALS AND METHODS

### 4.2.1 INSTRUMENTATION

#### 4.2.1.1. HOOD

Telstar Bio II Advance biosafety cabinet has been used to perform all the cell cultures and work with biological samples. The hood has a horizontal laminar flow system that maintains the necessary sterility conditions to work with biological samples such as cell cultures.

#### 4.2.1.2 CO$_2$ INCUBATOR

The Nuaire NU-5510E incubator has been used for optimal growth of cell culture. The incubator is equipped with $CO_2$, temperature and humidity controllers.

#### 4.2.1.3 LABORATORY WATER BATH

Memmert WNB 10 equipped with a temperature range 5 °C above ambient temperature to +95 °C, with additional boiling mode.

#### 4.2.1.4 INVERTED MICROSCOPE

The Olympus CKX53 has been used to perform cell counts.

#### 4.2.1.5 CENTRIFUGE

The Eppendorf 5810R equipped with a rotor A-4-62, refrigerated, and with adapters for 15/50 mL conical tubes has been used for routine cell cultures task and other experiments of this thesis.

#### 4.2.1.6 GLOMAX®-MULTI+ DETECTION SYSTEM

The GloMax®-Multi Detection System is equipped with Instinct® Software has been used for cell viability assays. It is an expandable, high performance, multimode reader for Luminescence, Fluorescence, Visible Absorbance and UV-Visible Absorbance. Different microwell plates (6, 12, 24, 96 and 384) can be used for high throughput analysis, providing a temperature range of 45 °C ± 0.75 °C. For this thesis, it was needed the fluorescence module, which light source is a wavelength matched LED. The detector is a PiN-photodiode, with a detection limit of 0.5 fmol/200 µL or 1 ppt of fluorescein in 96-well microplate.

#### 4.2.1.7 TECAN EVO 200 ROBOT

It is a versatile platform equipped with a robotic arm, a liquid handler with 8 independent channels, and a 96-channel arm with disposable tips. The instrument is currently capable of transferring samples and reagents in 1-384 well formats. The workstation includes a barcode reader, an incubator, a plate agitator and a microplate

reader (Tecan F200) that operates any UV absorbance, fluorescence or luminescence detection technology. The entire platform is contained within a laminar flow hood that allows working in a sterile environment.

### 4.2.1.8 OPERETTA HIGH-CONTENT IMAGING SYSTEM (PERKINELMER)

It is an automated fluorescent microscope for High Content Screening. Images are captured either in widefield mode or using a confocal spinning disk. The software Harmony (version 4.1) allows fully unsupervised automated image acquisition and autofocus for reliable high content imaging from slides to multiple plates and perform complex quantitative and multi-parametric data analysis. The system is equipped with a live cell chamber option to maintain environmental conditions (temperature, $CO_2$) and can perform a wide range of fluorescence-based kinetic and endpoint biological assays. The presence of Digital Phase contrast channel allows imaging and segmentation of cells that have not been fluorescently labelled. An integrated browser-based image analysis system (Columbus™ Image Date Storage and Analysis System, PerkinElmer) supports a wide range of file formats, allowing visualization of images, regardless of their origin.
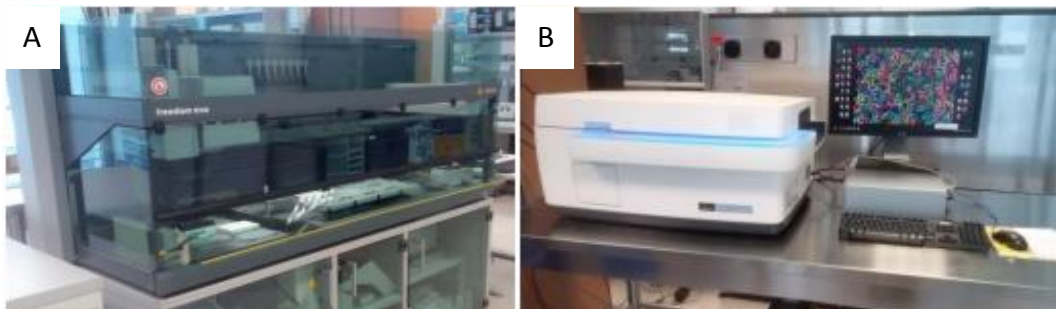


Figure 4.2.1. A) Tecan Evo 200 robot, and B) Operetta High-Content Images.

## 4.2.2 CELL CULTURE

To carry out this thesis, five breast cancer cell lines have been used to provide a representative subtype according to the current clinical classification, each cell line is classified within a different clinical subtype.

### 4.2.2.1 MCF7

The human breast cancer cell lines MCF7 was obtained from the American Type Culture Collection (ATCC; HTB-22). MCF7 belongs to the Luminal A classification group and has an immunological profile: $ER^+$, $PR^{+/-}$, $HER2^-$, corresponding the acronyms to estrogen receptor, progesterone receptor and human epidermal growth factor

receptor, respectively. Other remarkable features are: low expression of the cell proliferation marker (Ki67b), endocrine response and often chemotherapy responsive.

### 4.2.2.2 ZR751

The human breast cancer cell line ZR-75-1 was obtained from Leibniz-Institut DMSZ Deutsche Sammlung von Mikroorganismoen und Zellkulturen GmbH (DMSZ). This cell line is classified in the Luminal B group, and presents an immunological profile: $ER^+$, $PR^{+/-}$, $HER2^+$. Other notable characteristic are high Ki67 expression, endocrine response, chemotherapy variable, and response to anti-HER2 antibody Trastuzumab.

### 4.2.2.3 SKBR3

The human breast cancer cell line SKBR3 was obtained from the ATCC ( HTB-30). The classification for this cell line is defined as HER2 positive, and the inmunoprofile is: $ER^-$, $PR^-$ and $HER2^+$. SKBR3 also displays Ki67 high expression level, trastusumab responsive and chemotherapy responsive.

### 4.2.2.4 MDA-MB-231

The human breast cancer cell line MDA-MB-231 was obtained from the ATCC (CRM-HTB-26). This cell line is classified in the triple-negative group, specifically it is of the claudin-low type. The inmunoprofile is $ER^-$, $PR^-$ and $HER^-$. Other features of MDA-MB-231 are Ki67, E-cadherin, claudin-3, claudin-4 and claudin-7 low expression, and intermediate response to chemotherapy.

### 4.2.2.5 MDA-MB-468

The human breast cancer cell line MDA-MB-468 was obtained from the DSMZ. Like MDA-MB-231, the MDA-MB-468 cell line is classified in the triple-negative group, specifically in the basal subtype. The immune profile is triple negative for the expression of the hormone receptors: $ER^-$, $PR^-$ and $HER2^-$. MDA-MB-468 also presents other features: $EGRF^+$ and/or cytokeratin $5/6^+$, ki67 high, endocrine nonresponsive and often chemotherapy responsive.
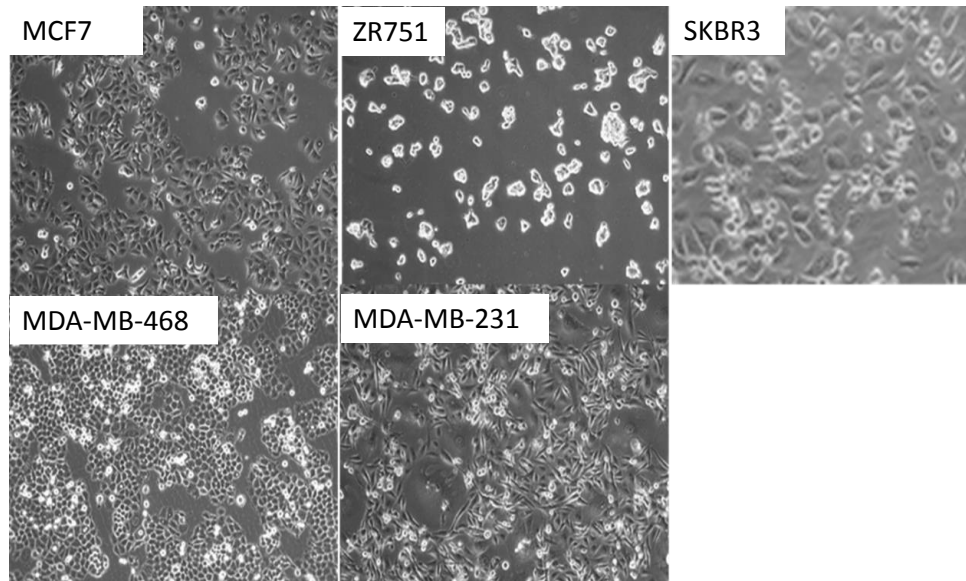
Figure 4.2.2. Light microscopy images from breast cancer cell lines (See Table 4.1.1 for features of each cell line).

### 4.2.2.6 NON-TRANSFORMED CELL LINES

The non-tumour cell lines MRC5 and MCF10A were used to compare the result of the effect produced by anti-tumour drugs between tumour and non-tumour cell cells.

- **MCR5**: Comes from the CIBIO cell bank, University of Trento (Italy). MCR5 is a human fibroblast cell line.
- **MCF10A**: Comes from the CIBIO cell bank, University of Trento (Italy). MCF10A is a human breast non-tumorogenic epithelial cell line.

## 4.2.3 REAGENTS

- Calcein-AM. Life Technologies.

- Celltiter Blue for cell viability metabolic activity assay. Promega.

- Celltiter Glo for cell viability metabolic activity assay . Promega.

- Dimethyl Sulfoxide (DMSO). Sigma-Aldrich.

- Phosphate Buffered saline (PBS). Gibco.

- Cell culture media:

  - DMEM (Dulbeco Modified Eagle Medium). Gibco.
  - MCoy's 5A. Sigma-Aldrich.

- MEM (Minimal Essential Media). Sigma-Aldrich.
- RPMI 1640. Sigma-Aldrich.

- Hoechst 33342. Life Technologies.

- Enzyme and chemical metabolic inhibitors:

- Aminooxyacetate. Sigma-Aldrich.
- Dichloroacetate. Sigma-Aldrich.
- Epigallocatechin gallate. Sigma-Aldrich.
- Phenformin hydrochloride. Sigma-Aldrich.
- Tiophene. Sigma- Aldrich.

- Mitochondrial membrane potential and organelle fluorescence microscopy tracking analysis probes:

- JC1 dye (tetraethylbenzimidazolylcarbocyanine iodide). Abcam
- Mitotracker Deep Red. Invitrogen

- Cell culture reagents:

- Asp (Aspartate). Sigma-Aldrich.
- FBS (Fetal Bovine serum). Gibco.
- Glutamax I. Gibco.
- NEAA (Non-essential amino acids). Sigma-Aldrich.
- P/S (Penicilin/Streptomicin). Gibco.
- NaPyr (Sodium pyruvate). Gibco.
- Tripsin-EDTA. Gibco.

## 4.2.4 MATERIALS

- Cell culture treated 6 well plastic plates. Corning.

- Cellcarrier-384 Ultra plate high throughput screening. PerkinElmer.

- Coverslip ⌀ 25mm

- Flask T75: Cell culture specific plastic. Sigma.

- Harmony software. PerkinElmer.

- Microplates for Fluorescence-based assays, 96W. Thermo Fisher.

## 4.2.5 EXPERIMENTAL METHODS

### 4.2.5.1 CELL CULTURE

The breast cancer cell lines were subcultured every 72-96h. The culture medium was refreshed the day before of the cell subculture. Cells were routinely plated in T75 flasks.

The MCF7 cell line was cultured with MEM media for optimal growth. MEM media was reconstituted with: 10% FBS, 1% Glutamax, 1% NEAA and 1%. Cells were subcultured with a density of $1.35x10^6$ for T75 flask for 72h, and $1.1x10^6$ for 96h.

The SKBR3 cell line was cultured with McCoy's 5A media for optimal growth. The media was reconstituted with: 10% FBS, 1% Glutamax and 1%P/S to be reconstituted. The cells were subcultured at $1.35x10^6$ for T75 flask for 72h, and $1.1x10^6$ for T75 flask 96h.

The MDA-MD-231 and MDA-MD-468 cell lines were cultured with DMEM. DMEM media was reconstituted with: 10% FBS and 1% P/S. MDA-MD-231 cells were subcultured at $1.35x10^6$ for T75 flask for 72h, and $1.1x10^6$ for 96h. MDA-MD-468 cells were subcultured at $1.2x10^6$ for T75 flask for 72h, and $9x10^5$ for T75 flask for 96h.

The ZR751 cell line was maintained in culture with a slightly different routine. This cell line has a longer doubling time than the other four lines. Accordingly, ZR751 cells were subcultured once a week, although the culture medium was changed twice between each seeding. RPMI 1640 media was used for optimal growth reconstituted with: 10% FBS, 1% Glutamax , 1% NaPyr and 1% P/S. ZR751 cells were subcultured with a density of $1.8x10^6$ for T75 flask.

The MCR5 cell line was cultured with DMEM culture medium. DMEM was reconstituted with 15% FBS, 1% NEAA, 1% glutamine and 1% P/S. For the experiments with 384 well plates 3000 cells were seeded.

The MCF10A cell line was cultured with DMEM culture medium. For the optimal growth of the cell, the culture medium was reconstituted with 12.5% Horse serum, 15 mM HEPES, 10 µL/mL insulin, 20 ng/mL EGF and 0.5 µg/mL hydrocortisone. For the experiments with 384 well plates 1000-2000 cells were seeded.

### 4.2.5.2 CELL VIABILITY ASSAYS WITH METABOLIC INHIBITORS

These experiments were designed to test the impact on cell viability using inhibitors for selected metabolic targets. The aim was to test whether the breast cancer subtypes represented by the five cell lines display a differential or similar response to key metabolic targets. The compounds tested and their metabolic targets were:

- Aminooxyacetate (AOA), pan inhibitor of transaminases.
- Epigallocatechin gallate (EGCG), inhibitor of glutamate dehydrogenase.
- Phenformin hydrochloride, inhibitor of the mitochondrial respiration complex I.
- Dichloroacetate (DCA), inhibitor of pyriuvate dehydrogenase kinase (thus indirect activator of pyruvate dehydrogenase).
- Dichloroacetate modified with thiophene (DCA-1-TP, DCA-2-TP).
- Dichloroacetate modified with thiazol (DCA-1-TZ1, DCA-1-TZ2).
- Dichloroacetate modified with benzothiophene (DCA-1-BTP).

The experiments were performed in real time for cells cultured in black 96 well plates for further fluorescence analysis. This approach resulted in an optimized, high throughput assay, providing high sensitivity and reproducibility. The Celltiter Blue cell viability assay (Promega) was chosen to test the impact of the selected drugs on cell viability. The Celltiter Blue is an assay based on the ability of living cells to convert resazurin (a redox dye) into resorufin (a fluorescent product). When the cells die, they lose the capable to carry out this reaction. Thus, cell viability can be quantified by fluorescence in real time for living cells. The experiments were designed as following:

### PLATE LAYOUT:

The design for the plate layout is crucial to achieve a good performance and high reproducibility in these experiments. Black fluorescence 96w plates were used to perform large sampling experimental points. The design of the plate layout is sketched in Figure 4.2.3B. All the wells around the edge of the plate were filled with PBS to avoid sample volume lost by well content evaporation due to the temperature of the incubator. For the optimized design, several wells are used for blank points only with fresh culture medium, followed by the untreated cell controls in the first row of the plate. The rest of the wells were used for the experimental treatments, usually with five replicates.

| PBS | PBS | PBS | PBS | PBS | PBS | PBS | PBS | PBS | PBS | PBS | PBS |
|-----|-----|-----|-----|-----|-----|-----|-----|-----|-----|-----|-----|
| PBS | Blank | Blank | Contr1 | Contr1 | Contr1 | Contr1 | Contr2 | Contr2 | Contr2 | Contr2 | PBS |
| PBS | Treat1 | Treat1 | Treat1 | Treat1 | Treat1 | Treat2 | Treat2 | Treat2 | Treat2 | Treat2 | PBS |
| PBS | Treat3 | Treat3 | Treat3 | Treat3 | Treat3 | Treat4 | Treat4 | Treat4 | Treat4 | Treat4 | PBS |
| PBS | Treat5 | Treat5 | Treat5 | Treat5 | Treat5 | Treat6 | Treat6 | Treat6 | Treat6 | Treat6 | PBS |
| PBS | Treat7 | Treat7 | Treat7 | Treat7 | Treat7 | Treat8 | Treat8 | Treat8 | Treat8 | Treat8 | PBS |
| PBS | Treat9 | Treat9 | Treat9 | Treat9 | Treat9 | Treat10 | Treat10 | Treat10 | Treat10 | Treat10 | PBS |
| PBS | PBS | PBS | PBS | PBS | PBS | PBS | PBS | PBS | PBS | PBS | PBS |

Figure 4.2.3. A) Black 96 well plates for fluorescence assays. B) Example of a typical experimental design.

### Cell culture protocol for the experimental drug treatments:

Cells were seeded in the wells with the corresponding culture medium. The cell line MCF7 was seeded at density $1x10^4$ and the cell lines ZR751, SKBR3, M231 and M468 were seeded at density $8x10^3$ in 100 µL of culture medium. After plating, the inhibitors or drugs were added and the plate was maintained for 96h in the incubator at 37°C.

### Celltiter assay and development method:

After 96h treatments, 20 µL of Celltiter Blue reagent were added per 100 µL of culture medium to each well, then the cells were incubated for 20 min at 37 °C, and then the fluorescence was measured in a GloMax®-Multi+ Detection System (Promega).

Figure 4.2.4. GloMax®-Multi+ Detection System.

### ANALYSIS OF THE RESULTS:

Average of all replicas was calculated, and then the value of the blank was subtracted from the average. The data were expressed as percentages relative to control samples, being assigned the control values as 100%.

### 4.2.5.3 HIGH THROUGHPUT MULTI-DRUG EXPERIMENTS

These experiments were performed during a stay in the Centre of Integrative Biology (CIBIO), Trento (Italy). Despite of the recent expectations about the anticancer therapeutic properties of DCA, its potential is questioned yet, mainly due to the high concentration/dose required to achieve satisfactory outputs, both in vitro and in vivo experiments. Thus, we aimed to test three DCA derivative compounds: two DCA-thiazol complexes and one DCA-benzothiophene complex (see structures in Figure 4.4.6). The goal was to answer whether these DCA derivatives displayed a higher impact on breast cancer cell viability at lower concentrations than traditional DCA treatments.

The experiments were designed in a large scale, high throughput approach; to test simultaneously all the breast cancer cell lines selected with multiple drug treatment points. For this purpose, we took advantage by using the high throughput 384w plate instruments available in CIBIO.

### PLATE LAYOUT:

384-well plates were used. Likewise in the former Celltiter viability experiments with inhibitors, the optimization of the plate layout was very important (Figure 4.2.5)

| Cell Line | 1 | | 2 | | 3 | | 4 | | 5 | | 6 | | 7 | | 8 | | 9 | | 10 | | 11 | | 12 | |
|---|---|---|---|---|---|---|---|---|---|---|---|---|---|---|---|---|---|---|---|---|---|---|---|---|
| | 1 | 2 | 3 | 4 | 5 | 6 | 7 | 8 | 9 | 10 | 11 | 12 | 13 | 14 | 15 | 16 | 17 | 18 | 19 | 20 | 21 | 22 | 23 | 24 |
| A | | | | | | | | | | | | | | | | | | | | | | | | |
| B | | | | | | | | | | | | | | | | | | | | | | | | |
| C | | | MCF7 | M231 | MCF7 | M231 | MCF7 | M231 | MCF7 | M231 | MCF7 | M231 | MCF7 | M231 | MCF7 | M231 | MCF7 | M231 | MCF7 | M231 | MCF7 | M231 | | |
| D | | | MCF7 | M231 | MCF7 | M231 | MCF7 | M231 | MCF7 | M231 | MCF7 | M231 | MCF7 | M231 | MCF7 | M231 | MCF7 | M231 | MCF7 | M231 | MCF7 | M231 | | |
| E | | | MCF7 | M231 | MCF7 | M231 | MCF7 | M231 | MCF7 | M231 | MCF7 | M231 | MCF7 | M231 | MCF7 | M231 | MCF7 | M231 | MCF7 | M231 | MCF7 | M231 | | |
| F | | | MCF7 | M231 | MCF7 | M231 | MCF7 | M231 | MCF7 | M231 | MCF7 | M231 | MCF7 | M231 | MCF7 | M231 | MCF7 | M231 | MCF7 | M231 | MCF7 | M231 | | |
| G | | | MCF7 | M231 | MCF7 | M231 | MCF7 | M231 | MCF7 | M231 | MCF7 | M231 | MCF7 | M231 | MCF7 | M231 | MCF7 | M231 | MCF7 | M231 | MCF7 | M231 | | |
| H | | | MCF7 | M231 | MCF7 | M231 | MCF7 | M231 | MCF7 | M231 | MCF7 | M231 | MCF7 | M231 | MCF7 | M231 | MCF7 | M231 | MCF7 | M231 | MCF7 | M231 | | |
| I | | | MCF7 | M231 | MCF7 | M231 | MCF7 | M231 | MCF7 | M231 | MCF7 | M231 | MCF7 | M231 | MCF7 | M231 | MCF7 | M231 | MCF7 | M231 | MCF7 | M231 | | |
| J | | | MCF7 | M231 | MCF7 | M231 | MCF7 | M231 | MCF7 | M231 | MCF7 | M231 | MCF7 | M231 | MCF7 | M231 | MCF7 | M231 | MCF7 | M231 | MCF7 | M231 | | |
| K | | | MCF7 | M231 | MCF7 | M231 | MCF7 | M231 | MCF7 | M231 | MCF7 | M231 | MCF7 | M231 | MCF7 | M231 | MCF7 | M231 | MCF7 | M231 | MCF7 | M231 | | |
| L | | | MCF7 | M231 | MCF7 | M231 | MCF7 | M231 | MCF7 | M231 | MCF7 | M231 | MCF7 | M231 | MCF7 | M231 | MCF7 | M231 | MCF7 | M231 | MCF7 | M231 | | |
| M | | | MCF7 | M231 | MCF7 | M231 | MCF7 | M231 | MCF7 | M231 | MCF7 | M231 | MCF7 | M231 | MCF7 | M231 | MCF7 | M231 | MCF7 | M231 | MCF7 | M231 | | |
| N | | | MCF7 | M231 | MCF7 | M231 | MCF7 | M231 | MCF7 | M231 | MCF7 | M231 | MCF7 | M231 | MCF7 | M231 | MCF7 | M231 | MCF7 | M231 | MCF7 | M231 | | |
| O | | | | | | | | | | | | | | | | | | | | | | | | |
| P | | | | | | | | | | | | | | | | | | | | | | | | |

| Compound | 1 | | 2 | | 3 | | 4 | | 5 | | 6 | | 7 | | 8 | | 9 | | 10 | | 11 | | 12 | |
|---|---|---|---|---|---|---|---|---|---|---|---|---|---|---|---|---|---|---|---|---|---|---|---|---|
| | 1 | 2 | 3 | 4 | 5 | 6 | 7 | 8 | 9 | 10 | 11 | 12 | 13 | 14 | 15 | 16 | 17 | 18 | 19 | 20 | 21 | 22 | 23 | 24 |
| A | PBS | PBS | PBS | PBS | PBS | PBS | PBS | PBS | PBS | PBS | PBS | PBS | PBS | PBS | PBS | PBS | PBS | PBS | PBS | PBS | PBS | PBS | PBS | PBS |
| B | PBS | PBS | PBS | PBS | PBS | PBS | PBS | PBS | PBS | PBS | PBS | PBS | PBS | PBS | PBS | PBS | PBS | PBS | PBS | PBS | PBS | PBS | PBS | PBS |
| C | PBS | PBS | PPF75 | PPF75 | PPF78 | PPF78 | PPF81 | PPF81 | PPF82 | PPF82 | PPF84 | PPF84 | F75C2 | F75C2 | F78A | F78A | F81A | F81A | F82A | F82A | F84A | F84A | PBS | PBS |
| D | PBS | PBS | PPF75 | PPF75 | PPF78 | PPF78 | PPF81 | PPF81 | PPF82 | PPF82 | PPF84 | PPF84 | F75C2 | F75C2 | F78A | F78A | F81A | F81A | F82A | F82A | F84A | F84A | PBS | PBS |
| E | PBS | PBS | PPF75 | PPF75 | PPF78 | PPF78 | PPF81 | PPF81 | PPF82 | PPF82 | PPF84 | PPF84 | F75C2 | F75C2 | F78A | F78A | F81A | F81A | F82A | F82A | F84A | F84A | PBS | PBS |
| F | PBS | PBS | PPF75 | PPF75 | PPF78 | PPF78 | PPF81 | PPF81 | PPF82 | PPF82 | PPF84 | PPF84 | F75C2 | F75C2 | F78A | F78A | F81A | F81A | F82A | F82A | F84A | F84A | PBS | PBS |
| G | PBS | PBS | PPF75 | PPF75 | PPF78 | PPF78 | PPF81 | PPF81 | PPF82 | PPF82 | PPF84 | PPF84 | F75C2 | F75C2 | F78A | F78A | F81A | F81A | F82A | F82A | F84A | F84A | PBS | PBS |
| H | PBS | PBS | PPF75 | PPF75 | PPF78 | PPF78 | PPF81 | PPF81 | PPF82 | PPF82 | PPF84 | PPF84 | F75C2 | F75C2 | F78A | F78A | F81A | F81A | F82A | F82A | F84A | F84A | PBS | PBS |
| I | PBS | PBS | PPF75 | PPF75 | PPF78 | PPF78 | PPF81 | PPF81 | PPF82 | PPF82 | PPF84 | PPF84 | F75C2 | F75C2 | F78A | F78A | F81A | F81A | F82A | F82A | F84A | F84A | PBS | PBS |
| J | PBS | PBS | PPF75 | PPF75 | PPF78 | PPF78 | PPF81 | PPF81 | PPF82 | PPF82 | PPF84 | PPF84 | F75C2 | F75C2 | F78A | F78A | F81A | F81A | F82A | F82A | F84A | F84A | PBS | PBS |
| K | PBS | PBS | PPF75 | PPF75 | PPF78 | PPF78 | PPF81 | PPF81 | PPF82 | PPF82 | PPF84 | PPF84 | F75C2 | F75C2 | F78A | F78A | F81A | F81A | F82A | F82A | F84A | F84A | PBS | PBS |
| L | PBS | PBS | PPF75 | PPF75 | PPF78 | PPF78 | PPF81 | PPF81 | PPF82 | PPF82 | PPF84 | PPF84 | F75C2 | F75C2 | F78A | F78A | F81A | F81A | F82A | F82A | F84A | F84A | PBS | PBS |
| M | PBS | PBS | PPF75 | PPF75 | PPF78 | PPF78 | PPF81 | PPF81 | PPF82 | PPF82 | PPF84 | PPF84 | F75C2 | F75C2 | F78A | F78A | F81A | F81A | F82A | F82A | F84A | F84A | PBS | PBS |
| N | PBS | PBS | PPF75 | PPF75 | PPF78 | PPF78 | PPF81 | PPF81 | PPF82 | PPF82 | PPF84 | PPF84 | F75C2 | F75C2 | F78A | F78A | F81A | F81A | F82A | F82A | F84A | F84A | PBS | PBS |
| O | PBS | PBS | PBS | PBS | PBS | PBS | PBS | PBS | PBS | PBS | PBS | PBS | PBS | PBS | PBS | PBS | PBS | PBS | PBS | PBS | PBS | PBS | PBS | PBS |
| P | PBS | PBS | PBS | PBS | PBS | PBS | PBS | PBS | PBS | PBS | PBS | PBS | PBS | PBS | PBS | PBS | PBS | PBS | PBS | PBS | PBS | PBS | PBS | PBS |

Figure 4.2.5. High throughput 384w plate layout for two cell lines.

### CELL CULTURE PROTOCOL:

The cell lines were subcultured in the 384w plates with 50 µL of media at a cell number of $4 \times 10^4$ cells/well for MCF7 and MDA-MD231, $2 \times 10^4$ cells/well for MDA-MD-468, $6 \times 10^4$ cells/well for SKBR3 and ZR751, $3 \times 10^4$ cell/well for MCR5 and $1\text{-}2 \times 10^4$ cells/well for MCF10A. The DCA derivatives were added in the culture media at seeding. Cells were incubated for 72h and subsequently the cell viability assay was performed.

### CELL VIABILITY ASSAY:

The operetta high content imaging system was used for high throughput analysis of cell viability by combination of Calcein-AM and Hoechst 33342 assays. Cell culture media were supplemented with 1 µg/mL Calcein-AM and 1 µg/mL Hoechst 33342 for 1 h. Calcein-AM is a non-fluorescent dye. In living cells, Calcein-AM non fluorescent is transformed in a green fluorescent product, after the hydrolysis of acetoxymethyl ester through intracellular esterases. Hoechst 33342 is a dye that penetrates into the cell and emits a blue fluorescence when it binds to dsDNA. This dye is commonly used to find apoptotic cells. The images were collected with the Operetta high content imaging system using a 10x objective. The Operetta identifies and counts the living cells.

### ATP PRODUCTION ASSAY:

In order to check the speed at which antitumor drugs had an effect, a test was carried out to measure the ability of cells to produce ATP. Celltiter Glo kit was used for this purpose. Celltiter Glo is a method based on luminescence, in which the metabolic activity of the cells present in a cell culture is determined through the quantification of

ATP. Low levels of ATP production are directly related to low metabolic activity. Loss of metabolic activity means loss of cell viability. Therefore, for these experiments, the cells were seeded as previously explained. After 24h, the antitumoral drugs were added into the well and the plates were incubated for 6h. After this incubation, 50 μL of Celltiter Glo was added per 50 μL of culture media in each well and 10 minutes were waited before to measure the luminescence.

### DATA ANALYSIS:

The Harmony software was used for the analysis of the images obtained by the Operetta system. By using the dyes described above, it was possible to analyse simultaneously in the cells the green fluorescence signal from the Calcein-derivative, and the segmented individual nuclei (by Hoechst 33342). Thus, the number of living cells was automatically counted, and then the percentage of cellular viability of each treatment was calculated relative to the values of untreated control cells.

## 4.3 METABOLIC PROFILING OF BREAST CANCER CELL LINES

Altered metabolism in breast cancer is well recognised. Until now, there is a clinical classification based on histological type, tumor grade, lymph node status and the immune profile. Molecular characteristics of these subtypes are summarized in Table 4.3.1. We aimed to answer whether the different subtypes of breast cancer cells display differential metabolic phenotypes, so-called metabophenotypes. This study could contribute to gain knowledge about metabolic key features in breast cancer and its functional relationship with molecular and genetic features, and, in addition, could open a pave for novel clinical classification, finding potential therapeutic antimetabolic targets, and diagnostic approaches.

Table 4.3.1. Clinical classification of breast cancer[148]

| Cell lines | Inmunoprofile | Classification |
|---|---|---|
| MCF7 | $ER^+$, $PR^{+/-}$, $HER2^-$ | Luminal A |
| ZR751 | $ER^+$, $PR^{+/-}HER2^+$ | Luminal B |
| MDA-MB-468 | $ER^-$, $PR^-$, $HER2^-$ | Basal |
| MDA-MB-231 | $ER^-$, $PR^-$, $HER2^-$ | Claudin-low |
| SKBR3 | $ER^-$, $PR^-$, $HER2^+$ | HER2 |

A representative cell line for each clinical subtype was selected for subsequent metabolic studies: MCF7, ZR751, MDA-MB-468, MDA-MB-231, and SKBR3.

### 4.3.1 LOOKING FOR THE TARGETS FOR METABOLIC CLASSIFICATION

First of all, it was necessary to identify what could be the best metabolic target to analyse whether our cell models show different metabophenotypes. Two metabolites which have to be essential for the cells were chosen: pyruvate and aspartate. These two metabolites are critical for the redox balance of the cells[257,293]. In fact, recent data from other laboratories and from our lab, have demonstrated that most cancer cell types can display a strong dependence for these metabolites. Therefore, breast cancer cells must be or not addictive to pyruvate, aspartate or both; thus these two metabolites are good targets to define breast cancer cell metabophenotypes.

A good approach to answer whether the selected cell lines were addictive/sensitive to pyruvate and aspartate was to target the aspartate/oxaloacetate transamination by using the pan inhibitor of aspartate transaminases aminooxyacetate (AOA) (Figure 4.3.1). Aspartate can be converted into oxaloacetate, and the oxaloacetate can be reduced to malate; thus consuming NADH and providing $NAD^+$.



Figure 4.3.1. Scheme of AOA inhibitory action.

## 4.3.2 BREAST CANCER CELL LINES DISPLAY DIFFERENT METABOPHENOTYPES BASED ON PYRUVATE AND ASPARTATE DEPENDENCE THROUGH TRANSAMINASE INHIBITION BY AOA

To perform this study, the selected cell lines were seeded in 96w plates and 1 mM of AOA was added in each well. The plate was incubated for 96h at 37 °C (see section 4.2.4.3 for further details).
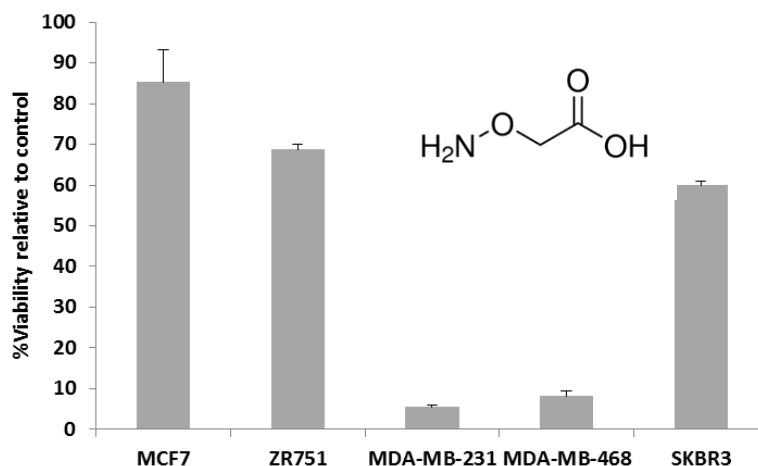


Figure 4.3.2. Breast cancer cell lines display differential resistance/sensitivity pattern to transaminases inhibition by AOA. Cells were treated with 1 mM AOA during 96h. The results show percentages of cell viability related to their control. Data represents percentage of cell viability relative to untreated controls, means ± SD.

As seen in the graph, the breast cancer cell lines displayed different resistance/sensitivity features to transaminase inhibition by AOA. From five cell lines tested, the triple negative cell lines MDA-MB-231 and 468 were dependent on aspartate transamination, displaying a strong sensitivity to AOA inhibition. On the other hand, MCF7 showed total resistance to AOA inhibition, and, displaying an intermediate fenotype, SKBR3 and ZR751 cell lines showed moderate sensitivity to AOA treatment.

In summary, these data allowed establishing different metabophenotypes between the breast cancer cell lines, based on their different sensitivity/resistance to transaminases inhibition.

In line with the differential sensitivity or resistance found to AOA treatment, and following recent data and our own observations in the laboratory where pyruvate is redirected to supply reducing power and aspartate becomes exhausted under AOA inhibition, we next wanted to answer whether pyruvate and/or aspartate could rescue cell viability. Thus, the cell lines were seeded in the 96w plate and 1 mM of pyruvate and 20 mM of aspartate was added in presence of 1 mM of AOA, and then, the plates were incubated for 96h at 37 °C, and cell viability was measured after 96h (Figure 4.3.3).

As it is shown in Figure 4.3.3, the cell lines displayed different responses to pyruvate and aspartate supplementation under transaminases inhibition by AOA. According to the differential profile to AOA inhibition showed above (Figure 4.3.2), the resistant cell line MCF7 was fully independent on pyruvate and aspartate addition. The cell lines ZR751 and SKBR3, which resulted moderately sensitive to transaminases inhibition by AOA, were dependent on pyruvate rescue and slightly dependent on aspartate. On the contrary, the cell lines MDA-MB-231 and MDA-MB-468, both very sensitive to AOA treatments, were completely rescued by extra supplementation of pyruvate and also aspartate to the growth media.

## MCF7



## ZR751



## SKBR3

## MDA-MB-231



## MDA-MB-468
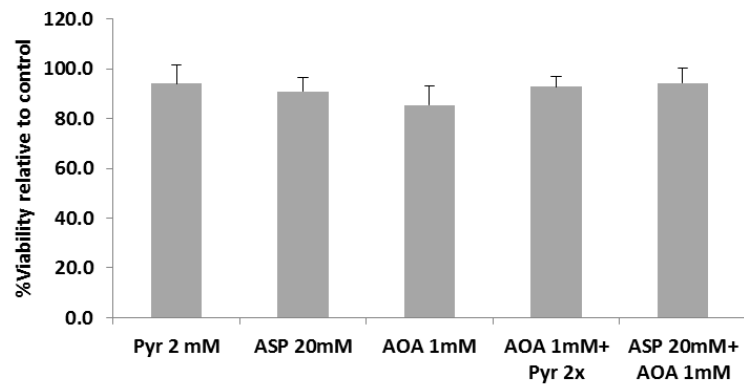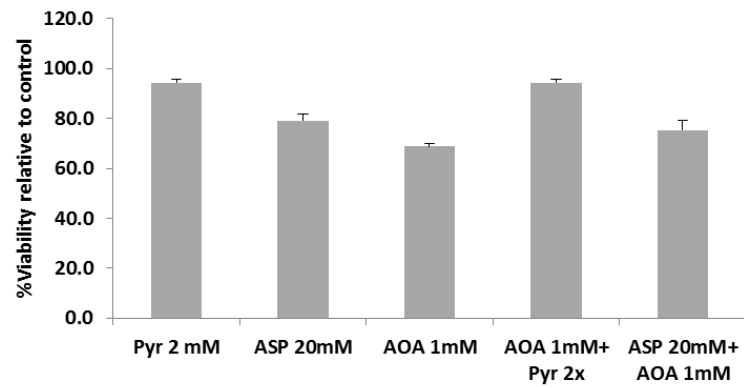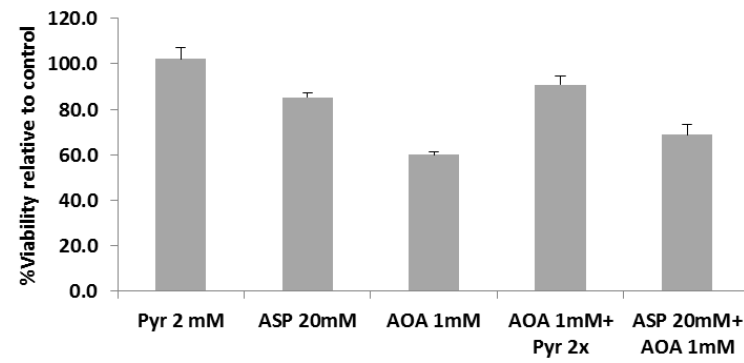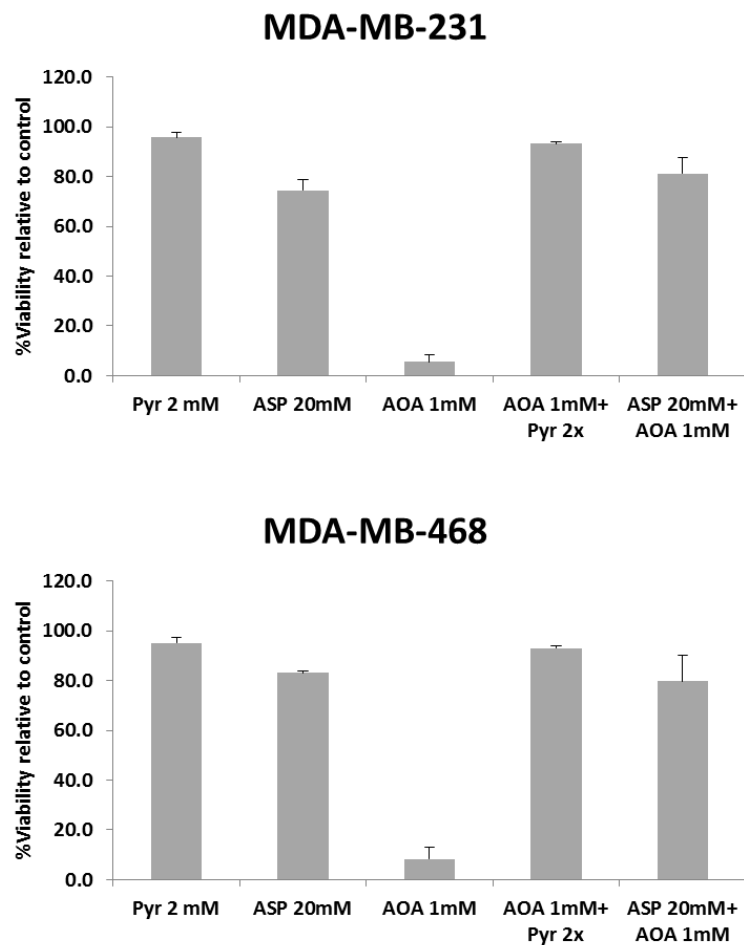


Figure 4.3.3. Breast cancer cell lines display different response to aspartate and pyruvate supplementation under transaminases inhibition by AOA. Cell lines were treated during 96h with or without 1mM AOA, with or without the supplementation of 20 mM aspartate or 1 mM pyruvate to the growth media, and then cell viability was measured in living cells. The results show percentages of cell viability relative to their untreated control. Data are means ± SD.

In summary, with these results have been found for the first time three different metabophenotypes associated with the current clinical and molecular classification of the different breast cancer subtypes:

- First the metabophenotype of MCF7, totally resistant to transaminase inhibition, and unneeded of pyruvate or aspartate supplementation.
- Second, the strongly sensitive metabophenotypes of MDA-MB-231 and MDA-MB-468, which are fully dependent on pyruvate and aspartate rescues.
- And finally, the moderately sensitive metabophenotype of ZR751 and SKBR3 cell lines, displaying strong dependence on pyruvate supplementation, and a mild dependence for aspartate.

### 4.3.3 BREAST CANCER CELLS DISPLAY A DIFFERENTIAL PHENOTYPE FOR MITOCHONDRIAL OXIDATIVE PHOSPHORYLATION DEPENDENCE

As it was previously explained in the Introduction section, nowadays it is well known that, from the perspective of functional adaptation during oncogenesis, cancer metabolism is not barely an accidental consequence of a previously acquired mitochondrial dysfunction, but on the contrary, mitochondrial metabolism remains active, and, moreover, many cancer cells are strongly dependent on mitochondrial oxidative metabolism.

To test whether breast cancer cell lines showed different mitochondrial metabolic features, we next performed experiments by using the mitochondrial uncoupler BAM15. BAM15 is a bona-fide mitochondrial membrane uncoupler that does not affect plasma membrane conductance and has a broad effective range[294], avoiding side effects as previously related to other classical uncouplers. Mitochondrial membrane uncoupling collapses the proton gradient across the inner membrane, therefore reducing proton-motive force, which in turns produces directly a lack on the ATP synthase catalytic efficiency to synthesize ATP.

For this purpose, cells were seeded with or without addition of 10 mM BAM15. After 96h, cell viability was measured and the results are shown in Figure 4.3.4. The concentration was chosen based on the existing bibliography.
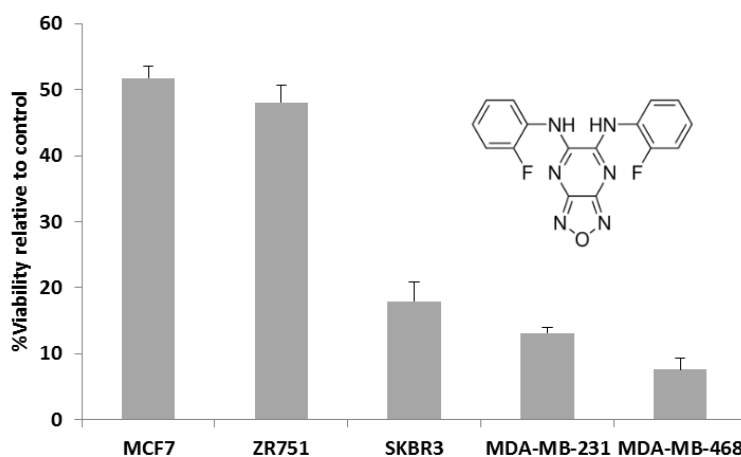


Figure 4.3.4. Breast cancer cells display differential sensitivity to mitochondrial uncoupling by BAM15, showing a different phenotype for mitochondrial oxidative phosphorylation-dependence. Cell lines were treated during 96h with 10 mM of the mitochondrial uncoupler BAM15 and then cell viability was measured in living cells. The results show percentages of cell viability relative to their untreated control. Data are means ± SD.

The cell line ZR751 showed a fall of cell viability until 50% in the presence of 10 mM BAM15. SKBR3 and MDA-MB-231 cell viability displayed a 15-20% of cell viability;

and finally, the cell line MDA-MB-468 showed cell viability below 10%. These results suggested that the cell subtypes ZR751 and MCF7 did not display at least a high dependence on mitochondrial ATP synthesis due to mitochondrial membrane uncoupling. However, the SKBR3, MDA-MB-231 and MDA-MB4-68 subtypes clearly showed greater dependence on mitochondrial oxidative metabolism.

### 4.3.4 BREAST CANCER CELL LINES DISPLAYED DIFFERENTIAL DEPENDENCE ON NAD$^+$ AVAILABILITY

Phenformin is a biguanide commonly used as therapy for type 2 diabetes. But, recently has been also described as a potential anticancer molecule by its ability to inhibit the mitochondrial complex I[295] . This compound inhibits the reactions of substrate oxidation in the mitochondrial respiratory complex I, therefore drastically reduces the conversion of NADH to NAD$^+$, affecting the cellular redox balance and, in particular, availability of NAD$^+$ to maintain the rate of glycolytic activity and synthesis of aspartate.

Cancer cell metabolism strikingly relies on NAD$^+$ dependence to sustain the glycolityc flux without affecting the rate of aspartate synthesis and avoiding exhaustion of pyruvate as an alternative electron acceptor to maintain NAD$^+$ supply[257, 293]. Accordingly, for this thesis, we planned to interrogate the potentially differential behaviour of the selected breast cancer cell lines under mitochondrial complex I inhibition by phenphormin. Thus, we could answer whether breast cancer subtypes could display differential dependence on NAD$^+$ availability, which, in turns, means another indicator of the overall metabolic needs from glycolisis and/or mitochondrial oxidative metabolism.

Accordingly, the response of the breast cancer cell models to a decrease in NAD$^+$ availability by inhibition of mitochondrial complex I was assayed by phenphormin treatments (Figure 4.3.5).  For this purpose, cells were seeded with or without addition of 50 µM phenphormin. After 96h, cell viability was measured in living cells.
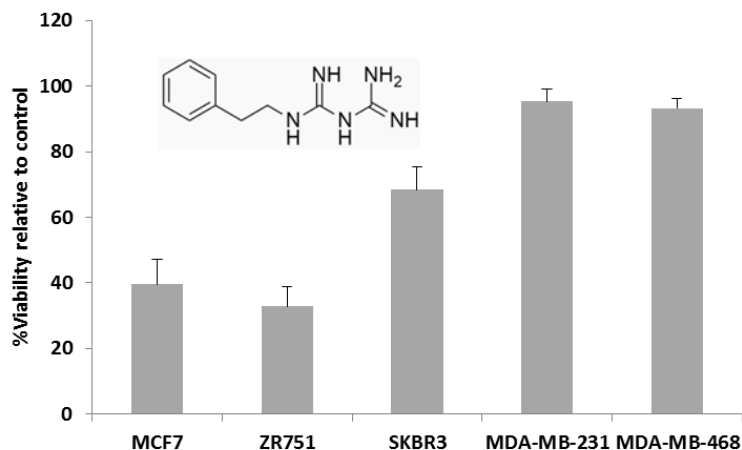
Figure 4.3.5. Breast cancer cell lines display differential sensitivity to a decrease in NAD+ availability induced by phenphormin treatment. Cell lines were treated during 96h with 50 μM of the mitochondrial complex I inhibitor phenphormin and then cell viability was measured in living cells. The results show percentages of cell viability relative to their untreated control. Data are means ± SD.

The data obtained show to different responses to phenphormin. The cell lines MCF7 and ZR751 were sensitive, displaying a decrease of cell viability to 30-40%. In the contrary, the other three cell lines were considered resistant. The cell lines MDA-MB-231 and MDA-MB-468 kept almost 100% viability, and the cell line SKBR3 showed a mild decrease to 70% cell viability.

Therefore, the breast cancer cell lines MCF7 and ZR751 showed high dependence to NAD$^+$ availability.

## 4.3.5 BREAST CANCER CELL LINES DISPLAY DIFFERENT GLYCOLYTIC DEPENDENCE IN LINE WITH THEIR NAD$^+$ DEPENDENCE

Up to now, from the data obtained we observed that the breast cancer cell lines had substantial differences for their metabolic preferences. Thus, the cell lines SKBR3, MDA-MB-231 and MBA-MB-468, relied more on mitochondrial oxidative metabolism, as showed by their high sensitivity to BAM15-induced uncoupling, and their resistance to phenphormin-induced inhibition of mitochondrial complex I (and subsequent decrease on NAD$^+$ availability). In the contrary, the cancer cell subtypes MCF7 and ZR751 showed less dependence on oxidative phosphorylation (BAM 1 resistant), and significant dependence on NAD$^+$ availability, therefore suggesting higher sensitivity to glycolytic flux, which is dependent on NAD$^+$ availability.

Hence, to better answer these observations, we next tested the response to a direct enzymatic deregulation of the glycolytic pathway. For this purpose the inhibition

of the Akt pathway was chosen to induce a decrease of the glycolytic flux. Akt is a serine/threonine kinase. The inhibition of Akt leads to a direct deregulation on some of the enzymes of the glycolytic pathway, blocking one of the main glycolytic activation pathways.

Thus, experiments were performed by using the Akt inhibitor BKM120. The experiments were performed following the previously described protocol for the former results. Cells were seeded with or without addition of 200 µM BKM120. After 96h at 37 °C, cell viability was measured in living cells (Figure 4.3.6)[296].
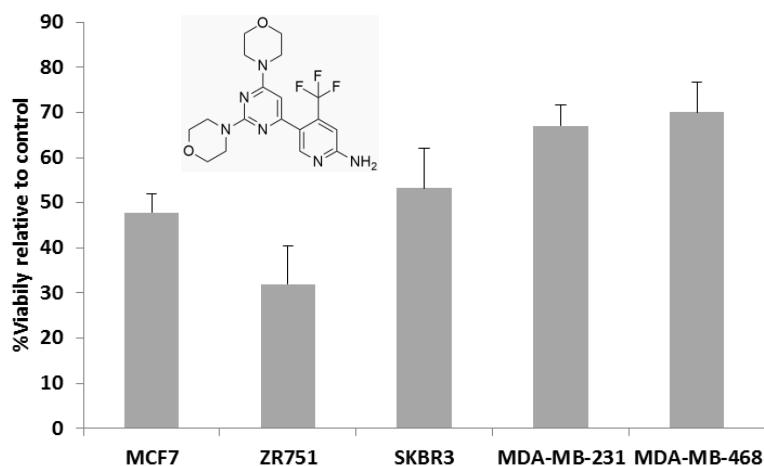


4.3.6. Breast cancer cell lines display a different sensitivity pattern to the decrease of glycolytic flux induced by Akt inhibition by BKM120[296].Cell lines were treated during 96h with 200 µM of the Akt inhibitor BKM120, and then cell viability was measured in living cells. The results show percentages of cell viability relative to their untreated control. Data are means ± SD.

The results came to support that there was two different metabophenotypes for the glycolytic dependency of the breast cancer cell subtypes. The data showed a metabophenotype, which relied on an active glycolytic flux and it was sensitive to BKM120-induced Akt inhibition. In this subtype were found the cell lines MCF7, displaying a 45% cell viability, and the ZR751 displaying a 30% cell viability. The cell line SKBR3 showed less sensitivity than the former subtype, displaying a 55% of cell viability, and thus a mild dependency. On the other hand, the MDA-MB-231 and MDA-MB-468 cell lines presented a resistant metabophenotype, displaying values of cell viability above 70-75%.

### 4.3.6 BREAST CANCER CELL LINES PRESENT DIFFERENT DEPENDENCY TO GLUTAMINE METABOLIC PATHWAYS

The other major supplier to sustain cell proliferation in cancer is the glutamine metabolism[163, 218]. To supply energy and carbons from glutamine metabolism, a key enzymatic process is the conversion of glutamate to α-ketobutyrate by the glutamate dehydrogenase (GDH). Thus, inhibition of GDH drives to a deregulation in the glutamine pathways.

Epigallocatechin gallate (EGCG) is a major component of green tea polyphenols, which displays potential anticancer properties. EGCG is an inhibitor of GDH, therefore impacts on the fundamental glutamine targets. Accordingly, the response of the breast cancer cell lines to EGCG treatments was conducted as a mean to test their potential differences for the dependency of glutamine metabolism. Cells were seeded with or without addition of 50 µM EGCG. After 96h at 37 °C, cell viability was measured in living cells (Figure 4.3.7).
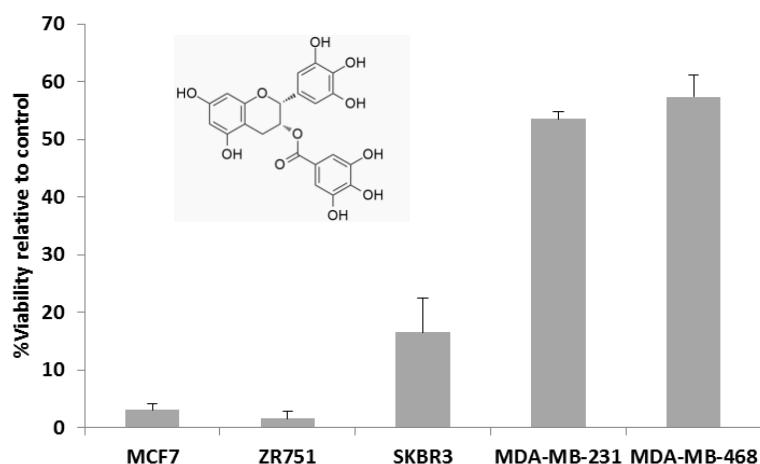


4.3.7. Breast cancer cell lines display different dependency to glutamine metabolic pathways indicated by their differential sensitivity to the GDH inhibitor EGCC. Cell lines were treated during 96h with 50 µM of the GDH inhibitor EGCG, and then cell viability was measured in living cells. The results show percentages of cell viability relative to their untreated control. Data are means ± SD.

Likewise for their dependency on glycolytic pathways showed above, the results came to support that there was two different metabophenotypes in line with their sensitivity to the deregulation of glutamine pathways induced by EGCG inhibition. The data showed a metabophenotype, which relied on an active glutamine metabolism and it was sensitive to EGCG-induced GDH inhibition. In this subtype were found the cell lines MCF7 and ZR751 displaying cell viability under 5%, and the cell line SKBR3, showing a decrease of cell viability up to 20%, hence milder than for the former two cell lines, but very sensitive yet. On the other hand, the MDA-MB-231 and MDA-MB-

468 cell lines presented a more resistant metabophenotype, displaying values of cell viability above 60%.

To summarize, breast cancer subtypes with positive expression for hormone receptors, including the luminal cell lines MCF7 and ZR751, and the HER2 positive SKBR3 showed great sensitivity to the alteration on glutamine metabolism induced by EGCG inhibition of GDH. In the contrary, the triple negative basal cell lines MDA-MB-231 and MDA-MB-468 displayed a resistant metabophenotype.

### 4.3.7 DCA INHIBITION

In the novel paradigm of cancer metabolism, the enzyme pyruvate dehydrogenase kinase (PDHK) has been considered an important target for potential antimetabolic therapeutic strategies. PDHK inhibits by phosphorylation the pyruvate dehydrogenase (PDH). Importantly, PDH diverts pyruvate towards its oxidative decarboxylation in the mitochondria.

Dichloroacetate (DCA) is an inhibitor of PDHK. Therefore DCA maintains PDH active, in general terms, DCA is considered an activating molecule of mitochondrial oxidative metabolism[297-299].

We thought important to test the response of the breast cancer cell lines to PDH over activation aiming to get a more accurate map of their metabolic differences. Accordingly, the impact on cell viability by the DCA-induced inhibition of PDHK was measured in living cells. For this purpose, cells were seeded with or without addition of 10 mM DCA. After 96h incubation at 37 °C, cell viability was measured in living cells (Figure 4.3.8).
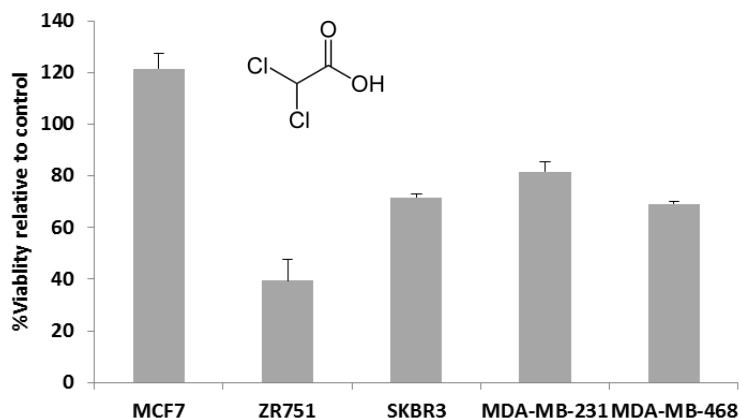


Figure 4.3.8. Impact of PDH over activation by DCA-induced PDHK inhibition. Cell lines were treated during 96h with 10 mM DCA, and then cell viability was measured in living cells. The results show percentages of cell viability relative to their untreated control. Data are means ± SD.

Unexpectedly, DCA induced an apparently randomized effect, which did not follow the profiling of metabophenotypes observed among the previous experiments. As it is observed in the graph, the MCF7 cell line showed not just total resistance to treatment, but even DCA promoted a higher rate of proliferation and cell viability than untreated cells. The cell lines SKBR3, MDA-MB-231 and MDA-MB-468 were resistant to DCA treatment, displaying cell viability between 75-90%. Only the cell line ZR751, with a decrease in cell viability up to 40%, resulted sensitive to DCA treatment.

After obtaining the results, it is not possible to observe significant metabolic differences between the five breast cancer cell lines.

In 2007, an article was published, explaining the potential use of DCA as an anticancer agent[300]. But the results obtained with the breast cancer lines were not shown according to this research. Even so, the studies of this group were very inspiring for the development of this thesis, since thanks to them a series of modifications to the DCA molecule was proposed, as explained in the chapter 4.4.

## 4.4 METABOLIC PRO-DRUGS

As it was previously described in the introduction (4.1.2), cancer cells extensively relay on the glycolytic pathway to get large amounts of metabolic intermediates, which are required as "building blocks "to sustain their high proliferative rate. The metabolic intermediates are obtained by means of the high rate of activity of the anabolic branches derived from glycolytic intermediate reactions. Therefore, this metabolic reprogramming process reflect a prominent Warburg effect, where piruvate is reduced at the end of glycolysis to lactate, thus feeding back the high glycolytic rate by means of sustaining a high level of $NAD^+$. Accordingly, in cancer cells a larger proportion of piruvate is reduced in the cytosol to lactate, and a minor proportion is transported into the mitochondria to be transformed to acetylCoA by piruvate dehydrogenase complex (PDC).

In line, nowadays some anticancer drug screening strategies have moved the focus to get advantage of this metabolic feature. Thus, molecules which could change the preferential metabolism of piruvate by means of forcing its entry into mitochondrial metabolism could result specifically toxic to cancer cells. For this work, the molecule chosen was dichloroacetate (DCA) (Figure 4.4.1). DCA is a small molecule, whose molecular weight is 128.94 g/mol. This molecule has been used in the clinic for lactic acidosis disorders for over 3 decades[301, 302] and as an anticancer drug[297]. The antitumoral features of DCA are due to its ability to inhibit the enzyme pyruvate dehydrogenase kinase (PDK), whose function is to inhibit the pyruvate dehydrogenase complex (PDC). Therefore, DCA acts by activating the PDC complex.
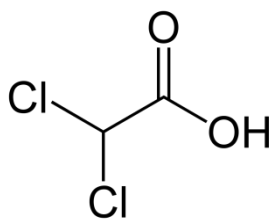


Figure 4.4.1. Chemical structure of DCA.

The mechanism of action of DCA can be summarized in the activation of PDC, favouring the transformation of pyruvate into AcetilCoA and promoting the Krebs cycle, which entails an increase in oxygen consumption in mitochondria and a decrease in lactate concentrations[303]. Due to Warburg Effect, glucose uptake increases and oxidative phosphorylation in tumour cells is repressed irrespectively of intracellular oxygen concentrations. It has been suggested the formation of hypoxic microenvironments in the early phases of tumour evolution that lead to the

development of a "glycolytic phenotype", which leads to an inhibition of oxidative phosphorylation by the action of PDK, and therefore to the development of the Warburg effect that facilitates tumour growth in the presence of lactic acid. PDK also acts as a regulator of two molecules related to oncogenesis: mTOR (target molecule of rapamycin) and the hypoxia inducible factor (HIF-1α)[304].

The deregulation of these molecules can increase the synthesis of GLUT type glucose receptors in tumour cells, favouring glucose uptake and glycolysis[305]. As a result of the action of HIF-1α, the activation of oncogenes (AKT, Myc or Bcl-2) occurs[306] and the increase in the expression of HIF-1α favours the increase of some types of reactive oxygen species (ROS) that cause damage to mitochondrial and nuclear DNA, further deteriorating the function of the mitochondrial respiratory chain and mitigating the protective functions of genes such as p-53 or ASK1.

The increase of the oxygen consumption by the tumour cells causes a depletion of this in the neoplastic tissue. This situation triggers a severe hypoxia that cannot be compensated as a consequence of the inhibitory action of DCA on PDK, causing the neoplastic tissue to die by ischemia[307].

The main effects of DCA are a decrease in HIF-1α and Bcl-2 in neoplastic cells, followed by an increase in the expression of PUMA (P-53 upregulated modulator of apoptosis), p-53 and caspases. As a consequence, a negative modulation for the transcription of GLUT receptors occurs, causing the uptake of glucose in the tumour cells to decrease[308]. Another effect of DCA on tumour cells is the increase in the generation of ROS respecting healthy cells[309]. Signalling ROS will allow the entry of the NADH generated in the Krebs cycle to complex I of the respiratory chain, reactivating PDH and favouring the "remodelling" of mitochondrial metabolism. All this "cascade" facilitates the opening of the mitochondrial transition pore which will allow the release to the cytoplasmic space of pro-apoptotic mediators such as cytochrome c (Cyt c) and the apoptosis inducing factor[310].

## 4.4.1 BREAST CANCER CELLS LINES DISPLAY DIFFERENT LEVEL OF SENSITIVITY TO DCA TREATMENT

To test the effect of DCA as antitumoral drug, the viability of the five breast cancer lines was measured in the presence of 10 mM DCA. The assay was performed as explained in the chapter 4.2.4.2.
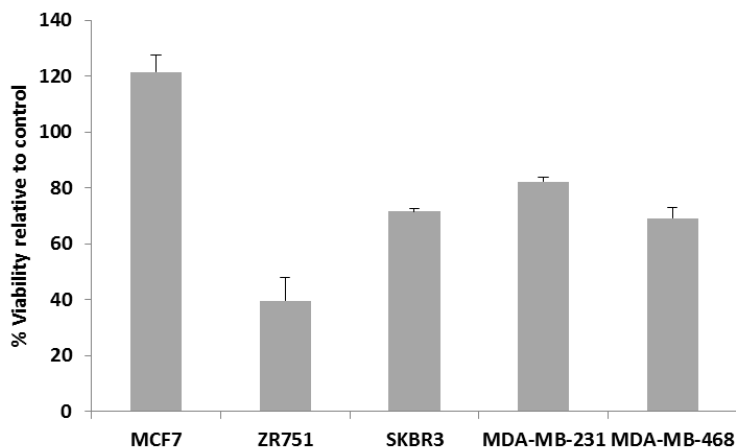
Figure 4.4.2. Breast cancer cell lines display different level of sensitivity to DCA treatment. The five breast cancer cell lines were treated with 10 mM DCA for 96h. The results show percentages of cell viability related to their control. Data represents percentage of cell viability relative to untreated controls, means ± SD.

The results displayed in Figure 4.4.2 confirmed a different sensitivity level to DCA. The MCF7 cell line showed to be resistant to DCA. The SKBR3, MDA-MB-231 and MDA-MB-468 cell lines, with a survival of 70%, 75% and 80% respectively, show a slight sensitivity to DCA, and the ZR751 cell line displayed more sensitivity, with a viability of less than 40% of the population.

Therefore, it can be assumed that each cell line presents different levels of sensitivity to DCA, with MCF7 being the most resistant and ZR751 the most sensitive.

## 4.4.2 IMPROVEMENT OF THE EFFECT OF DCA USING A DERIVATIVE WITH THIOPHENE

In order to improve the effect of DCA, it was decided to modify it with thiophene, since it was demonstrated by experimental observations of our research group that thiophene group could act as a selective carrier to the mitochondria. Thus, this drug should be delivered directly to the mitochondrial area where the enzyme pyruvate dehydrogenase kinase (PDK) acts, and therefore improving the effect of DCA by increasing its specificity, avoiding side effects, and thus reducing the concentrations required to impact cell viability.

Two different modifications were designed, in which the difference was the length of the chain between the thiophene group and the DCA. Figure 4.4.3 shows the structures of the proposed DCA derivatives: DCA-2-TP and DCA-1-TP.
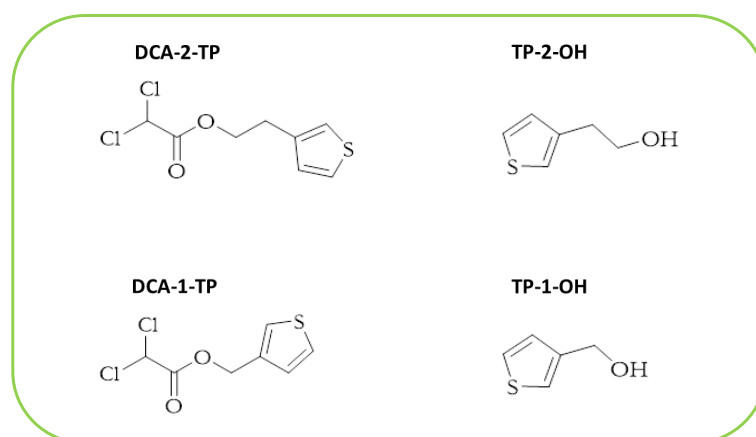
Figure 4.4.3. Structures of the DCA derivatives modified with thiophene and the precursor thiophene groups.

These first DCA derivatives modified with thiophene were tested with two cell lines, MCF7 and MDA-MB-468, and the cell viability assays were carried out following the procedure explained in chapter 4.2.5.2.

As it can be seen in Figures 4.4.4, there is a significant improvement in the antitumoral effect of the DCA derivatives modified with thiophene. In the cell line MCF7, the DCA-2-TP at concentration of 10 mM reduces cell viability to approximately 30%, although in the rest of treatments there is no notable effect. Interestingly, for the MDA-MB-468 cell line it is observed that 10 mM, 7.5 mM and 5 mM of DCA-2-TP have a significant effect on cell viability compared to free DCA. Importantly, just 2.5 mM of DCA-2-TP was required to achieve the toxic effect of 10 mM free DCA, thus lowering four times the doses of the drug.
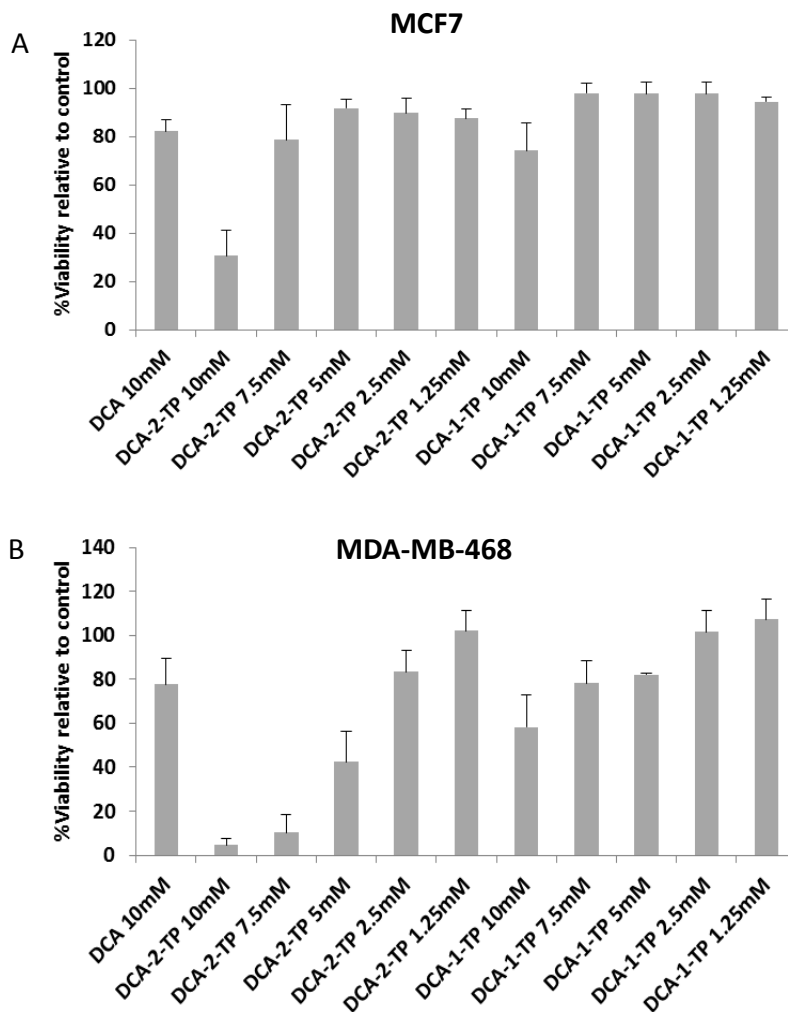
Figure 4.4.4. Improved antitumoral effect by DCA derivatives modified with thiophene. Graphs show the effect of different concentrations of DCA and the two DCA derivatives modified with thiophene on cell viability after 96h treatments. A) MCF7 cell line. B) MDA-MB-468 cell line. Data represents percentage of cell viability relative to untreated controls, means ± SD.

In contrast, DCA-1-TP did not improve the antitumoral activity, since no significant differences with free DCA were found for both MCF7 and MDA-MB-468 cell lines.

In order to study whether the effect produced by the DCA-2-TP on the cell viability was caused by the DCA and not because the thiophene group was toxic by itself, a new experiment was performed with the thiophene (TP-2-OH, Figure 4.4.3). Since DCA-1-TP did not show a representative improvement, only DCA-2-TP was tested in this experiment. The cell line SKBR3 was used as a model. The cells were treated with 10 mM free DCA, and 10 mM, 7.5 mM, 5 mM, 2.5 mM, and 1.25 mM of DCA-2-TP and TP-2-OH separately, and then cell viability was measured after 96h. The results are gathered in Figure 4.4.5.
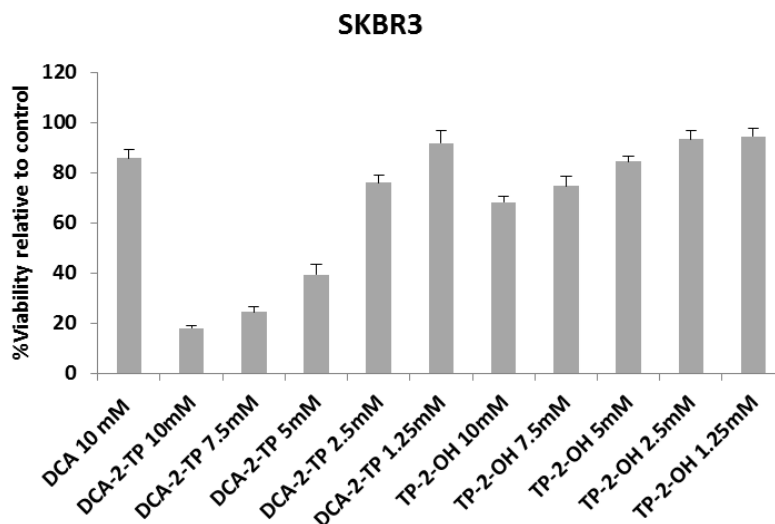
**SKBR3**



Figure 4.4.5. The antitumoral effect of the DCA-thiophene conjugated DCA-2-TP is specifically due to its DCA properties. SKBR3 cells were treated for 96h with DCA, DCA-2-TP and TP-2-OH. Data represents percentage of cell viability relative to untreated controls, means ± SD.

As can be seen in Figure 4.4.5, whereas DCA-2-TP exerted a significant impact on cell viability, much more efficient than free DCA, the thiophene TP-2-OH caused only a slight effect. Thus, it can be concluded that the antitumoral effect of DCA-2-TP is due to its DCA properties.

We could then argue that, as a consequence of the selective delivery of the DCA to the mitochondria by the conjugated thiophene group in the DCA-2-TP drug, DCA concentrated more efficiently its activity in the mitochondria, where it is located its enzymatic target. In fact, 2.5 mM of DCA-2-TP was required to achieve the toxic effect of 10 mM free DCA, thus lowering four times the dose of the drug.

### 4.4.3 HIGH THROUGHPUT SCREENING TO TEST THE EFFECT OF DCA-THIAZOL AND DCA-BENZOTHIOPHENE DERIVATIVES

After the results obtained in the previous section (4.4.2), it was decided to modify DCA with other compounds with similar structures to thiophene which could also act as selective carriers to the DCA into the mitochondria, and test their efficiency as antitumoral drugs in the different breast cancer cell lines.

For this purpose, we could perform a high throughput screening by using several next generation equipments (see details in the Methods, chapter 4.2.1.8), taking advantage of a thesis stay in the CIBIO Research Centre, Trento (Italy). The high

throughput approach allowed testing all the breast cancer cell lines using a large combination of drugs treatments.

The structures of the new compounds that were synthesized are shown in Figure 4.4.6. The DCA were modified with the thiazol group, at two different positions, and with a benzothiophene group.
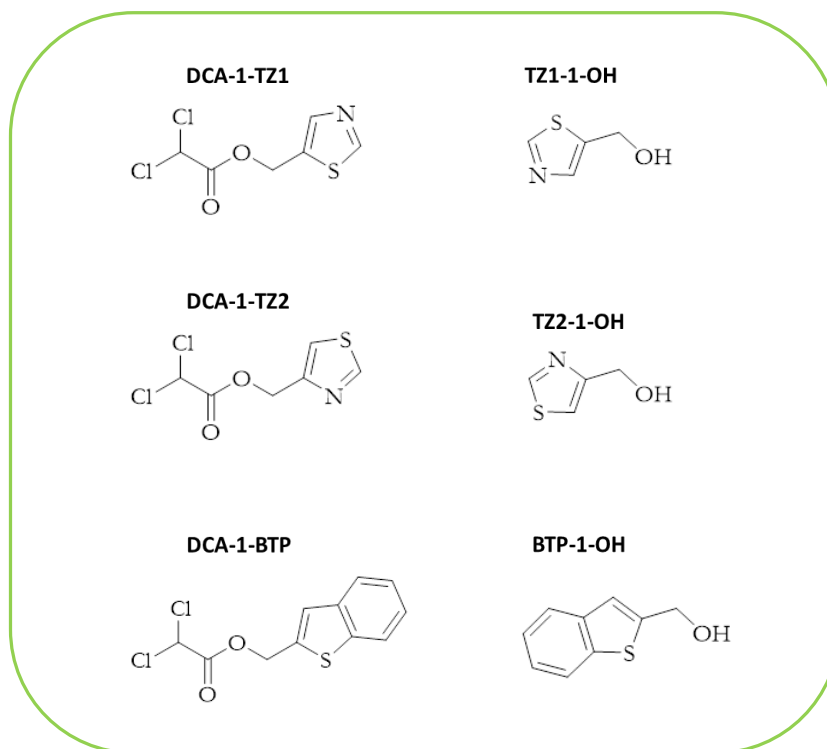


Figure 4.4.6. Structures of the DCA derivatives modified with thiazol and benzothiophene, and the corresponding precursor thiazol and benzothiophene groups.

To carry out the study, a different methodology, instrumental and analysis was used, all explained in detail in section 4.2.5.3. The cells were incubated in 384 well-plates during 72h at 37 °C in the presence of the compounds, and after this time the cell viability was measured with an Operetta high-content imaging system.

To check the effect of the three compounds (see structures in Figure 4.4.6), a first screening was performed in order to see if they produced any effect on the cell viability of the five breast cancer cell lines (Figures 4.4.7, 4.4.8 and 4.4.9). In these experiments, controls were carried out with the corresponding precursors containing only the thiazol or benzothiophene groups.
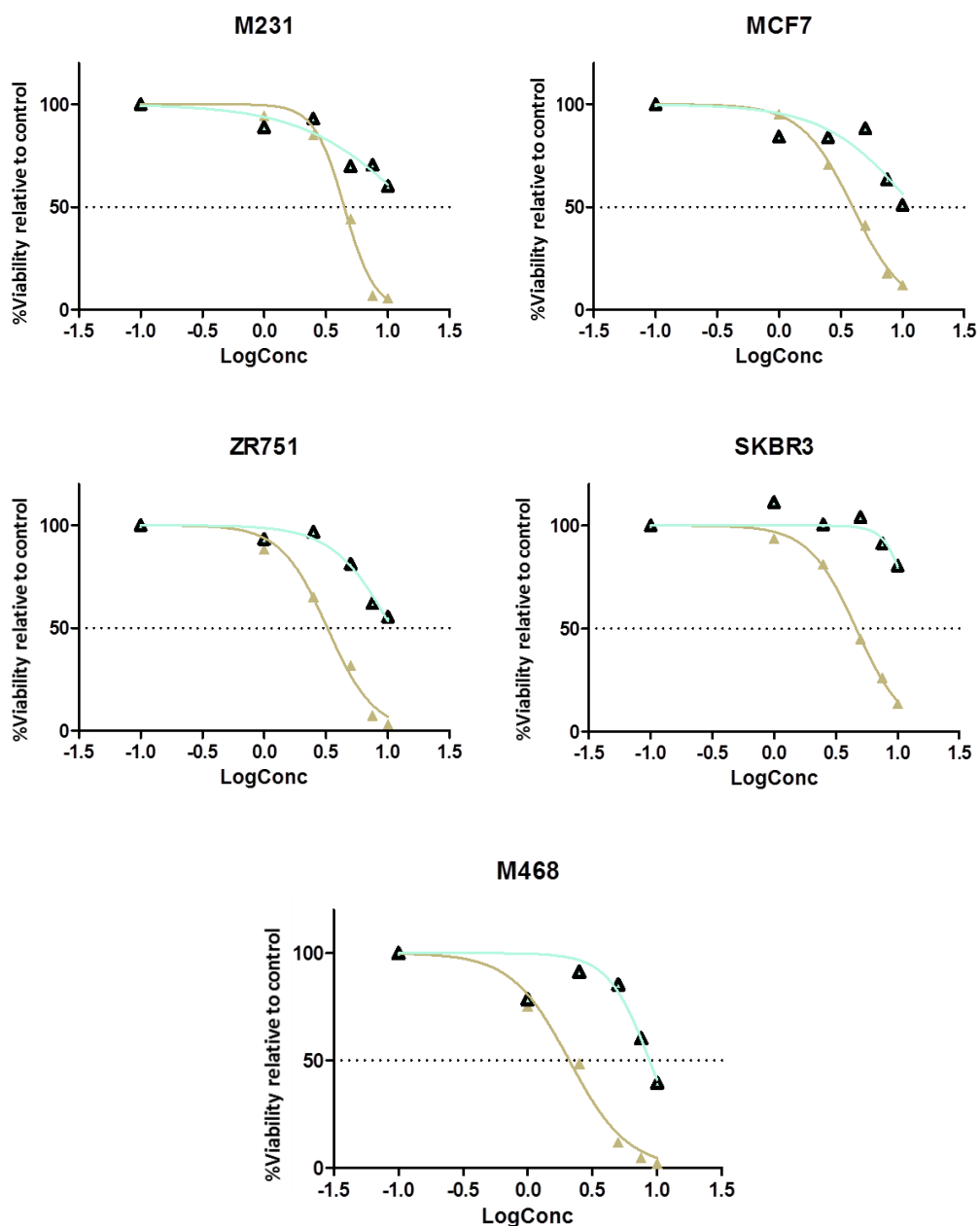
Figure 4.4.7. DCA-1-TZ1 displays an efficient antitumoral effect on the breast cancer cell lines. Cells were treated for 72h with different concentrations of DCA-1-TZ1 (green triangles) and the corresponding control TZ1-1-OH (black triangles). Data represents percentage of cell viability relative to the corresponding precursor containing only the thiazol group.

**Figure 4.4.8.** DCA-1-TZ2 displays an efficient antitumoral effect on the breast cancer cell lines. Cells were treated for 72h with different concentrations of DCA-1-TZ2 (pink triangles) and the corresponding control TZ2-1-OH (black triangles). Data represents percentage of cell viability relative to the corresponding precursor containing only the thiazol group.
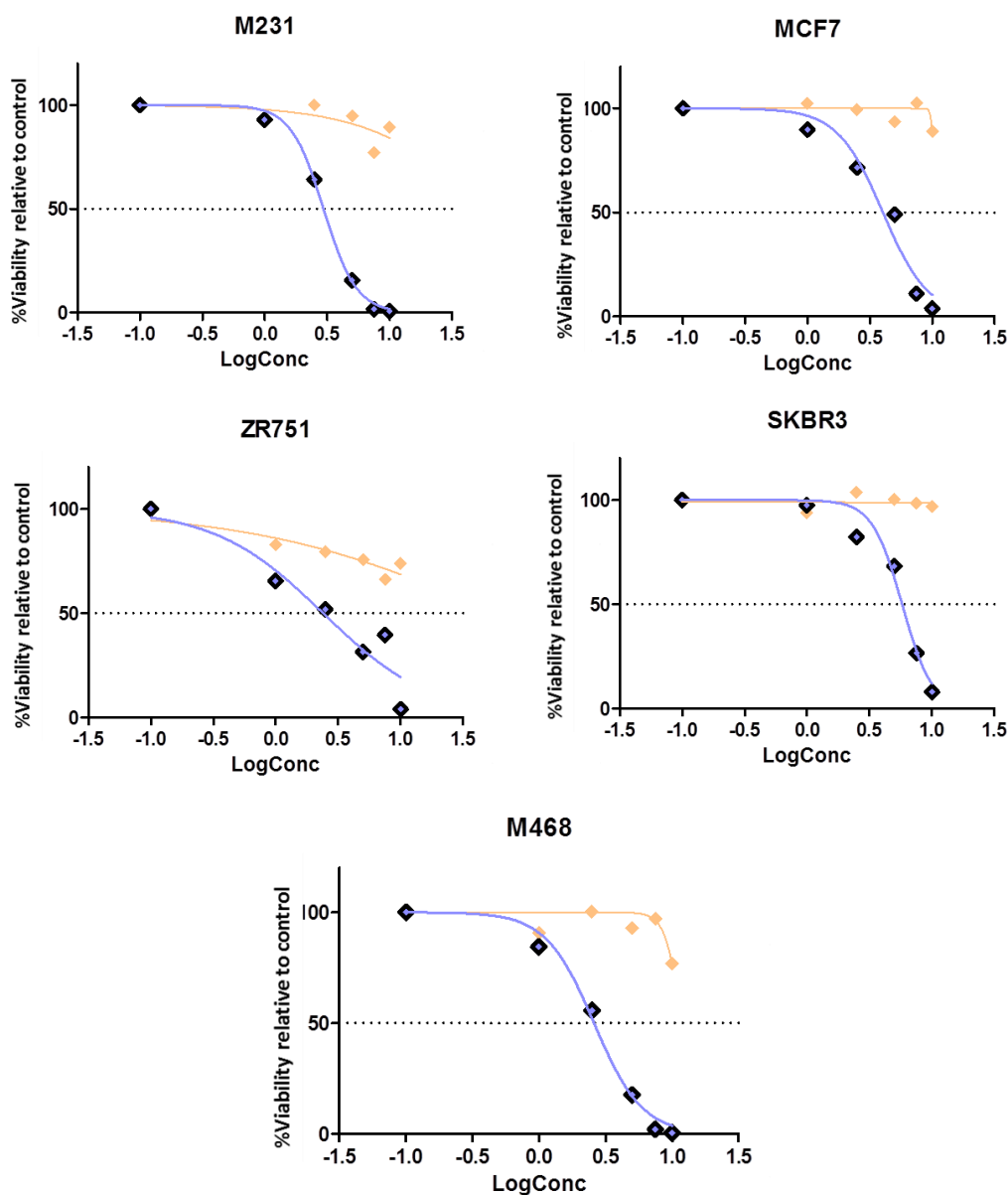
**Figure 4.4.9.** DCA-1-BTP resulted to be an inefficient antitumoral compound with the breast cancer cell lines. Cells were treated for 72h with different concentrations of DCA-1-BTP (yellow squares) and the corresponding control BTP-1-OH (black squares). Data represents percentage of cell viability relative to the corresponding precursor containing only the benzothiazol group.

The results on the cell viability of all the breast cancer cell lines after treatment with the compound DCA-1-TZ1 and its control TZ1-1-OH are shown in Figure 4.4.7. In all cases, the effect of the DCA-1-TZ1 was strikingly greater than the corresponding control containing only the thiazol carrier group. The controls reached the IC50 at very higher concentrations compared to the compound with DCA bound to the thiazol. The concentrations of the drug DCA-1-TZ1 at which IC50 was obtained varied from 2.096 mM in MDA-MB-468 cell line to 4.620 mM in SKBR3 cell line. From these results, it was

considered that DCA-1-TZ1 had a potential for its use as improved anticancer drug, and it was viable to continue the study.

Similar effects were found with DCA-1-TZ2 compound. The results are shown in Figure 4.4.8. The second DCA derivative with a coupled thiazol group showed an optimal efficiency for all the cancer cell line tested. Moreover, the precursor with free thiazol group only affected cell viability when it was added at high concentrations. The IC50 obtained with the DCA-1-TZ2 compound was ranged from 0.6146 mM in MDA-MB-468 cell line to 1.161 mM in SKBR3 cell line. With this preliminary experiment, the potential use of the DCA-1-TZ2 as antitumoral drug was also demonstrated. Next, a deeper study of the cellular viability, and therefore of the anticancer drug effect of this compound, was performed.

Nevertheless, the results obtained with the DCA which contained a benzothiophene group (DCA-1-BTP) in the five breast cancer cell lines were not satisfactory. The results of the cell viability obtained in these assays are shown in Figure 4.4.9. In contrast to the derivatives of the DCA with thiazol, the DCA coupled to a benzothiophene group did not display an efficient antitumoral effect. As seen in the graphs, the concentration of the compound containing only free benzothiophene (BTP-1-OH) needed to reach the IC50 was much lower than that of the DCA-benzothiophene derivative (DCA-1-BTP). In this case, the IC50 were reached with DCA-1-BTP concentrations ranged from 11.84 mM in MDA-MB-468 cell line to 60.35 mM in MDA-MB-231 cell line. Unfortunately, the solubility of the DCA-1-BTP compound was really low and it was not possible to dissolve completely the drug before treatment. As a consequence, some aggregates were formed and the real concentration of the DCA-1-BTP added to the cells was unknown and likely lower than the expected working concentration. Considering these experimental issues, DCA-1-BTP had to be discarded as potential antitumor compound.

Accordingly, only the two DCA derivatives modified with a thiazol group showed a potential improvement of the anticancer effect compared with the naked DCA. In order to study the reproducibility of these results, and to obtain more accurate IC50 values, three replicas of each set of cell viability experiments were carried out with the compounds DCA-1-TZ1 and DCA-1-TZ2.
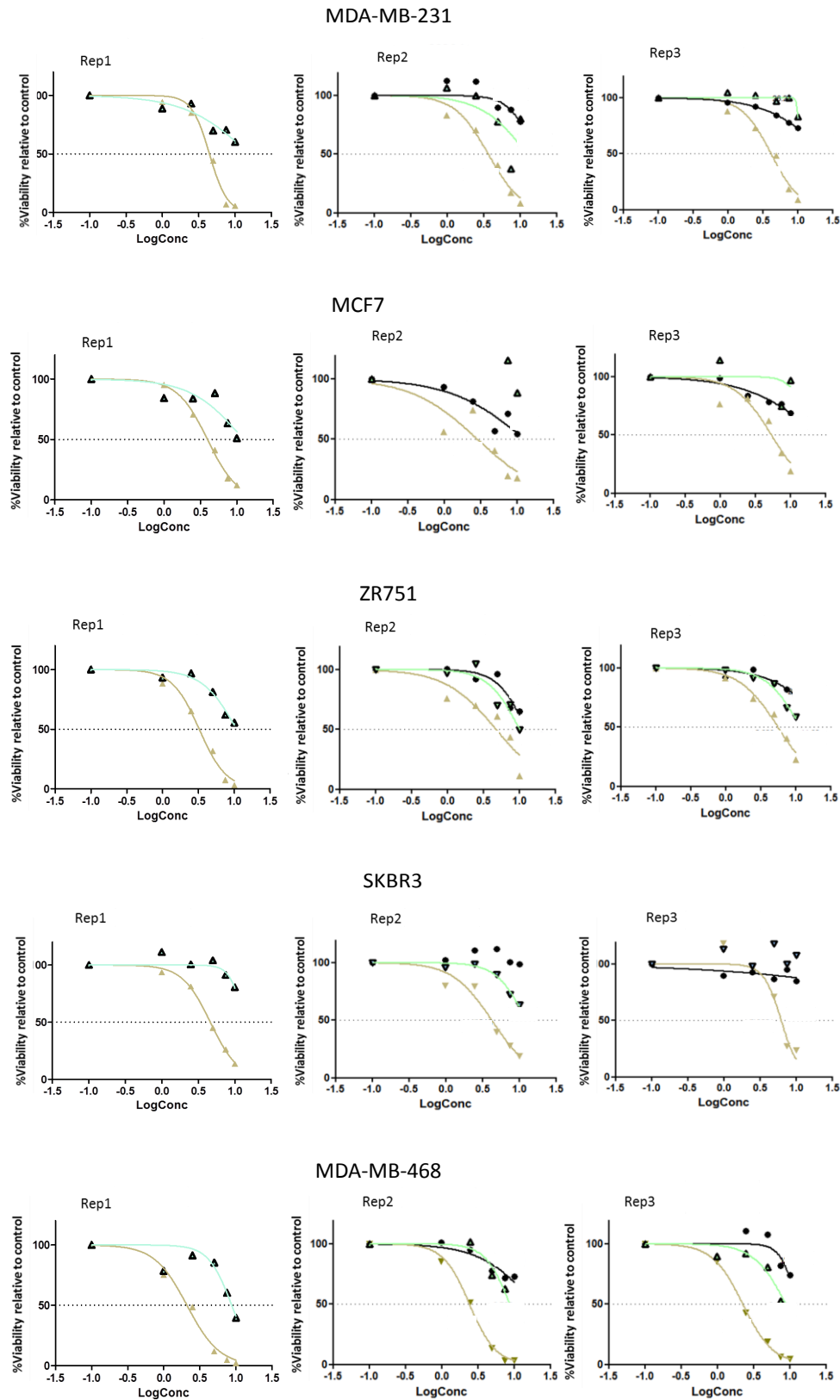
Figure 4.4.10. Experimental confirmation of the antitumoral efficiency of DCA-1-TZ1 on the breast cancer cell lines. Cells were treated for 72h with different concentrations of DCA-1-TZ1 (pink triangles) and the corresponding control TZ1-1-OH thiazol group (black triangles), and its impact on cell viability was measured in 3 replicas. Data represents percentage of cell viability relative to the corresponding precursor containing only the thiazol group.
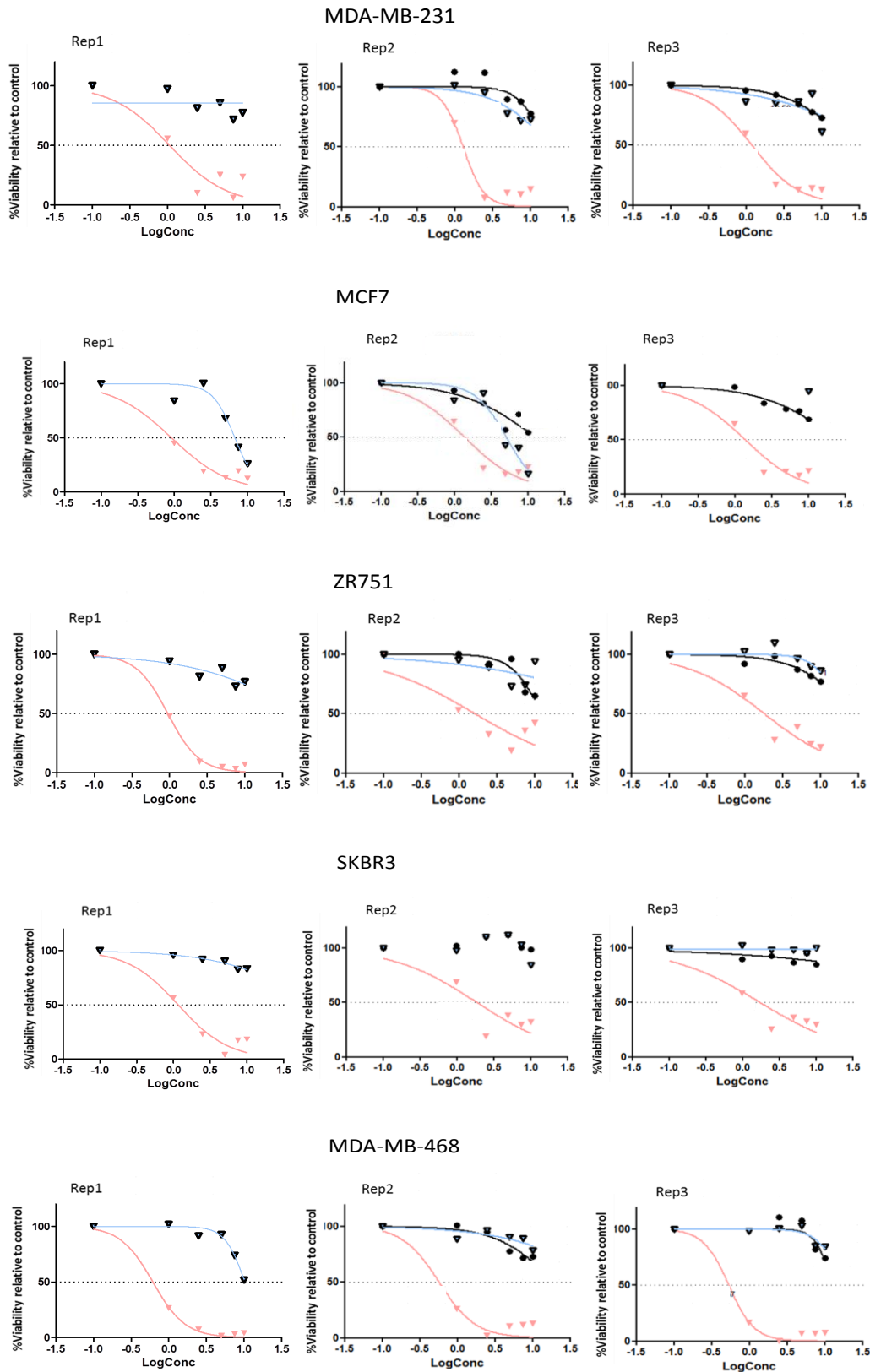
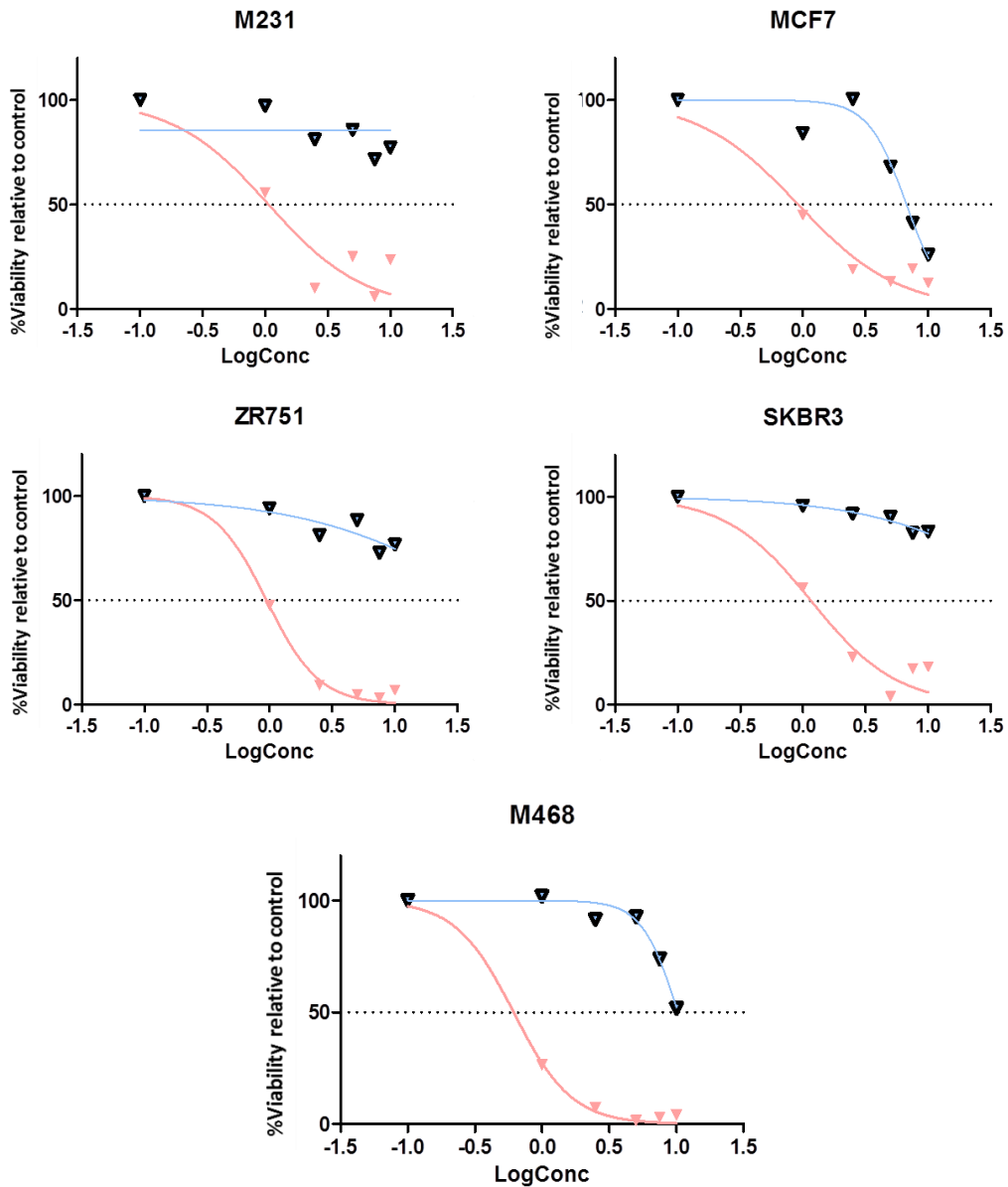Figure 4.4.11. Experimental confirmation of the antitumoral efficiency of DCA-1-TZ2 on the breast cancer cell lines. Cells were treated for 72h with different concentrations of DCA-1-TZ2 (pink triangles) and the corresponding control TZ2-1-OH thiazol group (black triangles), and its impact on cell viability was measured in 3 replicas. Data represents percentage of cell viability relative to the corresponding precursor containing only the thiazol group.

In agreement with the results found in the first experiments, DCA-1-TZ1 and DCA-1-TZ2 compounds displayed an strikingly efficient effect. The impact on the cell viability was actually higher than the effect of the same concentration of naked DCA, and also higher than the same concentration of the precursors TZ1-1-OH and TZ2-1-OH, respectively, used as control (Figure 4.4.10 and Figure 4.4.11). From each set of experiments the value of IC50 was calculated for every cell line. Table 4.4.1 shows the average IC50 values calculated with the results of each replica.

Table 4.4.1. Half maximal inhibitory concentration (IC50) obtained for DCA-1-TZ1 and DCA-1-TZ2 in each breast cancer cell line. Values represent average ± standard deviations of three replicas.

| | DCA-1-TZ1 | DCA-1-TZ2 |
|---|---|---|
| **MCF7** | 4.07 ± 1.27 mM | 1.23 ± 0.26 mM |
| **ZR751** | 4.55 ± 1.21 mM | 1.47 ± 0.46 mM |
| **SKBR3** | 5.04 ± 1.07 mM | 1.59 ± 0.38 mM |
| **MDA-MB-231** | 4.10 ± 0.38 mM | 1.16 ± 0.12 mM |
| **MDA-MB-468** | 2.26 ± 0.16 mM | 0.58 ± 0.04 mM |

As it can be seen in the Table 4.4.1, for the compound DCA-1-TZ1 the calculated IC50 varied between 2.26 mM in the MDA-MB-468 cell line and 5.04 mM in the SKBR3 cell line.  For DCA-1-TZ2 the concentrations to obtain the IC50 ranged from 0.58 mM in the MDA-MB-468 cell line to 1.59 mM in the SKBR3 cell line. These results indicate that antitumoral effect of DCA-1-TZ2 is slightly higher that the effect of DCA-1-TZ1.

## 4.4.4 ATP PRODUCTION

Next, the ATP synthesis capacity was further evaluated to gain insights of the impact on cell viability by its functional meaning. To perform this study, the five breast cancer cell lines were plated and incubated at 37 °C. After 24 h, the treatment was started by the addition of the different compound at concentrations ranging between 1 mM to 10 mM. After 6h incubation, the production of ATP was measured using Opereta High-Content Imagin system, as detailed in the Method chapter 4.2.1.8.
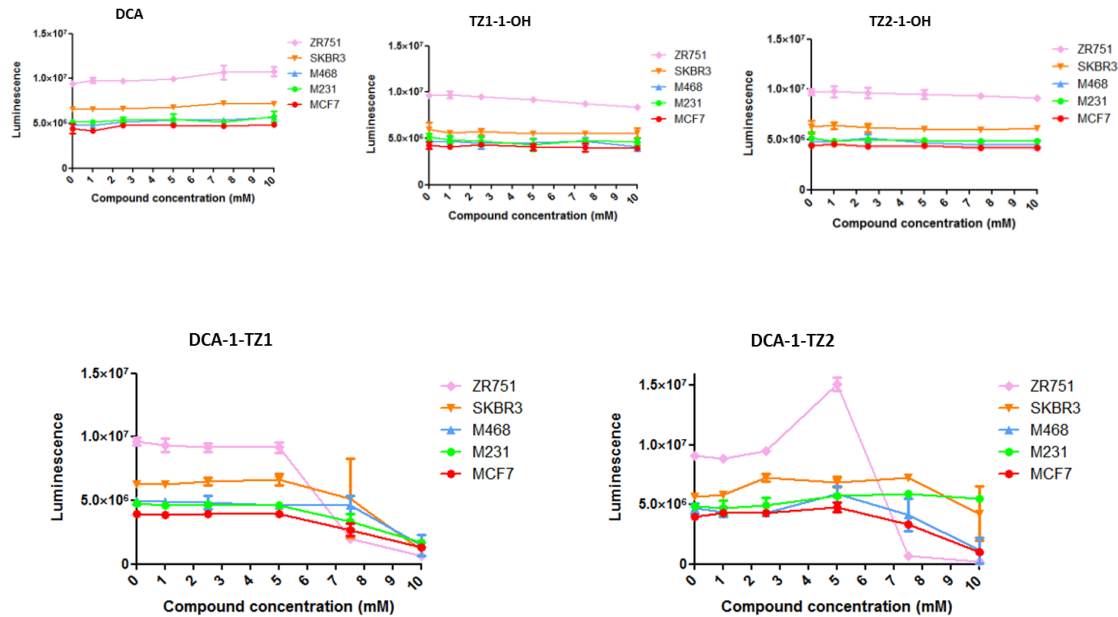
Figure 4.4.11. Effect of the treatments with DCA, DCA derivative compounds and their conjugation controls on the capacity of ATP synthesis. The five breast cancer cell lines were treated with DCA, TZ1-1-OH, TZ2-1-OH, DCA-1-TZ1 and DCA-1-TZ2 for 6h at different concentrations, and subsequently ATP production was measured. Data are represented as luminescence arbitrary units.

Five compounds were tested, DCA, DCA-1-TZ1, DCA-1-TZ2, TZ1-1-OH and TZ2-1-OH. As seen in the graphs, with DCA, TZ1-1-OH and TZ2-1-OH the amount of ATP produced by the cells remained constant in the five cell lines. In contrast, with DCA-1-TZ1 and DCA-1-TZ2 a decrease in the amount of ATP is seen from 5 mM, which reached zero at 10 mM of the corresponding drug. Interestingly, for the ZR751 cell line, with the compound DCA-1-TZ2 it was observed an increase of ATP production at 5 mM, followed by a decrease to zero at approximately 7.5 mM.

From these results, it can be concluded that only DCA-1-TZ1 and DCA-1-TZ2 significantly affect the production of ATP, where the amount of ATP is then directly proportional to the amount of viable cells remaining in culture after the treatments.

## 4.4.5 EFFECT OF DRUGS ON NON-TUMOR CELL LINES

In order to confirm the specificity of the anti-tumorogenic potential of the drugs (DCA-1-TZ1 and DCA-1-TZ2), it was necessary to test them in non-transformed cells using the cell lines MRC5 and MCF10A. The experiments were carried out following the same protocol as in Chapter 4.2.5.2).

The results of the non tumoral cell lines were compared with the results obtained from MDA-MB-468 cell line, which was the cell line most sensitive to the antitumoral drugs (Figure 4.4.12).
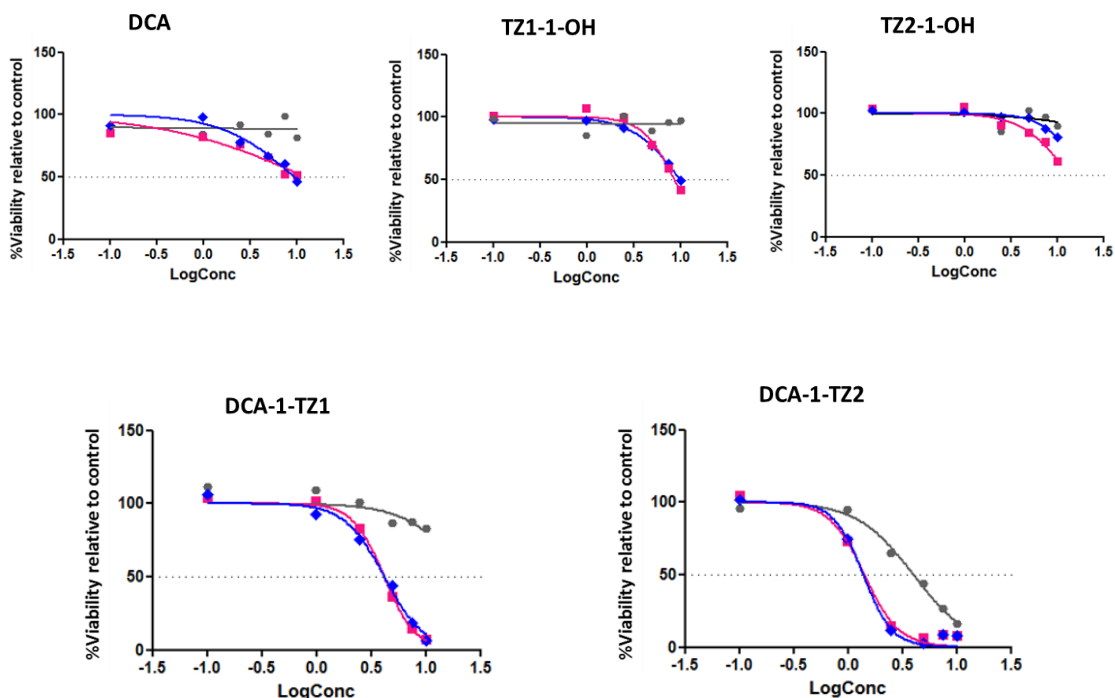


Figure 4.4.12. Comparative study to test the specific toxicity of the compounds DCA-1-TZ1 and DCA-2-TZ2 on cell viability between the breast cancer cell line MDA-MB-468 (blue line), and the reference non tumoral cell lines MCF10A (pink line) and MRC5 (black line). Cells were treated with different concentrations of the compounds DCA, DCA-1-TZ1, DCA-1-TZ2 and the corresponding controls TZ1-1-OH and TZ2-1-OH. Data represent the percentage of cell viability relative to untreated controls.

As seen in Figure 4.4.12, DCA-1-TZ1 and DCA-1-TZ2 displayed a similar impact on cell viability for the non-tumour cell line MCF10A and the tumour cell line MDA-MB-468. For the non-tumour cell line MRC5 the effect of DCA-1-TZ1 resulted less pronounced, but cannot be considered a resistant cell line. In summary, DCA-1-TZ1 and DCA-1-TZ2 cannot be considered potential anti-tumor compounds according to the data obtained by mean of the proposed experimental approaches, since the compounds displayed a non specific toxicity effect between the cancer cell lines and the non tumoral controls. Nonetheless, further works must be conducted, including other non tumoral reference cell models and *in vivo* experiments in order to definitively discard their antitumoral potential.

## 4.5 DISCUSSION

Recent research in cancer biology has shown the growing relevance of tumor metabolism during the oncogenic process. It has been immersed that the altered energy metabolism in cancer cells is essential to satisfy the high demands of growth and proliferation under so-called tumor metabolic reprogramming[1]. Even in the presence of adequate oxygen, cancer cells depend on glycolysis rather than oxidative phosphorylation for energy[2]. Recent studies in cancer metabolism have shed light on the role of alternative energy sources, especially glutamine and other amino acids, in cell proliferation and maintenance[3, 4], including participation of oncogenes and tumor-suppressor genes in regulating metabolic pathways in cancer cells[5, 6].

Nowadays, there are very few studies of breast cancer metabolism[7]). Of note, currently there is no other similar work in the recent literature to this thesis work, providing any comparative data aiming to study the possible association of a functional metabolic profiling with the current histological and genetic markers for the clinical classification of breast cancer subtypes. Therefore, studying breast cancer from the proposed metabolic approach herein, could provide new data, which in turn could facilitate in future a faster and valid diagnosis, tsand help to improve potential antimetabolic therapeutic strategies, which would positively impact on survival rates. The first goal approached in our study was to answer whether the breast cancer cell lines, representative of the current clinical subtypes, display differential metabolic phenotypes, or metabophenotypes, which correlate or not with the histological and genetic classification. By using the pull of metabolic inhibitors, we could establish three main metabophetypes as we can see in figure 4.5.1. Accordingly, the first metabophenotype resulted to be highly dependent on glycolysis. In this group were the breast cancer cell lines MCF7 and ZR751. These cell lines are clinically classified as luminal A and B respectively. The second metabophenotype grouped cell lines with remarkable dependence on mitochondrial oxidative metabolism. In this group we found the cell lines MDA-MD-231 and MDA-MD-468, clinically classified as triple negative or basal cells. Finally, another metabophenotype was found, which showed shared features between the two major metabolic phenotypes described above, displaying different degrees of sensitivity/resistance to the inhibitors used in this approach, thus we could propose a classification as an intermediate metabophenotype The cell line SKBR3 was located with this intermediate metabophenotype. According to the clinical classification, this cell line belongs to the HER2 positive group.

Of note, the classification of these three major metabophenotypes found may vary only slightly depending on the combination of inhibitors selected for profiling. This observation supports the reproducibility of the proposed metabophenotypes.

In line, it was important to start this study identify what could be the best metabolic targets to get a wide, but specific, landscape of the metabolic features of the breast cancer cell lines with potential for concise classification. . Recent observations in our lab and others have established that the balance in reducing power in cancer cells, mainly to sustain high levels of NAD+ in the cytosol, are critical to maintain a high glycolytic activity sustaining cell proliferation. Therefore, we chose two metabolites that have to be essential for the cells: pyruvate and aspartate, since in addition to their biosynthetic functions, these two metabolites are critical for the redox balance of the cells.

Pyruvate is the largest supplier of NAD+ in the cytosol. NAD+ is totally necessary to feed back glycolysis to sustain cell viability. When pyruvate is limited, aspartate must compensate for the production of NAD+ by increasing its spin in the aspartate/malate shuttle.Thus, the cancer cells must be addictive or not to pyruvate, aspartate or both, therefore, these metabolites were essential targets for defining the cellular metabophenotypes of breast cancer.

A very good approach to answer whether breast cancer cell lines were addictive/sensitive or not to pyruvate and aspartate was by using the pan inhibitor of aspartate transaminases aminooxyacetate (AOA).

AOA inhibits the interchange between aspartate and oxaloacetate by transamination. Aspartate can be converted into oxaloacetate, and then oxaloacetate can be reduced to malate; thus consuming NADH and providing NAD+. If the cells are dependent into aspartate production of NAD+, complementary to the major pyruvate source then AOA treatment must result toxic for the cells.

As seen in the figure 4.5.1, only two of the cell lines resulted very dependent on aspartate transamination MDA-MD-231 and MDA-MD-468. On the other hand, only the cell line MCF7 showed total resistance to AOA inhibition, and finally other two cell lines (ZR751 and SKBR3) displayed moderate sensitivity to AOA treatment.

In the line with the sensitivity or resistance to AOA treatment, we next made rescue experiments using pyruvate and aspartate: The cell lines sensitive to AOA, MDA-MD-231 and MDA-MD-468, were successfully rescued by extracellular addition of piruvate, and aspartate too. . Therefore, it could be concluded that these cell lines displayed "metabolic addiction" to piruvate and aspartate. . On the contrary, MCF7 cell line did not show any change, thus confirming its resistance to transaminase inhibition by AOA, which was in line with a less pronounced dependency on aspartate/piruvate. . Likewise, the other two cell lines SKBR3 and ZR751, which resulted partially sensitive to transaminases inhibition by AOA, were also dependent on pyruvate rescue and slightly dependent on aspartate. These observations suggested that, as expected when the selected approach is designed to cover a wide observation of metabolism, that give

result to establish such intermediate metabophenotypes, like SKBR3 and ZR751 for aspartate/piruvate dependency. It would be necessary now to propose further experimental projects to cover deeply in detail all the metabolic pathways and differences to refine the differences between phenotypes, such as, for example, by using metabolomic approaches by mass spectrometry dynamic metabolic flux analysis

Table 4.5.1. Summary table with the response of the different breast cancer cell lines to the inhibitors.

| | 1 | | 2 | 3 | |
|---|---|---|---|---|---|
| **METABOPHENOTYPE** | **Higher dependence Glycolisis (Warburg effect)/Glutamine** | | | **Mitochondrial oxidative metabolism** | |
| **Histology** | Luminal | | HER2 | Basal | |
| **Cell line** | **MCF7** | **ZR-751** | **SKBR3** | **MDA-MB-468** | **MDA-MB-231** |
| **Expression Hormone Receptors** | $ER^+$ / $PG^{+/-}$ | $ER^+$ / $PG^{+/-}$ | $ER^-$ / $PG^-$ | $ER^-$ / $PG^-$ | $ER^-$ / $PG^-$ |
| **HER2** | - | + | + | - | - |
| **Mitochondrial uncoupling/ ATP dependence (BAM15 sensitivity)** | - | - | + | + | + |
| **NAD+ dependence (Phenformin sensitivity)** | + | + | - | - | - |
| **Glycolisis dependence (Akt inhibition)** | + | + | + | - | - |
| **Aspartate/Malate shuttle dependence (AOA inhibition)** | - | + | + | +++ | +++ |
| **Pyruvate rescue (under AOA inhibition)** | independent | + | + | +++ | +++ |
| **Aspartate rescue (under AOA inhibition)** | independent | + | + | +++ | +++ |
| **EGCG inhibition** | + | + | + | - | - |
| **PDH activation / pyruvate entry to TCA (DCA sensitivity)** | + | + | - | - | - |

After these experiments, we have found three different metabophenotypes in response to AOA treatments.

Following the metabolic study centered in transaminase and asparttate/piruvate dependenciesof breast cancer cell lines, we next used the mitochondrial uncoupler BAM15((2-fluorophenyl){6-[(2-fluorophenyl)amino](1,2,5-oxadiazolo[3,4-e]pyrazin-5-

yl)}amine[8] in order to analyze the ATP dependence by mitochondrial oxidative metabolism of each cell line.

The treatment with BAM15 revealed that the triple negative basal cell lines (MDA-MD-231 and MDA-MD-468) and HER2 positive cell line (SKBR3) presented a marked sensitivity. The loss of cell viability due to mitochondrial uncoupling (sensitivity to BAM15) and reduction of the ATP synthesis indicates that these are cell lines that are more dependent on mitochondrial oxidative metabolism. In contrast, luminal cell lines, positive for hormone receptors (MCF7 and ZR751), showed resistance to treatment with BAM15. These data partially indicates greater independence over mitochondrial oxidative metabolism.

Next, complex I of the mitochondrial respiration chain was inhibited by treatment with phenphormin. This compound inhibits the reactions of substrate oxidation in complex I, therefore drastically reduces the conversion of NADH to $NAD^+$, affecting the cellular redox balance and in particular the availability of NAD+. Of note, affecting the availability of $NAD^+$ directly impact on the capacity to sustain a high glycolytic rate. As for the treatment with phenformin, the profile found was just the opposite of the profile displayed by the uncoupler BAM15, that is, the luminal lines were sensitive to treatment, while the triple negative basal lines were resistant. These data suggested that the luminal lines are more dependent on the redox balance at the $NAD^+$/NADH level, probably due to a greater reliance on $NAD^+$ recycling to maintain a high glycolytic rate.

Next, the results displayed by using the Akt inhibitor BMK-120 (a main oncoge activator of the glycolytic pathway), confirmed that, by its prominent sensitivity to its inhibition, the luminal cells MCF7 and ZR751 displayed a strikingly glycolytic dependent metabolism. s. It should be noted that the HER2 positive line, SKBR3 presented a different metabolic profile than the other two cell groups, being moderately sensitive to BAM15 and partially resistant to treatment with phenformin, it is nonetheless sensitive to treatment with BKM-120. Likewise we argued above, further metabolomic approaches should be done to decipher a detailed pattern of metabolic targets which could explain the slight differences found in this work.

To verify the sensitivity to an inhibition in the metabolism of glutamine, we found that the luminal cell lines, more glycolytic, were very sensitive to treatment with EGCG, while basal cell lines, more active at the mitochondrial oxidative level, showed resistance to treatment.

According to the results obtained using the different inhibitors, we found a difference according to the results obtained with AOA inhibitor. The main difference lies in that with AOA he three main metabophenotypes resulting were: MCF7 resistant, ZR751 and SKBR3 moderately sensitive and MDA-MB-231 and MDA-MB-468 very

sensitive. However, with the rest of the inhibitors used, the trend varies MCF7 and ZR751, present a highly glycolytic profile, showing approximately the same viability data. The triple negative cell lines MDA-MB-231 and MDA-MB-468 also present a very close profile between them, showing themselves to be dependent on oxidative mitochondrial respiration. And the SKBR3 cell line is shown as an intermediate profile between the two previous metabophenotypes, its viability data coinciding with one or the other profile, depending on the inhibitor used.

The last inhibitor used was dichloroacetate. DCA has the ability to promote mitochondrial metabolism. The results obtained were not favourable in four of the fives lines. Despite expecting favourable results, we found only the ZR751 cell line, DCA affected cell viability. In the SKBR3, MDA-MB-231 and MDA-MB-468 cell lines, a slight decrease in viability is observed, but they are considered resistant lines.

Our results corroborate other studies that call into question the fact that despite the high metabolic potential of DCA, it did not work as expected. We have found that the cell lines respond or not without following the apparent pattern they show in the presence of other inhibitors. In addition, the use of high concentrations is necessary. However, the DCA molecule is small, ubiquitous, and has easy access to any part of the cell. Therefore, we decided to continue the study of this molecule by linked it with different molecules to check whether or not we could improve its effect.

First, Tiophene was the molecule liked to DCA. The results obtained using DCA-tiophene shows an improvement compared to DCA. Therefore, the effect on breast cancer cell lines has been enhanced thanks to the use of a molecule (tiophene) that acts as a more specific directional DCA to the mitochondrial area. When the DCA arrives more precisely, the concentration in this area increases and the thiophene helps it to penetrate more easily into the mitochondria, in this way, the same concentration decreases cell viability up to 4 times.

After these promising results we decided to continue the study using three tiophene-like compounds (two thizols and one benzotiophene). Benzotiophene gave very bad results because it could not be dissolved well and was therefore discarded for further studies. However, the two thiazoles show very good results. The thiazol named DCA-1-TZ2 gave the best results, obtaining an IC50 with a concentration of approximately 1 mM, varying according to the cell line. The experiments to test the cancer "antimetabolic" potential of DCA derivatives shed very promising data considering only the breast cancer cell models. The treatments with DCA derivatives were much more efficient that naïve DCA on its impact in breast cancer cell viability. However, to provide additional data supporting the potential therapeutic features of DCA derivatives, when DCA-1-TZ1 and DCA-1-TZ2 were tested with non-transformed proliferative mammary cells and fibroblasts, the data were less promising, since DCA-

1-TZ1 and DCA-1-TZ2 resulted equally toxic with the non-transformed cellular models. Nevertheless, it is important to remark that, despite of the tumoral features of these cells, both mammary cell model and fibroblasts are proliferative cells. Thus, it is possible to argue that the metabolism of these proliferative non-transformed cell lines could display similar features of cancer cells, and therefore also showing high sensitivity to continuous activation of PDHA forced by the inhibitory capacity of DCA on PDHK. Accordingly, it was already proposed, and empirically demonstrated, in the essential works from 2008 supporting the metabolic reprogramming paradigm, that proliferative non-transformed and cancer cells share, at least in culture, most of their fundamental metabolic functions[162, 163, 293]. Therefore, these observations could at least partially explain why DCA-1-TZ1 and DCA-1-TZ2 exerted a similar degree of toxicity in both, the breast cancer cell lines and the non-transformed mammary and fibroblast cells. In line, we propose future experiments testing additional non-transformed cells, such us endothelial progenitors and/or adult multipotent stem cells, to compare with a representative number of non-transformed proliferative cells, with different ontogenic and functional features. In addition, to fully answer the question whether DCA derivatives could display promising therapeutic potential, it would be necessary in future to test DCA derivatives in vivo with animal models.

DCA-2-TP could not be tested in this work mainly due to time limitations during the thesis stay in Trento. Therefore testing this DCA derivative should be also done in short future.

# *Conclusions*

# 5. CONCLUSIONS

## 5.1 DEVELOPMENT OF FLIM NANOSENSORS

In this Thesis, several QD-based nanosensors have been designed and optimized, specifically taking advantage of the long PL lifetime of the QDs for the use of FLIM microscopy.

In this regard, we have described a family of nanosensors, in which QDs of different sizes were modified with cyclam or cyclen, exhibiting a selective response towards $Zn^{2+}$ ions. The sensing mechanism was based on a photo-induced electron transfer, causing the enhancement of the average PL lifetime of the QDs in the presence of $Zn^{2+}$ ions. The performance of these nanosensors was tested in bulk solution and by FLIM imaging on glass slides and inside living cells.

We have also developed a family of pH nanosensors with different applications in the study of the cellular metabolism. One of the sensors was employed in the estimation of the pH extracellular media. The second nanosensor was designed to be delivered inside mitochondria, and report on the intra-mitochondrial pH by means of FLIM imaging.

We applied these nanosensors in the study of the metabolic behavior of five different breast cancer cell lines, related to the current clinical classification of breast cancer tissues. These experiments demonstrated that MC7, ZR751 and SKBR3 cell lines showed an extracellular pH higher than that of MDA-MB-231 and MDA-MB-468 cells. In contrast, when the nanosensors were applied inside mitochondria, we found that MCF7 cells exhibited a lower intramitochondrial pH lower than that of SKBR3, MDA-MB-231 and MDA-MB-468 cells.

## 5.2 METABOLIC PROFILING

In this Thesis, we have performed a metabolic study of different breast cancer models. To do this, we have subjected the aforementioned breast cancer cell lines to different metabolic inhibitors to elucidate the sensitivity and response of the cellular populations.

After subjecting the cell lines to inhibition by AOA transaminase inhibitor, we obtained a first metabolic classification based on the dependence of the cell lines on the metabolites aspartate and pyruvate and, therefore, we established the importance of the redox balance for their metabolism.

In order to investigate whether the metabolism of the glycolytic cell lines depends on mitochondrial metabolism, we used a mitochondrial membrane-decoupling agent, BAM15, to explore the ATP dependence of the lines. The triple negative (MDA-MB-231 and MDA-MB-468) and SKBR3 cell lines were sensitive to this inhibition. Dependence on $NAD^+$ and glycolysis was then tested using the inhibitors phenformin and Akt, respectively. For both inhibitors, the cell lines MCF7, ZR751 and SKBR3 were sensitive.

With these results, we could clearly establish that the cell lines MCF7 and ZR751 show a glycolysis-dependent metabolism. However, the triple negative cell lines show a profile dependent on mitochondrial metabolism. Finally, the SKBR3 cell line exhibits a metabolism that shares some common features between the other two metabophenotypes.

## 5.3 USE OF NANOSENSORES FOR METABOLIC PROFILING

Finally, the ultimate aim of this Thesis was to correlate the pH differences found in different breast cancer cell lines using QD-based nanosensors with the metabolic classification proposed in this work. When analyzing the nanosensing results together, one may suggest that there are two clearly distinct profiles: the one composed of the triple negative cell lines, MDA-MB-231 and MDA-MB-468, and that of the MCF7 and possibly ZR751 (the tries to introduce the intramitochondrial nanosensor in these cells were unsuccessful).

These results are perfectly in line with the metabolic profiling and the metabophenotype classification proposed in this work. Table 5.3.1 shows the final full definition of the metabophenotypes, with the addition of the pH information gathered from the application of the QD nanosensors. The metabophenotype **3**, with dependence on the mitochondrial oxidative metabolism, displayed lower extracellular pH and high intra-mitochondrial pH (9.2-9.3). In contrast, the more glycolytic cell lines, metabophenotype **1**, exhibited extracellular values around 8, and we found a significantly lower intramitochondrial pH in MCF7 cells (8.6). Interestingly, the HER2 positive cell line SKBR3 may present an intermediate metabolic profile, with properties lying between the other two: extracellular pH closer to metabophenotype **1**, but intramitochondrial pH similar to metabophenotype **3**.

Table 5.3.1. Summary table with the response of the different breast cancer cell lines to the inhibitors.

| | 1 | | 2 | 3 | |
|---|---|---|---|---|---|
| **METABOPHENOTYPE** | Higher dependence Glycolisis (Warburg effect)/Glutamine | | | Mitochondrial oxidative metabolism | |
| **Histology** | Luminal | | HER2^{+} | Basal | |
| **Cell line** | MCF7 | ZR-751 | SKBR3 | MDA-MB-468 | MDA-MB-231 |
| **Expression Hormone Receptors** | ER$^+$ / PG$^{+/-}$ | ER$^+$/PG$^{+/-}$ | ER$^-$/PG$^-$ | ER$^-$ / PG$^-$ | ER$^-$ / PG$^-$ |
| **HER2** | - | + | + | - | - |
| **Mitochondrial uncoupling/ ATP dependence (BAM15 sensitivity)** | - | - | + | + | + |
| **NAD$^+$ dependence (Phenformin sensitivity)** | + | + | - | - | - |
| **Glycolisis dependence (Akt inhibition)** | + | + | + | - | - |
| **Aspartate/Malate shuttle dependence (AOA inhibition)** | - | + | + | +++ | +++ |
| **Pyruvate rescue (under AOA inhibition)** | independent | + | + | +++ | +++ |
| **Aspartate rescue (under AOA inhibition)** | independent | + | + | +++ | +++ |
| **EGCG inhibition** | + | + | + | - | - |
| **PDH activation / pyruvate entry to TCA (DCA sensitivity)** | + | + | - | - | - |
| **Extracellular pH** | 8.16±0.21 | 7.84±0.06 | 7.22±0.08 | 5.35±0.13 | 5.17±0.16 |
| **Mitochondrial pH** | 8.66±0.64 | | 9.23±0.71 | 9.30±069 | 9.17±0.94 |

In summary, the combined use of pH sensitive nanoparticles and FLIM technologies might be further considered for potential diagnostic approaches based in the metabolic features of cancer cells.

*References*

# 6. REFERENCES

1. Corbett, J., McKeown, P. A., Peggs, G. N., and Whatmore, R. (2000) Nanotechnology: International Developments and Emerging Products, *CIRP Annals 49*, 523-545.

2. Mohan Bhagyaraj, S., and Oluwafemi, O. S. (2018) Chapter 1 - Nanotechnology: The Science of the Invisible, In *Synthesis of Inorganic Nanomaterials* (Mohan Bhagyaraj, S., Oluwafemi, O. S., Kalarikkal, N., and Thomas, S., Eds.), pp 1-18, Woodhead Publishing.

3. Ramsden, J. J. (2018) Chapter 1 - What is Nanotechnology?, In *Applied Nanotechnology (Third edition)*, pp 3-13, William Andrew Publishing.

4. Goesmann, H., and Feldmann, C. (2010) Nanoparticulate Functional Materials, *Angew. Chem. Int. Ed 49*, 1362-1395.

5. Ruedas-Rama, M. J., Walters, J. D., Orte, A., and Hall, E. A. H. (2012) Fluorescent nanoparticles for intracellular sensing: A review, *Anal. Chim. Acta 751*, 1-23.

6. Penn, S. G., He, L., and Natan, M. J. (2003) Nanoparticles for bioanalysis, *Current Opinion in Chemical Biology 7*, 609-615.

7. Cuenca, A. G., Jiang, H., Hochwald, S. N., Delano, M., Cance, W. G., and Grobmyer, S. R. (2006) Emerging implications of nanotechnology on cancer diagnostics and therapeutics, *Cancer 107*, 459-466.

8. Makkar, H., and Patri, G. (2017) Fabrication and Appraisal of Poly (Lactic-Co-Glycolic Acid) - Moxifloxacin Nanoparticles using Vitamin E-TPGS: A Potential Intracanal Drug Delivery Agent, *Journal of clinical and diagnostic research : JCDR 11*, Zc05-zc08.

9. Bahrami, B., Hojjat-Farsangi, M., Mohammadi, H., Anvari, E., Ghalamfarsa, G., Yousefi, M., and Jadidi-Niaragh, F. (2017) Nanoparticles and targeted drug delivery in cancer therapy, *Immunology letters 190*, 64-83.

10. Schmälzlin, E., van Dongen, J. T., Klimant, I., Marmodée, B., Steup, M., Fisahn, J., Geigenberger, P., and Löhmannsröben, H.-G. (2005) An Optical Multifrequency Phase-Modulation Method Using Microbeads for Measuring Intracellular Oxygen Concentrations in Plants, *Biophysical journal 89*, 1339-1345.

11. Xue, J., Guan, Z., Zhu, X., and Lin, J. (2018) Cellular internalization of polypeptide-based nanoparticles: effects of size, shape and surface morphology.

12. Cao, Y., Lee Koo, Y.-E., and Kopelman, R. (2004) Poly(decyl methacrylate)-based fluorescent PEBBLE swarm nanosensors for measuring dissolved oxygen in biosamples, *Analyst 129*, 745-750.

13. Ruedas-Rama, M. J., and Hall, E. A. H. (2006) $K^+$-selective nanospheres: maximising response range and minimising response time, *Analyst 131*, 1282-1291.

14. Han, D. M., Zhang, Q. M., and Serpe, M. J. (2015) Poly (N-isopropylacrylamide)-co-(acrylic acid) microgel/Ag nanoparticle hybrids for the colorimetric sensing of H2O2, *Nanoscale 7*, 2784-2789.

15. Aso, E., Martinsson, I., Appelhans, D., Effenberg, C., Benseny-Cases, N., Cladera, J., Gouras, G., Ferrer, I., and Klementieva, O. (2019) Poly(propylene imine) dendrimers with histidine-maltose shell as novel type of nanoparticles for synapse and memory protection, *Nanomedicine : nanotechnology, biology, and medicine*.

16. Ekimov, A. I., Efros, A. L., and Onushchenko, A. A. (1985) Quantum size effect in semiconductor microcrystals, *Solid State Communications 56*, 921-924.

17. Brus, L. E. (1983) A simple model for the ionization potential, electron affinity, and aqueous redox potentials of small semiconductor crystallites, *The Journal of Chemical Physics 79*, 5566-5571.

18. Reed, M. A., Randall, J. N., Aggarwal, R. J., Matyi, R. J., Moore, T. M., and Wetsel, A. E. (1988) Observation of discrete electronic states in a zero-dimensional semiconductor nanostructure, *Physical Review Letters 60*, 535-537.

19. Henglein, A. (1982) Photo-Degradation and Fluorescence of Colloidal-Cadmium Sulfide in Aqueous Solution, *Berichte der Bunsengesellschaft für physikalische Chemie 86*, 301-305.

20. Itoh, T., Katohno, T., and Ueta, M. (1984) Relaxation Process of Excitonic Molecules in CuCl under the Two-Photon Resonant Excitation. I. Mutual Collision of Excitonic Molecules, *Journal of the Physical Society of Japan 53*, 844-853.

21. Norris, D. J., Sacra, A., Murray, C. B., and Bawendi, M. G. (1994) Measurement of the size dependent hole spectrum in CdSe quantum dots, *Phys Rev Lett 72*, 2612-2615.

22. Schmidt, M. E., Blanton, S. A., Hines, M. A., and Guyot-Sionnest, P. (1996) Size-dependent two-photon excitation spectroscopy of CdSe nanocrystals, *Physical review. B, Condensed matter 53*, 12629-12632.

23. Sabaeian, M., and Khaledi-Nasab, A. (2012) Size-dependent intersubband optical properties of dome-shaped InAs/GaAs quantum dots with wetting layer, *Applied Optics 51*, 4176-4185.

24. Esteve-Turrillas, F. A., and Abad-Fuentes, A. (2013) Applications of quantum dots as probes in immunosensing of small-sized analytes, *Biosens Bioelectron 41*, 12-29.

25. Wu, X., Liu, H., Liu, J., Haley, K. N., Treadway, J. A., Larson, J. P., Ge, N., Peale, F., and Bruchez, M. P. (2003) Immunofluorescent labeling of cancer marker Her2 and other cellular targets with semiconductor quantum dots, *Nat Biotech 21*, 41-46.

26. Shariatifar, H., Hakhamaneshi, M. S., Abolhasani, M., Ahmadi, F. H., Roshani, D., Nikkhoo, B., Abdi, M., and Ahmadvand, D. (2018) Immunofluorescent labeling of CD20 tumor marker with quantum dots for rapid and quantitative detection of diffuse large B-cell non-Hodgkin's lymphoma.

27. Ke, X., Zhang, Y., Zheng, F., Liu, Y., Zheng, Z., Xu, Y., and Wang, H. (2018) SpyCatcher-SpyTag mediated in situ labelling of progeny baculovirus with quantum dots for tracking viral infection in living cells, *Chem Commun (Camb) 54*, 1189-1192.

28. Zhao, J. Y., Chen, G., Gu, Y. P., Cui, R., Zhang, Z. L., Yu, Z. L., Tang, B., Zhao, Y. F., and Pang, D. W. (2016) Ultrasmall Magnetically Engineered Ag2Se Quantum Dots for Instant Efficient Labeling and Whole-Body High-Resolution Multimodal Real-Time Tracking of Cell-Derived Microvesicles, *J Am Chem Soc 138*, 1893-1903.

29. Pathak, S., Choi, S.-K., Arnheim, N., and Thompson, M. E. (2001) Hydroxylated Quantum Dots as Luminescent Probes for in Situ Hybridization, *Journal of the American Chemical Society 123*, 4103-4104.

30. Zhang, W., Hubbard, A., Pang, L., Parkinson, L. B., Brunhoeber, P., Wang, Y., and Tang, L. (2015) Protecting Quantum Dot Fluorescence from Quenching to Achieve a Reliable Automated Multiplex Fluorescence In Situ Hybridization Assay, *J Biomed Nanotechnol 11*, 1583-1596.

31. Jaiswal, J. K., Mattoussi, H., Mauro, J. M., and Simon, S. M. (2003) Long-term multiple color imaging of live cells using quantum dot bioconjugates, *Nat Biotech 21*, 47-51.

32. Sukhanova, A., Devy, J., Venteo, L., Kaplan, H., Artemyev, M., Oleinikov, V., Klinov, D., Pluot, M., Cohen, J. H. M., and Nabiev, I. (2004) Biocompatible fluorescent nanocrystals for immunolabeling of membrane proteins and cells, *Analytical Biochemistry 324*, 60-67.

33. Murray, C. B., Norris, D. J., and Bawendi, M. G. (1993) Synthesis and characterization of nearly monodisperse CdE (E ) S, Se, Te) semiconductor nanocrystallites, *J. Am. Chem. Soc. 115*, 8706-8715.

34. Bruchez, M., Moronne, M., Gin, P., Weiss, S., and Alivisatos, A. P. (1998) Semiconductor Nanocrystals as Fluorescent Biological Labels, *Science 281*, 2013-2016.

35. Chan, W. C. W., and Nie, S. (1998) Quantum Dot Bioconjugates for Ultrasensitive Nonisotopic Detection, *Science 281*, 2016-2018.

178

36.	Gao, X., Yang, L., Petros, J. A., Marshall, F. F., Simons, J. W., and Nie, S. (2005) In vivo molecular and cellular imaging with quantum dots., *Curr. Opin. Biotechnol. 16*, 63-72.

37.	Medintz, I. L., Uyeda, H. T., Goldman, E. R., and Mattoussi, H. (2005) Quantum dot bioconjugates for imaging, labelling and sensing, *Nat. Mater. 4*, 435-446.

38.	Michalet, X., Weiss, S., and Jäger, M. (2006) Single-Molecule Fluorescence Studies of Protein Folding and Conformational Dynamics, *Chemical Reviews 106*, 1785-1813.

39.	Goldman, E., Medintz, I., and Mattoussi, H. (2006) Luminescent quantum dots in immunoassays, *Anal. Bioanal. Chem. 384*, 560-563.

40.	Zhao, M., Chen, Y., Han, R., Luo, D., Du, L., Zheng, Q., Wang, L., Hong, Y., Liu, Y., and Sha, Y. (2018) A facile synthesis of biocompatible, glycol chitosan shelled CdSeS/ZnS QDs for live cell imaging, *Colloids and surfaces. B, Biointerfaces 172*, 752-759.

41.	Bilan, R., Fleury, F., Nabiev, I., and Sukhanova, A. (2015) Quantum dot surface chemistry and functionalization for cell targeting and imaging, *Bioconjug Chem 26*, 609-624.

42.	Chen, Y., and Rosenzweig, Z. (2002) Luminescent CdS Quantum Dots as Selective Ion Probes, *Anal. Chem. 74*, 5132-5138.

43.	Liang, J. G., Ai, X. P., He, Z. K., and Pang, D. W. (2004) Functionalized CdSe quantum dots as selective silver ion chemodosimeter, *Analyst 129*, 619-622.

44.	Chen, X., Guo, J., Peng, X., Guo, M., Xu, Y., Shi, L., Liang, C., Wang, L., Gao, Y., Sun, S., and Cai, S. (2005) Novel cyanine dyes with different methine chains as sensitizers for nanocrystalline solar cell, *J. Photochem. Photobiol. A: Chem. 171*, 231-236.

45.	Jin, W. J., Fernandez-Arguelles, M. T., Costa-Fernandez, J. M., Pereiro, R., and Sanz-Medel, A. (2005) Photoactivated luminescent CdSe quantum dots as sensitive cyanide probes in aqueous solutions, *Chem. Commun.*, 883-885.

46.	Nasri, S., Bardajee, G. R., and Bayat, M. (2018) Synthesis, characterization and energy transfer studies of fluorescent dye-labeled metal-chelating polymers anchoring pendant thiol groups for surface modification of quantum dots and investigation on their application for pH-responsive controlled release of doxorubicin, *Colloids and surfaces. B, Biointerfaces 171*, 544-552.

47.	Gattas-Asfura, K. M., and Leblanc, R. M. (2003) Peptide-coated CdS quantum dots for the optical detection of copper(II) and silver(I), *Chem Commun (Camb)*, 2684-2685.

48.	Pinaud, F., King, D., Moore, H.-P., and Weiss, S. (2004) Bioactivation and Cell Targeting of Semiconductor CdSe/ZnS Nanocrystals with Phytochelatin-Related Peptides, *Journal of the American Chemical Society 126*, 6115-6123.

49.	Tsay, J. M., Doose, S., and Weiss, S. (2006) Rotational and translational diffusion of peptide-coated CdSe/CdS/ZnS nanorods studied by fluorescence correlation spectroscopy, *J. Am. Chem. Soc. 128*, 1639-1647.

50.	Tsay, J. M., Doose, S., Pinaud, F., and Weiss, S. (2005) Enhancing the photoluminescence of peptide-coated nanocrystals with shell composition and UV irradiation, *The journal of physical chemistry. B 109*, 1669-1674.

51.	Mattoussi, H., Mauro, J. M., Goldman, E. R., Anderson, G. P., Sundar, V. C., Mikulec, F. V., and Bawendi, M. G. (2000) Self-Assembly of CdSe–ZnS Quantum Dot Bioconjugates Using an Engineered Recombinant Protein, *J. Am. Chem. Soc. 122*, 12142-12150.

52.	Goldman, E. R., Anderson, G. P., Tran, P. T., Mattoussi, H., Charles, P. T., and Mauro, J. M. (2002) Conjugation of luminescent quantum dots with antibodies using an engineered adaptor protein to provide new reagents for fluoroimmunoassays, *Anal Chem 74*, 841-847.

53.	Goldman, E. R., Balighian, E. D., Mattoussi, H., Kuno, M. K., Mauro, J. M., Tran, P. T., and Anderson, G. P. (2002) Avidin: a natural bridge for quantum dot-antibody conjugates, *J Am Chem Soc 124*, 6378-6382.

54. Lingerfelt, B. M., Mattoussi, H., Goldman, E. R., Mauro, J. M., and Anderson, G. P. (2003) Preparation of quantum dot-biotin conjugates and their use in immunochromatography assays, *Anal Chem 75*, 4043-4049.

55. Patolsky, F., Gill, R., Weizmann, Y., Mokari, T., Banin, U., and Willner, I. (2003) Lighting-Up the Dynamics of Telomerization and DNA Replication by CdSeâˆ'ZnS Quantum Dots, *J. Am. Chem. Soc. 125*, 13918-13919.

56. Mitchell, G. P., Mirkin, C. A., and Letsinger, R. L. (1999) Programmed Assembly of DNA Functionalized Quantum Dots, *Journal of the American Chemical Society 121*, 8122-8123.

57. Wei, Q., Lee, M., Yu, X., Lee, E. K., Seong, G. H., Choo, J., and Cho, Y. W. (2006) Development of an open sandwich fluoroimmunoassay based on fluorescence resonance energy transfer, *Anal Biochem 358*, 31-37.

58. Spanhel, L., Haase, M., Weller, H., and Henglein, A. (1987) Photochemistry of colloidal semiconductors. 20. Surface modification and stability of strong luminescing CdS particles, *Journal of the American Chemical Society 109*, 5649-5655.

59. Moore, D. E., and Patel, K. (2001) Q-CdS Photoluminescence Activation on Zn2+ and Cd2+ Salt Introduction, *Langmuir 17*, 2541-2544.

60. Liu, X. W., Shu, J. S., Xiao, Y., Yang, Y., and Zhang, S. B. (2017) Selective and Sensitive Detection of Silver(I) Ion Based on Tetracationic Complex and TGA/GSH Co-capped Quantum Dots as an Effective Fluorescent Sensing Platform, *Anal Sci 33*, 381-385.

61. Ripoll, C., Martin, M., Roldan, M., Talavera, E. M., Orte, A., and Ruedas-Rama, M. J. (2015) Intracellular $Zn^{2+}$ detection with quantum dot-based FLIM nanosensors, *Chem. Commun. 51*, 16964-16967.

62. Guo, C., Wang, J., Cheng, J., and Dai, Z. (2012) Determination of trace copper ions with ultrahigh sensitivity and selectivity utilizing CdTe quantum dots coupled with enzyme inhibition, *Biosens Bioelectron 36*, 69-74.

63. He, L., Bao, Z., Zhang, K., Yang, D., Sheng, B., Huang, R., Zhao, T., Liang, X., Yang, X., Yang, A., Zhang, C., Cui, P., Zapien, J. A., and Zhou, H. (2018) Ratiometric determination of copper(II) using dually emitting Mn(II)-doped ZnS quantum dots as a fluorescent probe, *185*, 511.

64. Bo, C., and Ping, Z. (2005) A new determining method of copper(II) ions at ng ml(-1) levels based on quenching of the water-soluble nanocrystals fluorescence, *Anal Bioanal Chem 381*, 986-992.

65. Fernández-Argüelles, M. T., Jin, W. J., Costa-Fernández, J. M., Pereiro, R., and Sanz-Medel, A. (2005) Surface-modified CdSe quantum dots for the sensitive and selective determination of Cu(II) in aqueous solutions by luminescent measurements, *Analytica Chimica Acta 549*, 20-25.

66. Zhu, J., Zhao, Z. J., Li, J. J., and Zhao, J. W. (2017) CdTe quantum dot-based fluorescent probes for selective detection of Hg (II): The effect of particle size, *Spectrochimica acta. Part A, Molecular and biomolecular spectroscopy 177*, 140-146.

67. She, S., Zhou, Y., Zhang, L., Wang, L., and Wang, L. (2005) Preparation of fluorescent polyvinyl alcohol keto-derivatives nanoparticles and selective determination of chromium(VI), *Spectrochimica Acta Part A: Molecular and Biomolecular Spectroscopy 62*, 711-715.

68. Wang, Y. M., Tegenfeldt, J. O., Reisner, W., Riehn, R., Guan, X.-J., Guo, L., Golding, I., Cox, E. C., Sturm, J., and Austin, R. H. (2005) Single-molecule studies of repressorâ€"DNA interactions show long-range interactions, *Proc. Natl. Acad. Sci. U.S.A. 102*, 9796-9801.

69. Vaishanav, S. K., Korram, J., Pradhan, P., Chandraker, K., Nagwanshi, R., Ghosh, K. K., and Satnami, M. L. (2017) Green Luminescent CdTe Quantum Dot Based Fluorescence Nano-Sensor for Sensitive Detection of Arsenic (III), *J Fluoresc 27*, 781-789.

70. Shamsipur, M., and Rajabi, H. R. (2014) Pure zinc sulfide quantum dot as highly selective luminescent probe for determination of hazardous cyanide ion, *Materials science & engineering. C, Materials for biological applications 36*, 139-145.

71. Palaniappan, K., Hackney, S. A., and Liu, J. (2004) Supramolecular control of complexation-induced fluorescence change of water-soluble, b-cyclodextrinmodified CdS quantum dots, *Chem. Commun.*, 2704-2705.

72. Fabbrizzi, L., Licchelli, M., Parodi, L., Poggi, A., and Taglietti, A. (1998) The Molecular Design of Fluorescent Sensors for Ionic Analytes, *Journal of Fluorescence 8*, 263-271.

73. Ai, X., Niu, L., Li, Y., Yang, F., and Su, X. (2012) A novel beta-Cyclodextrin-QDs optical biosensor for the determination of amantadine and its application in cell imaging, *Talanta 99*, 409-414.

74. Jin, T., Fujii, F., Sakata, H., Tamura, M., and Kinjo, M. (2005) Amphiphilic p-sulfonatocalix[4]arene-coated CdSe/ZnS quantum dots for the optical detection of the neurotransmitter acetylcholine, *Chem. Commun.*, 4300-4302.

75. Li, H., Xiong, W., Yan, Y., Liu, J. a., Xu, H., and Yang, X. (2006) Selenium calixarene for luminescent and stable quantum dots, *Materials Letters 60*, 703-705.

76. Engeser, M., Fabbrizzi, L., Licchelli, M., and Sacchi, D. (1999) A fluorescent molecular thermometer based on the nickel(II) high-spin/low-spin interconversion, *Chemical Communications*, 1191-1192.

77. Park, S. M., Kim, M. H., Choe, J. I., No, K. T., and Chang, S. K. (2007) Cyclams bearing diametrically disubstituted pyrenes as Cu2+- and Hg2+-selective fluoroionophores, *J Org Chem 72*, 3550-3553.

78. Chen, B., Liu, J., Yang, T., Chen, L., Hou, J., Feng, C., and Huang, C. Z. (2019) Development of a portable device for Ag(+) sensing using CdTe QDs as fluorescence probe via an electron transfer process, *Talanta 191*, 357-363.

79. Wang, S., Liu, R., and Li, C. (2018) Highly Selective and Sensitive Detection of Hg(2+) Based on Forster Resonance Energy Transfer between CdSe Quantum Dots and g-C3N4 Nanosheets, *Nanoscale Res Lett 13*, 235.

80. Kasha, M. (1950) Characterization of electronic transitions in complex molecules, *Discussions of the Faraday Society 9*, 14-19.

81. Suhling, K., Hirvonen, L. M., Levitt, J. A., Chung, P.-H., Tregidgo, C., Le Marois, A., Rusakov, D. A., Zheng, K., Ameer-Beg, S., Poland, S., Coelho, S., Henderson, R., and Krstajic, N. (2015) Fluorescence lifetime imaging (FLIM): Basic concepts and some recent developments, *Medical Photonics 27*, 3-40.

82. Resch-Genger, U., Grabolle, M., Cavaliere-Jaricot, S., Nitschke, R., and Nann, T. (2008) Quantum dots versus organic dyes as fluorescent labels, *Nat Meth 5*, 763-775.

83. Ruedas-Rama, M.-J., Orte, A., Hall, E. A. H., Alvarez-Pez, J. M., and Talavera-Rodriguez, E. M. (2011) Quantum Dot Photoluminescence Lifetime-Based pH Nanosensor, *Biophysical Journal 100*, 468-469.

84. Harvey, C. D., Ehrhardt, A. G., Cellurale, C., Zhong, H., Yasuda, R., Davis, R. J., and Svoboda, K. (2008) A genetically encoded fluorescent sensor of ERK activity, *Proc. Natl. Acad. Sci. U.S.A. 105*, 19264-19269.

85. Ruedas-Rama, M. J., Orte, A., Hall, E. A. H., Alvarez-Pez, J. M., and Talavera, E. M. (2012) A chloride ion nanosensor for time-resolved fluorimetry and fluorescence lifetime imaging, *Analyst 137*, 1500-1508.

86. Amos, W. B., and White, J. G. (2003) How the Confocal Laser Scanning Microscope entered Biological Research, *Biology of the Cell 95*, 335-342.

87. Eisaman, M. D., Fan, J., Migdall, A., and Polyakov, S. V. (2011) Invited Review Article: Single-photon sources and detectors, *Review of Scientific Instruments 82*, 071101.

88.  Smith, G. S., Ma, Y., Dhawan, V., Chaly, T., and Eidelberg, D. (2009) Selective serotonin reuptake inhibitor (SSRI) modulation of striatal dopamine measured with [11C]-raclopride and positron emission tomography, *Synapse 63*, 1-6.

89.  Cox, S., and Jones, G. E. (2013) Imaging cells at the nanoscale, *The International Journal of Biochemistry & Cell Biology 45*, 1669-1678.

90.  Becker, W. (2012) Fluorescence lifetime imaging – techniques and applications, *Journal of Microscopy 247*, 119-136.

91.  Becker, W. (2015) Fluorescence lifetime imaging by multi-dimensional time correlated single photon counting, *Medical Photonics 27*, 41-61.

92.  Berezin, M. Y., and Achilefu, S. (2010) Fluorescence Lifetime Measurements and Biological Imaging, *Chem. Rev. 110*, 2641-2684.

93.  Venetta, B. D. (1959) Microscope Phase Fluorometer for Determining the Fluorescence Lifetimes of Fluorochromes, *Review of Scientific Instruments 30*, 450-457.

94.  Wang, X. F., Uchida, T., and Minami, S. (1989) A Fluorescence Lifetime Distribution Measurement System Based on Phase-Resolved Detection Using an Image Dissector Tube, *Applied Spectroscopy 43*, 840-845.

95.  Chen, Y., Mills, J. D., and Periasamy, A. (2003) Protein localization in living cells and tissues using FRET and FLIM, *Differentiation 71*, 528-541.

96.  (!!! INVALID CITATION !!!).

97.  Benninger, R. K. P., Hofmann, O., McGinty, J., Requejo-Isidro, J., Munro, I., Neil, M. A. A., deMello, A. J., and French, P. M. W. (2005) Time-resolved fluorescence imaging of solvent interactions in microfluidic devices, *Opt. Express 13*, 6275-6285.

98.  Graham, E. M., Iwai, K., Uchiyama, S., Prasanna de Silva, A., Magennis, S. W., and Jones, A. C. (2010) Quantitative mapping of aqueous microfluidic temperature with sub-degree resolution using fluorescence lifetime imaging microscopy, *Lab on a Chip 10*, 1267-1273.

99.  Esposito, A. (2012) Beyond Range: Innovating Fluorescence Microscopy, *Remote Sensing 4*, 111.

100. Nguyen, T. A., Sarkar, P., Veetil, J. V., Koushik, S. V., and Vogel, S. S. (2012) Fluorescence Polarization and Fluctuation Analysis Monitors Subunit Proximity, Stoichiometry, and Protein Complex Hydrodynamics, *PloS one 7*, e38209.

101. Kwak, E.-S., Kang, T. J., and Vanden Bout, D. A. (2001) Fluorescence Lifetime Imaging with Near-Field Scanning Optical Microscopy, *Analytical Chemistry 73*, 3257-3262.

102. Micic, M., Hu, D., Suh, Y. D., Newton, G., Romine, M., and Lu, H. P. (2004) Correlated atomic force microscopy and fluorescence lifetime imaging of live bacterial cells, *Colloids and Surfaces B: Biointerfaces 34*, 205-212.

103. Levitt, J. A., Chung, P.-H., Alibhai, D. R., and Suhling, K. (2011) Simultaneous measurements of fluorescence lifetimes, anisotropy, and FRAP recovery curves, In *SPIE BiOS*, p 9, SPIE.

104. Forster, T. (1946) Energiewanderung und Fluoreszenz, *Naturwissenschaften 33*, 166-175.

105. Haidekker, M. A., Tsai, A. G., Brady, T., Stevens, H. Y., Frangos, J. A., Theodorakis, E., and Intaglietta, M. (2002) A novel approach to blood plasma viscosity measurement using fluorescent molecular rotors, *American Journal of Physiology-Heart and Circulatory Physiology 282*, H1609-H1614.

106. Kung, C. E., and Reed, J. K. (1986) Microviscosity measurements of phospholipid bilayers using fluorescent dyes that undergo torsional relaxation, *Biochemistry 25*, 6114-6121.

107. Loison, P., Hosny, N. A., Gervais, P., Champion, D., Kuimova, M. K., and Perrier-Cornet, J.-M. (2013) Direct investigation of viscosity of an atypical inner membrane of Bacillus

spores: A molecular rotor/FLIM study, *Biochimica et Biophysica Acta (BBA) - Biomembranes 1828*, 2436-2443.

108. Battisti, A., Panettieri, S., Abbandonato, G., Jacchetti, E., Cardarelli, F., Signore, G., Beltram, F., and Bizzarri, R. (2013) Imaging intracellular viscosity by a new molecular rotor suitable for phasor analysis of fluorescence lifetime, *Analytical and Bioanalytical Chemistry 405*, 6223-6233.

109. Kung, C. E., and Reed, J. K. (1989) Fluorescent molecular rotors: a new class of probes for tubulin structure and assembly, *Biochemistry 28*, 6678-6686.

110. Okabe, K., Inada, N., Gota, C., Harada, Y., Funatsu, T., and Uchiyama, S. (2012) Intracellular temperature mapping with a fluorescent polymeric thermometer and fluorescence lifetime imaging microscopy, *Nat. Commun. 3*, 705.

111. Lakowicz, J. R. (2006) *Principles of Fluorescence Spectroscopy*, 3rd ed., Springer.

112. Saxl, T., Khan, F., Ferla, M., Birch, D., and Pickup, J. (2011) A fluorescence lifetime-based fibre-optic glucose sensor using glucose/galactose-binding protein, *Analyst 136*, 968-972.

113. Hosny, N. A., Lee, D. A., and Knight, M. M. (2012) Single photon counting fluorescence lifetime detection of pericellular oxygen concentrations, *J Biomed Opt 17*, 016007.

114. Dmitriev, R. I., Zhdanov, A. V., Nolan, Y. M., and Papkovsky, D. B. (2013) Imaging of neurosphere oxygenation with phosphorescent probes, *Biomaterials 34*, 9307-9317.

115. Dmitriev, R. I., Kondrashina, A. V., Koren, K., Klimant, I., Zhdanov, A. V., Pakan, J. M. P., McDermott, K. W., and Papkovsky, D. B. (2014) Small molecule phosphorescent probes for O2 imaging in 3D tissue models, *Biomaterials science 2*, 853-866.

116. Wang, H.-W., Chen, C.-T., Guo, H.-W., Yu, J.-S., Wei, Y.-H., Gukassyan, V., and Kao, F.-J. (2008) Differentiation of apoptosis from necrosis by dynamic changes of reduced nicotinamide adenine dinucleotide fluorescence lifetime in live cells, *Journal of Biomedical Optics 13*, 054011-054011-054019.

117. Galletly, N. P., McGinty, J., Dunsby, C., Teixeira, F., Requejo-Isidro, J., Munro, I., Elson, D. S., Neil, M. A. A., Chu, A. C., French, P. M. W., and Stamp, G. W. (2008) Fluorescence lifetime imaging distinguishes basal cell carcinoma from surrounding uninvolved skin, *British Journal of Dermatology 159*, 152-161.

118. Esposito, A., Gralle, M., Dani, M. A. C., Lange, D., and Wouters, F. S. (2008) pHlameleons: A Family of FRET-Based Protein Sensors for Quantitative pH Imaging†, *Biochemistry 47*, 13115-13126.

119. Tantama, M., Hung, Y. P., and Yellen, G. (2011) Imaging Intracellular pH in Live Cells with a Genetically Encoded Red Fluorescent Protein Sensor, *J. Am. Chem. Soc. 133*, 10034-10037.

120. Kuimova, M. K., Yahioglu, G., Levitt, J. A., and Suhling, K. (2008) Molecular Rotor Measures Viscosity of Live Cells via Fluorescence Lifetime Imaging, *J. Am. Chem. Soc. 130*, 6672-6673.

121. Paredes, J. M., Giron, M. D., Ruedas-Rama, M. J., Orte, A., Crovetto, L., Talavera, E. M., Salto, R., and Alvarez-Pez, J. M. (2013) Real-Time Phosphate Sensing in Living Cells using Fluorescence Lifetime Imaging Microscopy (FLIM), *J. Phys. Chem. B 117*, 8143-8149.

122. Zhang, Y., Birch, D. J. S., and Chen, Y. (2011) Two-photon excited surface plasmon enhanced energy transfer between DAPI and gold nanoparticles: Opportunities in intra-cellular imaging and sensing, *Applied Physics Letters 99*, 103701-103703.

123. Dahan, M., Laurence, T., Pinaud, F., Chemla, D. S., Alivisatos, A. P., Sauer, M., and Weiss, S. (2001) Time-gated biological imaging by use of colloidal quantum dots, *Opt. Lett. 26*, 825-827.

124. Giraud, G., Schulze, H., Bachmann, T. T., Campbell, C. J., Mount, A. R., Ghazal, P., Khondoker, M. R., Ross, A. J., Ember, S. W. J., Ciani, I., Tlili, C., Walton, A. J., Ferry, J. G.,

and Crain, J. (2009) Fluorescence Lifetime Imaging of Quantum Dot Labeled DNA Microarrays, *Int. J. Mol. Sci. 10*, 1930-1941.

125. Pai, R. K., and Cotlet, M. (2011) Highly Stable, Water-Soluble, Intrinsic Fluorescent Hybrid Scaffolds for Imaging and Biosensing, *J. Phys. Chem. C 115*, 1674-1681.

126. Orte, A., Alvarez-Pez, J. M., and Ruedas-Rama, M. J. (2013) Fluorescence Lifetime Imaging Microscopy for the Detection of Intracellular pH with Quantum Dot Nanosensors, *ACS Nano 7*, 6387-6395.

127. Chimienti, F. (2013) Zinc, pancreatic islet cell function and diabetes: new insights into an old story, *Nutrition research reviews 26*, 1-11.

128. Frederickson, C. J., Koh, J.-Y., and Bush, A. I. (2005) The neurobiology of zinc in health and disease, *Nat. Rev. Neurosci. 6*, 449-462.

129. Barykin, E. P., Petrushanko, I. Y., Kozin, S. A., Telegin, G. B., Chernov, A. S., Lopina, O. D., Radko, S. P., Mitkevich, V. A., and Makarov, A. A. (2018) Phosphorylation of the Amyloid-Beta Peptide Inhibits Zinc-Dependent Aggregation, Prevents Na,K-ATPase Inhibition, and Reduces Cerebral Plaque Deposition, *Front Mol Neurosci 11*, 302.

130. Lagadic-Gossmann, D., Huc, L., and Lecureur, V. (2004) Alterations of intracellular pH homeostasis in apoptosis: origins and roles, *Cell death and differentiation 11*, 953-961.

131. Subramaniam, S. R., and Chesselet, M. F. (2013) Mitochondrial dysfunction and oxidative stress in Parkinson's disease, *Progress in neurobiology 106-107*, 17-32.

132. Ruhoy, I. S., and Saneto, R. P. (2014) The genetics of Leigh syndrome and its implications for clinical practice and risk management, *The application of clinical genetics 7*, 221-234.

133. Bonnen, P. E., Yarham, J. W., Besse, A., Wu, P., Faqeih, E. A., Al-Asmari, A. M., Saleh, M. A., Eyaid, W., Hadeel, A., He, L., Smith, F., Yau, S., Simcox, E. M., Miwa, S., Donti, T., Abu-Amero, K. K., Wong, L. J., Craigen, W. J., Graham, B. H., Scott, K. L., McFarland, R., and Taylor, R. W. (2013) Mutations in FBXL4 cause mitochondrial encephalopathy and a disorder of mitochondrial DNA maintenance, *American journal of human genetics 93*, 471-481.

134. Zorov, D. B., Juhaszova, M., and Sollott, S. J. (2014) Mitochondrial reactive oxygen species (ROS) and ROS-induced ROS release, *Physiological reviews 94*, 909-950.

135. Lee, S.-Y., Kang, J. M., Kim, D.-J., Park, S. H., Jeong, H. Y., Lee, Y. H., Kim, Y. G., Yang, D. H., and Lee, S. H. (2017) PGC1α Activators Mitigate Diabetic Tubulopathy by Improving Mitochondrial Dynamics and Quality Control, *Journal of diabetes research 2017*, 6483572-6483572.

136. Gorman, G. S., Chinnery, P. F., DiMauro, S., Hirano, M., Koga, Y., McFarland, R., Suomalainen, A., Thorburn, D. R., Zeviani, M., and Turnbull, D. M. (2016) Mitochondrial diseases, *Nature reviews. Disease primers 2*, 16080.

137. Boland, M. L., Chourasia, A. H., and Macleod, K. F. (2013) Mitochondrial dysfunction in cancer, *Frontiers in oncology 3*, 292-292.

138. Wallace, D. C. (2012) Mitochondria and cancer, *Nat Rev Cancer 12*, 685-698.

139. Warburg, O. (1956) On respiratory impairment in cancer cells, *Science 124*, 269-270.

140. Müller, B. K., Zaychikov, E., Bräuchle, C., and Lamb, D. C. (2005) Pulsed Interleaved Excitation, *Biophys. J. 89*, 3508-3522.

141. Ruedas-Rama, M. J., and Hall, E. A. H. (2008) Azamacrocycle Activated Quantum Dot for Zinc Ion Detection, *Anal. Chem. 80*, 8260-8268.

142. Szeto, H. H. (2008) Development of mitochondria-targeted aromatic-cationic peptides for neurodegenerative diseases, *Annals NY Acad. Sci. 1147*, 112-121.

143. Kaiser, E., Colescott, R. L., Bossinger, C. D., and Cook, P. I. (1970) Color test for detection of free terminal amino groups in the solid-phase synthesis of peptides, *Anal Biochem 34*, 595-598.

144. Hunter, T. M., McNae, I. W., Liang, X., Bella, J., Parsons, S., Walkinshaw, M. D., and Sadler, P. J. (2005) Protein recognition of macrocycles: binding of anti-HIV metallocyclams to lysozyme, *Proc Natl Acad Sci U S A 102*, 2288-2292.

145. Neuman, D., Ostrowski, A. D., Mikhailovsky, A. A., Absalonson, R. O., Strouse, G. F., and Ford, P. C. (2008) Quantum dot fluorescence quenching pathways with Cr(III) complexes. photosensitized NO production from trans-Cr(cyclam)(ONO)2+, *J Am Chem Soc 130*, 168-175.

146. Neuman, D., Ostrowski, A. D., Absalonson, R. O., Strouse, G. F., and Ford, P. C. (2007) Photosensitized NO release from water-soluble nanoparticle assemblies, *J Am Chem Soc 129*, 4146-4147.

147. Ruedas-Rama, M. J., Orte, A., Hall, E. A. H., Alvarez-Pez, J. M., and Talavera, E. M. (2011) Quantum dot photoluminescence lifetime-based pH nanosensor, *Chem. Commun. 47*, 2898-2900.

148. Holliday, D. L., and Speirs, V. (2011) Choosing the right cell line for breast cancer research, *Breast Cancer Research 13*, 215.

149. Huang, C.-P., Li, Y.-K., and Chen, T.-M. (2007) A highly sensitive system for urea detection by using CdSe/ZnS core-shell quantum dots, *Biosens. Bioelectron. 22*, 1835-1838.

150. Deng, Z., Zhang, Y., Yue, J., Tang, F., and Wei, Q. (2007) Green and Orange CdTe Quantum Dots as Effective pH-Sensitive Fluorescent Probes for Dual Simultaneous and Independent Detection of Viruses, *J. Phys. Chem. B 111*, 12024-12031.

151. Ruedas-Rama, M. J., and Hall, E. A. H. (2010) Analytical Nanosphere Sensors Using Quantum Dot-Enzyme Conjugates for Urea and Creatinine, *Analytical Chemistry 82*, 9043-9049.

152. Gao, X., Chan, W. C. W., and Nie, S. (2002) Quantum-dot nanocrystals for ultrasensitive biological labeling and multicolor optical encoding, *J. Biomed. Opt. 7*, 532-537.

153. Bradburne, C. E., Delehanty, J. B., Boeneman Gemmill, K., Mei, B. C., Mattoussi, H., Susumu, K., Blanco-Canosa, J. B., Dawson, P. E., and Medintz, I. L. (2013) Cytotoxicity of quantum dots used for in vitro cellular labeling: role of QD surface ligand, delivery modality, cell type, and direct comparison to organic fluorophores, *Bioconjug Chem 24*, 1570-1583.

154. Chen, N., He, Y., Su, Y., Li, X., Huang, Q., Wang, H., Zhang, X., Tai, R., and Fan, C. (2012) The cytotoxicity of cadmium-based quantum dots, *Biomaterials 33*, 1238-1244.

155. Winnik, F. M., and Maysinger, D. (2013) Quantum dot cytotoxicity and ways to reduce it, *Acc Chem Res 46*, 672-680.

156. DeBerardinis, R. J., and Thompson, C. B. (2012) Cellular metabolism and disease: what do metabolic outliers teach us?, *Cell 148*, 1132-1144.

157. Lunt, S. Y., and Vander Heiden, M. G. (2011) Aerobic glycolysis: meeting the metabolic requirements of cell proliferation, *Annual review of cell and developmental biology 27*, 441-464.

158. Ward, P. S., and Thompson, C. B. (2012) Metabolic reprogramming: a cancer hallmark even warburg did not anticipate, *Cancer Cell 21*, 297-308.

159. Vander Heiden, M. G., Cantley, L. C., and Thompson, C. B. (2009) Understanding the Warburg Effect: The Metabolic Requirements of Cell Proliferation, *Science 324*, 1029-1033.

160. Warburg, O. (1924) Über den Stoffwechsel der Karcinomzellen, *Naturwissenschaften 12*, 6.

161. Warburg, O. (1956) On the origin of cancer cells, *Science 123*, 309-314.

162. DeBerardinis, R. J., Lum, J. J., Hatzivassiliou, G., and Thompson, C. B. (2008) The biology of cancer: metabolic reprogramming fuels cell growth and proliferation, *Cell Metab 7*, 11-20.

163. Vander Heiden, M. G., Cantley, L. C., and Thompson, C. B. (2009) Understanding the Warburg effect: the metabolic requirements of cell proliferation, *Science 324*, 1029-1033.

164. Fantin, V. R., and Leder, P. (2006) Mitochondriotoxic compounds for cancer therapy, *Oncogene 25*, 4787-4797.

165. Moreno-Sanchez, R., Rodriguez-Enriquez, S., Marin-Hernandez, A., and Saavedra, E. (2007) Energy metabolism in tumor cells, *The FEBS journal 274*, 1393-1418.

166. Zu, X. L., and Guppy, M. (2004) Cancer metabolism: facts, fantasy, and fiction, *Biochem Biophys Res Commun 313*, 459-465.

167. Coller, H. A. (2014) Is cancer a metabolic disease?, *Am J Pathol 184*, 4-17.

168. Brand, K. (1985) Glutamine and glucose metabolism during thymocyte proliferation. Pathways of glutamine and glutamate metabolism, *The Biochemical journal 228*, 353-361.

169. Hedeskov, C. J. (1968) Early effects of phytohaemagglutinin on glucose metabolism of normal human lymphocytes, *The Biochemical journal 110*, 373-380.

170. Wang, T., Marquardt, C., and Foker, J. (1976) Aerobic glycolysis during lymphocyte proliferation, *Nature 261*, 702-705.

171. Levine, A. J., and Puzio-Kuter, A. M. (2010) The control of the metabolic switch in cancers by oncogenes and tumor suppressor genes, *Science 330*, 1340-1344.

172. Kroemer, G., and Pouyssegur, J. (2008) Tumor cell metabolism: cancer's Achilles' heel, *Cancer Cell 13*, 472-482.

173. Hanahan, D., and Weinberg, R. A. (2011) Hallmarks of cancer: the next generation, *Cell 144*, 646-674.

174. DeBerardinis, R. J., and Chandel, N. S. (2016) Fundamentals of cancer metabolism, *Sci Adv 2*, e1600200.

175. Hirschhaeuser, F., Sattler, U. G., and Mueller-Klieser, W. (2011) Lactate: a metabolic key player in cancer, *Cancer Res 71*, 6921-6925.

176. Kennedy, K. M., and Dewhirst, M. W. (2010) Tumor metabolism of lactate: the influence and therapeutic potential for MCT and CD147 regulation, *Future oncology (London, England) 6*, 127-148.

177. Hong, C. S., Graham, N. A., Gu, W., Espindola Camacho, C., Mah, V., Maresh, E. L., Alavi, M., Bagryanova, L., Krotee, P. A. L., Gardner, B. K., Behbahan, I. S., Horvath, S., Chia, D., Mellinghoff, I. K., Hurvitz, S. A., Dubinett, S. M., Critchlow, S. E., Kurdistani, S. K., Goodglick, L., Braas, D., Graeber, T. G., and Christofk, H. R. (2016) MCT1 Modulates Cancer Cell Pyruvate Export and Growth of Tumors that Co-express MCT1 and MCT4, *Cell reports 14*, 1590-1601.

178. Chaneton, B., and Gottlieb, E. (2012) Rocking cell metabolism: revised functions of the key glycolytic regulator PKM2 in cancer, *Trends in biochemical sciences 37*, 309-316.

179. Christofk, H. R., Vander Heiden, M. G., Harris, M. H., Ramanathan, A., Gerszten, R. E., Wei, R., Fleming, M. D., Schreiber, S. L., and Cantley, L. C. (2008) The M2 splice isoform of pyruvate kinase is important for cancer metabolism and tumour growth, *Nature 452*, 230-233.

180. Hitosugi, T., Kang, S., Vander Heiden, M. G., Chung, T. W., Elf, S., Lythgoe, K., Dong, S., Lonial, S., Wang, X., Chen, G. Z., Xie, J., Gu, T. L., Polakiewicz, R. D., Roesel, J. L., Boggon, T. J., Khuri, F. R., Gilliland, D. G., Cantley, L. C., Kaufman, J., and Chen, J. (2009) Tyrosine phosphorylation inhibits PKM2 to promote the Warburg effect and tumor growth, *Science signaling 2*, ra73.

181. Wong, N., De Melo, J., and Tang, D. (2013) PKM2, a Central Point of Regulation in Cancer Metabolism, *International journal of cell biology 2013*, 242513.

182. Vander Heiden, M. G., Locasale, J. W., Swanson, K. D., Sharfi, H., Heffron, G. J., Amador-Noguez, D., Christofk, H. R., Wagner, G., Rabinowitz, J. D., Asara, J. M., and

Cantley, L. C. (2010) Evidence for an alternative glycolytic pathway in rapidly proliferating cells, *Science 329*, 1492-1499.

183. Anastasiou, D., Yu, Y., Israelsen, W. J., Jiang, J. K., Boxer, M. B., Hong, B. S., Tempel, W., Dimov, S., Shen, M., Jha, A., Yang, H., Mattaini, K. R., Metallo, C. M., Fiske, B. P., Courtney, K. D., Malstrom, S., Khan, T. M., Kung, C., Skoumbourdis, A. P., Veith, H., Southall, N., Walsh, M. J., Brimacombe, K. R., Leister, W., Lunt, S. Y., Johnson, Z. R., Yen, K. E., Kunii, K., Davidson, S. M., Christofk, H. R., Austin, C. P., Inglese, J., Harris, M. H., Asara, J. M., Stephanopoulos, G., Salituro, F. G., Jin, S., Dang, L., Auld, D. S., Park, H. W., Cantley, L. C., Thomas, C. J., and Vander Heiden, M. G. (2012) Pyruvate kinase M2 activators promote tetramer formation and suppress tumorigenesis, *Nat Chem Biol 8*, 839-847.

184. Deberardinis, R. J., Sayed, N., Ditsworth, D., and Thompson, C. B. (2008) Brick by brick: metabolism and tumor cell growth, *Current opinion in genetics & development 18*, 54-61.

185. Christofk, H. R., Vander Heiden, M. G., Wu, N., Asara, J. M., and Cantley, L. C. (2008) Pyruvate kinase M2 is a phosphotyrosine-binding protein, *Nature 452*, 181-186.

186. Au, K. K., Liong, E., Li, J. Y., Li, P. S., Liew, C. C., Kwok, T. T., Choy, Y. M., Lee, C. Y., and Fung, K. P. (1997) Increases in mRNA levels of glucose transporters types 1 and 3 in Ehrlich ascites tumor cells during tumor development, *Journal of cellular biochemistry 67*, 131-135.

187. Suzuki, T., Iwazaki, A., Katagiri, H., Oka, Y., Redpath, J. L., Stanbridge, E. J., and Kitagawa, T. (1999) Enhanced expression of glucose transporter GLUT3 in tumorigenic HeLa cell hybrids associated with tumor suppressor dysfunction, *European journal of biochemistry 262*, 534-540.

188. Mullen, A. R., Hu, Z., Shi, X., Jiang, L., Boroughs, L. K., Kovacs, Z., Boriack, R., Rakheja, D., Sullivan, L. B., Linehan, W. M., Chandel, N. S., and DeBerardinis, R. J. (2014) Oxidation of alpha-ketoglutarate is required for reductive carboxylation in cancer cells with mitochondrial defects, *Cell reports 7*, 1679-1690.

189. Owen, O. E., Kalhan, S. C., and Hanson, R. W. (2002) The key role of anaplerosis and cataplerosis for citric acid cycle function, *The Journal of biological chemistry 277*, 30409-30412.

190. Yu, Y., Clippinger, A. J., and Alwine, J. C. (2011) Viral effects on metabolism: changes in glucose and glutamine utilization during human cytomegalovirus infection, *Trends in Microbiology 19*, 360-367.

191. Cheng, T., Sudderth, J., Yang, C., Mullen, A. R., Jin, E. S., Mates, J. M., and DeBerardinis, R. J. (2011) Pyruvate carboxylase is required for glutamine-independent growth of tumor cells, *Proc Natl Acad Sci U S A 108*, 8674-8679.

192. DeBerardinis, R. J., Mancuso, A., Daikhin, E., Nissim, I., Yudkoff, M., Wehrli, S., and Thompson, C. B. (2007) Beyond aerobic glycolysis: transformed cells can engage in glutamine metabolism that exceeds the requirement for protein and nucleotide synthesis, *Proc Natl Acad Sci U S A 104*, 19345-19350.

193. Altman, B. J., Stine, Z. E., and Dang, C. V. (2016) From Krebs to clinic: glutamine metabolism to cancer therapy, *Nat Rev Cancer 16*, 773.

194. Daye, D., and Wellen, K. E. (2012) Metabolic reprogramming in cancer: unraveling the role of glutamine in tumorigenesis, *Seminars in cell & developmental biology 23*, 362-369.

195. Le, A., Lane, A. N., Hamaker, M., Bose, S., Gouw, A., Barbi, J., Tsukamoto, T., Rojas, C. J., Slusher, B. S., Zhang, H., Zimmerman, L. J., Liebler, D. C., Slebos, R. J., Lorkiewicz, P. K., Higashi, R. M., Fan, T. W., and Dang, C. V. (2012) Glucose-independent glutamine metabolism via TCA cycling for proliferation and survival in B cells, *Cell Metab 15*, 110-121.

196. Metallo, C. M., Gameiro, P. A., Bell, E. L., Mattaini, K. R., Yang, J., Hiller, K., Jewell, C. M., Johnson, Z. R., Irvine, D. J., Guarente, L., Kelleher, J. K., Vander Heiden, M. G., Iliopoulos, O., and Stephanopoulos, G. (2011) Reductive glutamine metabolism by IDH1 mediates lipogenesis under hypoxia, *Nature 481*, 380-384.

197. Scott, D. A., Richardson, A. D., Filipp, F. V., Knutzen, C. A., Chiang, G. G., Ronai, Z. A., Osterman, A. L., and Smith, J. W. (2011) Comparative metabolic flux profiling of melanoma cell lines: beyond the Warburg effect, *The Journal of biological chemistry 286*, 42626-42634.

198. Hosios, A. M., Hecht, V. C., Danai, L. V., Johnson, M. O., Rathmell, J. C., Steinhauser, M. L., Manalis, S. R., and Vander Heiden, M. G. (2016) Amino Acids Rather than Glucose Account for the Majority of Cell Mass in Proliferating Mammalian Cells, *Developmental cell 36*, 540-549.

199. Wise, D. R., and Thompson, C. B. (2010) Glutamine addiction: a new therapeutic target in cancer, *Trends in biochemical sciences 35*, 427-433.

200. Lane, A. N., and Fan, T. W. (2015) Regulation of mammalian nucleotide metabolism and biosynthesis, *Nucleic acids research 43*, 2466-2485.

201. Gaglio, D., Soldati, C., Vanoni, M., Alberghina, L., and Chiaradonna, F. (2009) Glutamine deprivation induces abortive s-phase rescued by deoxyribonucleotides in k-ras transformed fibroblasts, *PloS one 4*, e4715.

202. DeBerardinis, R. J., and Cheng, T. (2010) Q's next: the diverse functions of glutamine in metabolism, cell biology and cancer, *Oncogene 29*, 313-324.

203. Tong, X., Zhao, F., and Thompson, C. B. (2009) The molecular determinants of de novo nucleotide biosynthesis in cancer cells, *Current opinion in genetics & development 19*, 32-37.

204. Sullivan, L. B., Gui, D. Y., and Heiden, M. G. V. (2016) Altered metabolite levels in cancer: implications for tumour biology and cancer therapy, *Nat. Rev. Cancer 16*, 680.

205. Vijayakumar, S. N., Sethuraman, S., and Krishnan, U. M. (2015) Metabolic pathways in cancers: key targets and implications in cancer therapy, *RSC Advances 5*, 41751-41762.

206. Medes, G., Thomas, A., and Weinhouse, S. (1953) Metabolism of neoplastic tissue. IV. A study of lipid synthesis in neoplastic tissue slices in vitro, *Cancer Res 13*, 27-29.

207. Currie, E., Schulze, A., Zechner, R., Walther, T. C., and Farese, R. V., Jr. (2013) Cellular fatty acid metabolism and cancer, *Cell Metab 18*, 153-161.

208. Baenke, F., Peck, B., Miess, H., and Schulze, A. (2013) Hooked on fat: the role of lipid synthesis in cancer metabolism and tumour development, *Disease models & mechanisms 6*, 1353-1363.

209. Mullen, A. R., Wheaton, W. W., Jin, E. S., Chen, P. H., Sullivan, L. B., Cheng, T., Yang, Y., Linehan, W. M., Chandel, N. S., and DeBerardinis, R. J. (2011) Reductive carboxylation supports growth in tumour cells with defective mitochondria, *Nature 481*, 385-388.

210. Phan, L. M., Yeung, S. C., and Lee, M. H. (2014) Cancer metabolic reprogramming: importance, main features, and potentials for precise targeted anti-cancer therapies, *Cancer biology & medicine 11*, 1-19.

211. Menendez, J. A., and Lupu, R. (2007) Fatty acid synthase and the lipogenic phenotype in cancer pathogenesis, *Nat Rev Cancer 7*, 763-777.

212. Yahagi, N., Shimano, H., Hasegawa, K., Ohashi, K., Matsuzaka, T., Najima, Y., Sekiya, M., Tomita, S., Okazaki, H., Tamura, Y., Iizuka, Y., Ohashi, K., Nagai, R., Ishibashi, S., Kadowaki, T., Makuuchi, M., Ohnishi, S., Osuga, J., and Yamada, N. (2005) Co-ordinate activation of lipogenic enzymes in hepatocellular carcinoma, *European journal of cancer (Oxford, England : 1990) 41*, 1316-1322.

213. Abramson, H. N. (2011) The lipogenesis pathway as a cancer target, *J Med Chem 54*, 5615-5638.

214. Rohrig, F., and Schulze, A. (2016) The multifaceted roles of fatty acid synthesis in cancer, *Nat Rev Cancer 16*, 732-749.

215. Coloff, J. L., Murphy, J. P., Braun, C. R., Harris, I. S., Shelton, L. M., Kami, K., Gygi, S. P., Selfors, L. M., and Brugge, J. S. (2016) Differential Glutamate Metabolism in Proliferating and Quiescent Mammary Epithelial Cells, *Cell Metab 23*, 867-880.

216. Yang, M., and Vousden, K. H. (2016) Serine and one-carbon metabolism in cancer, *Nat Rev Cancer 16*, 650-662.

217. Tedeschi, P. M., Markert, E. K., Gounder, M., Lin, H., Dvorzhinski, D., Dolfi, S. C., Chan, L. L., Qiu, J., DiPaola, R. S., Hirshfield, K. M., Boros, L. G., Bertino, J. R., Oltvai, Z. N., and Vazquez, A. (2013) Contribution of serine, folate and glycine metabolism to the ATP, NADPH and purine requirements of cancer cells, *Cell death & disease 4*, e877.

218. Pavlova, N. N., and Thompson, C. B. (2016) The Emerging Hallmarks of Cancer Metabolism, *Cell Metab 23*, 27-47.

219. Cantley, L. C. (2002) The phosphoinositide 3-kinase pathway, *Science 296*, 1655-1657.

220. Wong, K. K., Engelman, J. A., and Cantley, L. C. (2010) Targeting the PI3K signaling pathway in cancer, *Current opinion in genetics & development 20*, 87-90.

221. Cairns, R. A., Harris, I. S., and Mak, T. W. (2011) Regulation of cancer cell metabolism, *Nat. Rev. Cancer 11*, 85-95.

222. Duvel, K., Yecies, J. L., Menon, S., Raman, P., Lipovsky, A. I., Souza, A. L., Triantafellow, E., Ma, Q., Gorski, R., Cleaver, S., Vander Heiden, M. G., MacKeigan, J. P., Finan, P. M., Clish, C. B., Murphy, L. O., and Manning, B. D. (2010) Activation of a metabolic gene regulatory network downstream of mTOR complex 1, *Molecular cell 39*, 171-183.

223. Shim, H., Dolde, C., Lewis, B. C., Wu, C. S., Dang, G., Jungmann, R. A., Dalla-Favera, R., and Dang, C. V. (1997) c-Myc transactivation of LDH-A: implications for tumor metabolism and growth, *Proc Natl Acad Sci U S A 94*, 6658-6663.

224. Dang, C. V., Kim, J. W., Gao, P., and Yustein, J. (2008) The interplay between MYC and HIF in cancer, *Nat Rev Cancer 8*, 51-56.

225. Stine, Z. E., Walton, Z. E., Altman, B. J., Hsieh, A. L., and Dang, C. V. (2015) MYC, Metabolism, and Cancer, *Cancer discovery 5*, 1024-1039.

226. Dang, C. V. (2010) Rethinking the Warburg effect with Myc micromanaging glutamine metabolism, *Cancer Res 70*, 859-862.

227. Gao, P., Tchernyshyov, I., Chang, T. C., Lee, Y. S., Kita, K., Ochi, T., Zeller, K. I., De Marzo, A. M., Van Eyk, J. E., Mendell, J. T., and Dang, C. V. (2009) c-Myc suppression of miR-23a/b enhances mitochondrial glutaminase expression and glutamine metabolism, *Nature 458*, 762-765.

228. Wise, D. R., DeBerardinis, R. J., Mancuso, A., Sayed, N., Zhang, X. Y., Pfeiffer, H. K., Nissim, I., Daikhin, E., Yudkoff, M., McMahon, S. B., and Thompson, C. B. (2008) Myc regulates a transcriptional program that stimulates mitochondrial glutaminolysis and leads to glutamine addiction, *Proc Natl Acad Sci U S A 105*, 18782-18787.

229. Munoz-Pinedo, C., El Mjiyad, N., and Ricci, J. E. (2012) Cancer metabolism: current perspectives and future directions, *Cell death & disease 3*, e248.

230. di Magliano, M. P., and Logsdon, C. D. (2013) Roles for KRAS in pancreatic tumor development and progression, *Gastroenterology 144*, 1220-1229.

231. Son, J., Lyssiotis, C. A., Ying, H., Wang, X., Hua, S., Ligorio, M., Perera, R. M., Ferrone, C. R., Mullarky, E., Shyh-Chang, N., Kang, Y. a., Fleming, J. B., Bardeesy, N., Asara, J. M., Haigis, M. C., DePinho, R. A., Cantley, L. C., and Kimmelman, A. C. (2013) Glutamine supports pancreatic cancer growth through a KRAS-regulated metabolic pathway, *Nature 496*, 101.

232. Ying, H., Kimmelman, A. C., Lyssiotis, C. A., Hua, S., Chu, G. C., Fletcher-Sananikone, E., Locasale, J. W., Son, J., Zhang, H., Coloff, J. L., Yan, H., Wang, W., Chen, S., Viale, A., Zheng, H., Paik, J. H., Lim, C., Guimaraes, A. R., Martin, E. S., Chang, J., Hezel, A. F.,

Perry, S. R., Hu, J., Gan, B., Xiao, Y., Asara, J. M., Weissleder, R., Wang, Y. A., Chin, L., Cantley, L. C., and DePinho, R. A. (2012) Oncogenic Kras maintains pancreatic tumors through regulation of anabolic glucose metabolism, *Cell 149*, 656-670.

233. Semenza, G. L. (2008) Tumor metabolism: cancer cells give and take lactate, *The Journal of clinical investigation 118*, 3835-3837.

234. Eales, K. L., Hollinshead, K. E., and Tennant, D. A. (2016) Hypoxia and metabolic adaptation of cancer cells, *Oncogenesis 5*, e190.

235. Iyer, N. V., Kotch, L. E., Agani, F., Leung, S. W., Laughner, E., Wenger, R. H., Gassmann, M., Gearhart, J. D., Lawler, A. M., Yu, A. Y., and Semenza, G. L. (1998) Cellular and developmental control of O2 homeostasis by hypoxia-inducible factor 1 alpha, *Genes & development 12*, 149-162.

236. Semenza, G. L. (2009) Regulation of cancer cell metabolism by hypoxia-inducible factor 1, *Seminars in cancer biology 19*, 12-16.

237. Kim, J. W., Tchernyshyov, I., Semenza, G. L., and Dang, C. V. (2006) HIF-1-mediated expression of pyruvate dehydrogenase kinase: a metabolic switch required for cellular adaptation to hypoxia, *Cell Metab 3*, 177-185.

238. Papandreou, I., Cairns, R. A., Fontana, L., Lim, A. L., and Denko, N. C. (2006) HIF-1 mediates adaptation to hypoxia by actively downregulating mitochondrial oxygen consumption, *Cell Metab 3*, 187-197.

239. Vousden, K. H., and Ryan, K. M. (2009) p53 and metabolism, *Nat Rev Cancer 9*, 691-700.

240. Matoba, S., Kang, J. G., Patino, W. D., Wragg, A., Boehm, M., Gavrilova, O., Hurley, P. J., Bunz, F., and Hwang, P. M. (2006) p53 regulates mitochondrial respiration, *Science 312*, 1650-1653.

241. Shackelford, D. B., and Shaw, R. J. (2009) The LKB1-AMPK pathway: metabolism and growth control in tumour suppression, *Nat Rev Cancer 9*, 563-575.

242. Jose, C., Bellance, N., and Rossignol, R. (2011) Choosing between glycolysis and oxidative phosphorylation: a tumor's dilemma?, *Biochim Biophys Acta 1807*, 552-561.

243. Israelsen, W. J., Dayton, T. L., Davidson, S. M., Fiske, B. P., Hosios, A. M., Bellinger, G., Li, J., Yu, Y., Sasaki, M., Horner, J. W., Burga, L. N., Xie, J., Jurczak, M. J., DePinho, R. A., Clish, C. B., Jacks, T., Kibbey, R. G., Wulf, G. M., Di Vizio, D., Mills, G. B., Cantley, L. C., and Vander Heiden, M. G. (2013) PKM2 isoform-specific deletion reveals a differential requirement for pyruvate kinase in tumor cells, *Cell 155*, 397-409.

244. Feron, O. (2009) Pyruvate into lactate and back: from the Warburg effect to symbiotic energy fuel exchange in cancer cells, *Radiotherapy and oncology : journal of the European Society for Therapeutic Radiology and Oncology 92*, 329-333.

245. Le, A., Cooper, C. R., Gouw, A. M., Dinavahi, R., Maitra, A., Deck, L. M., Royer, R. E., Vander Jagt, D. L., Semenza, G. L., and Dang, C. V. (2010) Inhibition of lactate dehydrogenase A induces oxidative stress and inhibits tumor progression, *Proc Natl Acad Sci U S A 107*, 2037-2042.

246. Mayers, J. R., Wu, C., Clish, C. B., Kraft, P., Torrence, M. E., Fiske, B. P., Yuan, C., Bao, Y., Townsend, M. K., Tworoger, S. S., Davidson, S. M., Papagiannakopoulos, T., Yang, A., Dayton, T. L., Ogino, S., Stampfer, M. J., Giovannucci, E. L., Qian, Z. R., Rubinson, D. A., Ma, J., Sesso, H. D., Gaziano, J. M., Cochrane, B. B., Liu, S., Wactawski-Wende, J., Manson, J. E., Pollak, M. N., Kimmelman, A. C., Souza, A., Pierce, K., Wang, T. J., Gerszten, R. E., Fuchs, C. S., Vander Heiden, M. G., and Wolpin, B. M. (2014) Elevation of circulating branched-chain amino acids is an early event in human pancreatic adenocarcinoma development, *Nat Med 20*, 1193-1198.

247. Seyfried, T. N., and Mukherjee, P. (2005) Targeting energy metabolism in brain cancer: review and hypothesis, *Nutrition & metabolism 2*, 30.

248. Locasale, J. W., and Cantley, L. C. (2011) Metabolic flux and the regulation of mammalian cell growth, *Cell Metab 14*, 443-451.

249. Greenhouse, W. V., and Lehninger, A. L. (1976) Occurrence of the malate-aspartate shuttle in various tumor types, *Cancer Res 36*, 1392-1396.

250. Lopez-Alarcon, L., and Eboli, M. L. (1986) Oxidation of reduced cytosolic nicotinamide adenine dinucleotide by the malate-aspartate shuttle in the K-562 human leukemia cell line, *Cancer Res 46*, 5589-5591.

251. Greenhouse, W. V., and Lehninger, A. L. (1977) Magnitude of malate-aspartate reduced nicotinamide adenine dinucleotide shuttle activity in intact respiring tumor cells, *Cancer Res 37*, 4173-4181.

252. Liu, Q., Harvey, C. T., Geng, H., Xue, C., Chen, V., Beer, T. M., and Qian, D. Z. (2013) Malate dehydrogenase 2 confers docetaxel resistance via regulations of JNK signaling and oxidative metabolism, *The Prostate 73*, 1028-1037.

253. Lo, Y. W., Lin, S. T., Chang, S. J., Chan, C. H., Lyu, K. W., Chang, J. F., May, E. W., Lin, D. Y., Chou, H. C., and Chan, H. L. (2015) Mitochondrial proteomics with siRNA knockdown to reveal ACAT1 and MDH2 in the development of doxorubicin-resistant uterine cancer, *Journal of cellular and molecular medicine 19*, 744-759.

254. Ban, H. S., Xu, X., Jang, K., Kim, I., Kim, B. K., Lee, K., and Won, M. (2016) A Novel Malate Dehydrogenase 2 Inhibitor Suppresses Hypoxia-Inducible Factor-1 by Regulating Mitochondrial Respiration, *PloS one 11*, e0162568.

255. Lyssiotis, C. A., Son, J., Cantley, L. C., and Kimmelman, A. C. (2013) Pancreatic cancers rely on a novel glutamine metabolism pathway to maintain redox balance, *Cell Cycle 12*, 1987-1988.

256. Thornburg, J. M., Nelson, K. K., Clem, B. F., Lane, A. N., Arumugam, S., Simmons, A., Eaton, J. W., Telang, S., and Chesney, J. (2008) Targeting aspartate aminotransferase in breast cancer, *Breast cancer research : BCR 10*, R84.

257. Birsoy, K., Wang, T., Chen, W. W., Freinkman, E., Abu-Remaileh, M., and Sabatini, D. M. (2015) An Essential Role of the Mitochondrial Electron Transport Chain in Cell Proliferation Is to Enable Aspartate Synthesis, *Cell 162*, 540-551.

258. Chowdhury, S. K., Raha, S., Tarnopolsky, M. A., and Singh, G. (2007) Increased expression of mitochondrial glycerophosphate dehydrogenase and antioxidant enzymes in prostate cancer cell lines/cancer, *Free Radic Res 41*, 1116-1124.

259. Singh, G. (2014) Mitochondrial FAD-linked Glycerol-3-phosphate Dehydrogenase: A Target for Cancer Therapeutics, *Pharmaceuticals (Basel, Switzerland) 7*, 192-206.

260. Rabinovich, S., Adler, L., Yizhak, K., Sarver, A., Silberman, A., Agron, S., Stettner, N., Sun, Q., Brandis, A., Helbling, D., Korman, S., Itzkovitz, S., Dimmock, D., Ulitsky, I., Nagamani, S. C., Ruppin, E., and Erez, A. (2015) Diversion of aspartate in ASS1-deficient tumours fosters de novo pyrimidine synthesis, *Nature 527*, 379-383.

261. Allen, E. L., Ulanet, D. B., Pirman, D., Mahoney, C. E., Coco, J., Si, Y., Chen, Y., Huang, L., Ren, J., Choe, S., Clasquin, M. F., Artin, E., Fan, Z. P., Cianchetta, G., Murtie, J., Dorsch, M., Jin, S., and Smolen, G. A. (2016) Differential Aspartate Usage Identifies a Subset of Cancer Cells Particularly Dependent on OGDH, *Cell reports 17*, 876-890.

262. Xie, G., Zhou, B., Zhao, A., Qiu, Y., Zhao, X., Garmire, L., Shvetsov, Y. B., Yu, H., Yen, Y., and Jia, W. (2015) Lowered circulating aspartate is a metabolic feature of human breast cancer, *Oncotarget 6*, 33369-33381.

263. Roudier, E., and Perrin, A. (2009) Considering the role of pyruvate in tumor cells during hypoxia, *Biochimica et Biophysica Acta (BBA) - Reviews on Cancer 1796*, 55-62.

264. Hay, N. (2016) Reprogramming glucose metabolism in cancer: can it be exploited for cancer therapy?, *Nat Rev Cancer 16*, 635-649.

265. Tennant, D. A., Duran, R. V., and Gottlieb, E. (2010) Targeting metabolic transformation for cancer therapy, *Nat Rev Cancer 10*, 267-277.

266. Sun, R. C., Fadia, M., Dahlstrom, J. E., Parish, C. R., Board, P. G., and Blackburn, A. C. (2010) Reversal of the glycolytic phenotype by dichloroacetate inhibits metastatic breast cancer cell growth in vitro and in vivo, *Breast cancer research and treatment 120*, 253-260.

267. Lu, H., Forbes, R. A., and Verma, A. (2002) Hypoxia-inducible factor 1 activation by aerobic glycolysis implicates the Warburg effect in carcinogenesis, *The Journal of biological chemistry 277*, 23111-23115.

268. Gui, D. Y., Sullivan, L. B., Luengo, A., Hosios, A. M., Bush, L. N., Gitego, N., Davidson, S. M., Freinkman, E., Thomas, C. J., and Vander Heiden, M. G. (2016) Environment Dictates Dependence on Mitochondrial Complex I for NAD+ and Aspartate Production and Determines Cancer Cell Sensitivity to Metformin, *Cell Metab 24*, 716-727.

269. Skaane, P. (2009) Studies comparing screen-film mammography and full-field digital mammography in breast cancer screening: updated review, *Acta radiologica (Stockholm, Sweden : 1987) 50*, 3-14.

270. Bohm, D., Keller, K., Wehrwein, N., Lebrecht, A., Schmidt, M., Kolbl, H., and Grus, F. H. (2011) Serum proteome profiling of primary breast cancer indicates a specific biomarker profile, *Oncology reports 26*, 1051-1056.

271. SREE, S. V., NG, E. Y.-K., U, R. A., and TAN, W. (2010) BREAST IMAGING SYSTEMS: A REVIEW AND COMPARATIVE STUDY, *Journal of Mechanics in Medicine and Biology 10*, 5-34.

272. Chen, J., Zhang, X., Cao, R., Lu, X., Zhao, S., Fekete, A., Huang, Q., Schmitt-Kopplin, P., Wang, Y., Xu, Z., Wan, X., Wu, X., Zhao, N., Xu, C., and Xu, G. (2011) Serum 27-nor-5beta-cholestane-3,7,12,24,25 pentol glucuronide discovered by metabolomics as potential diagnostic biomarker for epithelium ovarian cancer, *Journal of proteome research 10*, 2625-2632.

273. Garcia, E., Andrews, C., Hua, J., Kim, H. L., Sukumaran, D. K., Szyperski, T., and Odunsi, K. (2011) Diagnosis of early stage ovarian cancer by 1H NMR metabonomics of serum explored by use of a microflow NMR probe, *Journal of proteome research 10*, 1765-1771.

274. Qiu, Y., Cai, G., Su, M., Chen, T., Liu, Y., Xu, Y., Ni, Y., Zhao, A., Cai, S., Xu, L. X., and Jia, W. (2010) Urinary metabonomic study on colorectal cancer, *Journal of proteome research 9*, 1627-1634.

275. Cai, Z., Zhao, J. S., Li, J. J., Peng, D. N., Wang, X. Y., Chen, T. L., Qiu, Y. P., Chen, P. P., Li, W. J., Xu, L. Y., Li, E. M., Tam, J. P., Qi, R. Z., Jia, W., and Xie, D. (2010) A combined proteomics and metabolomics profiling of gastric cardia cancer reveals characteristic dysregulations in glucose metabolism, *Molecular & cellular proteomics : MCP 9*, 2617-2628.

276. Qiu, Y., Zhou, B., Su, M., Baxter, S., Zheng, X., Zhao, X., Yen, Y., and Jia, W. (2013) Mass spectrometry-based quantitative metabolomics revealed a distinct lipid profile in breast cancer patients, *International journal of molecular sciences 14*, 8047-8061.

277. Poschke, I., Mao, Y., Kiessling, R., and de Boniface, J. (2013) Tumor-dependent increase of serum amino acid levels in breast cancer patients has diagnostic potential and correlates with molecular tumor subtypes, *Journal of translational medicine 11*, 290.

278. Nagata, C., Wada, K., Tsuji, M., Hayashi, M., Takeda, N., and Yasuda, K. (2014) Plasma amino acid profiles are associated with biomarkers of breast cancer risk in premenopausal Japanese women, *Cancer causes & control : CCC 25*, 143-149.

279. Sitter, B., Bathen, T. F., Singstad, T. E., Fjosne, H. E., Lundgren, S., Halgunset, J., and Gribbestad, I. S. (2010) Quantification of metabolites in breast cancer patients with different clinical prognosis using HR MAS MR spectroscopy, *NMR in biomedicine 23*, 424-431.

280.  Proenza, A. M., Oliver, J., Palou, A., and Roca, P. (2003) Breast and lung cancer are associated with a decrease in blood cell amino acid content, *The Journal of nutritional biochemistry 14*, 133-138.

281.  Lai, H. S., Lee, J. C., Lee, P. H., Wang, S. T., and Chen, W. J. (2005) Plasma free amino acid profile in cancer patients, *Seminars in cancer biology 15*, 267-276.

282.  Lasfargues, E. Y., and Ozzello, L. (1958) Cultivation of human breast carcinomas, *Journal of the National Cancer Institute 21*, 1131-1147.

283.  Cailleau, R., Olive, M., and Cruciger, Q. V. (1978) Long-term human breast carcinoma cell lines of metastatic origin: preliminary characterization, *In vitro 14*, 911-915.

284.  Soule, H. D., Vazquez, J., Long, A., Albert, S., and Brennan, M. (1973) A human cell line from a pleural effusion derived from a breast carcinoma, *Journal of the National Cancer Institute 51*, 1409-1416.

285.  Levenson, A. S., and Jordan, V. C. (1997) MCF-7: the first hormone-responsive breast cancer cell line, *Cancer Res 57*, 3071-3078.

286.  Ethier, S. P., Mahacek, M. L., Gullick, W. J., Frank, T. S., and Weber, B. L. (1993) Differential isolation of normal luminal mammary epithelial cells and breast cancer cells from primary and metastatic sites using selective media, *Cancer Res 53*, 627-635.

287.  Perou, C. M., Jeffrey, S. S., van de Rijn, M., Rees, C. A., Eisen, M. B., Ross, D. T., Pergamenschikov, A., Williams, C. F., Zhu, S. X., Lee, J. C., Lashkari, D., Shalon, D., Brown, P. O., and Botstein, D. (1999) Distinctive gene expression patterns in human mammary epithelial cells and breast cancers, *Proc Natl Acad Sci U S A 96*, 9212-9217.

288.  Perou, C. M., Sorlie, T., Eisen, M. B., van de Rijn, M., Jeffrey, S. S., Rees, C. A., Pollack, J. R., Ross, D. T., Johnsen, H., Akslen, L. A., Fluge, O., Pergamenschikov, A., Williams, C., Zhu, S. X., Lonning, P. E., Borresen-Dale, A. L., Brown, P. O., and Botstein, D. (2000) Molecular portraits of human breast tumours, *Nature 406*, 747-752.

289.  Sørlie, T., Perou, C. M., Tibshirani, R., Aas, T., Geisler, S., Johnsen, H., Hastie, T., Eisen, M. B., van de Rijn, M., Jeffrey, S. S., Thorsen, T., Quist, H., Matese, J. C., Brown, P. O., Botstein, D., Lønning, P. E., and Børresen-Dale, A.-L. (2001) Gene expression patterns of breast carcinomas distinguish tumor subclasses with clinical implications, *Proceedings of the National Academy of Sciences 98*, 10869.

290.  Badve, S., Dabbs, D. J., Schnitt, S. J., Baehner, F. L., Decker, T., Eusebi, V., Fox, S. B., Ichihara, S., Jacquemier, J., Lakhani, S. R., Palacios, J., Rakha, E. A., Richardson, A. L., Schmitt, F. C., Tan, P. H., Tse, G. M., Weigelt, B., Ellis, I. O., and Reis-Filho, J. S. (2011) Basal-like and triple-negative breast cancers: a critical review with an emphasis on the implications for pathologists and oncologists, *Modern pathology : an official journal of the United States and Canadian Academy of Pathology, Inc 24*, 157-167.

291.  Herschkowitz, J. I., Simin, K., Weigman, V. J., Mikaelian, I., Usary, J., Hu, Z., Rasmussen, K. E., Jones, L. P., Assefnia, S., Chandrasekharan, S., Backlund, M. G., Yin, Y., Khramtsov, A. I., Bastein, R., Quackenbush, J., Glazer, R. I., Brown, P. H., Green, J. E., Kopelovich, L., Furth, P. A., Palazzo, J. P., Olopade, O. I., Bernard, P. S., Churchill, G. A., Van Dyke, T., and Perou, C. M. (2007) Identification of conserved gene expression features between murine mammary carcinoma models and human breast tumors, *Genome biology 8*, R76.

292.  Prat, A., Parker, J. S., Karginova, O., Fan, C., Livasy, C., Herschkowitz, J. I., He, X., and Perou, C. M. (2010) Phenotypic and molecular characterization of the claudin-low intrinsic subtype of breast cancer, *Breast Cancer Research 12*, R68.

293.  Sullivan, L. B., Gui, D. Y., Hosios, A. M., Bush, L. N., Freinkman, E., and Vander Heiden, M. G. (2015) Supporting Aspartate Biosynthesis Is an Essential Function of Respiration in Proliferating Cells, *Cell 162*, 552-563.

294.  Kenwood, B. M., Weaver, J. L., Bajwa, A., Poon, I. K., Byrne, F. L., Murrow, B. A., Calderone, J. A., Huang, L., Divakaruni, A. S., Tomsig, J. L., Okabe, K., Lo, R. H., Cameron

Coleman, G., Columbus, L., Yan, Z., Saucerman, J. J., Smith, J. S., Holmes, J. W., Lynch, K. R., Ravichandran, K. S., Uchiyama, S., Santos, W. L., Rogers, G. W., Okusa, M. D., Bayliss, D. A., and Hoehn, K. L. (2014) Identification of a novel mitochondrial uncoupler that does not depolarize the plasma membrane, *Mol. Metab. 3*, 114-123.

295. Weinberg, S. E., and Chandel, N. S. (2015) Targeting mitochondria metabolism for cancer therapy, *Nature chemical biology 11*, 9-15.

296. Jiang, Z., Huang, J., Xie, C., Li, X., Liu, L., He, J., Pan, H., Huang, L., Fan, X.-X., Yao, X.-J., Xie, Y., Li, N., Liu, L., He, J.-X., and Lai-Han Leung, E. (2016) *Combined use of PI3K and MEK inhibitors synergistically inhibits lung cancer with EGFR and KRAS mutations*, Vol. 36.

297. James, M. O., Jahn, S. C., Zhong, G., Smeltz, M. G., Hu, Z., and Stacpoole, P. W. (2017) Therapeutic applications of dichloroacetate and the role of glutathione transferase zeta-1, *Pharmacology & therapeutics 170*, 166-180.

298. Kankotia, S., and Stacpoole, P. W. (2014) Dichloroacetate and cancer: New home for an orphan drug?, *Biochim. Biophys. Acta 1846*, 617-629.

299. Michelakis, E. D., Webster, L., and Mackey, J. R. (2008) Dichloroacetate (DCA) as a potential metabolic-targeting therapy for cancer, *British Journal Of Cancer 99*, 989.

300. Bonnet, S., Archer, S. L., Allalunis-Turner, J., Haromy, A., Beaulieu, C., Thompson, R., Lee, C. T., Lopaschuk, G. D., Puttagunta, L., Bonnet, S., Harry, G., Hashimoto, K., Porter, C. J., Andrade, M. A., Thebaud, B., and Michelakis, E. D. (2007) A Mitochondria-K+ Channel Axis Is Suppressed in Cancer and Its Normalization Promotes Apoptosis and Inhibits Cancer Growth, *Cancer Cell 11*, 37-51.

301. Stacpoole, P. W., and Greene, Y. J. (1992) Dichloroacetate, *Diabetes Care 15*, 785-791.

302. Stacpoole, P. W., Harman, E. M., Curry, S. H., Baumgartner, T. G., and Misbin, R. I. (1983) Treatment of lactic acidosis with dichloroacetate, *The New England journal of medicine 309*, 390-396.

303. Li, J., Kato, M., and Chuang, D. T. (2009) Pivotal role of the C-terminal DW-motif in mediating inhibition of pyruvate dehydrogenase kinase 2 by dichloroacetate, *The Journal of biological chemistry 284*, 34458-34467.

304. Finlay, D. K., Rosenzweig, E., Sinclair, L. V., Feijoo-Carnero, C., Hukelmann, J. L., Rolf, J., Panteleyev, A. A., Okkenhaug, K., and Cantrell, D. A. (2012) PDK1 regulation of mTOR and hypoxia-inducible factor 1 integrate metabolism and migration of CD8+ T cells, *The Journal of Experimental Medicine 209*, 2441-2453.

305. Denko, N. C. (2008) Hypoxia, HIF1 and glucose metabolism in the solid tumour, *Nat Rev Cancer 8*, 705-713.

306. Hiller, K., and Metallo, C. M. (2013) Profiling metabolic networks to study cancer metabolism, *Current opinion in biotechnology 24*, 60-68.

307. Chen, Y., Cairns, R., Papandreou, I., Koong, A., and Denko, N. C. (2009) Oxygen consumption can regulate the growth of tumors, a new perspective on the Warburg effect, *PloS one 4*, e7033.

308. Kumar, A., Kant, S., and Singh, S. M. (2012) Novel molecular mechanisms of antitumor action of dichloroacetate against T cell lymphoma: Implication of altered glucose metabolism, pH homeostasis and cell survival regulation, *Chem Biol Interact 199*, 29-37.

309. Anderson, K. M., Jajeh, J., Guinan, P., and Rubenstein, M. (2009) In vitro effects of dichloroacetate and CO2 on hypoxic HeLa cells, *Anticancer research 29*, 4579-4588.

310. Ayyanathan, K., Kesaraju, S., Dawson-Scully, K., and Weissbach, H. (2012) Combination of sulindac and dichloroacetate kills cancer cells via oxidative damage, *PloS one 7*, e39949.

311. Warburg, O. (1956) On the origin of cancer cells, *Science 123*, 309-314.

312. Possemato, R., Marks, K. M., Shaul, Y. D., Pacold, M. E., Kim, D., Birsoy, K., Sethumadhavan, S., Woo, H. K., Jang, H. G., Jha, A. K., Chen, W. W., Barrett, F. G., Stransky, N., Tsun, Z. Y., Cowley, G. S., Barretina, J., Kalaany, N. Y., Hsu, P. P., Ottina, K., Chan, A. M., Yuan, B., Garraway, L. A., Root, D. E., Mino-Kenudson, M., Brachtel, E. F., Driggers, E. M., and Sabatini, D. M. (2011) Functional genomics reveal that the serine synthesis pathway is essential in breast cancer, *Nature 476*, 346-350.

313. Maddocks, O. D., Berkers, C. R., Mason, S. M., Zheng, L., Blyth, K., Gottlieb, E., and Vousden, K. H. (2013) Serine starvation induces stress and p53-dependent metabolic remodelling in cancer cells, *Nature 493*, 542-546.

314. Korangath, P., Teo, W. W., Sadik, H., Han, L., Mori, N., Huijts, C. M., Wildes, F., Bharti, S., Zhang, Z., Santa-Maria, C. A., Tsai, H., Dang, C. V., Stearns, V., Bhujwalla, Z. M., and Sukumar, S. (2015) Targeting Glutamine Metabolism in Breast Cancer with Aminooxyacetate, *Clin. Cancer Res. 21*, 3263-3273.